Scanning Probe and Electron Spectroscopy Studies of Adsorbed Inorganic Systems

by

Fiona Frehill B.Sc.

A Thesis presented to Dublin City University for the degree of

Doctor of Philosophy.

Supervisors: Professor Johannes G. Vos

School of Chemical Sciences

Dublin City University

Professor Philip Moriarty

School of Physics and Astronomy

University of Nottingham

2005

Authors Declaration

I hereby certify that this material, which I now submit for assessment on the programme of study leading to the award of Doctor of Philosophy by research and thesis, is entirely my own work and has not been taken from work of others, save and to the extent that such work has been cited within the text of my work.

Signed: Fiona Frehill

Fiona Frehill

I.D. No. **50161598**

Date: 11th April '05

Abstract

The field of nanoscience is a rapidly expanding area of research with numerous applications for technology. The development of this field has been largely helped by the invention of the atomic force microscope, as well as other surface analytical techniques such as photoelectron spectroscopy. The studies described in this thesis cover a varied range of topics. These include polymeric systems, carbon nanotube and an organostannoxane cluster system. The common theme within these studies is in improving understanding of the fundamental processes that may occur in the self assembly of these systems on substrates.

Chapter 1 is an introductory chapter in that the basic concepts regarding the field of nanotechnology are introduced. In Chapter 2 the important analytical probes used in this thesis are described i.e. atomic force microscopy and photoelectron spectroscopy.

The 'parent' complex of the systems explored in Chapter 3 and Chapter 4, $[Ru(bpy)_3]^{2+}$, is introduced in Chapter 3. This is followed by an exploration of the self-assembly and the morphology observed for the redox polymer $[Ru(bpy)_2PVP_{10}Cl]Cl$ on a $SiO_2/Si(111)$ substrate. The electronic structure of this polymer is also described using synchrotron radiation photoemission.

Chapter 4 describes the modification of multi-wall carbon nanotubes with the inorganic ruthenium complex [*bis*-(2,2'-bipyridine)-(4,4'-dicarboxy-2,2'-bipyridine) ruthenium (II)]. The resulting assembly is characterised using spectroscopic and atomic force microscopy techniques. An introduction to carbon nanotubes with a discussion on some of their potential applications is also given.

In Chapter 5 atomic force microscopy imaging with subsequent statistical crystallographic analysis is used to investigate the morphology observed when an organostannoxane cluster is deposited onto a $SiO_2/Si(111)$ substrate. Advanced image analysis techniques based on Minkowski functionals is also used to provide a detailed quantitative analysis of the morphology of the organostannoxane overlayers. Variations in both the surface roughness and the in-plane correlation length are followed as a function of annealing time in order to probe the surface dewetting dynamics. The solid state electronic structure of the cluster is described using synchrotron radiation photoemission and resonant photoemission.

Finally, in Chapter 6 the results of the work undertaken are summarised with suggestions on further possible research directions.

Acknowledgements

I would like to sincerely thank and acknowledge my supervisors Prof. Han Vos and Prof. Philip Moriarty. They provided me with the opportunity, support and encouragement to do this work.

I would like to dedicate this thesis to my family; Elizabeth, Martin, Catherine and Louise, Ronan, Tadhg and Stephen.

Thanks to all the technical staff in Nottingham, DCU and DTU. No lab could ever run smoothly without their help.

Thanks to Dr. Marc in Het Panhuis and Dr. Manuel Ruther for collaboration on the nanotube work.

Prof. Jens Ulstrup, Dr. Jingdong Khang, Dr. Allan Hansen and Mikala Grubb in DTU in Denmark.

Dr. Tony Cafolla in Physics in DCU.

Dr. Jason Roche and Dr. Mick Phillips for all the helpful conversations especially near the end!

Thanks to Stephen for proof reading my thesis.

Friends past and present who have been there along the way:

The gang in Nottingham: Dave, James, Karina, Mick, the two Richie's, and my old housemates Nicola and Kevin! Friday afternoons in the Rose & Crown were certainly the most productive.

The gang in DCU: Andrea, Adrian, Bill, Dec, Eric, Helen, Johnny, Jason, Kieran, Lynda, Noel, Rob, Stefania, Tony, Marco, Mohammed, Scott and Wes. Also Clare Brady, Deirdre, Darren, Dave, Johan, Yann and Michael.

Darby, Desrae, Julie, Matt, Ronan's family, Maja, Susan and my furry housemates!

Finally, a quote from the band that has kept me sane over the last few years seems appropriate

"With your feet on the air and your head on the ground
Try this trick and spin it, yeah
Your head will collapse if there's nothing in it
And you'll ask yourself

Where is my mind?"

Francis Black of The Pixies, 1988

Table of Contents

List of Abbreviations

2D-FFT	2D Fast Fourier transform
AFM	Atomic force microscope
CA	Potential step chronoamperometry
CM	Contact mode
CNT	Carbon nanotube
CVD	Chemical vapour deposition
CV	Cyclic voltammetry
DCM	Dichloromethane
DI	Digital Instruments
DOS	Density of States
DPN	Dip-pen nanolithography
DRAM	Dynamic random access memory
DSP	Digital signal processing
E_b	Binding energy
E_f	Final energy
E_F	Fermi level energy
E_i	Initial energy
E_{kin}	Kinetic energy
E_{vac}	Vacuum level energy
EFM	Electrostatic force microscopy
EIS	Electrochemical Impedence spectroscopy
ESCA	Electron Spectroscopy for Chemical Analysis
EQCM	Electrochemical quartz crystal microbalance
FWHM	Full-width-at-half-maximum
GS	Ground state
HOMO	Highest occupied molecular orbital
HOPG	Highly oriented pyrolytic graphite
IMFP	Inelastic mean free path
ISC	Intersystem crossing
I_t	Tunnelling current
I –V	Current – Voltage
LC	Ligand centred
LDOS	Local density of states
LINAC	Linear accelerator
LUMO	Lowest unoccupied molecular orbital
MC	Metal-centred
MEM	Micro-electromechanical System
MFM	Magnetic force microscopy
MLCT	Metal-to-ligand charge transfer
MRFM	Magnetic resonance force microscopy
MWCT	Multi-wall carbon nanotube
NCM	Non-contact mode
NEXAFS	Near-edge x-ray absorption fine structure spectroscopy
PES	Photoelectron spectroscopy
RESPES	Resonant photoelectron spectroscopy
RF	Radio frequency
R_{rms}	Root-mean-square-roughness
R_A	Average roughness
SAM	Self-assembled monolayer
SCLS	Surface core level shift

SECM	Scanning electrochemical microscopy
SEM	Scanning electron microscopy
SFM	Scanning force microscopy
SNOM	Scanning near-field optical microscopy
SNTM	Scanning near-field thermal microscopy
SPM	Scanning probe microscopy
SR	Synchrotron radiation
STM	Scanning tunnelling microscopy
TEM	Transmission electron microscopy
TM	Tapping mode
UHV	Ultra-high vacuum
VdW	Van der Waals

bpy	2,2-bipyridine
dcbpy	4,4'-dicarboxy-2,2'-bipyridine
Fc	ferrocenyl
PVP	poly(4-vinyl)pyridine

List of Figures

List of Tables

Chapter 1

Introduction

In this chapter, an introduction to the concepts of nanotechnology is given followed by a description of some of its historical origins. No attempt to include the whole of this area is made; rather areas relevant to the studies presented in the remaining chapters will be introduced. The motivation and layout of the thesis are also given.

"Imagination is the true magic carpet"

Norman Vincent Peale

1.1 Nanoscience

Introduction

The 20th century is generally regarded as the era of the silicon revolution and of micro-scale electronics, whereas the 21st century is becoming known as the "nano-age". The scientific field of research designated by many as 'nanoscience' or 'nanotechnology' is one of the largest and fastest growing areas of scientific and commercial interest. 'Nanoscience' is a term used to describe studies of physical phenomena on the length scale of 1-100nm and concerning the properties of objects containing a countable number of atoms or molecules, as opposed to *infinitely* extended solids or individual atoms and molecules [1]. Nanostructured objects constitute a bridge between single molecules and bulk systems. Individual nanostructures involve nanotubes, nanowires, nanoparticles, clusters and quantum dots, while collections of nanostructures involve arrays, assemblies and superlattices. 'Nanotechnology' is the term used to describe all activities concerned with the nanoscience of atoms and molecules which have applications in the real world.

The nanotechnology revolution was first proposed in 1959 when Richard P. Feynman gave his well known lecture '*There's plenty of room at the bottom*' [2]. His presentation stated that there is no fundamental reason why devices should not be built atom-by-atom, molecule-by-molecule. This effectively moved the idea of nanoscience from 'science-fiction' to 'science-fact'. The concept of assembling devices from individually positioned atoms and molecules has since come to be known as the 'bottom-up' approach to fabrication as opposed to the 'top-down' approach. The top-down approach exploits the ability to realize smaller and smaller structures using lithography and related techniques for the construction of electronic components and microelectromechanical systems (MEMs) [3]. The bottom-up approach builds nanodevices and/or nanomachines starting from molecular building

blocks instead of carving lithographically bigger pieces of matter into smaller and smaller chunks. Feynman postulated that nanoscale engineering would require the development of complex instrumentation that would act as our 'eyes' and 'fingers' in the nanoworld. A spectrum of scientific and technical instrumentation is now well established.

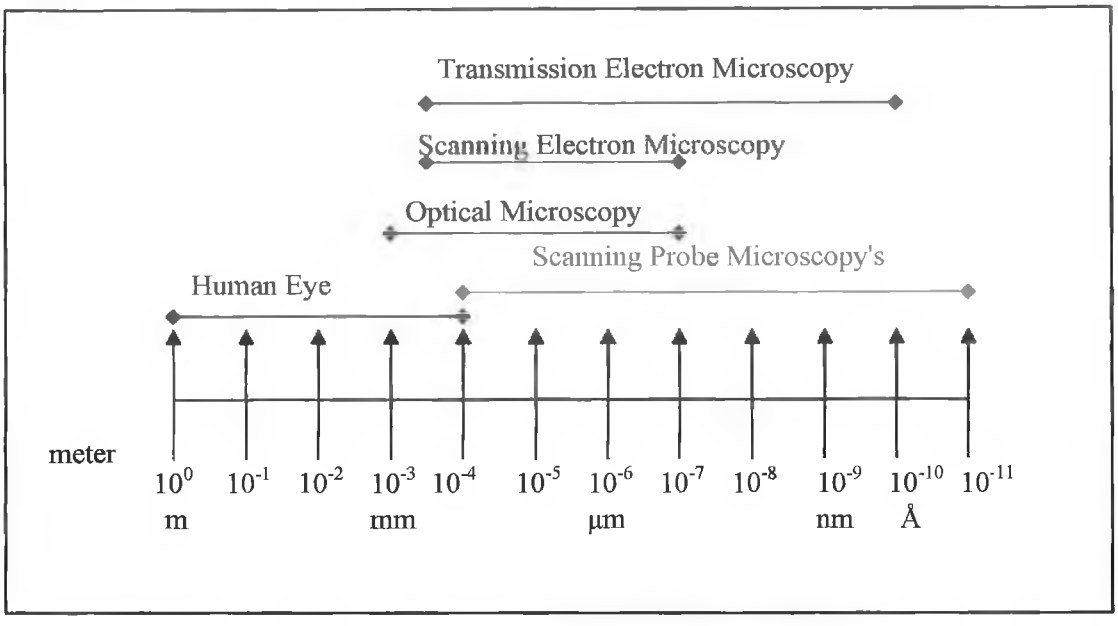

***Figure 1.1** Spatial resolution of some microscopial techniques*

Up to the early 1980's, information on the sub-micrometer scale length was accessible using only indirect techniques such as electron or x-ray diffraction or with electron microscopies that required a vacuum environment. However, Binnig and Rohrer opened up the door to the bottom-up approach with the invention of the scanning tunnelling microscope (STM) in 1982 [4]. Their project aimed at developing a microscopical technique able to generate real-space images of a surface with a resolution on the nanometre scale. This discovery represented also a big improvement for the development of miniaturised electronic devices. A family of related scanning probe instruments was developed in the decade following the

invention of the STM. With each new scanning probe technique came a new method of investigating material properties at the nano-level.

With the STM, it is not only possible to image atoms or molecules at, or adsorbed on a surface, but by careful control of tip-surface interactions, individual adsorbates may be controllably positioned. The first demonstration of controllable manipulation of atoms was achieved in 1990 by Eigler and Schweizer [5], who positioned over thirty xenon atoms on a surface to spell 'IBM'. In other experiments, nanometer-scale mounds of material (typically gold) have been deposited in a controlled manner through electric field-induced evaporation with an STM tip [6]. Magnetic properties of a sample have been modified with near-atomic precision [7], individual atoms have been selectively desorbed from surfaces [8], and charge has been stored on nitride-on-silicon samples on a nanometre scale [9].

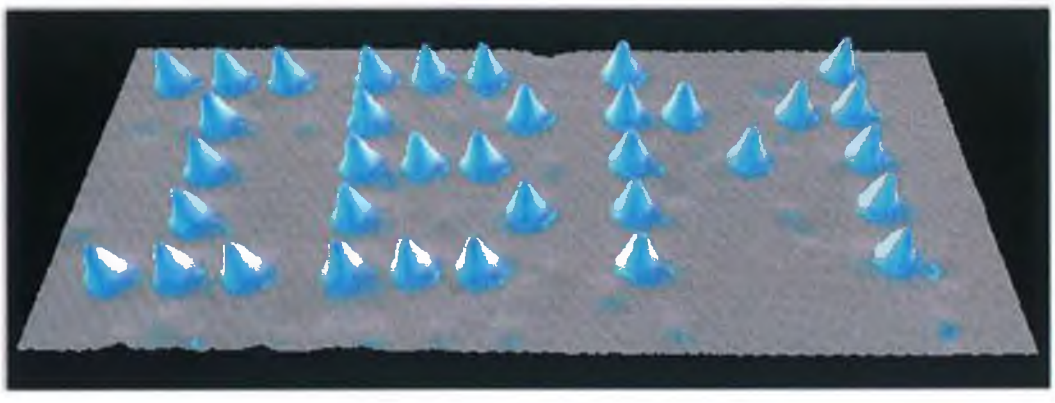

***Figure 1.2** A STM constructed structure: Individual Xe atoms positioned on a Ni surface at a temperature of 4K to form the IBM logo [5].*

Another related technique, dip-pen nanolithography (DPN) developed by the group of Mirkin [10] is a powerful nanopatterning technique which allows molecules to be placed on a surface via a solvent meniscus by directly writing molecular inks from a coated atomic force microscopy (AFM) tip to a substrate of interest.

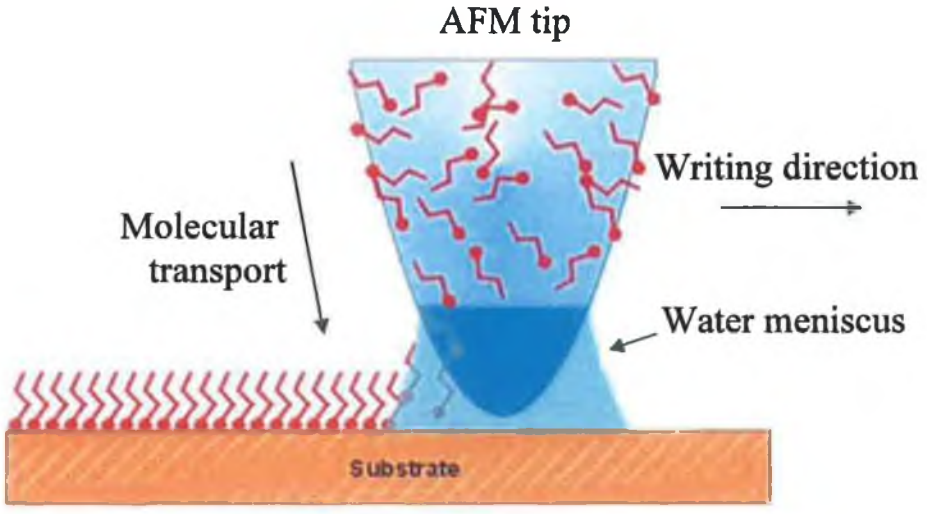

Figure 1.3 *Dip-Pen Nanolithography; a technique allowing the delivery of molecules to a suitable substrate from a solvent meniscus by directly writing molecular inks from a coated atomic force microscope tip [10].*

The merging of chemical, physical and biological knowledge has resulted in the extension of a number of macroscopic concepts to the nanoworld and in the design and creation of devices and machines that operate via electron and/or nuclear rearrangements [11]. After a period of three decades, Feynman's foresight was becoming reality.

1.1.1 Electronic Properties

Miniaturisation in microelectronics is moving from microscale to nanoscale devices. There is now more of a requirement to understand the physical and electronic properties of matter on this scale [12]. The fabrication and analysis of nanoscale structures are important aims within the field of nanotechnology, as is the linking of the nanoscopic and macroscopic dimensions. This remorseless drive to miniaturisation is rapidly approaching the 'quantum wall' where bulk properties become less certain and quantum properties 'kick in'[13]. The property of a bulk material is largely determined by the types of the constituent chemical elements and

the nature of the chemical bonds that 'hold' the atoms and molecules together to form the material. However, this 'conventional wisdom' no longer holds in the nanometre regime in which, in addition to the chemical bonds, the size, dimensionality, and shape also play important roles in determining the properties of the materials, especially the electronic, magnetic, and optical properties. These properties are strongly size-dependent. Confining electrons to such small geometries gives rise to 'particle in a box' type energy levels where the size reduction influences the electronic behaviour. Depending on their relative sizes in different spatial directions, materials may be divided into categories of different dimensionality ranging from three-dimensional to two-dimensional, one-dimensional and zero-dimensional.

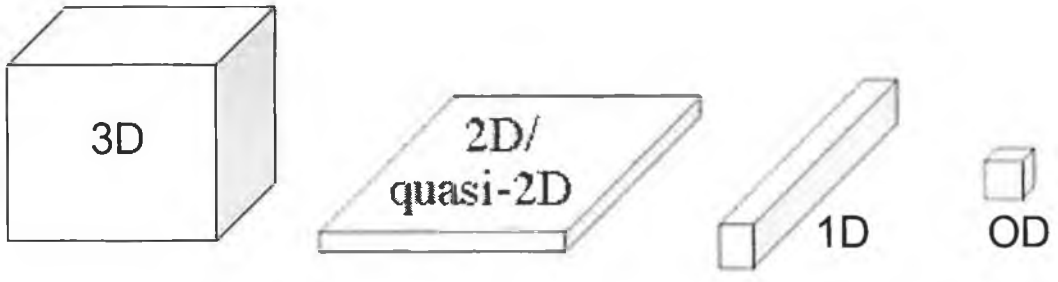

Figure 1.4 *Schematic illustrations of materials of different dimensionality ranging from 0D to 3D*

In a bulk three-dimensional (3D) metal for example, the electrons can move in three dimensions, however, if the metal is made thinner and thinner until the electrons could only move in two dimensions (2D), then this quantum confinement is called a 'quantum well'. Continued reduction to one dimension (1D) leads to a 'quantum wire' and zero dimensions (OD) to a 'quantum dot'. In three dimensions the band structure of the bulk solid originates from large numbers of electrons available for conduction. As the size of the solid decreases, the energy levels become further apart so individual atoms have well separated energy levels.

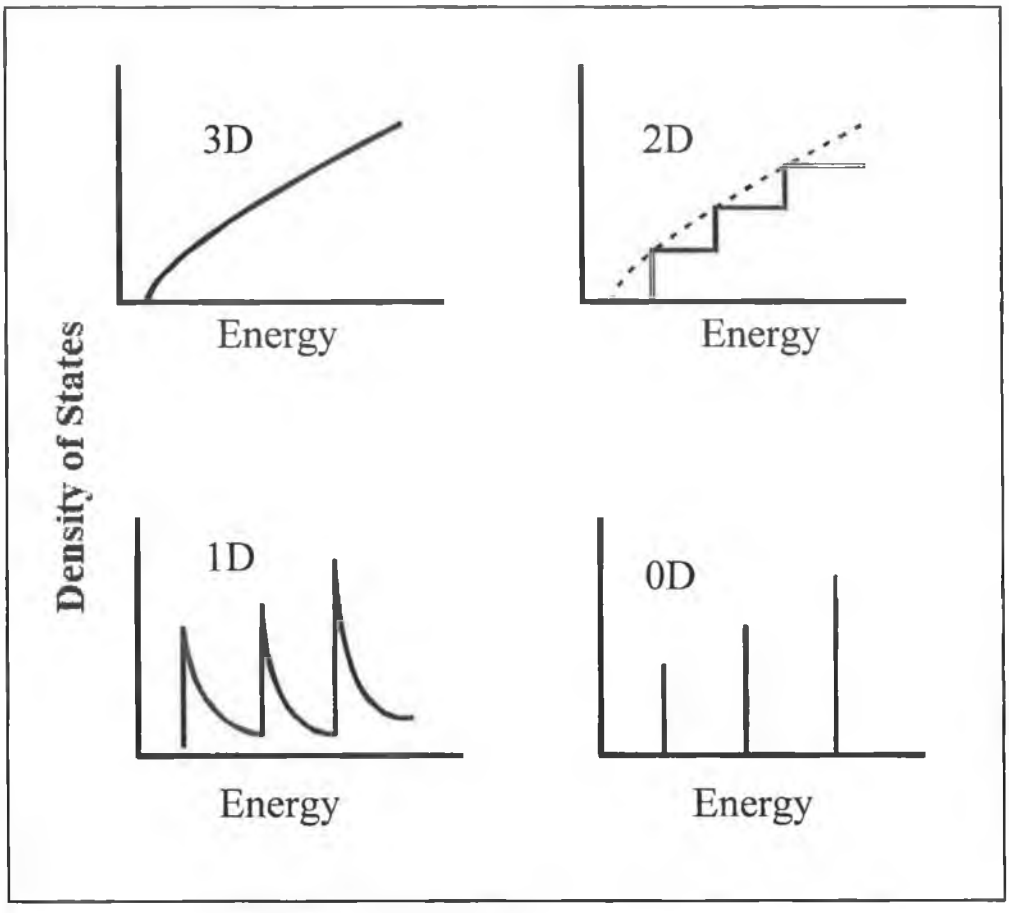

Figure 1.5 *The relationship between the structure dimension and the density of states [14]. A 3D solid has a (density of state) DOS with a smooth* $\sqrt{E}$ *dependence. In a 2D case the DOS is a step-wise distribution and in a 1D a* $\frac{1}{\sqrt{E}}$ *dependence gives singularities at the band edges. In 0D the energy states are represented as discrete delta-functions.*

The production of individual nanostructures is crucial to nanotechnology in order to form basic components that may be combined into more complex devices. However, it doesn't make sense to fabricate a nanoscale material that is complex yet does nothing when its environment is changed. It has to be a functional material. This realisation of molecule-based miniature devices with advanced functions requires the development of new and efficient approaches for combining molecular building blocks into desired functional structures, ideally with these structures supported on suitable substrates [15,16,17].

1.1.2 Device Applications

One example of a method of forming nanostructures is based on the phenomenon of self-assembly. In this technique, the many nanostructures form spontaneously due to interactions between constituent parts of the self-assembling system. It requires very precise tailoring of the interactions of the systems such that the desired structures are formed. A widely used application of the self-assembly process in surface science is that of the self-assembled monolayer (SAM), which consist of a monolayer of a particular type of molecule. The interactions between the molecules cause the monolayer to adopt a specific morphology. Self-assembly is not limited to complete monolayers. At sub-monolayer coverage interactions between adsorbates may lead to the formation of large quantities of self-assembled nanostructures [18].

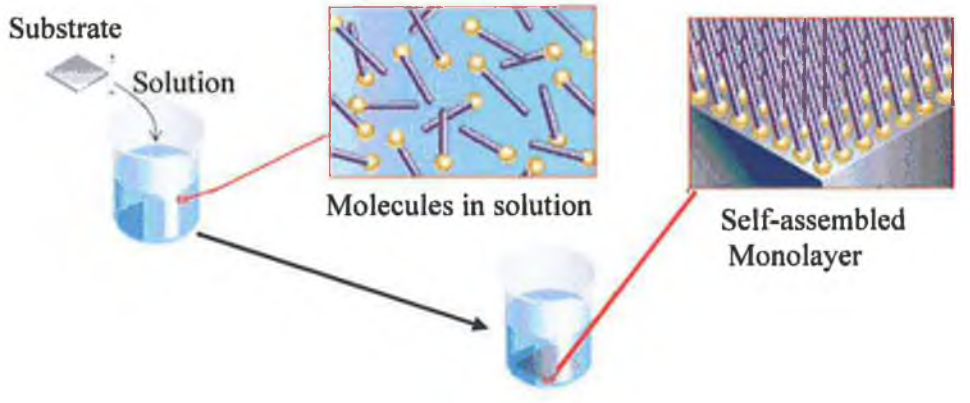

***Figure 1.6** Self-assembly occurs spontaneously as molecules with a specially chosen end group (yellow) attach themselves to a substrate material. Typically the molecules do not end up perpendicular to the substrate [19].*

Moore's law indicates that the performance of semiconductor devices doubles every 18 months [20]. This observation has been valid for three decades and for it to continue to apply, transistor sizes will have to shrink to the molecular scale. An important area of research is molecular electronics, for which molecules that are quantum electronic devices are designed and synthesised using the batch processes of

chemistry and then assembled into useful circuits through the process of self-organisation and self-alignment. This bottom-up approach is widely regarded as a viable alternative approach towards the further miniaturisation of devices.

Molecular scale electronics is a field emerging around the premise that it is possible to build individual molecules that can perform functions identical or analogous to those of the transistors, diodes, conductors and other key components of microcircuits. The idea comes from a farsighted paper by Aviram and Ratner predicting that single molecules with a donor-spacer-acceptor structure would have rectifying properties when placed between two electrodes [21]. If molecular electronics achieves the ultimate goal of using individual molecules as switches and for example, carbon nanotubes as the wires in the circuit, non-volatile memories with one million times the bit area density of today's DRAMs (dynamic random access memory) could be anticipated.

In 1999 researchers at UCLA experimentally demonstrated an electronically addressable molecular switch that operates in a totally 'dry' environment [22]. As illustrated in Figure 1.7, logic gates were fabricated from an array of configurable molecular switches, each consisting of a monolayer of electrochemically active rotaxane molecules sandwiched between metal electrodes [17]. Molecular transistors could be the building blocks of electronics on the nanometre scale. Rotaxane conducts via resonant tunnelling through unoccupied molecular orbitals when it is in its reduced chemical state (switch closed), but it is a tunnelling barrier in its oxidised state (switch open). The switch can be closed electronically in a solid-state circuit by applying the appropriate voltage across the molecule [23,24].

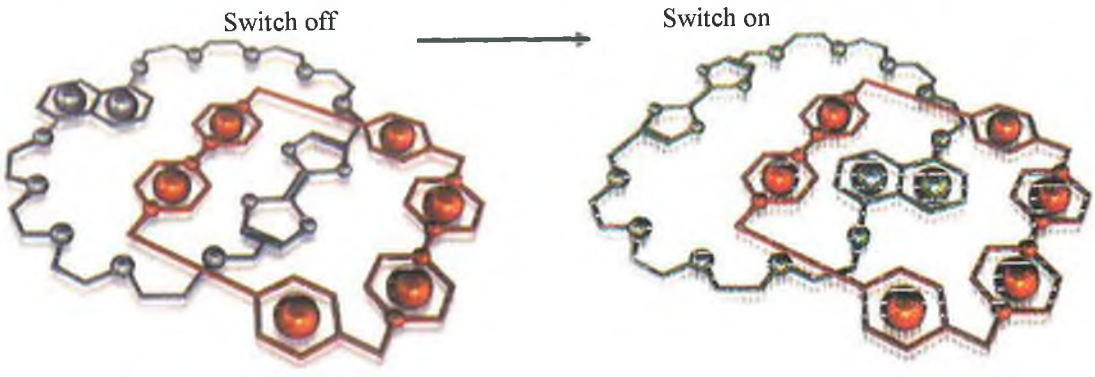

***Figure 1.7** Molecular transistor 'Rotaxane' [17].*

The 'rotaxane nanotransistor' is just one example. Extensive research efforts have been directed over the last years to the organisation of miniaturised devices on monolayer-functionalised surfaces [25]. Photolithographic and lithographic patterning of monolayers led to the selective microstructured association of biomaterials such as oligonucleotides [26], antibodies [27], and cells [28], onto metal surfaces. Thin metal films [29,30], and especially metal island films [31,32], have attracted considerable interest in view of their unique optical properties [33], and the enhanced photophysical phenomena exhibited by adsorbates on these films, such as surface enhanced Raman scattering [34], absorption and luminescence [35], and surface-plasmon resonance [36]. The development of integrated nanostructured interfaces has recently become an increasingly active area of research both from the fundamental interest and the perspective of a wide range of innovative applications in catalysis, sensor science, non-linear optics, and molecular electronics [37]. With the discovery of carbon nanotubes [38], sheets of graphite wrapped to form molecular tubes, nanotechnology has taken considerable steps forward. The combination of scanning probe microscopy (SPM) and nanotubes has resulted in the creation of molecular devices such as a nanotube transistor [39].

1.2 Surface Analysis

The difficulties of producing and maintaining a clean, uncontaminated surface limited surface science to the study of 'real' surfaces in the early part of the 20th century [40]. However, many important discoveries in surface science were still made in this period, such as the photoelectric which was rationalised by Einstein [41]. Photoelectron spectroscopy (PES), based on his explanation has become an important tool to study the electronic structure of atoms and molecules, since its first introduction in the 1960s [42]. Constantly improving experimental techniques and availability of high flux dedicated photon sources (synchrotron storage rings) have advanced PES. It has evolved from the study of the total photo-absorption spectra of gaseous samples [37], to high resolution angle-resolved differential measurements, which allow one to investigate not only the main electronic transitions but also different decay channels, giving thus an insight into electron-electron correlation in atoms and molecules, as well as nuclei dynamics, and vibrational structures of molecules.

Surface science approaches to molecular interactions with metallic and non-metallic surfaces have rested on electrochemical methods (voltammetry, electrochemical impedance spectroscopy, capacitance measurements), spectroscopy (PES, fluorescence, surface plasmon, reflection spectroscopy and ellipsometry, surface-enhanced Raman spectroscopy), adsorption isotherms and piezoelectric techniques (quartz microbalance and cantilever sensor techniques). In recent years as mentioned already, these approached have been combined with scanning probe microscopy instruments and scanning tunnelling microscopy. The atomic force microscope (AFM) was invented in 1986 by Binnig, Quate and Gerber [43] to extend scanning probe investigations to include non-conducting samples.

1.3 Thesis Motivation

Many of the important properties of materials depend critically on the structure of their surfaces and how these surfaces interact with their environment. In recent years considerable effort has been expended to studying the interaction of a range of small organic molecules with atomically clean, reconstructed silicon surfaces under ultra-high vacuum (UHV) conditions. In this thesis however, research will be presented motivated by the need to develop an understanding of the behaviour of specific polymer- and organometallic molecular-assemblies on solid surfaces deposited *from solution*. This is important in fundamental respects, for many applications necessitate an understanding of the self-organisation, interactions, and morphology of molecular and polymeric systems deposited from solution. Also, to exploit surface-scale phenomena in devices, there must be a better understanding of the chemical and physical interactions that occur on, and are unique to, this size scale.

Three different types of molecular systems are investigated:

i). Redox polymers of the type $[M(bpy)_2(PVP)_nCl]Cl$ where M is ruthenium or osmium, bpy is 2,2'-bipyridine and PVP is poly(4-vinyl)pyridine are investigated in Chapter 3. The pursuit of a complete understanding of these polymer systems and their applications has been ongoing for many years. There have been extensive electrochemical studies on these systems [44-48], but little non-electrode based surface studies and photoemission studies. Chapter 3 in some fashion was therefore motivated by the need to obtain more information about the structure of thin layers of such materials.

ii). Chapter 4 concerns itself with the systematic approach to the functionalisation of multi-walled carbon nanotubes with a ruthenium poly(pyridyl) based complex. The synthesis, spectroscopic and scanning

probe microscopy characterisation of the functionalised complex will be described.

iii). An organometallic cluster comprised of six ferrocene units connected to a stannoxane central core $[BuSn(O)OC(O)Fc]_6$ (Fc is ferrocenyl) is examined in Chapter 5.

Photoemission spectroscopy is a common theme throughout this thesis and reflects the increasingly important role high resolution techniques have in modern material characterisation. The atomic force microscopy technique plays a pivotal role in this work as it allows the mechanical properties of both conducting and insulating samples to be investigated.

1.4 Thesis Layout

The thesis has three main experimental chapters (3-5), which were written to be somewhat 'stand alone'. However, a central theme of this thesis is the application of AFM and PES as probes. Prior to the experimental chapters, Chapter 1 has given an introduction to the area of nanoscience, and a background to the development of the most relevant surface analytical techniques used in nanoscience.

In Chapter 2, the background theory of the primary techniques used throughout this thesis will be discussed. While several experimental techniques are used, the most relevant have been:

i). Atomic force microscopy, used in studies ranging from relatively simple visualisation of morphology to more advanced examination of structures and properties on the nanometre scale.

ii). Photoemission spectroscopy, used to investigate the solid state electronic structures of a redox polymer and an organometallic molecule used in this work.

Chapter 3 will describe the synthesis and characterisation of a range of polymers containing poly(pyridyl) complexes of ruthenium^{II} and osmium^{II}. The main part of this chapter is the surface analysis of the polymers on native oxide covered silicon substrates. This analysis serves as an introduction to AFM imaging, and will describe the morphology of the polymeric systems deposited from solution. PES will then be used to analyse the solid state core level and valence band electronic states of one of the ruthenium polymers.

In Chapter 4 the covalent attachment of an inorganic ruthenium complex to amino-functionalised multi-walled carbon nanotubes will be described. Characterisation of the resulting complex will be discussed using spectroscopic methods and AFM imaging.

Chapter 5 will present an extensive study of an organometallic molecule. This molecule was first reported by Chandrasekhar at al., thus the synthesis and characterisation will only be briefly described [49]. The remainder of this chapter will focus on the studies of the self-organisation, interactions and morphology of the molecule when deposited on a solid substrate from solution. Having previously introduced analysis using AFM and PES methods in studies of the polymeric systems in chapter 3, both techniques are extensively used in this section of the work. AFM studies that will be described range from visualisation of morphology to a more in-depth examination that will include annealing experiments, statistical crystallographic analysis, and electrical contact measurements of the surface. The solid state electronic structure of the molecule will be described using PES and RESPES. The emphasis throughout will be on surface structural properties. Chapter 6 will bring the thesis to a close by discussing some of the conclusions of the experimental results and recommendations for future work will be given.

Last but not least, the acknowledgements underline the importance of the collaborative efforts required for this thesis to be presented here. Chapter 4 is based on a collaborative effort with Dr. Marc In Het Panhuis. The remaining thesis work is based on time spent at Nottingham University in collaboration with Dr. Philip Moriarty, who acts as a second supervisor for this thesis.

1.5 References

1. Moriarty P., **2001**, *Rep. Prog. Phys.*, 64, 297, and references therein.
2. Feynman R.P. **1960**, *Sci. Eng.*, 23,22.
3. The Internet Technology Roadmap for Semiconductors (ITRS) http://public.itrs.net
4. Binnig G., Roher H., Gerber C., Weibel E., **1982**, *Phys. Rev. Lett.* 49, 57.
5. Eigler D.M., Schweizer E.K., **1990**, *Nature,* 344, 524.
6. Mamin H.J., Chiang S., Birk H., Guethner P.H., Rugar D., **1991**, *J. Vac. Sci. Tech. B.*, 9, 1398.
7. Wiesendanger R., Schvets I.V., Burgler D., Tarrach G., Guntherodt H. –J., Coey J.M.D., **1992**, *Z. Phys. B.*, 86, 1.
8. Lyo I.-W., Avouris P.H., **1990**, *J. Chem. Phys.*, 93, 4479.
9. Barrett R.C., Quate C.F., **1991**, *J. Appl. Phys.*, 70, 2725.
10. Piner D., Zhu J., Xu F., Hong S., Mirkin C.A., **1999**, *Science*, 283, 661.
11. Balzani V., Venturi M., Credi A., **2002**, in *Molecular Devices and Machines – A Journey into the Nanoworld*, Wiley – VCH Publications, New York.
12. Timp G., **1999**, in *Nanotechnology*, AIP Publications, New York.
13. Gross M, **2002**, *Chemistry in Britain*, 38, 36.
14. Castro T., Reifenberger R., Choi E., Andres R.P., **1990**, *Phys. Rev. B.,* 13, 8548.
15. Collier C.P., **1999**, *Science,* 285, 391.
16. Lopinski G.P., Wayner D.D.M., Wolkow R.A., **2000**, *Nature*, 406, 48.
17. Joachim C., Gimzewski J.K., Aviram A., **2000,** *Nature*, 408, 541.
18. Yokoyama T., Yokoyama S., Kamikado T., Okuno Y., Mashiko S., **2002**, *Nature*, 413, 619.
19. Whitesides G.M., **2002**, *Science,* 295, 2418.

20. Moore G., **1965**, *Electronics*, 38, 114.

21. Aviram A., Ratner M.A., **1974**, *Chem. Phys. Lett.*, 29, 277.

22. Collier C.P., Wang E.W., Belohradsky M., Raymo F.M., Stoddart J.F., Kuekes P.J., Williams R.S., Heath J.R., **1999**, *Science*, 285, 391.

23. Balzani V., Gomez-Lopez M., Stoddart J.F., **1998**, *Acc. Chem. Res.*, 31, 405.

24. Credi A., Balzani V., Langford S.J., Stoddart J.F., **1997**, *J. Amer. Chem. Soc.*, 119, 2679.

25. Brown R., Smith E.W., Graham D., **2001**, *Tetrahedron*, 42, 2197.

26. Victor H., Perez L., **2002**, *Biosen. & Bioelec.*, 17, 71.

27. Wink T., Van Zuilen S.J., **1997**, *Analyst*, 122, 43R.

28. Hart J.P., Abass A.K., Cowell D., **2002**, *Biosen. & Bioelec.*, 17, 389.

29. Setkus A., Razumiene J., Galsikas A., **2002**, *Sensor. Actuat. B.*, 85, 1.

30. Bright R.M., Musick M.D., Natan M.J., **1998**, *Langmuir*, 14, 5695.

31. Anno E., Tanimoto M., **2000**, *J. Appl. Phys.*, 88, 3426.

32. Sandrock M.L., Pibel C.D., Geiger F.M., **1999**, *J. Phys. Chem. B.*, 103, 2668.

33. Felidj N., Aubard J., Levi G., **2002**, *Phys. Rev. B.*,65, 075149.

34. Salamon F., Tollin G., **2001**, *J. Int. Spec.*, 15, 161.

35. Han L., Daniel D.R., Maye M.M., **2001**, *Anal. Chem.*, 73, 4441.

36. Lavrik N.V., Tipple C.A., **2001**, *Chem. Phys. Lett.*, 336, 371.

37. Brust M., Kiely C.J., **2002**, *J. Colloid. Sur. A.*, 202, 175.

38. Iijima S., **1991**, *Nature*, 354, 56.

39. Tans S.J., Verschueren A.R.M, Dekker C., **1998**, *Nature*, 393, 49.

40. Zangwill A., **1988**, in *Physics at Surfaces*, University Press Publications, Cambridge.

41. Einstein A., **1905**, *Ann. Physik*, 17, 132.

42. Madden R.P., Codling K., **1963**, *Phys. Rev. Lett.*, 10, 516.

43. Binnig G., Quate C.F., Gerber Ch., **1986**, *Phys. Rev. Lett.*, 56, 930.

44. Forster R. J., Vos J. G., **1992**, *Electrochim. Acta.*, 37, 159.

45. Forster R. J., Vos J. G., **1994**, *Langmuir*, 10, 4330.

46. Doherty A. P., Vos J. G., **1997**, *Anal. Chim. Acta.*, 344, 159.

47. Hogan C. F., Forster R. J., **1999**, *Anal. Chim. Acta.*, 396, 13.

48. Forster R. J., Figgemeir E., Lees A. C., Hjelm J., Vos J. G., **2000**, *Langmuir*, 16, 7867.

49. Chandresekhar V., Nagendran S., Bsal S., Kozec M.A., Powell D.R., **2000**, *Angew. Chem. Int. Ed.*, 39, 1833.

Chapter 2

Review of Experimental Techniques

Chapter 2 serves as an introduction to the theories behind the main experimental techniques used in this thesis: atomic force microscopy and photoelectron spectroscopy. Both techniques are described in detail and a description of the commercial instruments used is also given.

"I not only use all the brains I have, but all I can borrow"

Woodrow Wilson

2.1 Scanning Probe Microscopy

Introduction

Scanning probe microscopic techniques describe collectively a range of closely related imaging techniques that are used in a broad class of surface science instruments. These instruments have introduced a new approach in the investigation of conducting, semiconducting and insulating surfaces. SPMs are based on a few common principles:

i) An atomically sharp probe (tip) interacts with the sample surface.

ii) The tip probes local physical properties of the sample. The tip-sample interaction is very sensitive to small changes in the tip-sample distance.

iii) A piezoelectric circuit allows displacements of the tip and/or the sample in the x, y, and z directions to be performed, with a precision of a fraction of an Ångstrom.

iv) A feedback system controls the distance between the tip and the sample.

SPMs exhibit high vertical and lateral resolution with the possibility to measure at solid-liquid interfaces, i.e. at surfaces in their local environment. One of the main advantages of SPMs is the ability to investigate a sample outside of a vacuum, i.e. in air or in solution. Dynamic processes that may occur on a time scale that ranges from a few milliseconds to several days may also be visualised. The SPM is composed of three parts: the probe; the scanning system; and the system that detects the interaction. The last two may be controlled by a personal computer or a workstation through an analog/digital converter and a Digital Signal Processing (DSP) card.

In all SPMs, a piezoelectric scanner is used as an extremely fine positioning stage to either move the probe over the sample or the sample under the probe. Piezoelectric materials are ceramics that change dimensions in response to an applied

voltage. Piezoelectric scanners may be designed to move in x, y and z by expanding in some directions and contracting in others. They are usually fabricated from lead zirconium titanate with various dopants added to create specific material properties. The result is a polycrystalline solid. Each of the crystals in a piezoelectric material has its own electric dipole moment. These dipole moments are the basis of the scanners' ability to move in response to an applied voltage. Figure 2.1 shows the scanner piezoelectric tube [1]. Electrodes are attached to the outside of the tube, segmenting it electrically into vertical quarters, for +x, +y, -x, -y travel. The inside of the tube is connected to the ground. To move the tube in a z-direction some voltage with respect to the ground is applied to all four quadrants. Piezoelectric scanners are critical elements in all SPMs, valued for their sub-angstrom resolution, their compactness and their high-speed response.

The SPM electronics drive the scanner in a type of raster pattern as shown in Figure 2.2 [1]. SPM data are collected in only one direction – commonly called the fast-scan direction – to minimise line-to-line registration errors that result from scanner hysteresis. While the scanner is moving across a scan line, the image data are sampled digitally at equally spaced intervals. The data recorded are the tip-sample interaction that varies from SPM to SPM. The scan length of the image may span from tens of Ångstroms to over 100microns. The image is usually a square grid of measurements (data points). To investigate the morphology of the inorganic polymer thin films and organometallic cluster of interest in this thesis, atomic force microscopy is the SPM tool of choice. As the scanning tunnelling microscope (STM) was the first in the family of SPM instruments to be invented [2], it is also described briefly as an introduction to the origins of SPM techniques. Table 2.1 shows the main SPM techniques

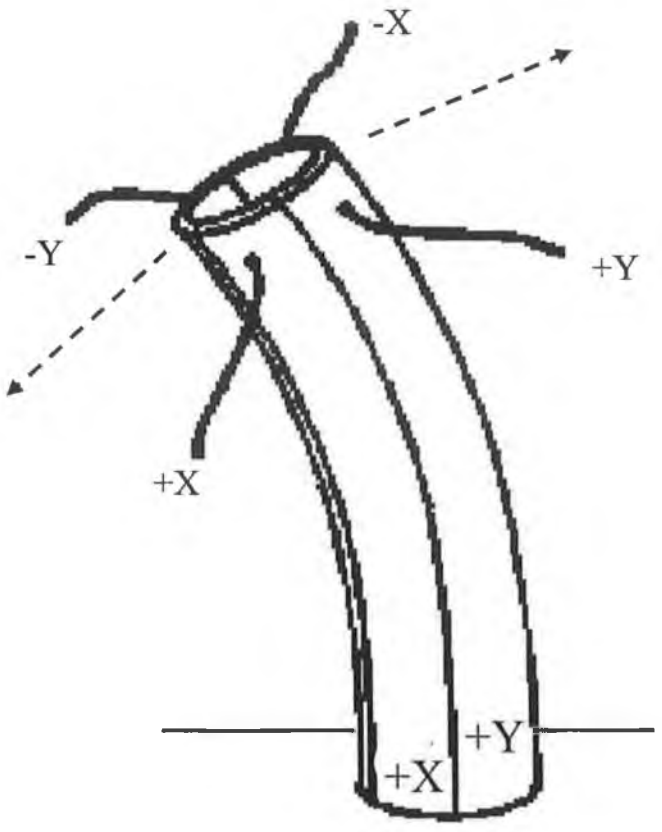

Figure 2.1 *The Scanner Tube [1].*

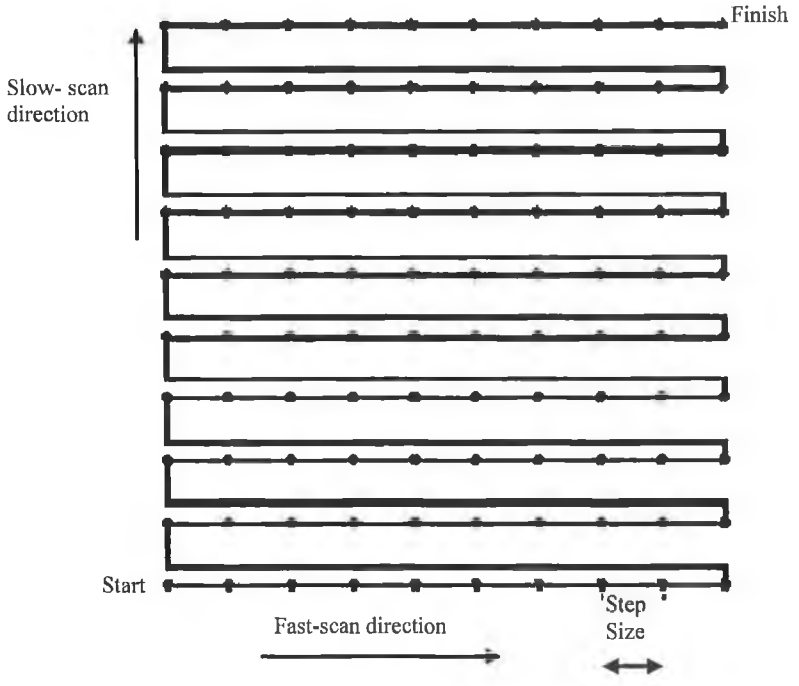

Figure 2.2 *Scanner motion during data acquisition [1].*

SPM Technique	Physical Interaction Tip – Sample	Type of Samples
STM Scanning Tunnelling Microscopy [2]	Electron tunnelling	Conductors, Semiconductors
AFM Atomic Force Microscopy [3]	Forces	Conductors, Semiconductors, Insulators
MFM Magnetic Force Microscopy [4]	Magnetic forces	Ferromagetic materials
SECM Scanning Electrochemical Microscopy [5]	Ion transfer	Conductors, Semiconductors, Insulators, adsorbates and biological films
SNOM Scanning Near-field Optical Microscopy [6]	Optical properties under the diffraction limit	Conductors, Semiconductors, Insulators, adsorbates and biological films
SNTM Scanning Near-field Thermal Microscopy [7]	Heat transfer	Conductors, Semiconductors, Insulators, adsorbates and biological films

Table 2.1 *Main Scanning Probe Microscopy techniques. They differ by virtue of the type of physical property that governs the interacting tip-sample.*

2.2 Scanning Tunnelling Microscopy

The First SPM Technique

The STM was invented by Binning, Rohrer *et al.,* in 1982 [2,8], for which they were subsequently awarded the Nobel Prize for Physics in 1986. It was the first instrument to generate real-space images of surfaces with atomic resolution. In less than two decades this invention has revolutionised nanometre-scale measurement and analysis. The STM technique involves an atomically sharp metal tip and a conducting sample that is to be investigated. It employs the principle of quantum mechanical tunnelling: if two conducting surfaces are positioned sufficiently close together, it is possible for electrons to tunnel through the potential barrier between them. The STM provides an image of the tunnelling current in a plane across a conductive sample, which, in a first approximation, corresponds to a topographical map of the sample. More

accurately the tunnelling current images give evidence of the electronic density of states (LDOS) at the surfaces [9,10]. STMs may in fact sense the density of filled or unfilled electron states near the Fermi surface, within an energy range determined by bias voltage [11].

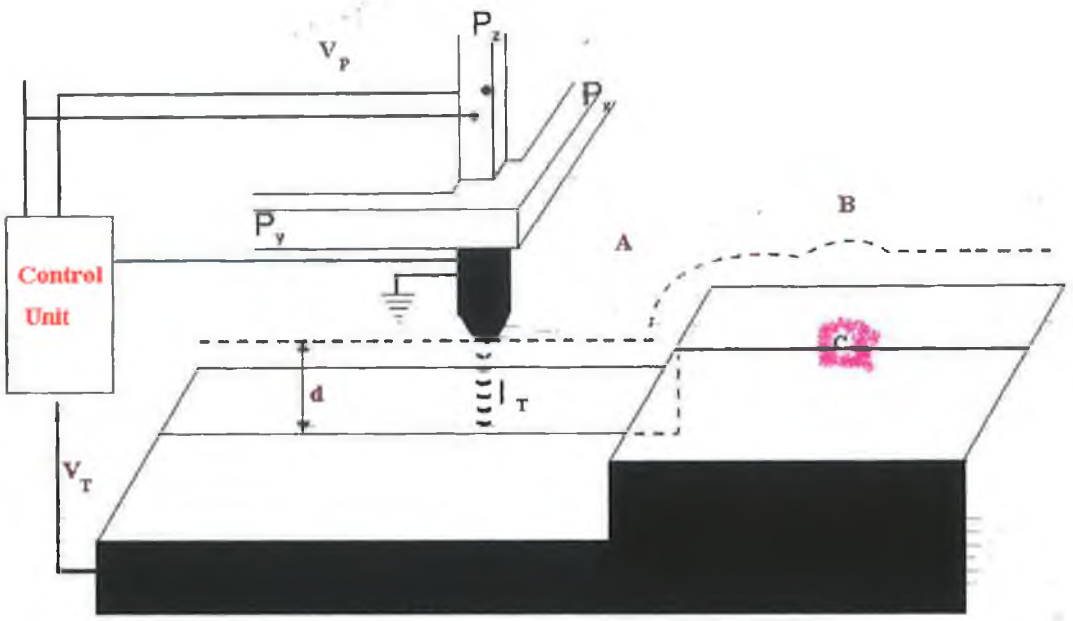

Figure 2.3 *Schematic of a STM. Piezoelectric elements P_x and P_y scan the metal tip over the surface. The control unit modulates the voltage applied the z-piezo to maintain a constant tunnel current, I_T, for a given sample bias V_T. Dashed black line indicates path of tip, whilst traversing a step edge (A), and a region with lower work function (B and C) [12].*

A schematic of the basic operation of the STM is shown in Figure 2.3. An atomically sharp metal tip, typically tungsten, gold or an alloy of platinum and iridium, is scanned across a surface by two piezoelectric elements aligned parallel to the surface (P_X and P_Y). A third piezoelectric element (P_Z), mounted perpendicular to the surface, controls the vertical position of the tip. A bias is applied to the sample relative to the tip, causing a tunnel current to flow. In the most common modes of operation, constant current mode, the Z height is adjusted by a feedback system to maintain a constant tunnel current while the tip is raster scanned over the surface. By

recording the voltage applied to the Z-piezo, a topographic image is produced. STM may provide local information with atomic resolution in real-space. An individual atom can be probed and non-periodic features on the surface analysed.

2.3 Atomic Force Microscopy

Introduction

While STM is capable of resolving individual atoms on conducting surfaces, it may not be used on insulating surfaces. Besides repulsive contact forces, both attractive and repulsive non-contact forces (electrostatic, magnetostatic and Van der Waals) may influence the tip far beyond typical STM tip-sample separations. The related technique of scanning force microscopy (SFM) was developed to address this. Utilising a range of different probes, SFM has become one of the most widely used SPM techniques. As already mentioned atomic force microscopy (AFM) is the SPM tool used throughout the research described in this thesis

Atomic force microscopy (AFM) utilises the force between an atomically sharp tip (with a terminal radius often less than 100 Ångstrom) and a sample surface, as opposed to the tunnel current measured in STM. There are three main types of AFM imaging mode: contact mode (CM), non-contact mode (NCM) and tapping mode (TM), which differ by the nature of the forces between the tip and surface. A schematic diagram of the operation of an AFM is shown in Figure 2.4. The tip is located at the free end of a cantilever that is 100 to 200μm long. Forces between the tip and the sample surface cause the cantilever to bend or deflect. A detector measures the cantilever deflection either as the tip is scanned over the sample or the sample is scanned under the tip. The measured cantilever deflection allows a computer to generate a map of surface topography. Each method has its advantages and disadvantages depending on the nature of the sample under investigation.

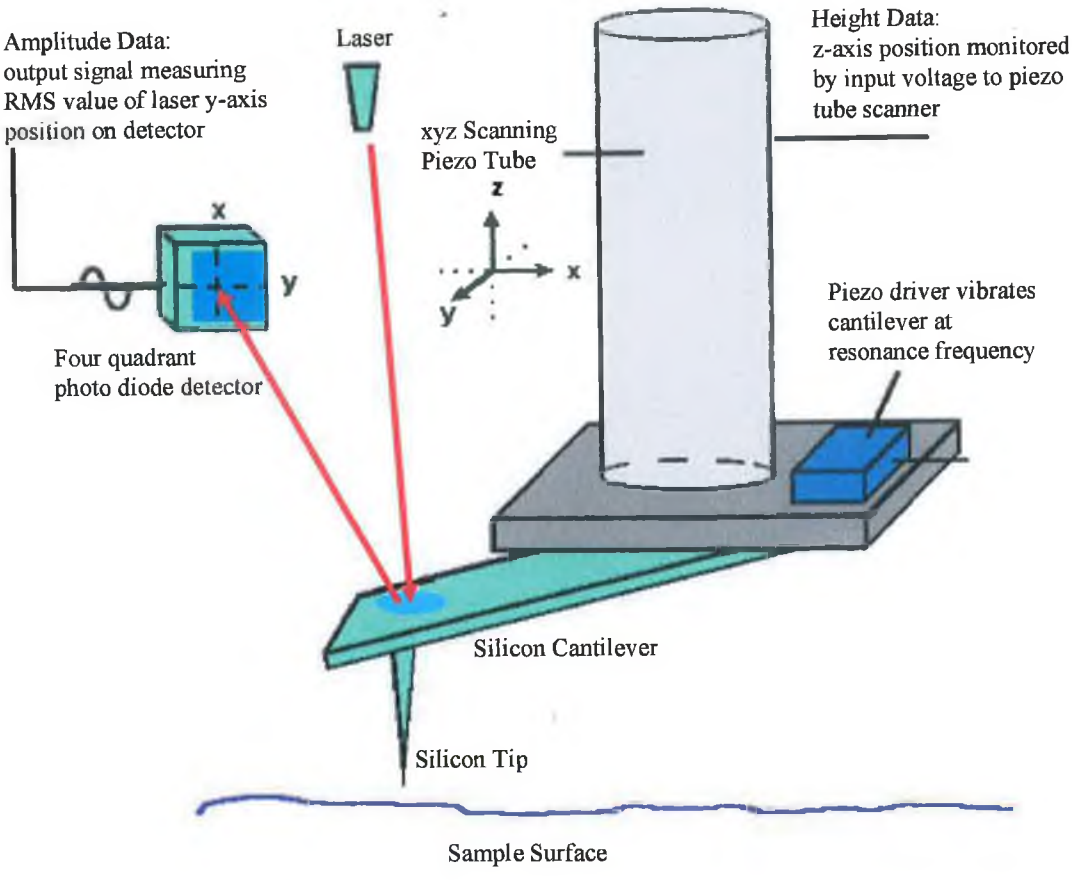

Figure 2.4 *Schematic diagram of an atomic force microscope.*

2.3.1 Interaction Forces in Atomic Force Microscopy

As the AFM tip approaches the sample it experiences an interaction with the surface. The extent of this interaction is governed by the shape of the Van der Waals (VdW) force curve as shown in Figure 2.5 [1]. The interaction forces in the AFM are often quite complex due to several factors:

i) Even if the tip apex should be mono-atomic, the number of atoms from the tip involved in the interaction is not one, due to the contribution of rather long-range forces.

ii) The forces are dependent on the environment (gas, liquid or vacuum).

iii) The scan is a dynamic process, which means that velocity dependent forces need to be considered.

iv) The tip may deform the sample.

It is important to distinguish the type of forces between the tip and the sample in order to separate the contributions and correctly interpret the experimental results [13]. At a first approximation, the forces contributing to the deflection of an AFM cantilever may be considered the attractive Van der Waals forces, and the repulsive forces. These contributions form the basis of the Lennard-Jones potential [12]. The interatomic force between point-like objects or atoms is usually described by this potential:

$$U(r) = -U_o\left[\left(\frac{r_o}{z}\right)^{12} - \left(\frac{r_o}{z}\right)^{6}\right] \tag{2.1}$$

where z equals the distance between atoms, U_o and r_o are the energy and the distance between atoms in equilibrium, respectively.

Interatomic force interactions change their character from attractive to repulsive when the distance becomes smaller than r_o. When the outermost atoms of the probing tip come close to the atoms of a sample, an overlap of electronic charge clouds causes the appearance of a strong repulsive force, and that force is proportional to the total electron density. Dispersive long-range forces are responsible for the attractive part of the Lennard-Jones potential. The main interaction forces between tip and surface of most relevance may be divided into two categories: long-range and short-range forces.

2.3.1.1 Long Range Forces

i) *Van der Waals:*

VdW forces exist between every type of atom or molecule. VdW interactions arise from dipolar interactions, and are always present between the tip and the surface. The

range of VdW interactions extend for hundreds of Ångstroms and are the dominant forces in AFM. The strengths of VdW interactions do not usually follow a simple power law with regard to tip to sample distance (d), changing from d^{-2} to d^{-7} depending on a given situation [14,15].

ii) *Electrostatic*:

These forces are due to Coulombic interactions. In AFM, they may occur between an electrically charged tip and a charged area of an insulating surface. They are important in the range from one to thousands of Ångstroms (i.e. long-ranged). They are useful in the monitoring of surface dielectric properties.

iii) *Capillary Forces:*

The curvature at the contact between the tip and the sample causes the condensation of vapour from the ambient, including water from air. Also surfaces exposed to an air environment are typically coated by a layer of water, whose thickness depends on the relative humidity of the atmosphere and on the physical-chemical nature of the object. It results in strong attractive capillary forces (about 10^{-8} N) that hold the tip in contact with the surface.

2.3.1.2 Short Range Forces

i) *Repulsive forces:*

These forces are proportional to $1/r^n$ with $n > 8$. The interatomic repulsion forces have two origins. Firstly, the repulsion between nuclei, the overlap of two electronic clouds gives rise to an incomplete screening of the nuclear charges and generates coulombic repulsions, secondly, Pauli repulsion. According to the Pauli Exclusion principle, two electrons with the same spin cannot occupy the same orbital. Thus the

electrons may only overlap when the energy of one electron is increased, which causes a repulsive interaction.

ii) *Forces of covalent bonds*:

They originate from the overlap of the wavefunctions of two or more atoms. In this case, the density of electron charges is concentrated between the two nuclei. This force decreases abruptly for separations over a few Ångstrom.

iii) *Metallic adhesion:*

They derive from the interaction between strongly delocalised electronic clouds, which cause strong interactions that decay exponentially with distance. They are important when two metallic surfaces approach to the extent that the electronic wavefunctions overlap [16].

iv) *Friction:*

During the scan there is a force component parallel to the surface, since the tip is not always oriented exactly perpendicular to the surface. This friction tends to twist the cantilever, and since the torsion angle depends on the composition of the surface, the measurement of the twist provides chemical information [17]. It was also shown that this kind of friction force may be detected on an atomic scale [18].

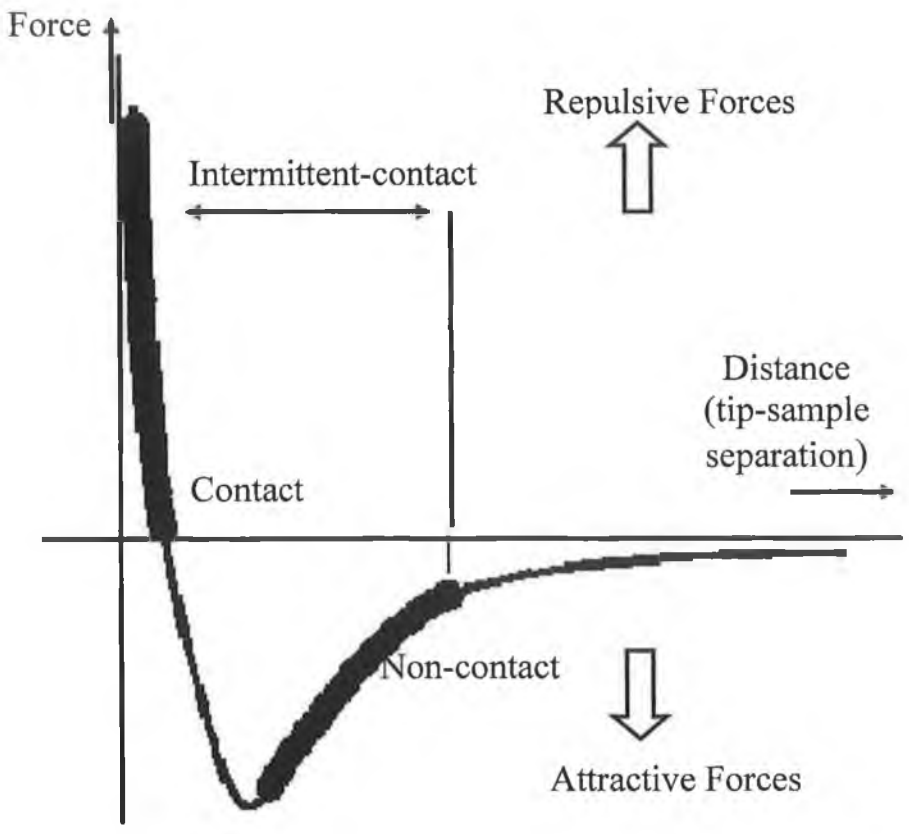

Figure 2.5 *The sign and magnitude of the Van der Waals force between tip and sample is dependent on the tip sample separation [1].*

Two distance regimes are highlighted in Figure 2.5: a) the contact regime; and b) the non-contact regime. In the contact regime, the cantilever is held less than a few angstroms from the sample surface, and the interatomic force between the cantilever and the sample is repulsive. In the non-contact regime, the cantilever is held on the order of tens to hundreds of angstrom from the sample surface, and the interatomic force between the cantilever and sample is attractive (largely a result of the long-range Van der Waals interactions). Both contact and non-contact imaging techniques are described in detail in the following sections.

2.3.2 Contact-Mode AFM

In contact-mode AFM, a constant deflection of the cantilever is maintained by a feedback loop controlling the z-piezoelectric element. The cantilever is raster scanned across the surface and the voltage applied to the z-piezo is stored to form an image. The image represents a surface of constant force. The tip-sample distance is such that the tip-sample interaction is predominately repulsive and is caused by Coulombic interaction (i.e. the tip is in physical contact with the surface). Problems arise with contact mode because of excessive tracking forces applied by the probe to the sample. In ambient conditions, a contamination layer of water vapour and nitrogen exist in the outer layer of samples. When the probe touches this contamination layer, a meniscus forms and the cantilever is pulled by surface tension toward the sample surface. In addition, many samples, such as insulators and semiconductors, may trap electrostatic charge and this charge may contribute to additional substantial attractive forces between the probe and the sample. This problem is illustrated in Figure 2.6 [19]. The effects may be reduced by minimising the tracking force of the probe on the sample, but there are practical limits to the magnitude of the force that may be controlled by the user during AFM operation.

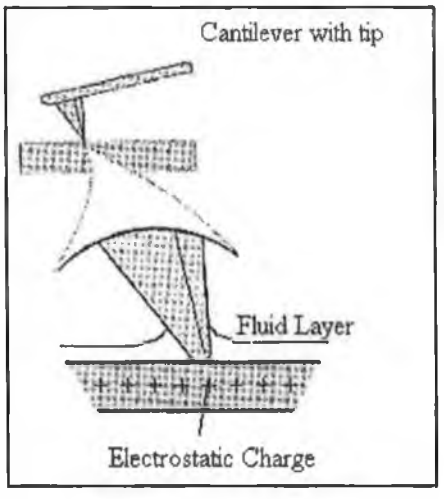

Figure 2.6 *The formation of the meniscus between the tip and surface contamination coupled with sample charging in insulator and semiconductor samples combine to exert an attractive force on the tip toward the sample surface [20].*

2.3.3 Non-Contact Mode AFM

Alternative modes of AFM operation have been invented where the cantilever vibrates near the surface of a sample. These modes are necessary for a number of reasons: in order to overcome the problem of the friction component during scanning in contact mode; to minimise the forces exerted from the tip on the sample; and the effect of the capillary forces. Collectively termed vibrating modes, these modes are non-contact and tapping mode AFM. In NC-AFM, a stiff cantilever vibrates near its resonant frequency with an amplitude of a few tens of an Ångstrom. The tip oscillates near the surface. As the tip is brought close to the sample, the system monitors the change in resonant frequency or vibrational amplitude of the cantilever through the use of feedback signals which move the scanner up and down. Changes in the resonant frequency of the cantilever may be used as a measure of changes in the force gradient which reflect changes in the tip-sample-spacing or topography. In NC-AFM, the cantilever is set into oscillation near the sample surface but does not touch it. The spacing between the tip and surface is on the order of 10 to 100 Ångstroms as shown in the Van der Waals force curve [1] in Figure 2.5. The total force between the tip and sample is low, typically 10^{-12} N, and allows the study of soft, fragile or elastic samples.

Problems arise with non-contact mode in trying to follow the sample topography when water exists on the surface. AFM operating in contact mode will penetrate the liquid layer to image the underlying surface whereas NC-AFM will image the surface of the liquid layer. The problem is illustrated in Figure 2.7 [20]. In order to achieve high resolution (vertical) in NC-AFM, it is necessary to measure force gradients from Van der Waals forces which may extend only a nanometre from the sample surface. Generally, the fluid contamination layer is substantially thicker than the range of the Van der Waals force gradients and therefore, attempts to image

the true surface fail as the oscillating probe becomes trapped in the fluid layer or hovers beyond the effective range of the forces it attempts to measure.

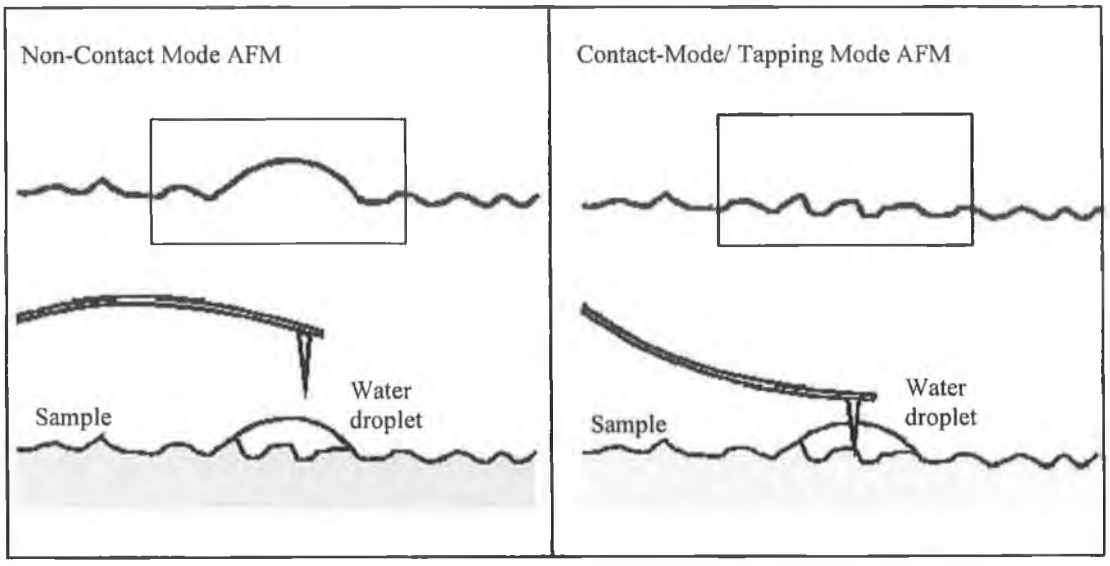

Figure 2.7 *The relatively small tip-sample interaction of non-contact mode AFM allows soft samples to be imaged non-invasively but is not strong enough to image 'through' adsorbed contamination or water droplets. In contact mode AFM the tip maintains contact with the surface and images the sample surface. In tapping mode AFM the water layer is also penetrated. [20].*

2.3.4 Tapping Mode AFM

Tapping mode AFM is similar to NC-AFM except that the vibrating cantilever tip is brought closer to the sample so that the tip just taps or hits the surface [20]. The tip is positioned ~ 50 Ångstroms from the surface and is driven into oscillation close to its natural resonant frequency. Variations in the Van der Waals forces produce force gradients that change both this resonant frequency and the amplitude of oscillation. The effective spring constant of the cantilever, k_{eff}, is modified according to:

$$k_{eff} = k_O - F' \tag{2.2}$$

$F' = \delta F_Z / \delta z$ is the force gradient and k_O is the spring constant of the cantilever without the presence of the force gradient. The resonance frequency, ω, of the cantilever is given by:

$$\omega = \left(\frac{k_{eff}}{m}\right) = \omega_O\left(1 - \frac{F'}{k_O}\right) \tag{2.3}$$

where m is the effective mass and ω_O is the natural resonant frequency. A force gradient will consequently shift the frequency of the cantilever. The oscillating tip is rastered across the sample surface line by line. The feedback loop maintains constant oscillation amplitude and produces an image of constant force gradients. TM-AFM is less likely to damage the surface like CM-AFM as it eliminates lateral forces during scanning and it may produce a greater resolution than NC-AFM.

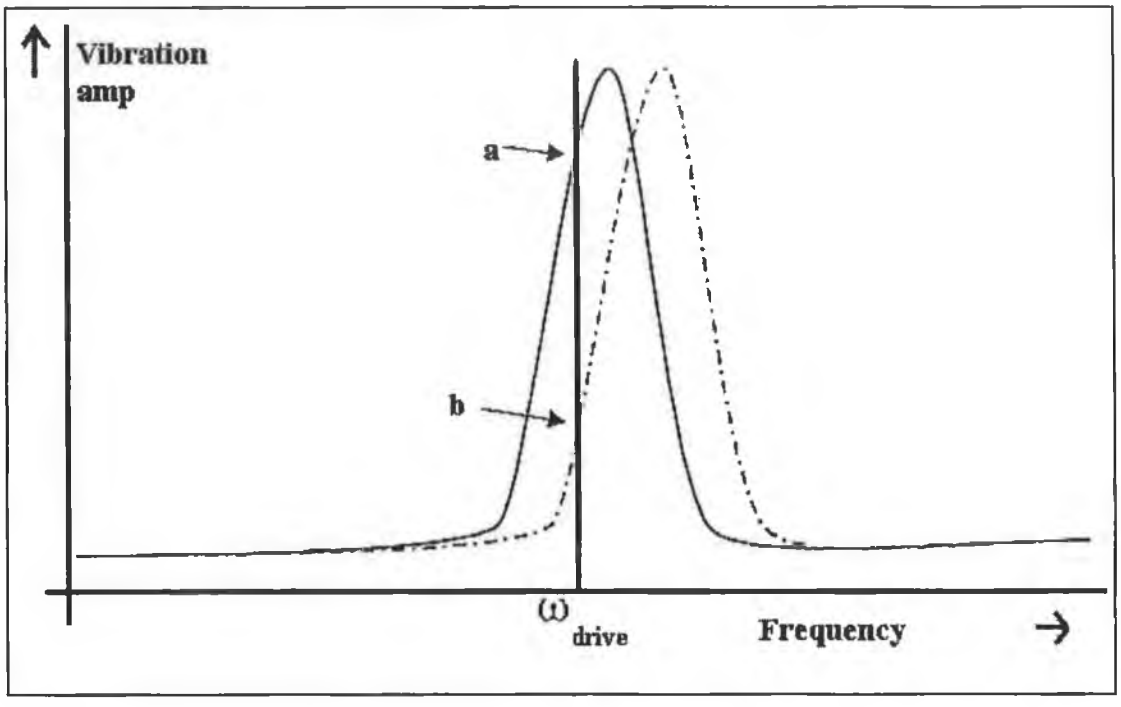

Figure 2.8 *Non-contact and tapping modes of AFM operation. Cantilever is driven at a frequency ω_{drive}. With no force gradient the cantilever oscillates with an amplitude marked by the letter "a". In the presence of a force gradient, the resonance peak shifts, resulting in a change in cantilever oscillation amplitude, marked "b".*

2.3.5 Commercial AFM Description

The two AFM systems used for the experiments detailed in this thesis are a Digital Instruments (DI) Multimode and a DI Nanoscope IIIa. Both allow contact mode, non-contact mode and tapping mode imaging. Laser alignment is performed

manually, and cantilever tuning and drive frequency selection is automatically performed by the DI software on both instruments. The cantilevers used are made of silicon, have a triangular pyramid shape and a tip radius < 10nm, force constant of 25-60 N/m and a resonant frequency of 150-190 kHz. A schematic and scanning electron microscope image of a cantilever is shown in Figure 2.9 [21].

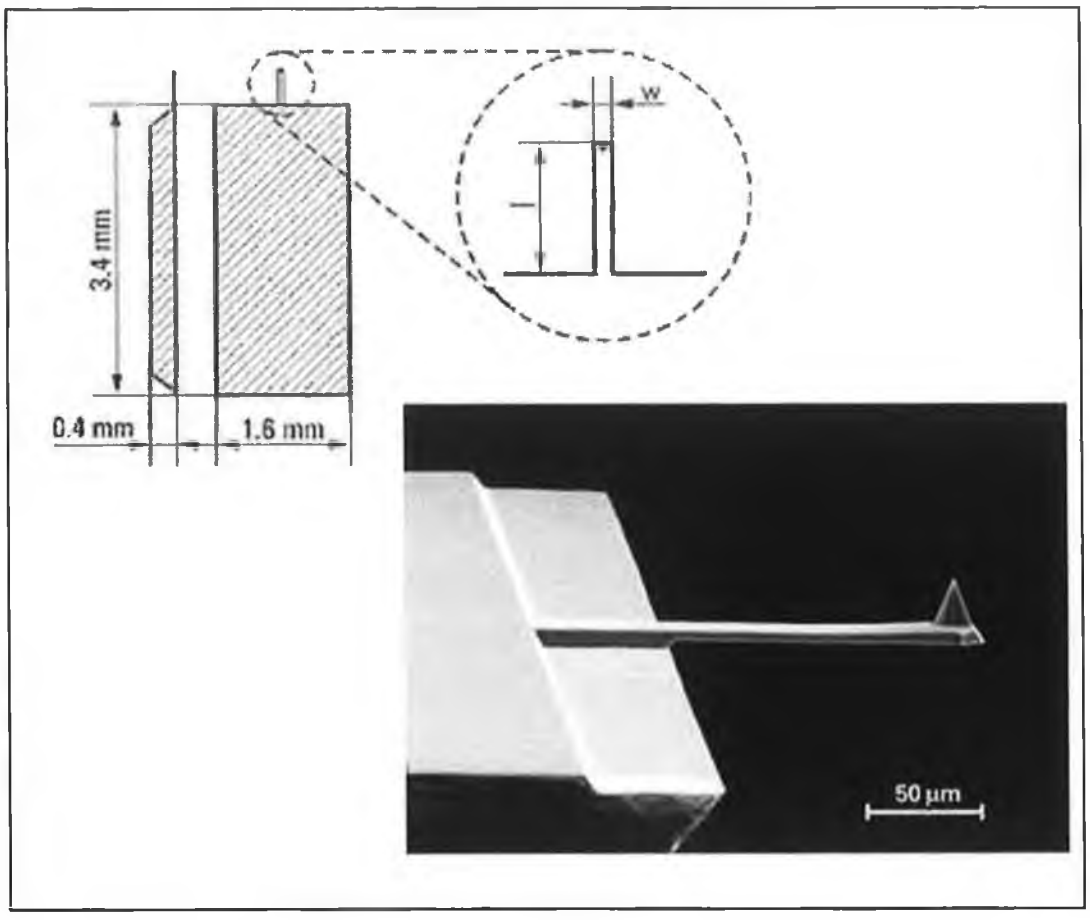

Figure 2.9 *Inset: SEM image of tapping-mode silicon cantilever. Top: The thickness of the entire chip is 0.4mm. l is the cantilever length and is ~ 125µm. W is the cantilever width and is ~ 35µm [21].*

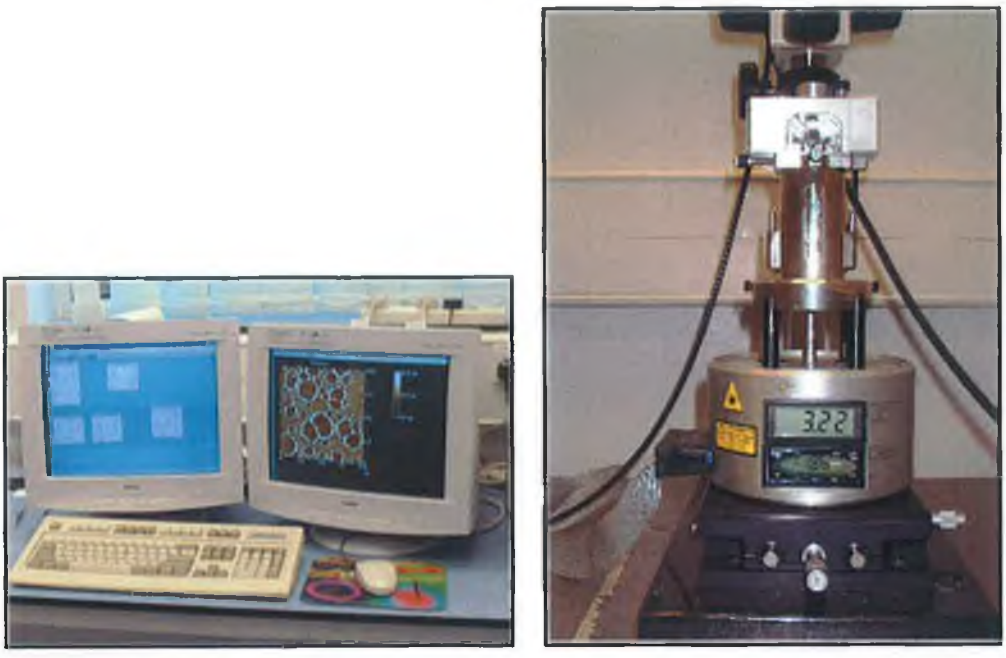

Figure 2.10 (a) *Digital Instruments AFM PC workstation and Multimode System*

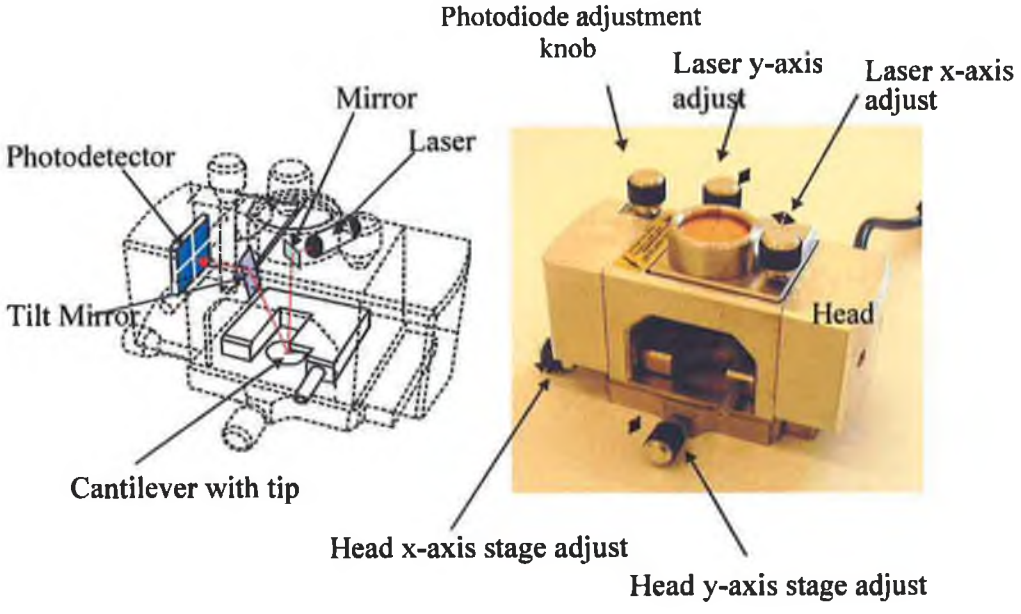

Figure 2.10 (b) *Digital Instruments Multimode Close up of head.*

2.3.6 AFM Data Presentation

There are two formats in which the data will be presented: height data and amplitude data.

i) Height Data.

The vertical position of the probe tip is monitored by noting changes in the length scale of the z-axis on the xyz scanning piezo tube. Input voltage to the scanning piezo tube is proportional to the change in the length of the tube. The change in the z-axis is plotted as a topographical map of the sample surface. Height data is a good measure of the height of surface features but does not show distinct edges of these features.

ii) Amplitude Data.

The amplitude of the cantilever is monitored by the photodiode detector. The root-mean-square (R_{rms}) value of the laser signal on the y-axis of the detector is recorded for each of the 512 segments on a given raster of the probe tip. These values are plotted as an amplitude map of the sample surface. Amplitude images tend to show edges of surface features well.

In addition to the surface topography, the current line being scanned may be viewed in scope mode where the trace and the retrace of the line scan may be superimposed to gauge the stability of the scan (i.e. how well the tip is tracking the surface), and also to optimise the feedback controls. The sensitivity of the amplitude mode to sharp features is evident in Figure 2.11. This shows the scope modes of the height and the amplitude data of a tapping mode image. There is a large signal associated with the local trace/retrace disagreement at the edges in amplitude mode compared to

height mode. In this case the amplitude data scale has been set to an extremely sensitive value to emphasise the difference in the scope modes.

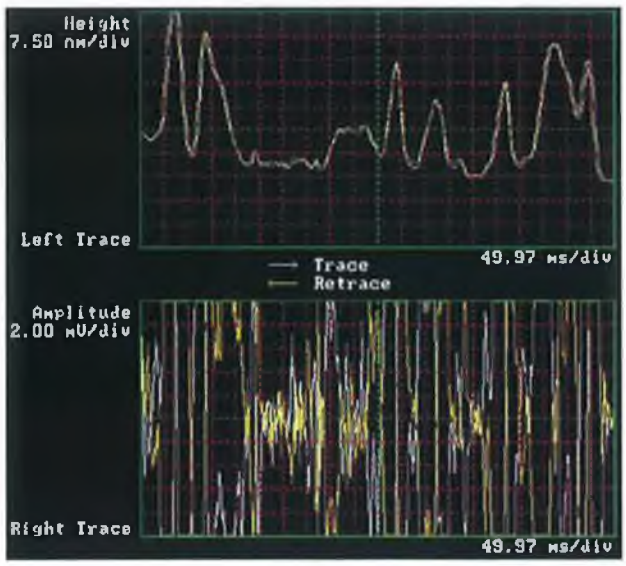

Figure 2.11 *Line scan trace (yellow line) and retrace (white line) for (top) height mode and (bottom) amplitude mode. The agreement between the trace and retrace allows the feedback corrections to be optimised for the sample terrain.*

Figure 2.12 shows height data images representing different types of common image artefacts. Every data point in an image represents a spatial convolution of the shape of the tip and the shape of the feature imaged. The smaller the radius of curvature of the tip (i.e. the sharper the tip), the smaller the feature that may be resolved. Thus, when the feature is sharper than the tip the image will be dominated by the shape of the tip. This imaging phenomenon known as 'tip-imaging' is recognised by a particular shape that is repeated throughout an image. The shape may be different sizes as the tip is convolved with features of different sizes, but it always maintains the same orientation. This is evident in Figure 2.12. The accumulation of debris on the end of the tip may also dull the tip and result in image distortion. Loose debris on the sample surface may cause loss of image resolution and produce streaking in the image. The loss of resolution is due to the build up of contamination on the tip when

scanning from bottom to top, or vice-versa. For example, small elongated features become represented as larger rounded features, until the debris detaches from the tip. Another complication is that the tip sometimes changes shape while scanning. For instance, if a small piece of Si is broken off the tip, changing its shape, this changes the apparent shape of the features on the surface.

Typically, images contain artefacts due to the condition of the tip or from ambient perturbations. The scan image is also susceptible to scan instabilities such as high frequency noise, tip jumps, tip lift-offs, drift and scanner hysteresis. Optimising scan parameters such as scan rate, gains and amplitude set point, in order to follow the topography as closely as possible, is necessary. As AFM is a local probe technique it reveals local features which are not necessarily representative for the whole sample surface. Because of this reason, it is appropriate to record and process several images. This allows the minimisation of the influence of a particular sample area, and to determine the average behaviour. While it is important to follow the surface topography as closely as possible, it is also necessary to be able to compare images from different samples and so it is also important to be reproducible in scan parameters and procedure. All the evaluations that are described in this thesis have been carried out quantitatively and averaged over a large number of samples.

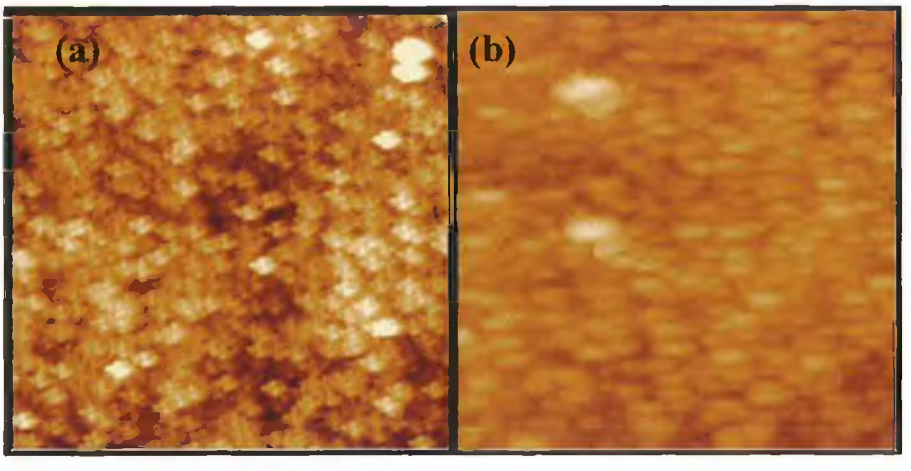

***Figure 2.12** Height images showing typical image artefacts: (a) 5μm x 5μm, Z range is 25nm; (b) 2μm x 2μm, Z range is 75nm.*

2.3.6.1 Calibration Surfaces in AFM

For AFM cantilever and distance calibration of the piezo controller, images of a surface with a known topography and known dimensions are employed routinely. Figure 2.13 shows this calibration surface. The surface is made up of a periodic square arrays of wells of length 5μm and depth 0.2 μm and separated by 5μm. Figure 2.14 shows two tapping mode AFM images of the calibration standard. The images are represented in height mode and the data is displayed from a top-down perspective. The height information is represented by the colour at a given point. The full z-heights are 0.483μm and 0.2μm and so a feature this high or higher will see white where as smaller features are seen as darker brown.

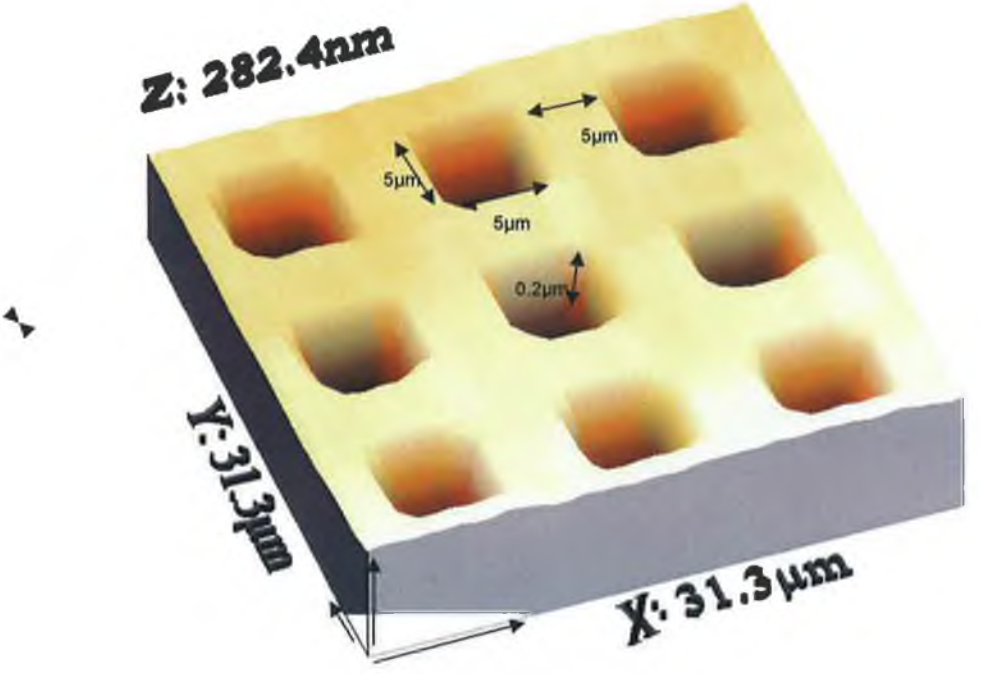

***Figure 2.13** The calibration surface. The surface is made up of a periodic square arrays of wells of length 5μm and depth 0.2μm and separated by 5μm.*

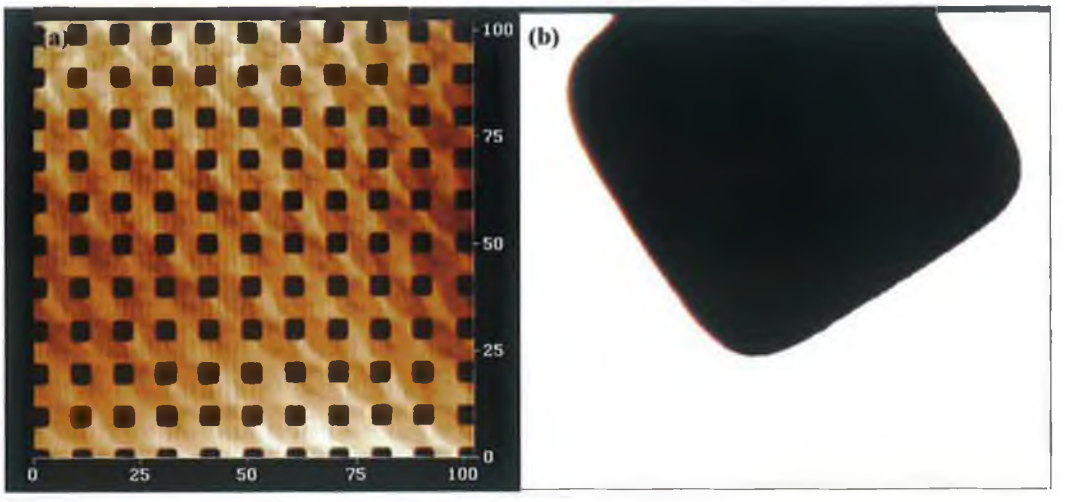

***Figure 2.14** Tapping mode images of calibration standard. Images are in height mode: **(a)** Scan size is 102.4μm². The z-range is 483nm; **(b)** Scan size is 7.0μm x 6.5μm. The z-range is 200nm.*

2.4 Photoelectron Spectroscopy

Introduction

Photoelectron spectroscopy (PES) is a powerful experimental technique that may be used for chemical analysis and for studies of electronic properties at surfaces. It is based on the photoelectric effect. The first documented evidence of this effect was reported by Hertz [22] in 1887. In 1905, Einstein [23] explained the emitted electron velocity dependence on the frequency of the incident light with the simple relationship:

$$E_{kin} = h\nu - \phi \qquad (2.4)$$

The maximum kinetic energy (E_{kin}), of a photoemitted electron is equal to a quantum of energy $h\nu$, related to the classical frequency of the incident light, minus the work-function energy ϕ which is defined as the minimum energy necessary to emit an electron from a solid. Einstein was awarded a Nobel Prize in 1921 for his work. Crudely, electrons in the core levels and valence bands of a sample are sufficiently

excited by photons to escape from the solid, and in PES to be detected by an energy resolving electron spectrometer. An analysis of the energy distribution of the emitted electrons provides information about the binding energies and the electronic structure of the solid. In 1914, Robinson and Rawlinson performed a study in which photoemission from x-ray irradiated gold produced a distinguishable gold photoelectron spectrum [24]. This was followed in 1951, when Steinhardt used photoemission as an analytical tool [25]. Between the period of 1950 to 1970, Kai Siegbahn and his research group developed the theory and instrumentation of electron spectroscopy for chemical analysis (ESCA), providing the method used widely today. Siegbahn was awarded the Nobel Prize in Physics in 1981 for this work [26, 31]. In 1972, Brundle and Roberts performed ultra-high vacuum (UHV) work, and PES truly became a surface technique [27].

2.4.1 The Photoemission Process

In the photoemission process, high-energy monochromatic photons, of energy $h\nu$, are directed onto a sample. The photons are absorbed by atoms within the sample which result in the emission of a photoelectron (see Figure 2.15). The photoelectrons are counted (detected), where the energy of the detected photoelectron is given by an extension of Einstein's equation:

$$E_{kin} = h\nu - E_b - \phi \qquad (2.5)$$

E_b is the binding energy of the electron, and ϕ is the work function of the spectrometer. Electrons within the sample with a binding energy less than that of the incident photon energy are excited. The PES spectrum is obtained by using an electron spectrometer and sweeping through some range of electron energies. The

usual approach to modelling the photoemission is to use a three-step model [28]. The three steps involved are:

i) Ionisation of an atom in the bulk material.

ii) Propagation of the excited electron to the surface.

iii) Emission of the photoelectron into the vacuum.

A photoelectron which escapes the sample without being scattered by other electrons, "remembers" its bonding history when its kinetic energy is being analysed, because each excited atom (except hydrogen) possesses "core electrons" not directly involved in the bonding. The binding energy of each core electron is characteristic of the elemental atom to which it is bound. Information on the binding energies of core electrons within a sample allows qualitative elemental analysis. In photoemission the number of photoelectrons produced from any given core level for a given photon energy flux per unit time is characterised by a transition probability called the photoionisation cross section. Each stage in the three-step model has its own interaction cross section that contributes to the intensity distribution of the photoelectrons.

The primary photoelectrons are those electrons which reach the surface without scattering. Secondary electrons are those which are inelastically scattered en route to the surface in step two. These electrons contribute a rapidly decreasing tail to the spectrum produced. If the secondary electrons are ignored the spectrum is related to the density of electron states in the solid. The resulting line shapes in the spectrum are determined by a convolution of the photon energy distribution, the initial state structure (electron energy distribution in the ground state), lifetime broadening effects, electron energy loss structure acquired during transfer from the atom to the

surface, and the spectrometer resolution function. Figure 2.16 shows a typical PES spectrum. The contributions to the spectrum will be discussed next.

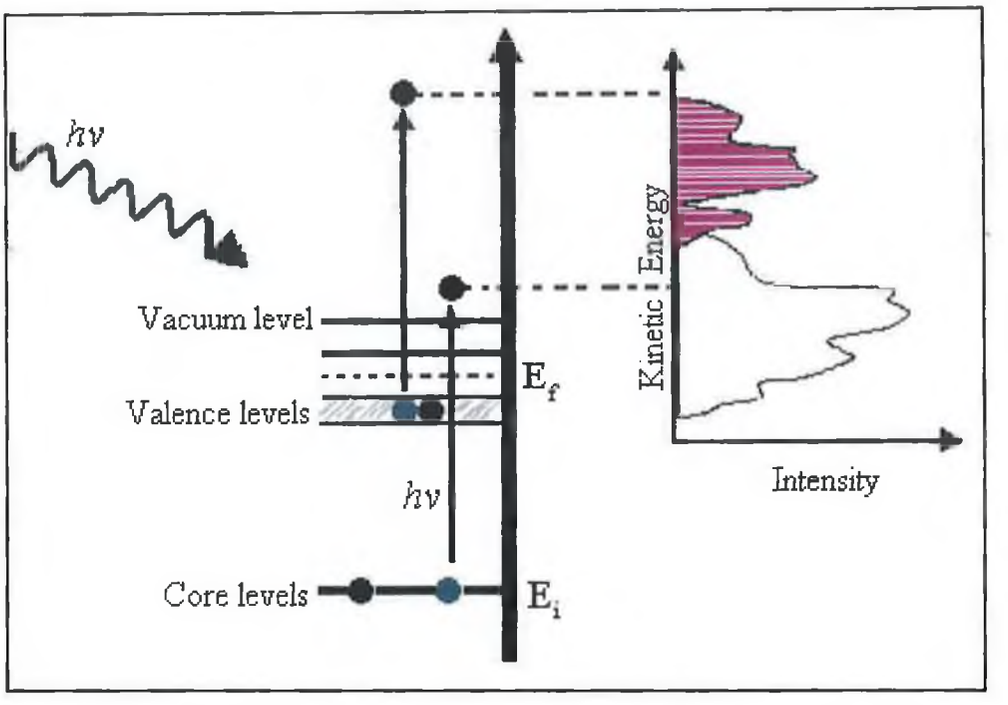

Figure 2.15 *Schematic illustration of the basic photoemission process. States below the Fermi level are probed.*

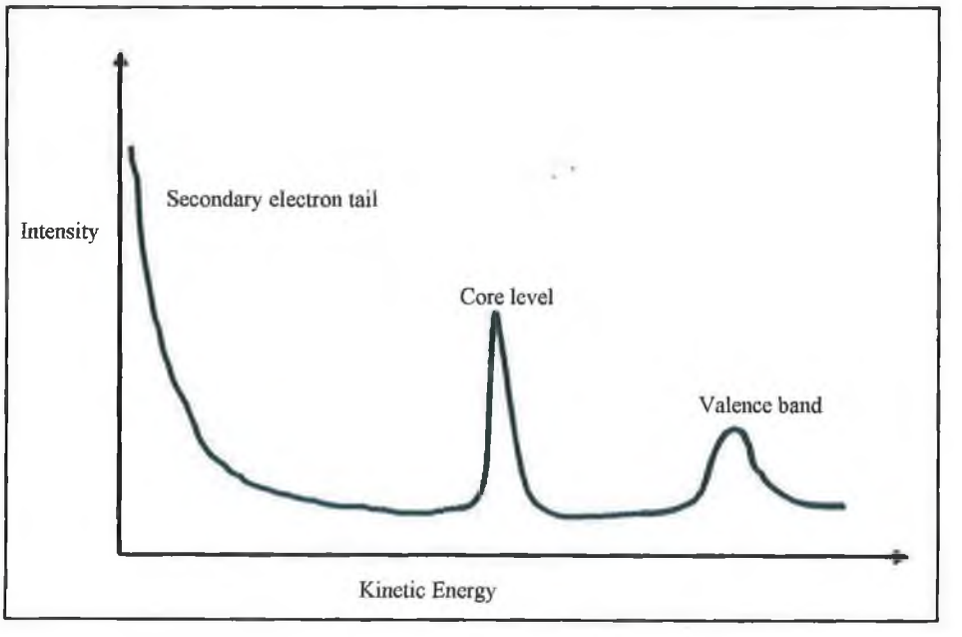

Figure 2.16 *Typical photoelectron spectrum. The valence band states are broad and complex. The core level states are narrow and well defined. The spectrum sits on a secondary electron tail [29].*

2.4.2 Photoemission Peaks

As previously stated a series of peaks are obtained in a photoelectron spectrum reflecting the binding energies of the electrons in the solid. There are three types of peaks due to I) core levels, II) valence levels and III) peaks due to Auger emission. These peaks are termed 'primaries'. The primary peaks are superimposed on a broad continuous background. This 'secondary' background increasingly dominates the low binding energy region of the spectrum, and is due to electrons resulting from inelastic multiple scattering photoemission processes.

i) *Core level* peaks:

These are due to photoelectrons that are emitted from the atomic (core) levels of the electron present, such as that of O1s which is the electron emitted from the 1s level of oxygen.

ii) *Auger* peaks:

Auger peaks are broader peaks caused by Auger electrons which arise from the relaxation of an excited atom or ion following the photoemission of a core level electron. Figure 2.17 gives a schematic representation of what is involved in the generation of a $KL_1L_{2,3}$ Auger electron. Initially an electron must be ejected from a surface atom in the ground state (a K electron). This process leaves a "hole" or vacancy which may be filled by an electron dropping down from a higher level, L_1. This in turn releases considerable energy $E_K - E_{L1}$, part of which is absorbed by an electron in a higher orbital $L_{2,3}$ which is ejected with a kinetic energy representing the excess of $E_K - E_{L1}$ over $E_{L\,2,3}$; this is known as a $KL_1L_{2,3}$ Auger electron. The energy released by the electron dropping down must be equal to the energy taken up

by the ejection electron with kinetic energy E_{Auger}: $E_{Auger} = E_K - E_{L1} - E_{L2,3}$ (2.6)

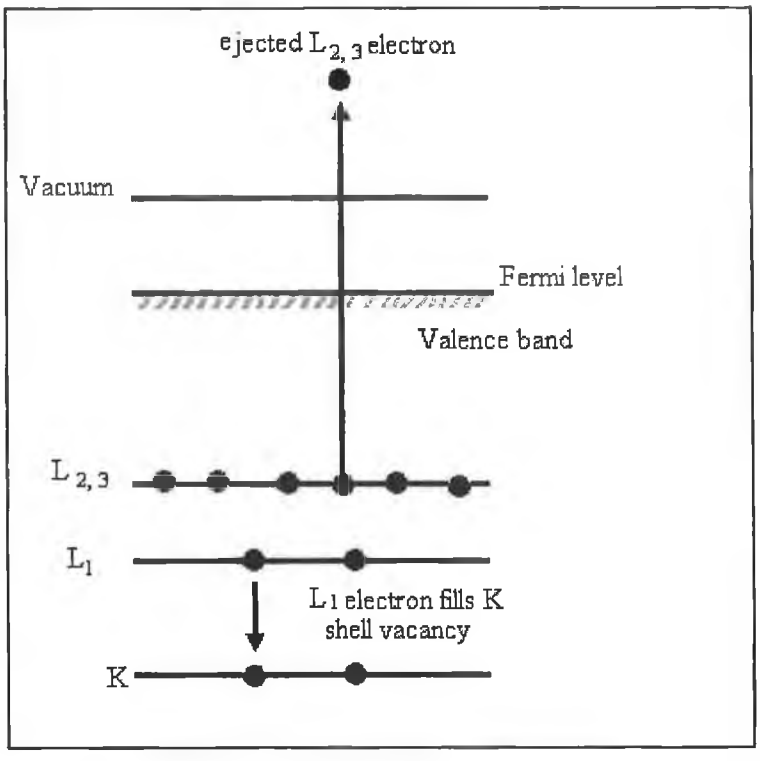

Figure 2.17 *Energy level diagram for a $KL_1L_{2,3}$ Auger electron emission [30].*

iii) *Valence level*:

Valence level peaks are due to low energy electrons involved in bonding and the spectrum consists of many closely spaced levels giving rise to a band structure.

The intensity of all photoemission peaks is determined by the photoemission cross-section, which depends on the exciting energy. The fate of this energy can be considered in terms of:

i) Initial state effects (absorption and ionisation).

ii) Final state effects (response of atom and creation of photoelectron).

iii) Extrinsic losses (transport of electron to surface and escape).

The initial state can be considered as the atomic or molecular orbital prior to excitation. The final state is the system after excitation. All can contribute to the final spectrum.

2.4.3 Initial State Effects

i) *Spin-orbit coupling*

For any electron in an orbit with angular momentum, coupling between magnetic fields of spin (s) and angular momentum (l) occurs. Coupling occurs for core levels except for symmetric s-level shells (due to no net angular momentum). Spin-orbit coupling gives rise to doublets (for p orbitals) in the spectrum for values of $l > 0$ (or multiplets for d and f orbitals). The intensity of the doublet peaks is proportional to their degeneracies, which are given by $(2j + 1)$, where the total angular momentum $j = |l + s|$.

n	l	s	j	Term
2	1	+½	3/2	$2p_{(3/2)}$
2	1	-½	½	$2p_{(½)}$

For example in the Ti_{2p} line.

In the case of parallel coupling, $j = l + s$, the electrons are shifted to lower binding energy while for electrons with antiparallel coupling, $j = l - s$, the state is shifted to higher binding energy. This has resulted in a spectral degeneracy of 2:1 for $2p_{(3/2)}$ and $2p_{(1/2)}$. Figure 2.18(a) shows the presence of the spin-orbit interaction in an experimental spectrum [30]. The energy split is resolved into two peaks.

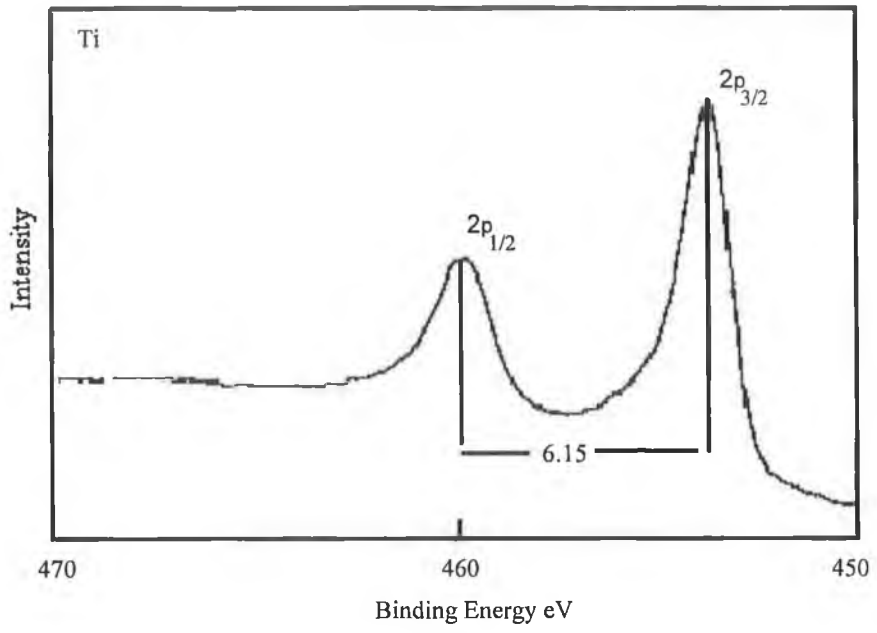

Figure 2.18 (a) *A Ti spectrum reveals the presence of two spectral components associated with each atomic state as the spin-orbit split / coupling ($2p_{1/2}$, $2p_{3/2}$) degeneracy is resolved [30].*

ii) *The Chemical Shift*

Surface atoms of the same element may have different binding energies due to a difference in the atoms' environment (e.g. oxidation state, molecular environment) compared to the bulk material atoms. This binding energy difference between the two situations is called a chemical shift or a surface core level shift (SCLS). Chemical shifts also arise when the valence electrons are involved in bonding to adsorbates, i.e. if the co-ordination or bonding is different to that of the bulk atoms then the distribution of the valence electrons will be different causing the core electrons to experience a different potential and thus changing the binding energy. Siegbahn et al. first detected chemical shifts when the so-called 'fixed' binding energies of core level atoms were affected by their environment leading to detectable (0.1 to 10eV) shifts in their photoelectron energies [31]. The chemical shift in PES spectra has become a powerful tool for functional group, chemical environment and oxidation state information. Figures 2.18 (a-b) show the Ti$2p_{1/2}$ and Ti$2p_{3/2}$ chemical

shift for Ti and Ti^{4+} respectively [30]. In Figure 2.18 (b) the positive charge increases by formation of chemical bonds and there is a chemical shift as the binding energy increases.

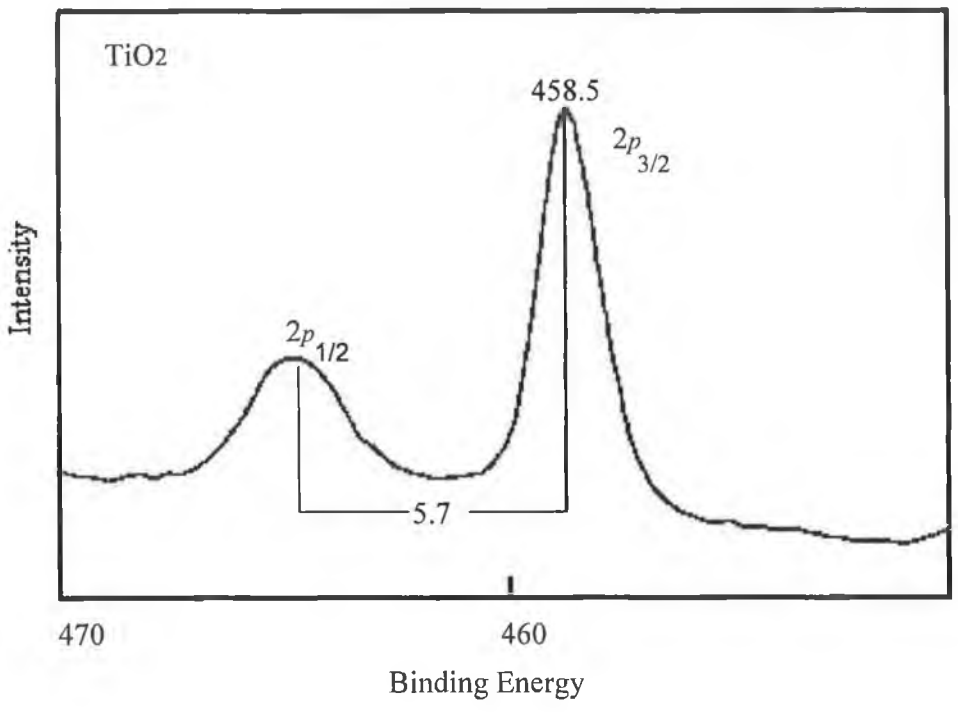

Figure 2.18 (b) *$Ti2p_{1/2}$ and $2p_{3/2}$ chemical shift for Ti (figure 2.19 (a)) and Ti^{4+}. Charge is withdrawn as $Ti \rightarrow Ti^{4+}$, so the 2p orbital relaxes to a higher binding energy.*

2.4.4 Final State Effects

i) Relaxation

Final state effects arise from differences in energy due to relaxation following emission of a photoelectron. Other electrons in the sample respond to the creation of a core hole by rearranging to shield, or minimise, the energy of the ionised atom. These other electrons relax due to both this extra attraction and the reduction in screening of the nuclear charge from electrons in higher orbits. Relaxation of electrons from the atom containing the core hole is known as atomic relaxation and from electrons on surrounding atoms as extra-atomic relaxation. Most of the atomic relaxation component is due to the rearrangement of outer shell electrons which have

a smaller binding energy than the photoelectron. The inner shell electrons, whose binding energy is larger than the emitted photoelectron, have a small contribution and are neglected. The form of extra-atomic relaxation depends on the material being examined.

ii) *Koopman's theorem [30]*

This states that '*the binding energy of an emitted photoelectron is simply the energy difference between the (N -1) electron final state and the N electron initial state*'. The binding energy, E_b, is the most obvious final state effect. It may be defined in terms of the initial energy E_i and the final energy E_f of a photoelectron by :

$$E_b = E_f (N-1) - E_i (N) \qquad (2.6)$$

These energies are not easy to calculate. The photoemission process is extremely rapid ($\sim 10^{-15}$ sec). The assumption that the other electrons remain "frozen" forms the basis of Koopman's theorem. If after the transition there is no electron rearrangement then "the binding energy equals the negative of the orbital energy from which the photoelectron is emitted". If no relaxation follows photoemission, then the binding energy E_b is equal to the orbital energy which may be calculated from Hartree-Fock calculations. However, other electrons do not remain "frozen" during the photoemission process. Despite this the spectral implications of electron relaxation processes may be catered for during peak fitting and so Koopman's theorem provides a working basis.

iii) Peak Broadening

In photoemission the spectrum is broad, not just a single line. This broadening is due to a number of factors: experimental; surface disorder; and phonon broadening. The

experimental broadening results from both the spread of the photon source and the electron analyser resolution. Experimental broadening is Gaussian in nature. The line shape due to the lifetime of the core hole is a Lorentzian function, and represents the uncertainty in energy due to the lifetime of the core hole after photoemission has taken place. Lifetime broadening results in symmetric broadening and can be gauged from the Heisenberg Uncertainty principle:

$$\Gamma = \frac{h}{\tau} \tag{2.7}$$

Γ is the intrinsic peak width in eV

h is Planck's constant in eV seconds

τ is the core hole lifetime in seconds.

For an excited state lifetime of ~10^{-15}s, Γ is approximately 0.2eV. In the atomic case the core level width is given by:

$$\Delta E = \sqrt{\Gamma^2 + (\Delta E_{Source})^2 + (\Delta E_{Analyser})^2} \tag{2.8}$$

ΔE_{Source} and $\Delta E_{Analyser}$ are the full-width-at-half-maximum (FWHM) of Gaussian functions which represent the resolution of the photon source and the electron analyser respectively. Γ is the FWHM of the Lorentzian function. When fitting the peak components, a Voigt curve is used which is a convolution of the two. The spin-orbit coupling described earlier is also a final state effect. Other effects are due to the atom being left in an excited state after emission of a core electron. *Shake up* effects occur if the excited electron remains bound to the system and *shake off* effects occur if the excited electron is emitted.

2.4.5 Surface Sensitivity: The Universal Curve

The surface sensitivity of the PES technique is due to the inelastic mean free path (IMFP) of the photoelectron. The IMFP depends on the kinetic energy of the electron and the nature of the material. The IMFP, whose functional relationship for the elements is described by Dench and Seah, is the average distance an electron with a given energy travels between inelastic collisions [32].

$$IMFP = \lambda = (538)\left(\frac{1}{E_k^2}\right) + (0.4)(aE_k)^{1/2} \qquad (2.9)$$

λ is in units of monolayers,

'a' is the monolayer thickness (nm),

E_k electron kinetic energy (eV).

Photoelectrons with kinetic energies in the 5 to 2000eV energy range, above the Fermi energy, must originate very close (5 – 30 Ångstroms) to the surface in order to emerge unscattered and make up the primary photoelectron peak. Inelastically scattered electrons contribute to the secondary electron background. Figure 2.19 shows a sketch of the IMFP as a function of kinetic energy (known as the universal curve). The minimum point of the curve at 50eV is because, at this energy, the electrons are more likely to scatter with other electrons to excite plasmons. In synchrotron studies, the minimum in the universal curve is exploited when an incident photon with a given energy results in photoelectrons emerging exclusively from the outermost atomic layers due to the strong interaction of low kinetic energy electrons with the sample.

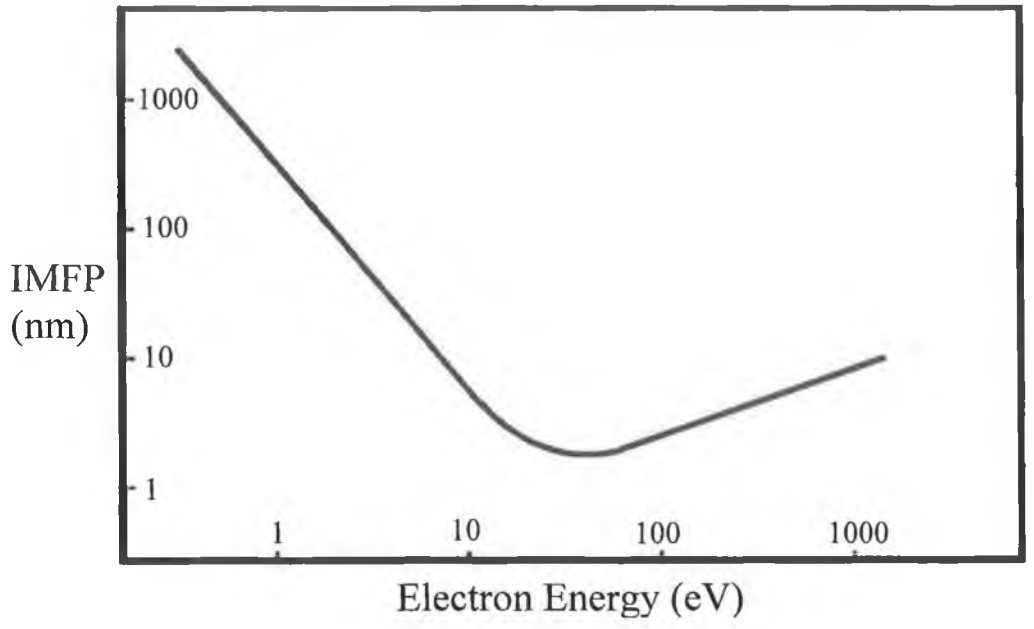

Figure 2.29 *The Universal Curve shows the electron inelastic mean free path in solids as a function of the electron energy (measured with respect to the Fermi level) [30].*

2.4.6 Peak Fitting

Due to the composite nature of the photoemission spectra, many chemical species may contribute to the line shape of the band envelope observed. A mathematical function is chosen to describe the spectral lineshape. The number of peaks, peak heights and the binding energies are selected. The components are then fitted using a least squares fitting routine using a convolution of Gaussian and Lorenzian curves known as a Voigt curve [33]. In order to obtain a reliable fit, the core fitting parameters used must be mutually consistent. The background is also removed using the fitting procedure. The simplest method of estimating the background under a peak is to use a linear or higher order polynomial line between the low and high kinetic energy sides of the peak. A Shirley background [30] is used which assumes that the background intensity under a peak arises from the scattering of electrons of higher kinetic energy and is proportional to the partial integrated intensity under the peak.

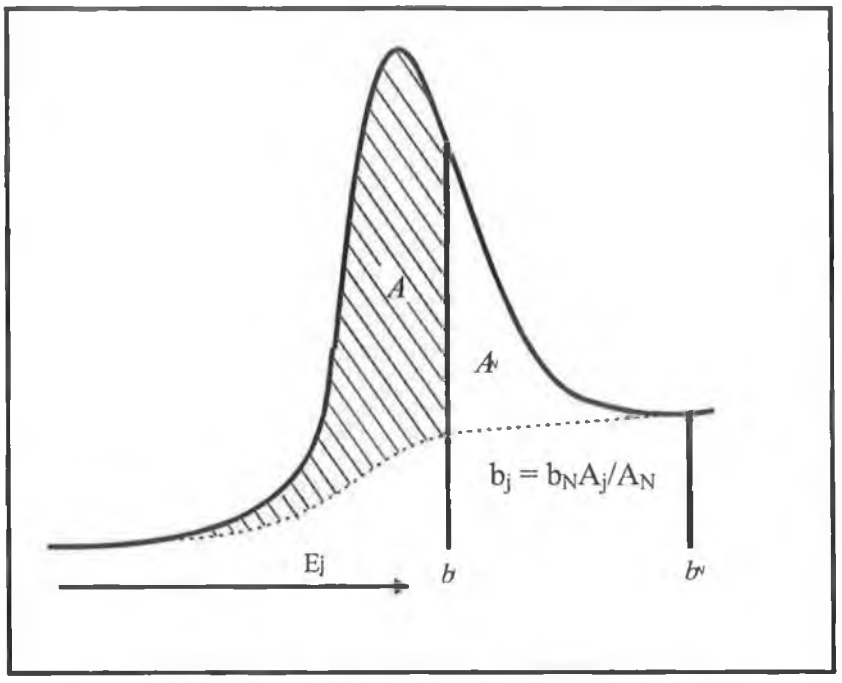

Figure 2.20 *The calculation of a Shirley background [32].*

2.5 Synchrotron Radiation

When charged particles, in particular electrons, are forced to move in a circular orbit, photons are emitted. With charged particles at relativistic velocities, these photons are emitted in a narrow cone in the forward direction, at a tangent to the circular orbit. This radiation is called synchrotron radiation (SR). Such emission was first observed at General Electric's 70MeV synchrotron in 1946 [34]. A synchrotron is a useful radiation source for performing a wide range of spectroscopy experiments. The distinguishing characteristics of synchrotron radiation are a continuous spectrum from the infrared to the hard X-rays, offering linear polarisation and high intensity relative to conventional discharge tube radiation. In a SR source, a beam of electrons is injected into a storage ring which is under ultra-high vacuum (UHV). The electrons are accelerated to energies of the order of GeV by a radio frequency (RF) accelerating cavity operated in phase with the arrival of the electron bunches. The electrons travel in bunches close to the speed of light and are confined to a circular

path by bending and focusing magnets. Because the electrons are travelling at relativistic speeds, the SR is emitted in a narrow core in a tangential direction from the bending curve at the time of emission.

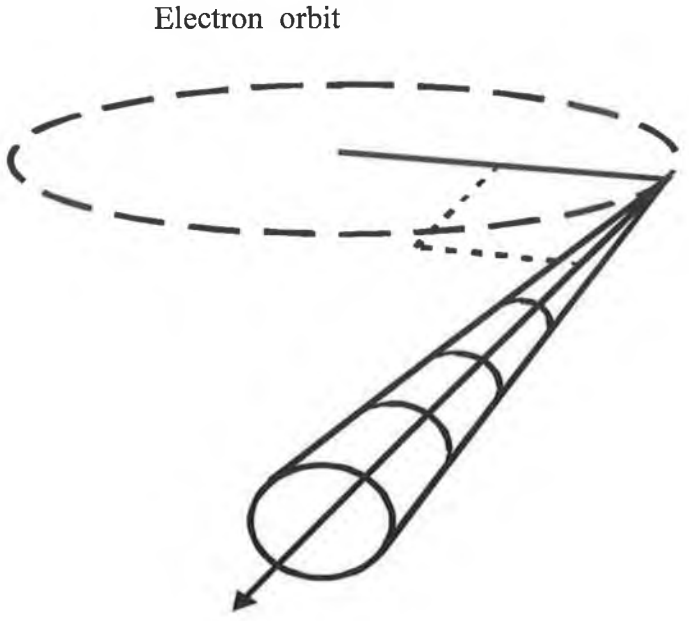

Figure. 2.21 *Schematic representation of radiation pattern emitted by electrons in a synchrotron orbit with relativistic energy.*

The emitted radiation is broadband (i.e. the high temporal localisation is realised through the addition of many frequencies), extremely intense, collimated and highly plane polarised (which facilitates wavelength selection). In a synchrotron, the radiation is collected through beamlines, which are tangential to the ring. Figure 2.22 shows a schematic of a typical electron storage ring for the production of SR.

Experiments in this thesis were carried out at the SR facility on beamline 5U.1 at Daresbury Laboratories in the U.K. At this facility electrons are accelerated to relativistic speeds by three stages. The electrons are initially accelerated to an energy of ~ 1 MeV by a linear accelerator (LINAC), and then to ~ 600 MeV by the booster ring. These electrons are then injected in bunches into the main storage ring

where they are accelerated to energy of ~ 2 GeV by 16 dipole magnets and a RF electric field. There are a further 32 quadropole magnets for focussing the electron beam and confining it to a circular orbit of radius ~ 15m. The storage ring is made up from a series of straight sections linked by curved sections at the position of the accelerating magnets. At each accelerating magnet, a beam of radiation is emitted tangentially to the electron path and is directed along a beam to the experimental section.

SR gets its name from the fact that the beam energy and magnetic field are increased synchronously so as to keep the electrons in a constant orbit. In the storage ring the electron beam is kept stable for several hours so that experiments may be performed without interruption. The beam gradually decays due to collisions between electrons or between electrons and the walls of the ring. The beam is replaced with a new beam at regular intervals. The advantages of synchrotron light for photoemission are in its intensity, resolution, and ability to tune the energy (frequency) of the light. The resolution is a function of the beamline rather than the SR site itself. These properties allow the energy dependence of surface sensitivity to be exploited and thus depth a sample in the sub-nanometre regime or to resolve close lying chemical states.

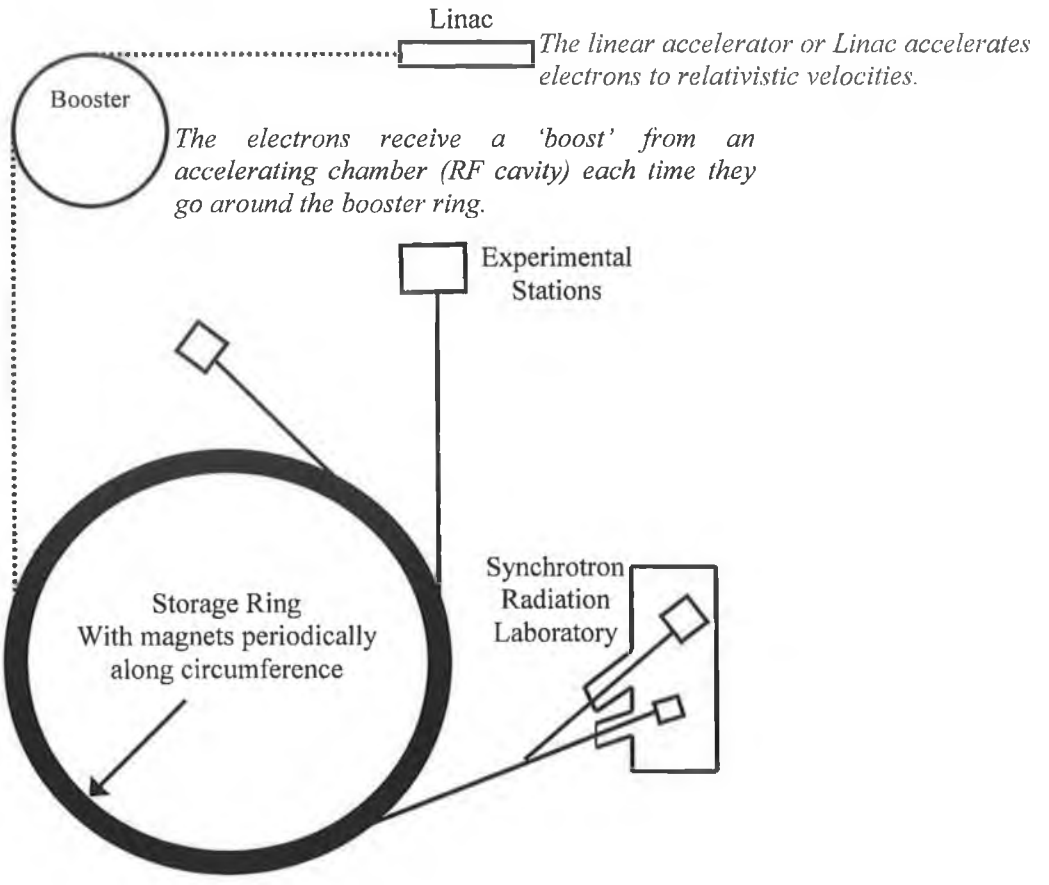

Figure 2.22 *Schematic of a typical electron storage ring for the production of synchrotron radiation[35]. Once the electrons reach their target energy in the booster synchrotron, a system transfers them into the storage ring where they circulate for hours.*

2.5.1 Daresbury Beamline 5U.1

The function of a beamline is to gather and monochromate the light emitted from the ring and finally to focus the light into a small a spot as possible onto the sample in the analysis chamber. Figure 2.23 shows the optical layout of beamline 5U.1 at Daresbury Laboratories [35]. It is a soft x-ray spectroscopy beamline providing monochromatic photons over the range 60 – 1000eV. It utilises a permanent magnet undulator as the photon source, followed by a plane grating monochromator. The diffracted light passes through the exit slit where finally the beam illuminates the sample in the analysis chamber. The experimental station consists of one UHV chamber. Samples are introduced into the chamber using a fast-entry load lock and

magnetic linear transfer arm. The sample is mounted on a manipulator that allowed accurate positioning in the lateral position (x, y, z motions), in the rotational positioning and in the azimuthal angle. UHV is achieved using suitably arranged rotary, turbo-molecular and ion pumps. Data acquisition and control is provided by a VSW hemispherical analyser. Scanning modes available include: photoelectron spectroscopy and auger Spectroscopy. In addition, the end station affords the opportunity for NEXAFS spectroscopy.

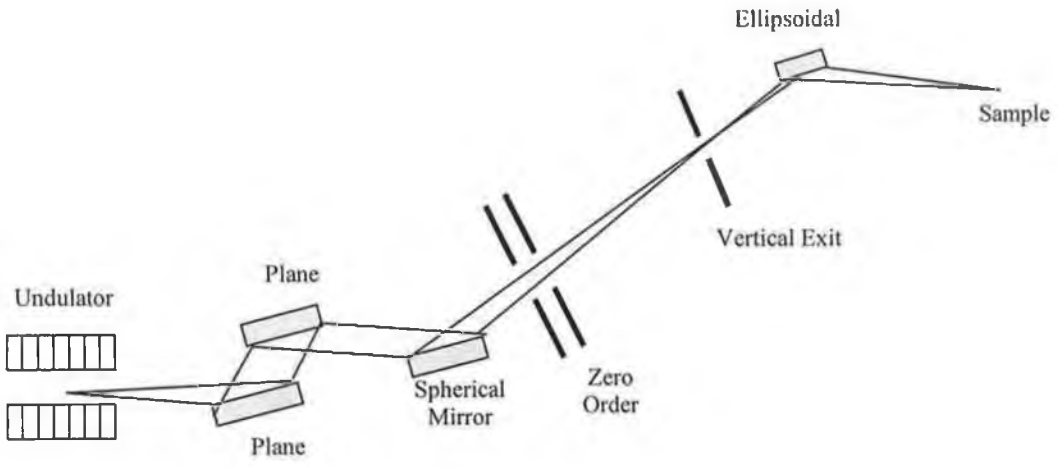

Figure 2.23 *Schematic of beamline 5U.1 at Daresbury Laboratories [35].*

2.6 References

1. Thermo Micro Web page http://thermomicro.com/spmguide/1-2-0.htm (03/00 Edition)
2. Binnig G., Roher H., Gerber C., Weibel E., **1982**, *Phys. Rev. Lett.* 49, 57.
3. Binnig G., Quate C. F., Gerber C., **1986**, *Phys. Rev. Lett.* 56, 930.
4. Martin Y., Wickramasinghe K. H., **1987**, *Appl. Phys. Lett.* 50, 1455.
5. Liu H. Y., Fan F. F., Bard A. J., **1986**, *J. Amer. Chem. Soc.* 108, 2824.
6. Pohl D. W., Denk W., Lanz M., **1984**, *Appl. Phys. Lett.* 44, 651.
7. Williams C. C., Wickramasinghe K. H., **1986**, *Appl. Phys. Lett.* 49, 1587.
8. Binnig G., Roher H., Gerber C., Weibel E., **1983**, *Phys. Rev. Lett.* 50, 120.
9. Gimzewski J. K., Möller R., **1987**, *Phys. Rev. B* 36, 1284.
10. Lang N. D., **1985**, *Phys. Rev. Lett.* 55, 230.
11. Hansma P. K., Tersoff J., **1987**, *J. Appl. Phys.* 61, R1.
12. Stefanis A. De., Tomlinson A. A. G., **2001**, in *Scanning Probe Microscopies,* TransTech Publications, Switzerland.
13. Israelchvili J., **1992**, in *Intermolecular and Surface Forces*, Academic Press Publications, San Diego.
14. Moiseev Y. N., Mosteoanenko V. M., Panov V. I., Sokolov I. Y., **1988**, *Phys. Lett. A.* 132, 354.
15. Hartmann U., **1990**, *Phys. Rev. B.* 42, 1541.
16. Banerjea A., Smith J. K., Ferrante J., **1990**, *J. Phys. Condens. Matt.*, 2, 8841.
17. Mate C. M., **1992**, *Phys. Rev. Lett.*, 68, 3323.
18. Mate C. M., McClelland G. M., Erlandsson R., Chiang S., **1987**, *Phys. Rev. Lett.* 59, 1942.
19. Digital Instruments Web page http://www.di.com/AppNotes/Semi/SemiMain.html#SRC1

20. Q. Zhong, D. Inniss, K. Kjoller and V. B. Elings, **1993**, *Surf. Sci. Lett.* 290 L688.

21. Image from μmasch http://www.spmtips.com

22. Hertz H., **1887**, *Berliner Berichte* 487.

23. Einstein A., **1905**, *Ann. Physik,* 17, 132.

24. Robinson H.R., Cassie A.M., **1926**, *Prog. Roy. Soc.,* A113, 282.

25. Steinhardt R.G., **1951**, *Anal. Chem.,* 23, 1585.

26. Vickerman, J.C., **1997**, in *Surface Analysis- The Principal Technique,* Wiley Publications, Chichester.

27. Brundle C.R., Roberts M.W., **1972**, *Proc. Roy. Soc.,* A331, 383.

28. Berglund C. N., Spicer W. E., **1964**, *Phys. Rev.* 136 A1030.

29. Hüfner, **1996**, in *Photoelectron Spectroscopy : Vol. 2,* Springer-Verlag Press Publications, Heidelberg.

30. Walls J. M., Smith R., **1994**, in *Surface Science Techniques,* Pergamon Press Publications, Oxford.

31. Siegbahn K., Nordling C., Fahlam A., **1967**, *Nova Acta Societatis Scientiararum Upsaliensis*, Ser IV, 20, 5.

32. Seah M. P., Dench W. A., **1979**, *Surf. Interface Anal.* 1, 2.

33. Curve fitting carried out using Igor Pro 4.0 by WaveMetrics. http://www.wavemetrics.com

34. Elder F. R., Gurewitsch A. M., Langmuir R. V., Pollock H. C., **1947**, *Phys. Rev.,* 71, 829.

35. Daresbury Laboratories Synchrotron Radiation Source (SRS) web page. http//srs.dl.ac.uk/info/STATION_INFO/stat5_1.html

Chapter 3

Studies of Redox Polymer Systems

Chapter 3 describes the synthesis and characterisation of a series of metallopolymers, based on poly(4-vinyl) pyridine (PVP) containing either ruthenium or osmium bis(2,2'-bipyridly) centres. The morphology of the polymers is examined in detail when deposited on SiO_2 from solution, using tapping mode atomic force microscopy, with subsequent advanced imaging analysis. Synchrotron radiation spectroscopy is also used to study the electronic structure of thin films of a metallopolymer on a silicon substrate.

"A good plan executed right now is far better than a perfect plan executed next week"

George S. Patton

3.1 Polymers

Introduction

Popularly known as "plastics", polymers are large molecules constructed from smaller structural units (monomers), covalently bonded together in any conceivable pattern. By modifying the monomer building blocks and the bonding scheme, the mechanical and thermal properties of the polymers may be controlled. Polymers can be made hard, soft, soluble, insoluble, rubbery or brittle. The properties of polymers also allows for a variety of processing: for example "spray" painting, injection moulding and spin-casting. These convenient techniques are in contrast to the processing of metals and inorganic semiconductors. Polymers are therefore pervasive and can be found in almost all products in our present day society, for example in the form of protective coatings, adhesives, inks, sealants, and in composites with inorganic components as structural materials. The idea of utilising the electrically conducting properties of polymers was first proposed in the 1960's [1], and since then polymers have been used as active components in a variety of electronic applications, e.g., polymers and organic molecules long have served as photoreceptors in electro-photographic copying machines.

In 1977 it was discovered that an alternating-bond conjugated polymer, trans-poly(acetylene), could be transformed into a good electrical conductor upon p- and n-doping [2]. This was the first report of such a 'conducting' polymer. The key finding was a chemical species characterised by a delocalised π-electron system along the polymer backbone. The semiconductor properties of the material arise from the overlap of the p_z orbitals that originate from the double bonds. If the overlap is over several sites, delocalised π-valence and π*-conduction bands occur with a relatively small energy gap. The limitations in the first experiments was the chemical stability of the trans-poly(acetylene) in air and difficult material processing. Its discovery

however, opened new avenues of exploration for chemistry, physics and technology and resulted in the Nobel Prize in Chemistry being awarded to Prof. A.J. Heeger, A.G. MacDiarmid and H. Shirakawa in 2000.

There is a huge interest in the application of conducting polymer systems in the development of a variety of organic-based devices: light-emitting devices, photo-voltaic devices, lasers and transistors. Electronically conductive polymers are just one class of polymer that can be used as active components in electronic devices. Another electroactive group is the family of redox polymers. An obvious advantage of electroactive polymers compared to inorganic semiconductors is that polymers can be soluble and spin-cast as thin films from solution. Instead of building up thin multi-layers in ultra-high vacuum, for example, one can make a blend of polymers, spin-cast them as a film in air and have interfaces already built into the layer [3].

Thin polymer films have important applications for advanced microelectronics device fabrication and packaging. A whole range of deposition techniques exist which may be employed to deposit monolayer and multilayer polymer films on various substrates. These include Langmuir-Blodgett and spin-coating techniques, as well as solvent evaporation, dip-coating and chemical grafting processes. Methods to modify electrodes with polymer coatings include using electrochemical polymerisation and deposition techniques, and electrostatic self-assembly.

3.1.1 Redox Polymers

Redox polymers are characterised by the presence of specific spatially and electrostatically-isolated electrochemically active sites. Electroactivity is highly localised. A redox polymer consists of a system where a redox-active transition metal based pendant group is covalently bound to some sort of polymer backbone which

may, or may not be electroactive. Unlike electrically conducting polymers, redox polymers characteristically exhibit conductivity over a very narrow potential range. Electronically conducting π-conjugated polymers are organic materials in which the polymer backbone itself is conducting [4,5]. Figure 3.1 shows examples of redox and conducting polymers.

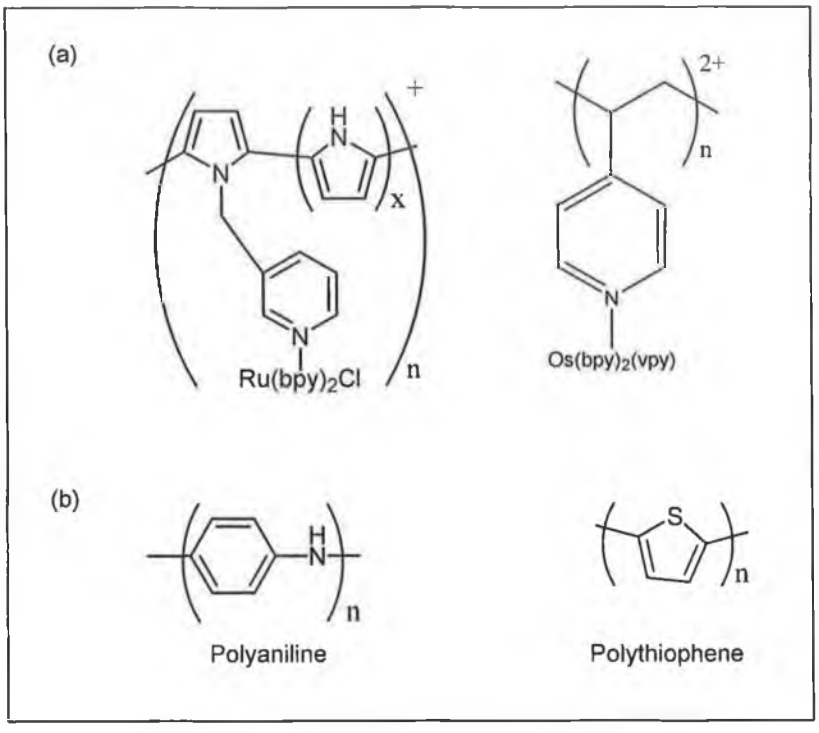

Figure 3.1 *Representative examples of* ***(a)*** *Redox Polymers;* ***(b)*** *Conducting Polymers*

The widespread interest in redox polymers has been spurred by their applicability in the area of molecular electronic devices, such as in, for example, chemically modified electrodes [6,7,8]. One goal of coating electrodes with electroactive polymers is the development of new materials with very active catalytic properties.The majority of the work has been with systems where the polymer itself is inert and serves only as a support for the electrocatalytic metal sites. The electrocatalytic site functions as a mediator, facilitating the transfer of electrons between the electrode and the substrate. Heller has shown that polycationic redox polymers adsorbed on graphite can bind polyanionic enzymes such as glucose

oxidase [9]. More efficient catalysis is then attained after cross-linking the redox polymers and the enzyme with a biofunctional reagent. Calvo et al. show the applicability of multilayer structures of redox polymers and glucose oxidase to biosensor design [10]. In these studies, the build up of multilayer structures is electrostatically driven by alternate immersion of the electrodes in solutions containing positively charged ferrocene-attached redox polymers and negatively charged polyanionic enzymes, providing effective mediation due to the redox sites in the polymer. These redox sites allow 'wiring' of the enzyme by an electron hopping charge propagation mechanism. Electrocatalysis in general is of great economic importance and the aim of these modified electrodes is to drive electrochemical reactions selectively and/or at moderate potentials, and with better control than could be possible by the direct interaction between the substrate and the electrode. Electron and charge transfer through thin films of redox polymers has been studied extensively [11-14].

3.1.2 $[Ru(bpy)_3]^{2+}$ The 'Parent' Complex

It is highly desirable to incorporate redox centres with well behaved properties when seeking to create redox polymers with useful electrochemical, optical or photophysical properties. Much attention has been paid to polymers containing poly(pyridyl) complexes of ruthenium^{II} and osmium^{II}. $[Ru(bpy)_3]^{2+}$ and $[Os(bpy)_3]^{2+}$, (where bpy is 2,2'-bipyridine) are logical choices for metal centres to form complexes of these redox polymers because of their many attractive properties:

i) They exhibit a rich range of photophysical properties that can be used to probe film properties (which is useful in developing photonic devices).

ii) They form stable low-spin d^6 complexes.

iii) Their electrochemistry is well behaved.

iv) They are chemically stable in a range of oxidation states.

The properties of ruthenium- and osmium-tris(bipyridyl) complexes are generally well understood, and they have become standard models and reference complexes for comparison with many other Ru^{II} and Os^{II} complexes, including those described in this chapter and chapter four. In the next section, the excited state structures, photophysical processes and photochemistry of these two 'parent' complexes are discussed.

Paris and Brandt first reported $[Ru(bpy)_3]Cl_2$ as a luminescent species in fluid solution in 1959 (see Figure 3.2) [15]. Since then the interest in this complex has flourished, and as a result much is known about its photophysical and photochemical properties [16-20]. This molecule, along with the osmium analogue, has become a building block for the ever-expanding array of photoactive molecules. Ru^{II} and Os^{II} form octahedral coordination complexes with a diamagnetic t_{2g}^6 electronic configuration. The metal-tris(bipyridyl) complexes exist in two enantiomeric forms. These two forms have indistinguishable electrochemical properties and the only difference in their spectroscopic properties in that they exhibit opposite rotations of polarised light.

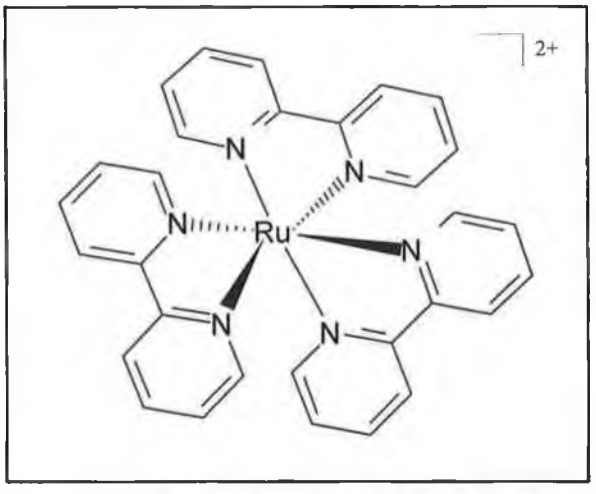

***Figure 3.2** Structure of $[Ru(bpy)_3]^{2+}$*

The electronic absorption spectrum of $[Ru(bpy)_3]^{2+}$ exhibits an intense absorption band at 452nm. This band has been assigned to a metal-to-ligand charge-transfer (MLCT) transition. In $[Ru(bpy)_3]^{2+}$ the three bipyridyl ligands contain σ-donor orbitals localised on the nitrogen atoms, and π-donor and π*-acceptor orbitals delocalised on the aromatic rings. The ligand-centred π* orbitals are low lying, and lower in energy than the metal-centred σ* (e_g) orbitals. When $[Ru(bpy)_3]^{2+}$ absorbs the energy of an incident light beam an electron from the ground state orbital (π_{metal}) of ruthenium is promoted to a ligand orbital (π^*_{ligand}) localised on one of the bipyridyl rings, resulting in a MLCT excited state. The excited state can be represented as follows: $[Ru^{II}(bpy)_3]^{2+} + h\nu \rightarrow [Ru^{III}(bpy)_2(bpy^{-})]^{2+}$

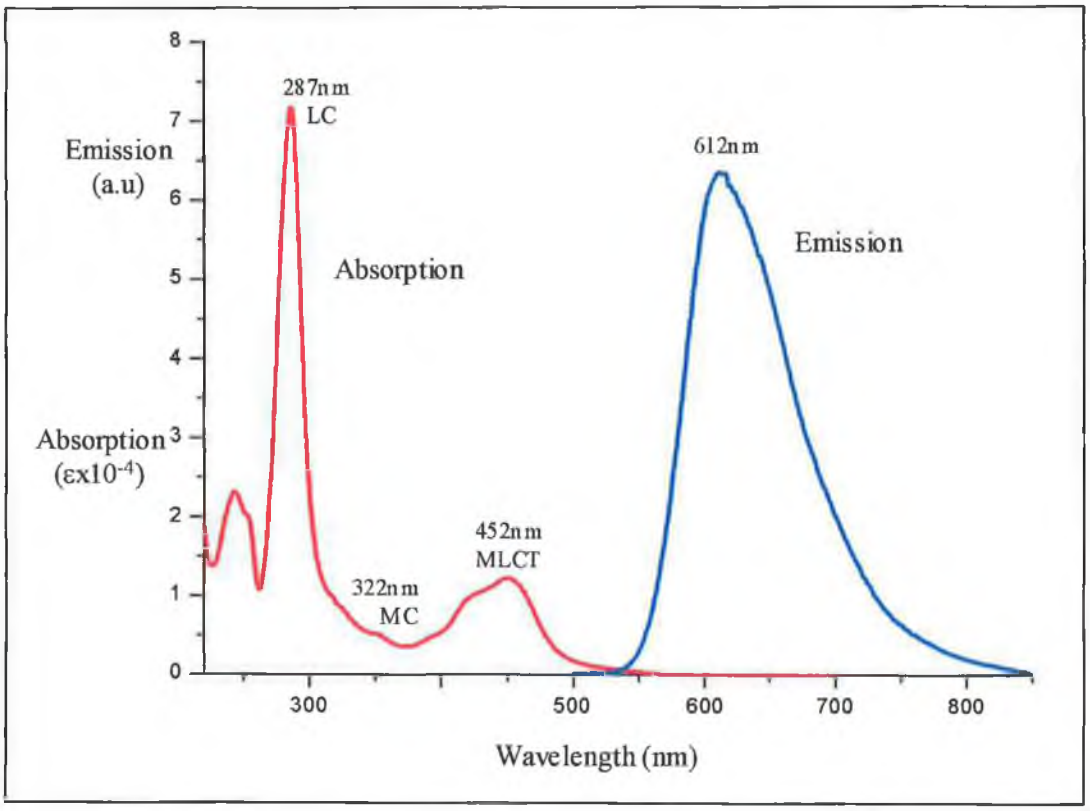

***Figure 3.3** Absorption and emission spectra of $[Ru(bpy)_3]^{2+}$ in acetonitrile (Where bpy is 2,2-bipyridine).*

The other important excited states that can arise following the other transitions are the metal-centred (MC) excited states, between π_{metal} and σ^*_{metal} orbitals, and ligand-centred (LC) excited states, between π_{ligand} and π^*_{ligand} orbitals. The relative ordering

of these excited states, together with the possible radiative, non-radiative and deactivation pathways are shown in Figure 3.4. The singlet state ^{1}MLCT has a very short lifetime and converts into a triplet excited state (^{3}MLCT) by fast intersystem crossing (ISC). This is a spin forbidden transition but is made possible by spin-orbit coupling. Emission from the triplet state (^{3}MLCT) to the ground state (k_r), or radiationless deactivation (k_{nr}) to the ground state can take place [21]. Radiative decay can occur as fluorescence or phosphorescence. Another deactivating pathway is population of the metal-centred (^{3}MC) excited state, giving rise to either radiationless deactivation (k_{nr}) or photodecomposition of the complex. Population of the ^{3}MC is dependent on ΔE_{act}, the energy separation between the ^{3}MLCT and ^{3}MC states, and is thermally activated. When photodecomposition of the complex occurs the electron occupies an antibonding metal-based orbital, resulting in distortion of the metal ligand axes and weakening the Ru-N bonds. Photodecomposition manifests itself as ligand loss followed by coordination of a substitute ligand, often solvent.

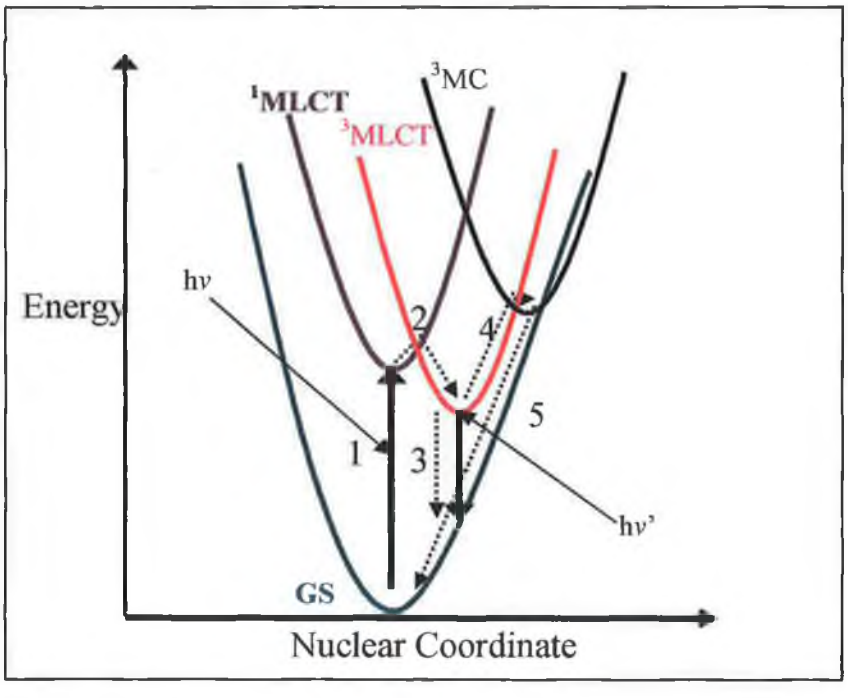

Figure 3.4 *The photophysical properties of $[Ru(bpy)_3]^{2+}$ showing the relative order of the excited states.* ***1****: Absorption of light with excitation from the ground state (GS) to the ^{1}MLCT stat;* ***2****: ISC;* ***3****: Radiative (hν') and non-radiative relaxation to GS from ^{3}MLCT state;* ***4****: Thermal population of the ^{3}MC state;* ***5****: Radiationless deactivation of the ^{3}MC state to the ground state.*

Ru^{II} and Os^{II} compounds are redox active and the most widely used method to determine redox potentials is cyclic voltammertry, typically performed in non-aqueous aprotic solvents such as acetonitrile or DMF. Ru^{II} complexes can be oxidised (removal of a metal-localised electron) or reduced (addition of an electron in a ligand π^* orbital).

Metal Complex	$M^{II/III}$	Ligand Reduction
$[Ru(bpy)_3]^{2+}$	1.26V	-1.35V
$[Os(bpy)_3]^{2+}$	0.83V	1.28V

Table 3.1 *The ground state standard potentials of tris(bipyridyl) moieties in acetonitrile vs. SCE*

The most interesting feature of both Ru^{II} and Os^{II} polypyridyl redox chemistry is that typically both metal and ligand redox processes are fully reversible. This is advantageous in that it allows for the investigation of the spectroscopic properties of the oxidised and reduced forms of the complex in both the ground and excited states.

$$[M(bpy)_3]^{2+} \rightleftharpoons [M^{III}(bpy)_3]^{3+} + e^-$$

where M is either ruthenium or osmium.

All molecular excited states are potential redox reagents since the absorption of light leads to excitation of an electron to a higher level (where it is more weakly bound) and at the same time leads to the production of an electron hole in the lower level. Excited state species hence can be better oxidants as well as reductants than the corresponding ground state. This correlation is described by an orbital diagram in Figure 3.5 for the $[Ru(bpy)_3]^{2+}$ species. The basis for such correlations is derived from the fact that the lowest energy MLCT transition involves the promotion of an

electron from a metal-centred π_{metal} orbital to the lowest antibonding 'spatially isolated' ligand-centred π^* orbital which bears strong resemblance to the lowest π^* orbital of the free ligand. The metal-centred and ligand-centred orbitals involved in these charge transfer transitions are also involved in the oxidation and reduction process of the molecule. $[Ru(bpy)_3]^{2+}$ possesses a long-lived excited state, which in correlation with the large excited state redox potentials may participate in a range of energy transfer or biomolecular redox processes [22-25].

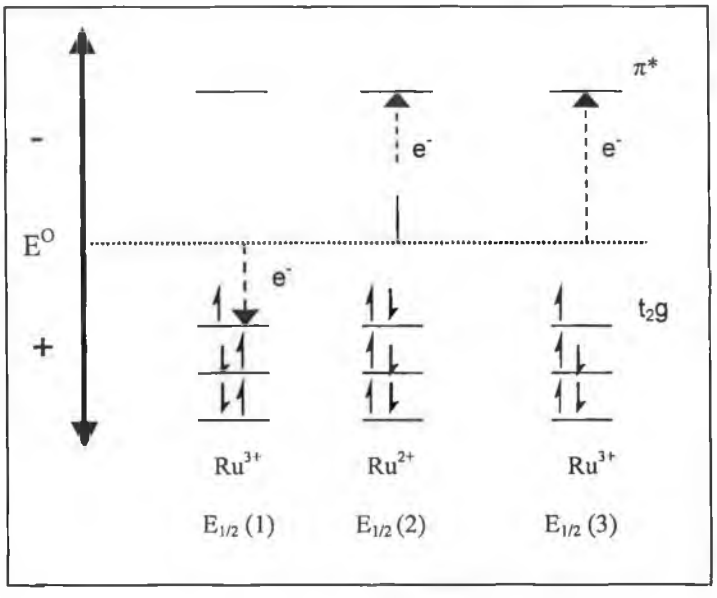

Figure 3.5 *Schematic representation of the relationship between the electronic and the redox orbitals in* $[Ru(bpy)_3]^{2+}$ *[26].*

Osmium complexes exhibit chemistry closely related to that of ruthenium. For $[Os(bpy)_3]^{2+}$ the ^{3}MLCT excited state lifetime is 10-30 times shorter than for $[Ru(bpy)_3]^{2+}$ and the ^{3}MC state lies at a higher energy. For this reason osmium complexes are photochemically inert [27]. The oxidation potentials of Os^{II} compounds are generally lower than those of the analogous Ru^{II} complexes (Table 3.1). This means that higher oxidation states are more stabilised for osmium complexes. Another difference between Ru^{II} and Os^{II} is spin-orbit coupling, which is much larger for third-row transition elements than the second-row metals. This result

in mixing of the singlet and triplet states, and formally forbidden transitions will often be observed. An example is the $\pi - \pi^*$ ^{3}MLCT absorption band which is very weak for $[Ru(bpy)_3]^{2+}$ but quite intense for $[Os(bpy)_3]^{2+}$.

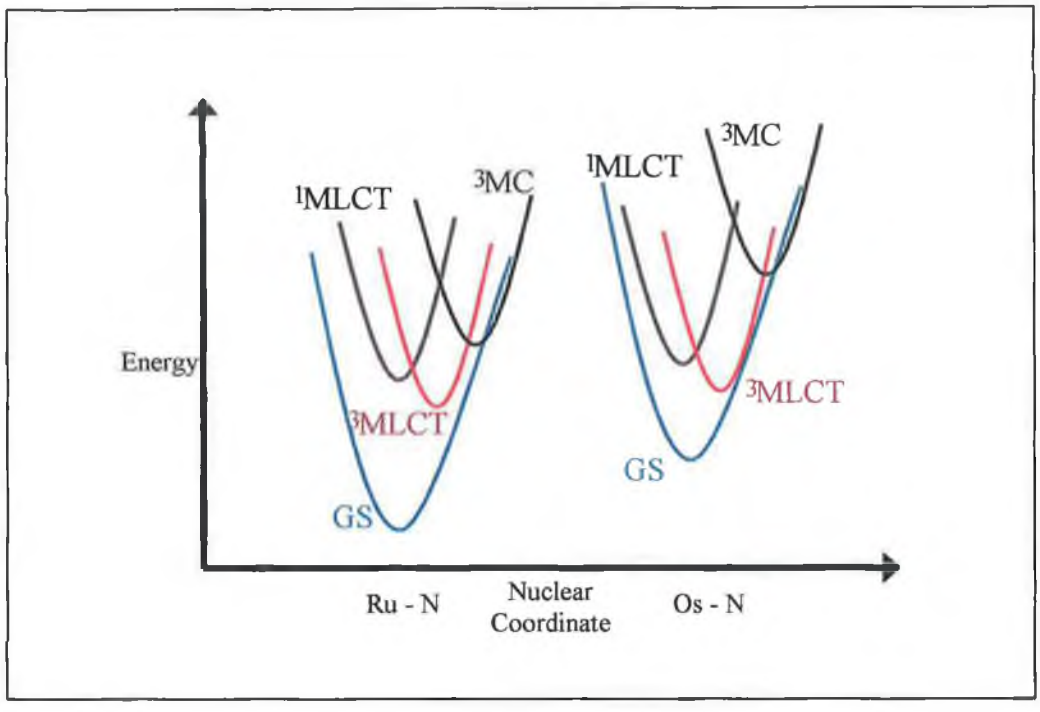

Figure 3.6 *Excited state structures of $[Ru(bpy)_3]^{2+}$ compared to that of $[Os(bpy)_3]^{2+}$.*

3.1.3 Redox Polymers containing Poly(pyridyl) Complexes of Ru^{II} and Os^{II}

In 1979 Clear et al., reports the first evidence of a redox polymer containing a poly(pyridyl) complex of Ru^{II} [28]. This complex $[Ru(bpy)_2(PVP)Cl]^+$, where PVP is poly(4-vinylpyridine), was investigated as a potential catalyst for the photodecomposition of water by visible light. In 1981 Haas at al., went on to report the first instance of a photosubstitution reaction of surface attached systems by coating a glassy-carbon electrode with the $[Ru(bpy)_2(PVP)Cl]^+$ moiety [29]. Since then these types of systems have extensively been studied and developed [30-34]. There is now a well developed background of synthetic chemistry for the attachment of Ru^{II} and Os^{II} poly(pyridyl) complexes to preformed polymer backbones. This can be achieved through the covalent attachment of the metal centre to any polymer

containing a pendant coordinating group, [35-47] or through the electrostatic incorporation of the charged complexes into cationic/anionic polymer films [48-56]. Through these methods, the physical properties of the monomeric compounds can be transferred to their polymeric analogues. The redox reactions and chemical behaviours of the metallopolymers produced can be predicted and tuned [37].

Preparation through the covalent attachment method offers a high degree of synthetic control, structural control and reproducibility. The synthesis of metallopolymers containing poly(pyridyl) Ru^{II} or Os^{II} compounds is based on the different lability of the chloride ligands in the complex $M(bpy)_2Cl_2$, where M is either Ru^{II} or Os^{II} [57,58]. The removal of the first chloride occurs readily by refluxing in methanol or ethanol, while removal of the second chloride requires aqueous-solvent mixtures [37,38,44,45]. Consequently, for the synthesis of a mono-substituted polymer, $[M(bpy)_2(Pol)Cl]^{2+}$, refluxing in ethanol is sufficient, whereas for bis-substituted materials $[M(bpy)_2(Pol)_2]^{2+}$, water is added to the reaction mixture.

Ru^{II} and Os^{II} polymers (where M denotes the metal) of the type $\{[M(bpy)_2PVP_nCl]Cl\}$, where n is 5 or 10 are prepared in this chapter. These redox polymers have been previously reported in the literature [34,37]. Forster et al. first reported the synthesis of a soluble osmium-based polymer [37]. Prior to this, reports of osmium poly(pyridyl) containing polymeric materials were of heavily cross-linked polymers that were formed by electropolymerisation at electrode surfaces. This procedure typically gives rise to insoluble product, which are difficult to control and characterise [59,60,61].

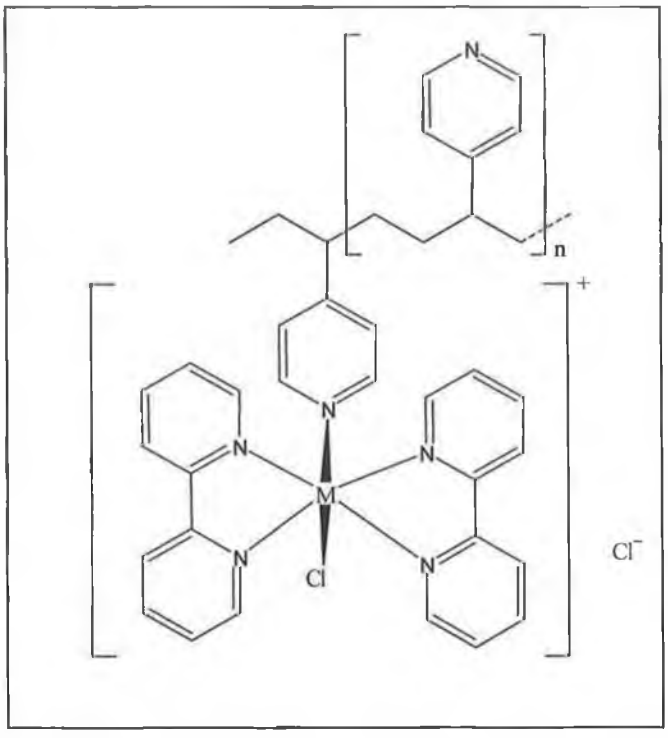

Figure 3.7 *Structure of the monosubstituted redox polymer* $[M(bpy)_2PVP_nCl]Cl$.

In this chapter, materials of different metal loadings are prepared by simply varying the relative molar amounts of the reactants, polymer-to-metal loadings ranging from 1:5 (n = 5, one metal complex per five monomer units) to 1:10. Although more dilute loadings may be synthesised, the presence of both bis- and mono-substituted centres prevents a precise evaluation of the metallopolymer composition [44,47,62-65]. The backbone may be changed, provided it has a pendant coordinating group, thus enabling materials of differing physico-chemical characteristics to be prepared. Previously, polymers that have been considered in this type of synthesis include poly(4-vinyl)pyridine [30,31,66-68], poly(N-vinylimidazole) (PVI) [38,46,47], and a series of 4-vinylpyridine/styrene copolymers (PVP/PS) [36]. The only polymer backbone used throughout this work is poly(4-vinylpyridine). By reacting the metal complexes with preformed polymers, cross-linking during synthesis is avoided and soluble polymers are obtained.

The materials may therefore be characterised and investigated in great detail as solution phase species, as well as in an immobilised state. Conventional spectroscopic and electrochemical methods have been used to probe the nature of the coordination sphere around the metal ion, and electron and charge transfer through thin films on electrode surfaces has been studied extensively [12-14,60,69-72]. Conventional techniques employed to study charge transport in these redox polymers include cyclic voltammerty (CV), potential step chronoamperometry (CA) and electrochemical impedence spectroscopy (EIS). Electrochemical quartz crystal microbalance (EQCM) techniques have provided important information about solvent and ion content of the modifying layers [73]. Elemental analysis, molecular weight and thermal methods have also been used in the characterisation of these materials [38]. For example, thermal analysis of the PVP-based redox polymers has shown that the glass transition temperature is above 100°C, therefore for most solvent/electrolyte systems, glass transitions do not have to be taken into account when analysing the electrochemical behaviour of these polymer coatings.

3.1.4 Assembly of Polymers at SurfacesT KJSBFB

Polymers are being used in an increasingly wide range of applications. Precise surface characterisation is an important part in the development of new materials, and in the understanding of the problems and behaviour in existing materials. Surface properties are critical to the end-use or performance of the polymeric article. These include properties related to adhesion, wear properties, electrical properties, optical properties, permeability and chemical reactivity. These are dependent upon the detailed physical and chemical structure of the polymer surface. Analysis of thin layers of the redox polymers may be carried out using normal surface analysis techniques. STM has been used to investigate the surface structure of

$[Os(bpy)_2(PVP)_{10}Cl]Cl$ films on polycrystalline graphite [74]. The topographical images, obtained of the samples before and after the electrochemical cycling in a sulphuric acid electrolyte solution show a considerable change. Prior to electrochemical cycling the films are characterised by ordered domains with rows of fibrillar structure, while after, ordered domains with rows of granular structure are observed. Brown at al. reports that this is most likely as a result of the swelling of the film in the electrolyte used [74].

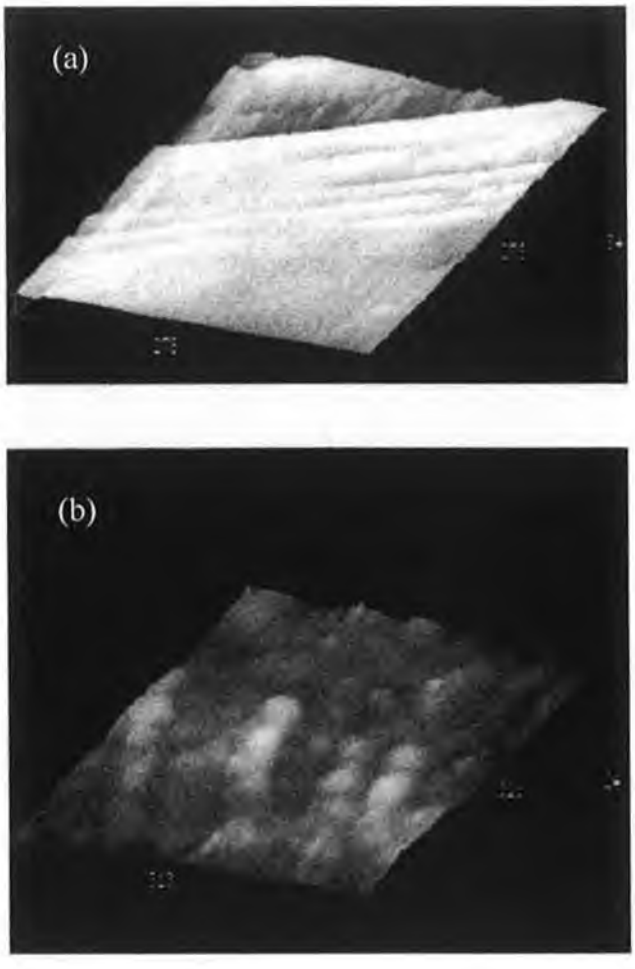

Figure 3.8 *STM images of an osmium-containing metallopolymer modified polycrystalline graphite electrode:* ***(a)*** *Before electrochemical cycling a rod-like structure is observed;* ***(b)*** *After electrochemical cycling rows of granular structure are observed [74].*

Many applications of redox polymers necessitate an understanding of the self-organisation, interactions, and morphology of the polymeric systems when deposited

from solution onto non-electrode substrates such as silicon, mica or glass. Upon such an investigation issues which need to be addressed include; a) the deposition process used; b) the surface morphology; c) the chemical bonding to the substrate surface; d) the stability and integrity of the film; and e) the reactivity at the film surface. Atomic force microscopy with its high-resolution surface mapping capabilities, and photoelectron spectroscopy, may be used as key components of this characterisation.

The next section moves on to describe the synthesis, characterisation and surface analysis of the redox polymers in this chapter. This is followed by a discussion of the results.

3.2 Experimental

3.2.1 Equipment and Materials

All solvents employed were of HPLC grade or better and used as received unless otherwise stated. For all spectroscopic measurements Uvasol (Merck) grade solvents are employed. All reagents employed in synthetic procedures were of reagent grade or better. *Cis*-$[Ru(bpy)_2Cl_2].2H_2O$, *Cis*-$[Os(bpy)_2Cl_2].2H_2O$, and tetraethylammonium perchlorate (TEAP) were prepared by previously reported procedures [28,75,76].

^1H NMR spectra were recorded on a Bruker AC400 (400MHz) NMR spectrometer. All measurements of starting materials *Cis*-$[Ru(bpy)_2Cl_2].2H_2O$ and *Cis*-$[Os(bipy)_2Cl_2].2H_2O$ were recorded in d_6-dimethylsulfoxde. Chemical shifts are recorded relative to TMS. The spectra were converted from their free induction decay (FID) profiles using XWINNMR software.

UV-Visible absorption spectra were recorded on a Shimadzu UV/Vis-NIR 3100 spectrophotometer interfaced with an Elonex-466 PC using UV/Vis data manager software. Emission spectra were obtained both at 298K and 77K using a

LS50-B luminescence spectrophotometer, equipped with a red sensitive Hamamatsu R298 PMT detector, interfaced with an Elonex-466 PC using Windows-based fluorescence data manager software. Emission and excitation slit widths of 5nm were used for all measurements except at low temperature, where an emission slit width of 2nm was used.

Electrochemical measurements were carried out on a Model 660 electrochemical workstation (CH Instruments). Measurements were carried out in dry acetonitrile with TEAP as electrolyte. A 3mm glassy carbon disk shrouded in Teflon was used as the working electrode, a platinum wire as the counter electrode and a saturated calomel electrode (SCE) served as the reference electrode. A methanolic 1% (w/v) solution of the metallopolymer was pipetted directly onto the clean glassy carbon surface. The solvent was then allowed to evaporate slowly overnight (12 hours) in a solvent saturated chamber, followed by air-drying. Peak positions for the redox couples of the metallopolymer coatings are obtained at slow sweep rates.

Section 2.3.5 describes in detail the AFM instruments used throughout this thesis: the Digital Instruments Multimode and the Digital Instruments Nanoscope IIIa. Descriptions of the cantilevers used are also given. Two different scanners have been used to explore different ranges of scan length. Most of the studies have been performed with the multimode scanner. However, the Nanoscope IIIa is used to get an overview of the surface on a hundred micrometers scale. The photoemission and NEXAFS measurements were taken on beam line 5.U1 of the Synchrotron Radiation Source, Daresbury, U.K. as described in section 2.5.1.

3.2.2 Synthesis of Polymers

Poly(4-vinylpyridine) was purchased from Aldrich and used as received. *Cis-$[Ru(bpy)_2Cl_2].2H_2O$* and *cis-$[Os(bpy)_2Cl_2].2H_2O$* were prepared as described previously [77].

cis-$[Ru(bpy)_2Cl_2].2H_2O$

10.3g (66 mmol) of bpy, 8g (33 mmol) of $RuCl_3.xH_2O$ and 2g LiCl in 60ml of DMF were heated at reflux for 8h. The solution was then cooled to 25°C and transferred to 100ml of acetone and kept at - 4°C overnight. The product was filtered and washed with ice water (until the filtrate became colourless) and 50ml cooled diethyl ether, yielding a dark purple powder. Yield 12.9g (25 mmol, 76%).

^{1}H NMR (400MHz): 9.97 (2H, d), 8.64 (2H, d), 8.49 (2H, d), 8.07 (2H, dd), 7.79 (2H, dd), 7.685 (2H, dd), 7.51 (2H, d), 7.10 (2H, dd).

cis-$[Os(bpy)_2Cl_2].2H_2O$

193mg (1.24 mmol) of bpy and 300g (0.62mmol) of K_2OsCl_6 were dissolved in 3ml of ethylene glycol and heated at reflux for 45min. The reaction mixture was cooled to room temperature and 5ml of saturated sodium dithionite solution was added. The mixture was stirred for a further 30min and the black precipitate formed was filtered and washed with water (until the filtrate became colourless) and then 50ml of diethyl ether. Yield 320mg (0.52mmol, 83%)

^{1}H NMR (400Hz): 9.61 (2H, d), 8.59 (2H, d), 8.37 (2H, d), 7.61 (2H, dd), 7.58 (2H, dd), 7.29 (4H, m), 6.8 (2H, dd).

[Ru(bpy)$_2$(PVP)$_n$Cl]Cl

[Ru(bpy)$_2$(PVP)$_5$Cl]Cl and [Ru(bpy)$_2$(PVP)$_{10}$Cl]Cl were prepared as described by Forster et al., with a variation in the reflux method [37]. The required amounts (see Table 3.2) of PVP and cis-[Ru(bpy)$_2$Cl$_2$].2H$_2$O were dissolved in ethanol. They were microwave refluxed in the dark, at 300-Watts power at one minute intervals for up to thirty minutes. The reactions were continuously monitored by UV-visible and emission spectroscopy. The solvent was removed in vacuo until 5ml remained. This was slowly added dropwise, while being constantly stirred to ice-cold diethyl ether. The solution was then filtered, washed with diethyl ether and dried. Yields ranged between 67% - 78%.

[Os(bpy)$_2$(PVP)$_n$Cl]Cl

[Os(bpy)$_2$(PVP)$_5$Cl]Cl and [Os(bpy)$_2$(PVP)$_{10}$Cl]Cl were prepared using the previous method. A longer reflux time was required. However, this was reduced from up to eight days as described by Forster et al., [37] to under two hours using the microwave reflux set up. Although no photochemical reactions were observed, the reactions were carried out in the dark. The reactions were monitored by UV-visible spectroscopy and cyclic voltammetry. Yields ranged between 80% - 89%.

Ratio	PVP	Ru(bpy)$_2$Cl$_2$	Yield	Os(bpy)$_2$Cl$_2$	Yield
1:5	52mg 0.5mmol	52mg 0.1mmol	88mg	57mg 0.1mmol	97mg
1:10	104mg 1.0mmol	52mg 0.1mmol	111mg	57mg 0.1mmol	155mg

Table 3.2 *Required amount of reactants and final yields*

3.2.3 Surface Preparation and Analysis of Polymers

Atomic Force Microscopy

Methanol solutions of the different polymers have been applied to substrates of native-oxide covered silicon (100) or silicon (111) wafers 1cm^2 in area. The silicon substrates were solvent rinsed by sonication in four stages with: a) ethyl lactate; b) acetone; c) methanol; and d) isopropyl alcohol, and then blow-dried with N_2 before sample deposition. The concentrations of the polymer solutions and the method of deposition have been varied systematically. Molecular assembly was achieved in two different ways using two different rates of the adsorption process:

i) Spin-coating. Unless otherwise stated, 20µl of a 0.005M solution of the polymer in methanol was placed on the substrate. This was then rotated for a specified time (usually 30 seconds). The adsorption therefore occurs very rapidly. Spinning speeds are varied and were between the ranges of 2500rpm (rotations per minute) and 4500rpm.

ii) Solution-casting. Unless otherwise stated, 20µl of a 0.005M solution of the polymer in methanol was placed on the substrate. The solvent was then allowed to evaporate. The evaporation of the solvent for the case of methanol required the sample to be left overnight (10 – 12 hours).

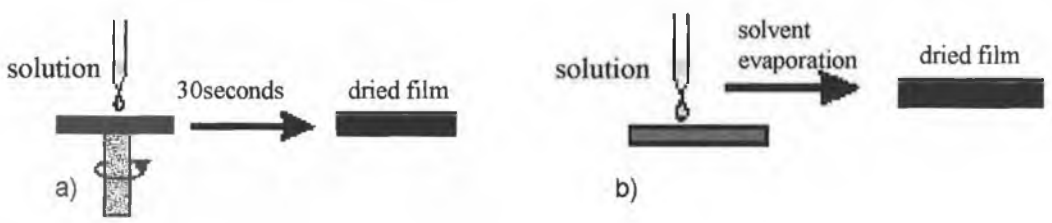

Figure 3.9 *Methods of sample preparation:* ***a)*** *Spin-coating deposition;* ***b)*** *Solution-casting deposition.*

The dried films prepared by the different routes have been investigated by tapping mode AFM in an air environment.

Photoemission Spectroscopy

For all photoelectron spectroscopy samples, 20μl of a 0.005M solution of the polymer in methanol was spin-cast onto a solvent-cleaned 0.7cm^2 native-oxide covered Si(111) wafer. For all PES measurements the binding energies are referenced to the Fermi edge of the Ta sample holder and photon energies were calibrated against NEXAFS TiO_2 spectra recorded at similar times to the PES spectra.

3.3 Results and Discussion

3.3.1 Characterisation of Metallopolymers

For metallopolymers, the nature of the coordination sphere around the central atom is of importance since it determines the redox potential and photophysical properties of the material obtained. The coordination around the metal ions was examined by comparison of these spectroscopic and electrochemical properties, with those of appropriate model compounds, and of results obtained for the same metallopolymers previously prepared in the literature [37]. The data obtained for the metallopolymers in this work have been given in Table 3.3. Both emission and absorption spectroscopy have proven useful in the characterisation of these metallopolymers [45-47,78-80].

Microwave radiation provides an alternative to conventional heating as it utilises the ability of liquids or solids to transform electromagnetic energy into heat. It is an excellent method for carrying out reactions quickly and efficiently. This technology has been applied to a number of useful processes such as application to

waste treatment, organic synthesis and polymer technology. For example, microwave assisted synthesis of the optically active poly(amide-imide) was carried out by Mallakpour at al., [81] who demonstrated that the synthesis could be completed within ten minutes as opposed to a five hour conventional synthesis. Several hazards are present in the use of microwave radiation. Anti-bumping agents are ineffective and can cause several solvents to decompose in the presence of microwave radiation. Choice of solvent is limited as the solvent in use must have a permanent electric dipole moment. Also superheating of the reaction solution normally occurs and can cause problems in cases where regulation of the reaction temperature is necessary [82-86].

Compound	$\lambda_{max\ (absorpn)}$ [a]	$\lambda_{max\ (emission)}$ [a]	$\lambda_{max\ (emission)}$ [b]	$^{c}E_{1/2}^{oxidation}$
	nm	298K, nm	77K, nm	V
$[Ru(bpy)_3]^{2+}$	452, 322	608	582	1.26
$[Os(bpy)_3]^{2+}$	479,[d]	725[e]	712[e]	0.83
$[Ru(bpy)_2PVP_5Cl]Cl$	496, 356	709	665 (605)	0.75
$[Ru(bpy)_2PVP_{10}Cl]Cl$	491, 355	704	680 (640)	0.75
$[Os(bpy)_2PVP_5Cl]Cl$	431, 360	-	-	0.35
$[Os(bpy)_2PVP_{10}Cl]Cl$	440, 362	-	-	0.36

Table 3.3 *Results obtained for redox polymer and model compounds.* ***a****: measured in methanol solution;* ***b****: measured in 50:50 methanol : ethanol solution;* ***c****: electrolyte is 0.1M TEAP/acetonitrile, scan rate 100mv/s;* ***d****: measured in acetonitrile solution;* ***e****: measured in butyronitrile solution.*

As discussed in section 3.2.1 ruthenium poly(pyridyl) complexes typically exhibit two bands in the visible region of the spectrum. These have been assigned to metal-to-ligand charge transfer (MLCT) transitions from the metal localised orbital Ru(dπ) to the ligand localised orbital, bpy(π*) orbitals. The positions of the absorption maxima are governed by the δ-donor and π-acceptor properties of the ligands. A ruthenium complex with a strong δ-donating ligand such as chloride is electron rich

and the MLCT band is present at a lower energy. This also results in a lower oxidation potential for the compound [41]. Through comparisons of the UV-visible spectra, the $[Ru(N)_5Cl]Cl$ coordination sphere of the ruthenium centre in the polymeric material is verified. The visible region MLCT bands for the polymer complex occurs (for n=5 and 5=10 respectively) at 496nm and 491nm, while the bands at approximately 356nm and 355nm, like the shoulders at 322 and 344nm in the spectrum of $Ru(bpy)_3^{2+}$, are metal centred (MC) transitions[3]. The remaining bands in the ultraviolet region of the spectra are assigned to ligand centred (LC) π - π^* transitions, apart from the bands which occurs at about 240nm, which are also due to MLCT transitions [38].

The absorption spectra of the osmium metallopolymers, while comparable to the monomeric models [37], are typically more complicated than those of the analogous ruthenium compounds. This is a consequence of the mixing of singlet and triplet excited states in Os^{II} complexes which enable formally forbidden transitions, which are not seen for ruthenium complexes, to be observed for osmium [87]. Because of the complicated nature of the UV-visible absorption spectrum, definitive assignments to the coordination sphere of the osmium centre are rarely made by this technique alone. However, the results obtained in Table 3.3 are comparable and in agreement with those obtained in the literature [37].

Further evidence of the $[MN_5Cl]Cl$ nature of the coordination sphere is provided by the emission spectra of the polymers. The ruthenium polymers display only very weak luminescence at 298K and the wavelengths of maximum emission shows a low energy 709nm (1:5 polymer) and 704nm (1:10). Because of the strong similarities in the electronic spectra of the ruthenium polymers with those of the monomeric analogues, emission is thought to originate from bpy-based ^{3}MLCT states.

The most important characteristic for the metallopolymers is their electrochemical behaviour. They possess a metal-based $M^{II/III}$ oxidation. The formal potential of the $M^{II/III}$ oxidation, coated as thin films on electrode surfaces, is sensitive to the nature of the metal coordination sphere [35-37,38-47]. The ruthenium polymers show a formal potential for the $Ru^{II/III}$ redox couples at 0.75V in acetonitrile. The oxidation potentials for the $Os^{II/III}$ redox couple is approximately 300mV to 500mV lower compared to the analogous $Ru^{II/III}$ oxidation [61,64] and, the osmium polymers show a formal potential for the $Os^{II/III}$ redox couples at 0.35V in acetonitrile. This lower oxidation potential has been reported in previous studies and is caused by the higher energy of the 5d orbitals compared to the 4d orbitals of ruthenium [88]. Also in the metallopolymers the low oxidation potential is due to the electron donating effect of the electronegative chlorine substituent. Scanning in the negative potential region shows irreversible peaks, presumably due to bipyridine reduction situated at -1.5V for the ruthenium polymers and -1.47V for the osmium polymers [37].

The spectroscopic and electrochemical behaviour of the metallopolymers from Table 3.3 is consistent with the $[M(N)_5Cl]Cl$ moiety, and compares with those of analogous polymeric compounds [37]. In general, the ratio of metal centres to repeating units of polymer backbone is based on the ratio of the starting materials, assuming complete reaction. Extinction coefficients are also useful in verifying the metal loading [35,38,39,79].

3.3.2 Atomic Force Microscopy Analysis

Introduction

Atomic force microscopy was first applied to polymer surfaces in 1988, shortly after its invention [89]. It is used primarily to reveal surface morphology, nano-structure, chain packing and conformation. It is a very sensitive technique and many problems

may arise. Choosing the right mode of operation is necessary in order to optimise experimental conditions to provide non-destructive and reliable imaging. All measurements were performed in tapping mode as opposed to contact mode to avail of better sensitivity and reduced interaction with surface contamination. As discussed in section 2.1.3.2, in contact mode imaging the sample experiences both compressive forces that originate from the tip-sample contact, and shear forces that are attributed to the lateral scan movement. Both forces could induce elastic and/or plastic sample deformation. One disadvantage to tapping mode is that a slower scan speed is required than when in contact mode. The data is presented in both height mode and amplitude mode.

The commercial availability of an atomically smooth highly polished silicon wafer, along with a low cost and importance in the microelectronics industry has rendered it the most standard hard substrate used in polymer studies [90]. However, defects, roughness, inhomogeneties, or instabilities of the top layer of the silicon substrate influence experiments and are not under absolute control. A parameter characterising the substrate is the contact angle θ [91]. It determines the wetting ability and measurement of flow. When the contact angle of a solid is $\leq 90°$ it progressively becomes more hydrophilic as the angle decreases (i.e. the lower the contact angle the more hydrophilic the substrate).The silicon substrates were characterised prior to polymer deposition by measurement of the dynamic contact angle, and investigation of the surface topography by tapping mode AFM. For the solvent-rinsed substrates the contact angle was $45° \pm 5°$ [92].

Figure 3.10 shows AFM height data for the solvent cleaned silicon substrate. The silicon surface is atomically flat, and has a maximal height variation within 1nm. This precludes any influence of the substrate topography on the observed morphology after polymer deposition. The image was acquired with the maximum

available number of pixels in each scan direction (i.e. the highest resolution), yet scan lines appear across the images. These are artefacts of the data acquisition. Poler at al. reports that imaging a silicon substrate in air with AFM is difficult, and it is rare when the entire surface is homogeneous [93]. The image shown in Figure 3.10 and in the rest of this thesis, were subjected to a first-order plane fitting procedure to compensate for sample tilt, and if necessary, to a second-order flattening using Dimension imaging analysis tools. The flatten command removes the background. It calculates individual least-squares fit polynomials from all scan lines. The polynomials are then subtracted from each scan line. This has proved useful for samples that have sporadic, tall features in predominantly flat areas.

Figure 3.10 *5μm x 5μm tapping mode AFM height data of solvent rinsed native oxide covered silicon (100) substrate. The z-range is 2nm.*

Morphology at different adsorption technique and concentration.

$[Ru(bpy)_2(PVP)_{10}Cl]Cl$ exhibits a good solubility in organic solvents like methanol. This allows for the formation of free-standing films by solution deposition and spin-casting techniques. The assembly and morphology of this polymer has been investigated on a solvent-cleaned native oxide covered silicon (100) substrate, as a

function of the adsorption technique, and in the next section as a function of the concentration of the spin-cast solution. In this section the TM-AFM results of a series of polymer films formed by drop-deposition and spin-casting deposition will be presented. The main goal of this work is not to find a suitable functionalisation of the silicon substrate for stable polymer adsorption, but to observe the self-organisation and the morphology when the polymers are deposited from solution by applying different adsorption techniques.

Figure 3.11 shows height images of the polymer prepared by solution deposition. Solution drop-deposition involves adsorption where the solvent is allowed to evaporate slowly until complete (approximately 12 hours for methanol). No external sources such as spinning are used to speed up the evaporation process. The morphology of the polymer may be characterised as droplet-like islands with lateral dimensions ranging from 45 to 50nm, and heights ranging from 80 to 90nm. These small islands form randomly across the surface. The surface is not homogeneous and larger features also form as indicated by the arrow (in Figure 3.11 (c)). Layers of polymer are observed within this 500nm structure. This also has an average height of ~100nm. This type of sample preparation does not provide any representative information as each area imaged varies randomly across the surface.

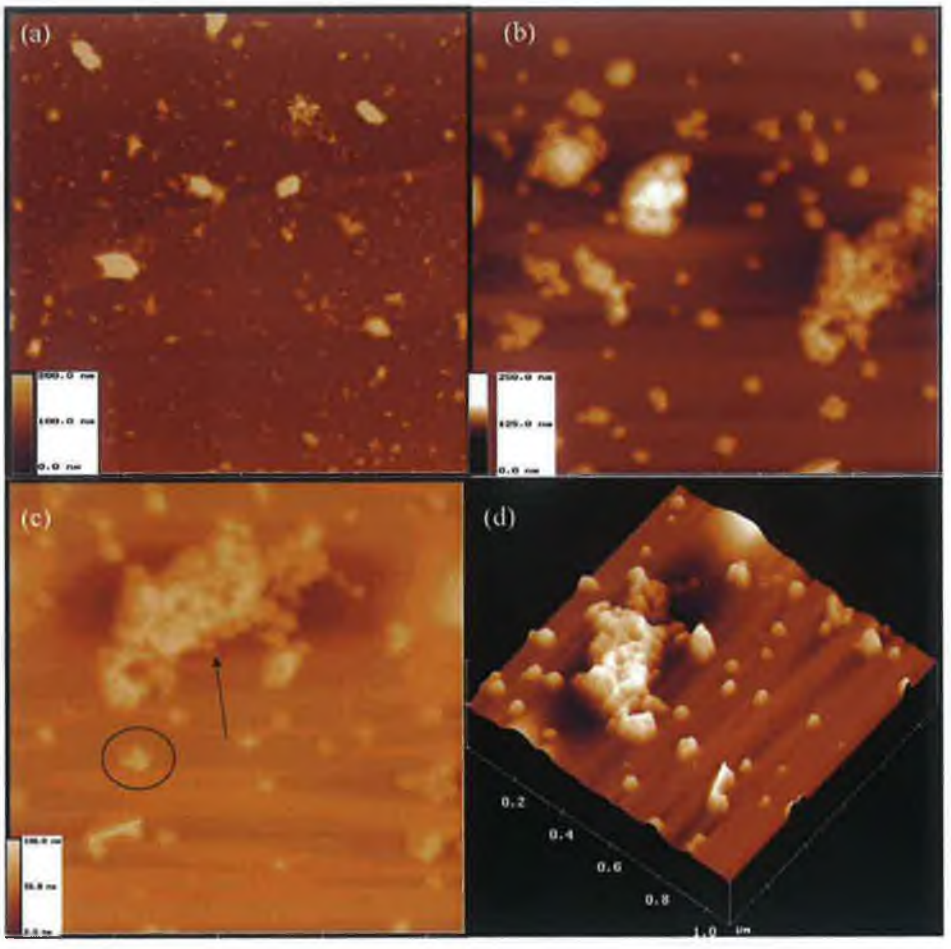

Figure 3.11 *Tapping mode AFM images of [Ru(bpy)$_2$(PVP)$_{10}$Cl]Cl] deposited by solution deposition:* ***(a)*** *10μm x 10μm height image, z-range 200nm;* ***(b)*** *1.227μm x 1.227μm height image, z-range 250nm;* ***(c)*** *1.090μm x 1.090μm height image, z-range 100nm;* ***(d)*** *1.090μm x 1.090μm 3 dimensional plot of the surface topography in height mode, z-range 100nm.*

Figures 3.12 and 3.15 show height and amplitude data for the same polymer sample when spin-cast from solution. Spin-casting represents a technical process exerting shear stresses during film growth. It is a widely used process for applying a thin uniform film to a flat substrate. An excess amount of polymer solution is placed on the substrate. The substrate is then rotated at high speed in order to spread the fluid by centrifugal force. Rotation is continued, with fluid being spun off the edges of the substrate until the desired film thickness is achieved. The solvent (methanol in these experiments) is usually volatile, providing for its simultaneous evaporation.

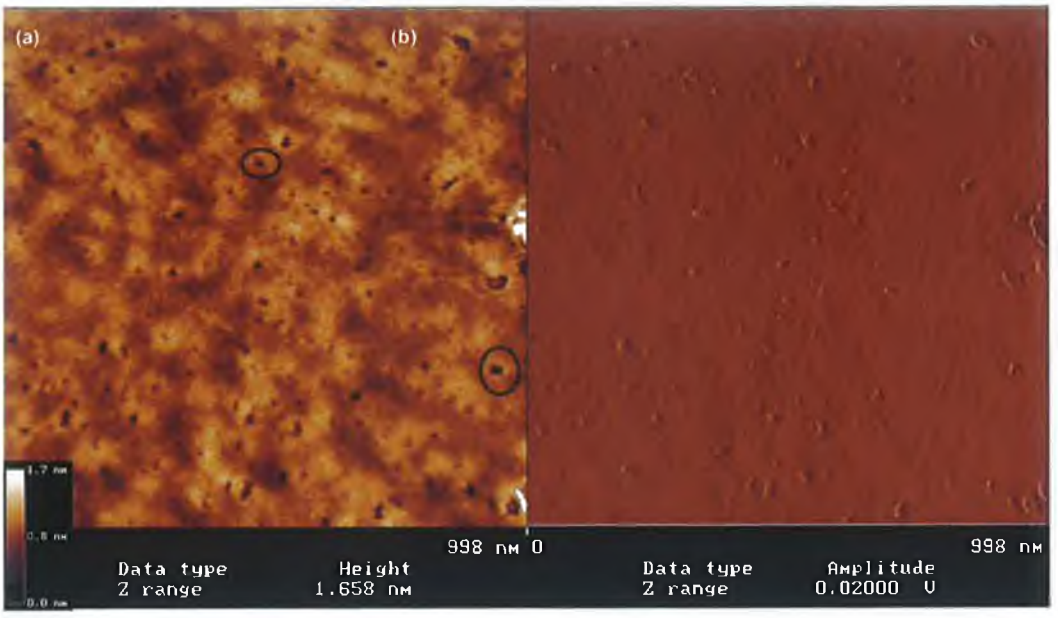

Figure 3.12 *Tapping mode AFM images of [Ru(bpy)$_2$(PVP)$_{10}$Cl]Cl] deposited by spin-casting:* ***(a)*** *0.998μm x 0.998μm height data, z-range 1.7nm;* ***(b)*** *0.998μm x 0.998μm amplitude data, z-range 0.02V.*

The mechanics of spin-coating of polymer films has been investigated in detail [94-98]. The process is a complex one to analyse because there are so many possible mechanisms to consider. Lawrence reports that spin-coating of polymer films may be considered as a three-stage process, where the final thickness and the uniformity of the polymer film are the most important physical quantities [94].

i). In the initial phase fluid is ejected rapidly. The effects of fluid inertia, Coriolis forces, and surface tension are important. In the first second of the process approximately 90% of the fluid is flung from the substrate leaving a much thinner film.

ii). The second phase incorporates most of the mechanisms that control the final film thickness: the flow is now a balance between viscous and centrifugal forces. During this stage there is a decrease in film thickness which is mainly due to the fluid flow, and the concentration boundary layer gradually becomes thicker.

iii). The final phase is a transition to the final dry film. The fluid viscosity rises rapidly so that flow virtually ceases and further fluid loss is primarily due to solvent evaporation.

The higher the spin-speed, the thinner the films that are produced. In these experiments as the sample spins a colour change is observed on the silicon wafer. The variety in colour is dependent on the polymer and the density of the solution. The colours are due to the fact that different thicknesses of polymer film diffract different wavelengths of light. In spinning, the polymers thickness changes as it disperses evenly across the silicon wafer. The darker the colour observed, the thicker the film. The two processes of solvent evaporation used are very different. The striking difference between both methods of application is the presence of a centrifugal force in spin-coating and near-equilibrium adsorption in solution casting.

The structure of $[Ru(bpy)_2(PVP)_{10}Cl]Cl$ spin cast from methanol reveals a thin granular film where the height of the scan in Figure 3.12 (a) is 1.658nm. The image reveals that the polymer forms sequences of 'brighter' and 'darker' regions with a repeat distance of between 25-40nm. The areas located between the 'bright' deposits (Circled areas in Figure 3.12 and 3.15) reveal the presence of small isolated areas that appear to have been 'left behind' during the deposition process. On zooming-in on such an area it appears that all these small objects are similar in size and shape; they are round-shaped, with what appears to be a 'pinhole' in the middle. It was checked that the appearance of these 'doughnut-like' shapes are independent of the parameters used for imaging, which indicates that they do represent the true structure of the polymer. The 'doughnut-like' like holes observed could be explained due to the spinning-process. One explanation is the dewetting process whereby an initially uniform film becomes unstable and breaks up into an array of droplets or

holes [99]. One mechanism of dewetting involves the nucleation and growth of isolated holes. The initial distribution of these holes is random and hence there is no particular length scale that characterises the morphology [100]. Another possibility is that the initial stages of dewetting consist of the unstable growth of capillary waves driven by attractive dispersion forces across the film. In this case the morphology is characterised by one particular length scale i.e. holes of similar size [101] A more detailed study of the formation of these holes is warranted. Film viscosity, interfacial tension and the thickness of the polymer film also effect the polymer film formation.

Digital Instruments Nanoscope IIIa roughness analysis software was used to interpret the morphologies further. By surveying the samples with several images it was observed that the surface was not fully homogeneous, and that a comparison of roughness analyses for the data of Figures 3.13 and 3.16 found that the first image was slightly smoother. However, overall the average value and ranges of the roughness parameters are used to draw conclusions about the degree of roughness on the surface. Table 3.4 lists the results from the roughness analysis.

	Figure 3.17	***Figure 3.20***	***Box1***	***Box 2***
Rms Roughness	0.119nm	0.218nm	0.108nm	0.187nm
Z-Range	1.910nm	3.265nm	1.141nm	1.571nm

Table 3.4 *Comparison of Rms (roughness) values for Figures 3.18 and Figures 3.21*

The surface is evaluated in terms of its R_{rms} roughness. Figures 3.13 and 3.16 show the roughness parameters. 'Image statistics' pertain to the whole image; 'box statistics' pertain to the region contained in the outlined box. The value of the mean roughness *Ra* is calculated as the deviations in height from the profile mean value

[102] where Z is the sum of all height values divided by the number of data points (N) in the profile [103]. Definitions of the values in the roughness analysis are:

i). Z-range: the difference between the maximum and minimum height recorded in the image.

ii). Mean: the mean value of data contained within the image.

iii). Raw mean: the mean value of data without application of plane fitting.

iv). Img. Srf. Area: The three dimensional area of the analysed region. This area is the sum of all the areas of all the triangles formed by three adjacent points.

v). Img. Srf. Area Diff: The percentage difference of the integrated area of the image compared to the areas of the square, which would be represented by a flat surface (i.e. the difference between the images three dimensional surface area and its two dimensional footprint area).

vi). Rms (Rq): This is the root-mean-square of the roughness relative to a plane drawn through the surface at the mean surface height (i.e., the standard deviation of the Z values within a given area).

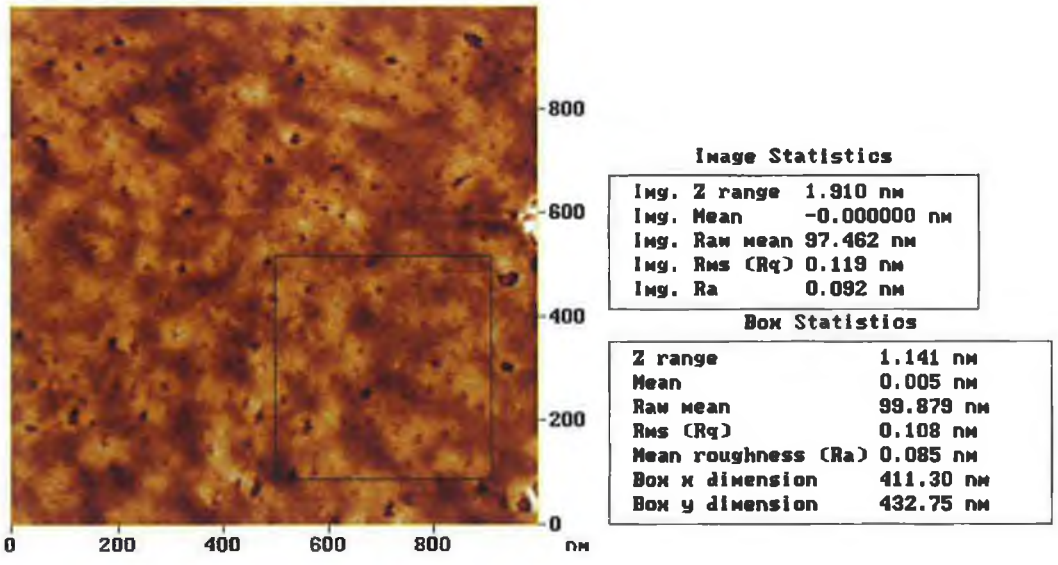

***Figure 3.13** Roughness analysis of of [Ru(bpy)$_2$(PVP)$_{10}$Cl]Cl] thin film. The surface topography is characterised by its R_{rms} roughness value.*

In Figure 3.16 the height around the 'doughnut-like' areas is higher that those found in Figure 3.13. This is apparent on examination of the Z-ranges in the roughness analysis. The z-range in Figure 3.13 is 1.910nm and this increases to nearly double the height to 3.265nm in Figure 3.16. Along with this increase in Z-range the R_{rms} roughness increases significantly to 0.218nm. On analysis of the box R_{rms} roughness for Figure 3.16 a lower value of 0.187nm is observed. This corresponds to a decrease in the number of 'doughut-like' regions with a z-range of only 1.571nm. The values of the surface R_{rms} roughness are a good characterisation method for describing the surface properties of the investigated samples. By the roughness value it is possible to determine alternating height differences better than just by height parameters alone.

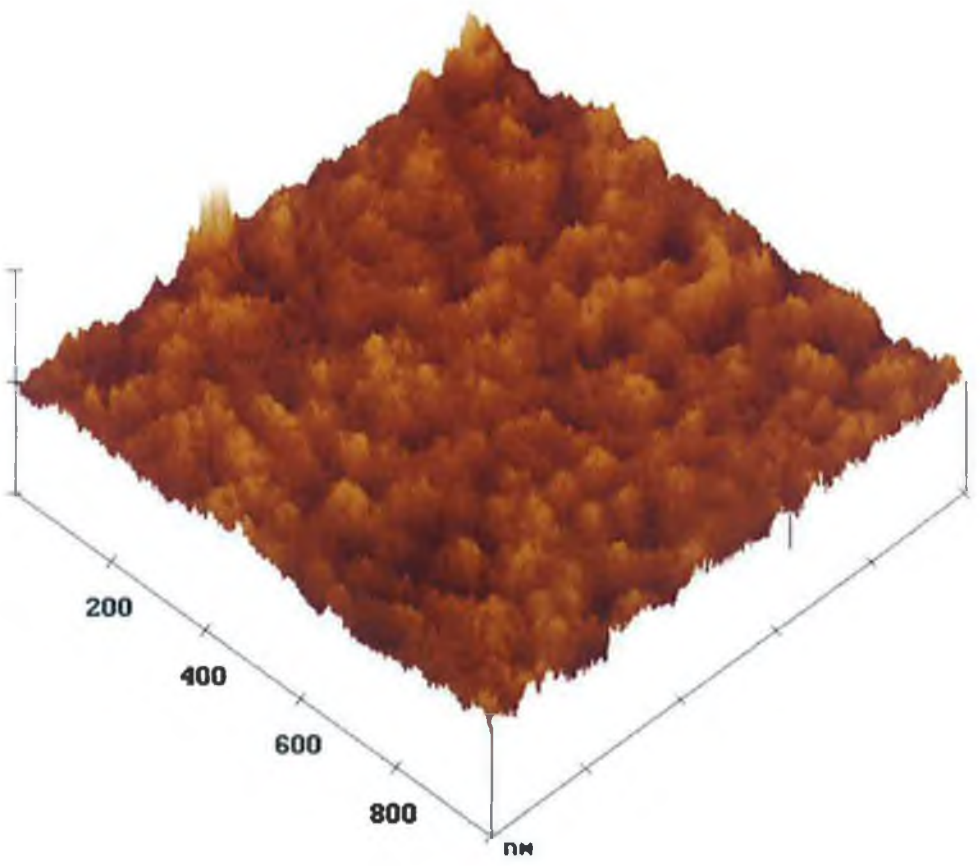

Figure 3.14 *Three dimensional plot of the surface topography from Figure 3.12 (a) in height mode, z-range 1.7nm.*

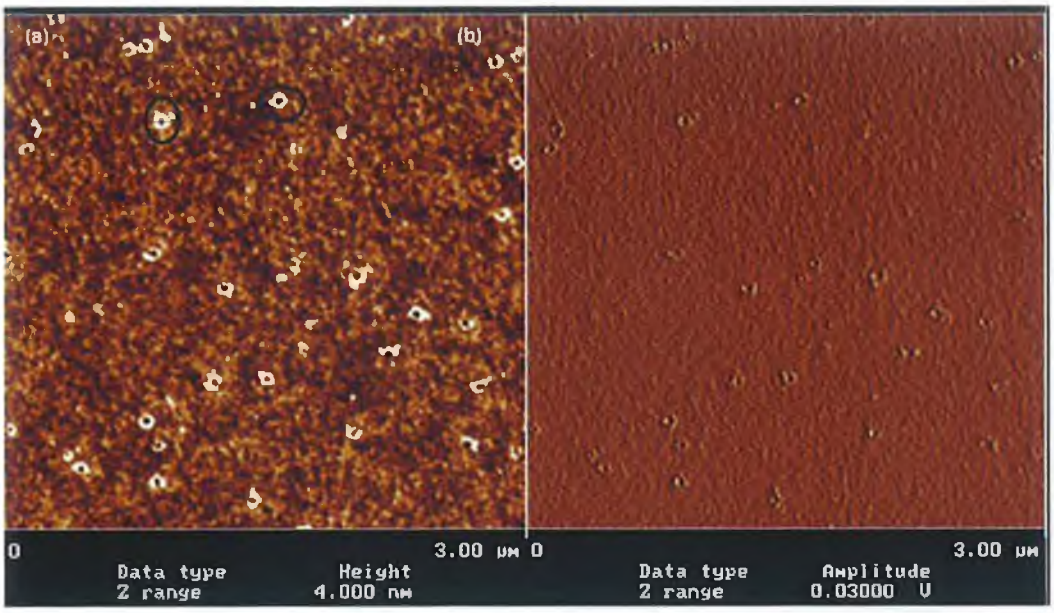

Figure 3.15 *Tapping mode AFM images of $[Ru(bpy)_2(PVP)_{10}Cl]Cl$ deposited by spin-casting:* ***(a)*** *3.0µm x 3.0µm height image, z-range 4nm;* ***(b)*** *3.0µm x 3.0µm amplitude image, z-range 0.03V.*

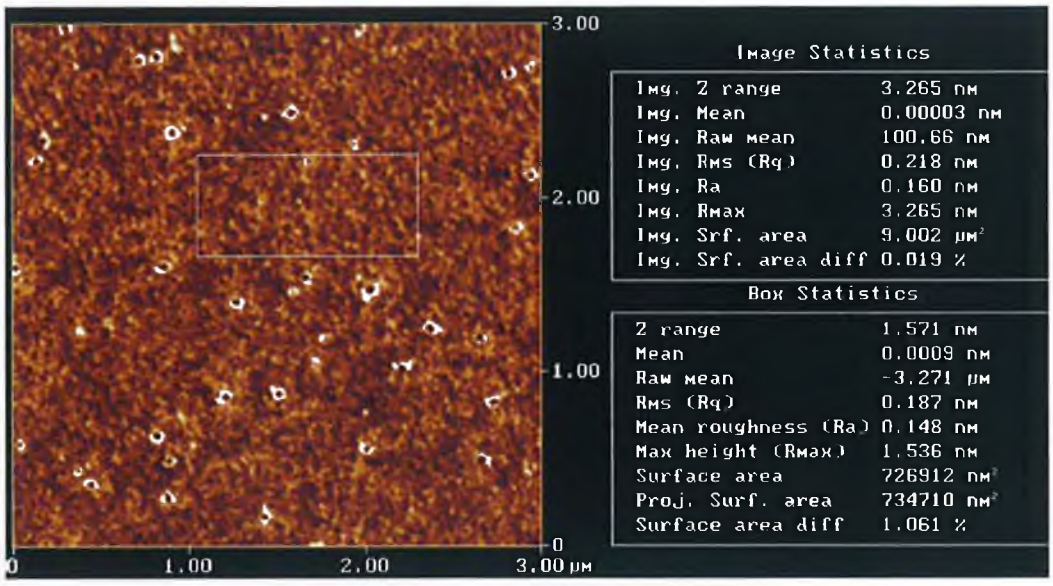

Figure 3.16 *Roughness analysis of of $[Ru(bpy)_2(PVP)_{10}Cl]Cl$ thin film.*

In Figure 3.17 a typical cross-section of the image shows the topography in the direction of the black line. When analysing line scans across the sample typically a direction parallel or diagonal to the scanning line is used so they do not contribute to the line morphology [93]. The uniformity of the sample topography across the extent of the sample is affirmed by the agreement in each section analysis. The frequency

spectrum of the line spectrum is mostly DC with a continuous tail. Any periodicity in the surface would be evident in the frequency spectrum as peaks at well-defined coherence lengths.

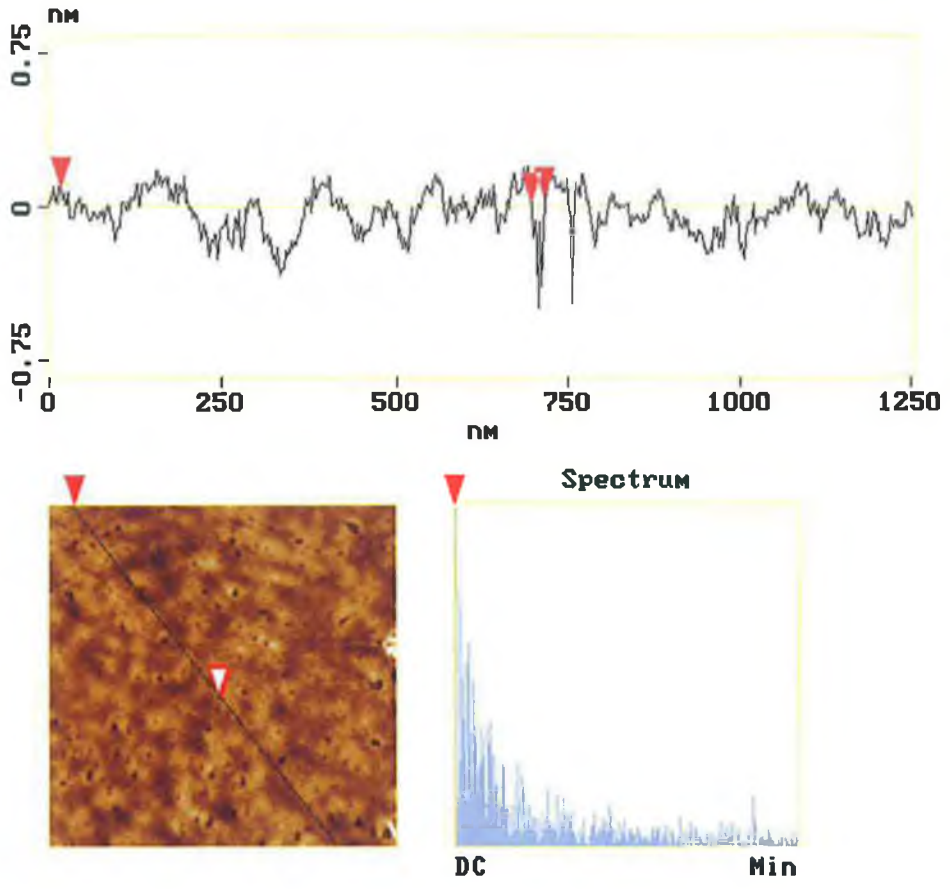

***Figure 3.17** Section analysis of of [Ru(bpy)$_2$(PVP)$_{10}$Cl]Cl] thin film. The spectrum gives information of possible periodicity in surface features.*

Figure 3.18 shows height data for a more concentrated sample of the [Ru(bpy)$_2$(PVP)$_{10}$Cl]Cl polymer (0.0075M solution) which was spun on the native-oxide covered Si(100) surface using the same parameters as the samples just discussed. The height scale is between 4nm and 5nm. The granular periodic features of 'light' and 'dark' areas are present, along with the doughnut-shaped holes. However, one difference between this sample and the previous is the presence of multilayers of polymer film. Roughness R_{rms} analysis shows that with the thicker

film the R_{rms} and z-range values have more than doubled to between 0.400nm, 0.412nm and 9.061nm, 6.897nm respectively. An even more concentrated thicker polymer film is shown in the height data in Figure 3.20. The 0.0075M polymer solution was spin-cast at a slower speed and for a shorter period of time (2.0krpm for 15 sec). The polymer morphology shows a fairly open porous structure, which is not completely homogeneous across the structure as shown in Figure 3.20 (c). The differences in the morphologies in Figures 3.18 and 3.20 clearly show that the dependency of film formation depend not only on the type of deposition process used, but also a strict control on the parameters chosen within that process (i.e. the solvent used; the spin-speed; the amount of solution used).

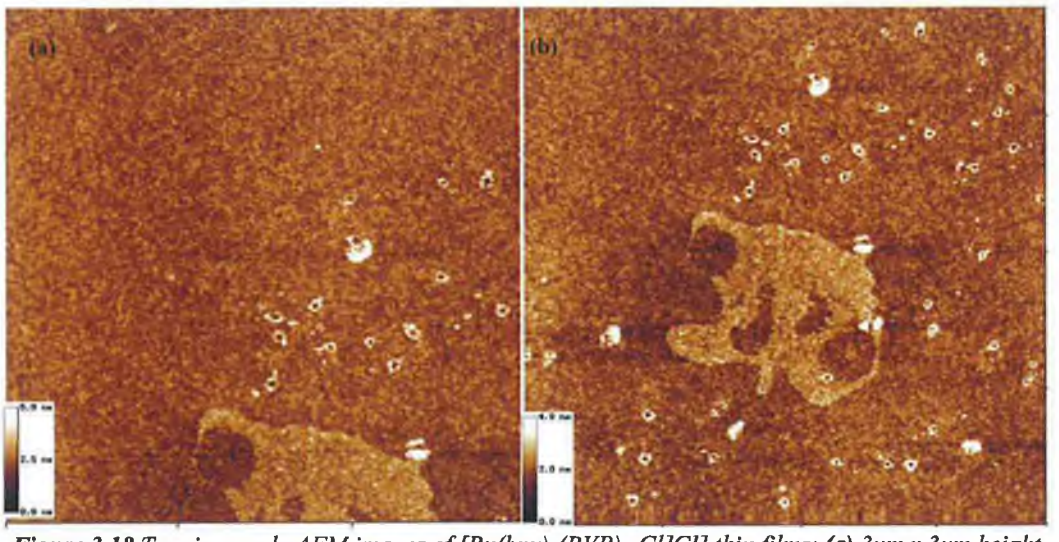

***Figure 3.18** Tapping mode AFM images of [Ru(bpy)$_2$(PVP)$_{10}$Cl]Cl] thin films: **(a)** 3μm x 3μm height image, z-range 5nm; **(b)** 3.796μm x 3.796μm height image, z-range 4nm.*

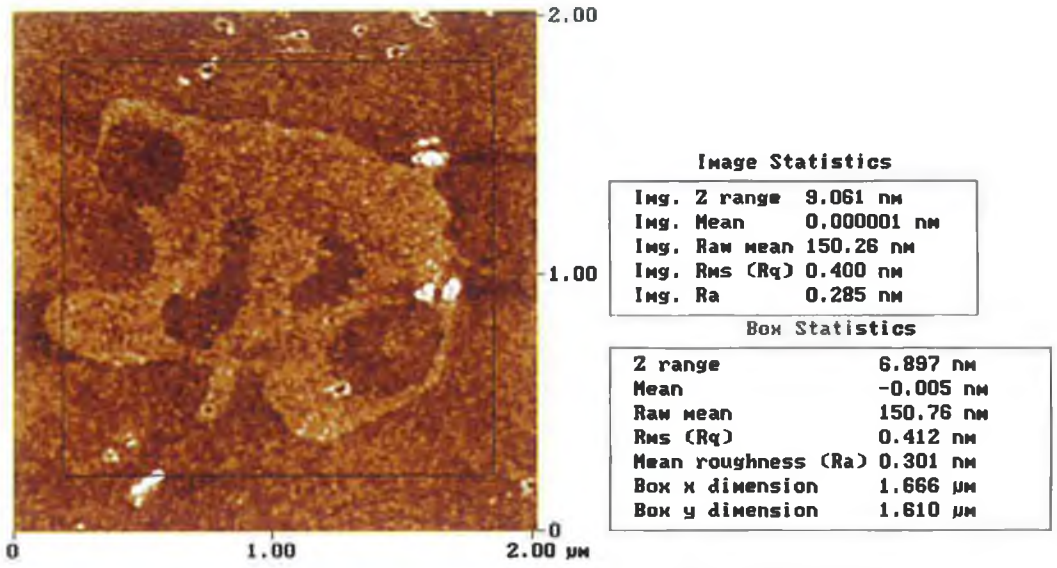

Figure 3.19 *Roughness analysis of of [Ru(bpy)$_2$(PVP)$_{10}$Cl]Cl] thin film.*

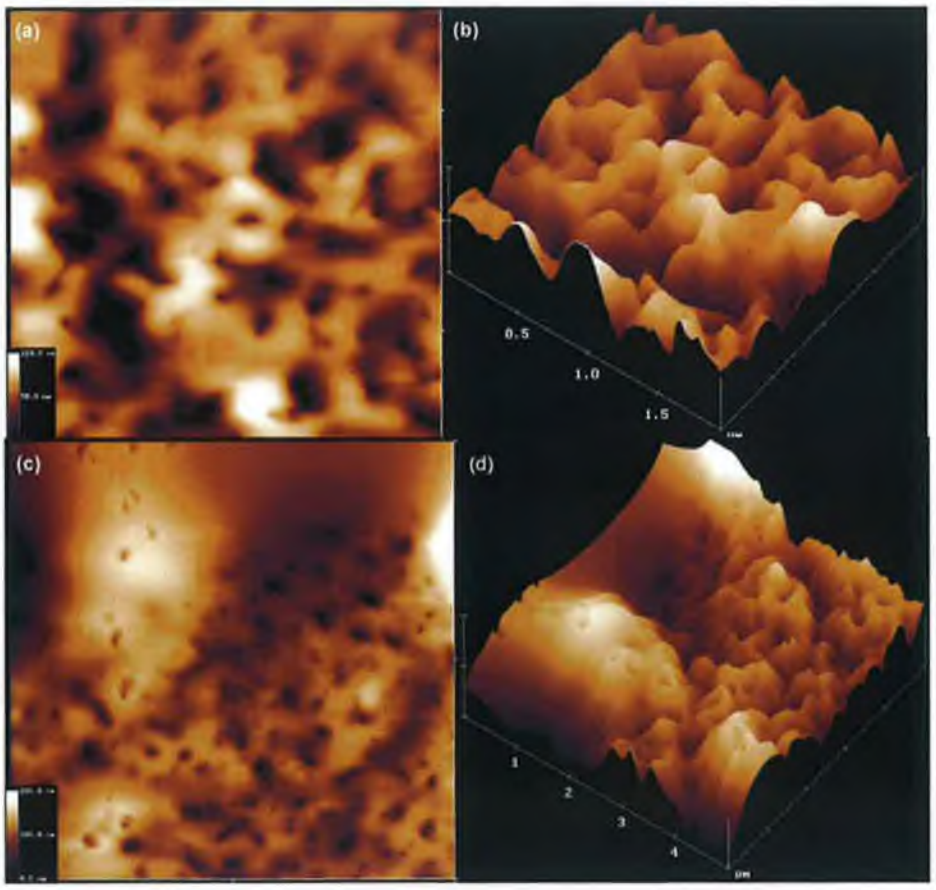

Figure 3.20 *Tapping mode AFM images of [Ru(bpy)$_2$(PVP)$_{10}$Cl]Cl] deposited by spin-casting:* ***(a)*** *1.957µm x 1.957µm height image, z-range 100nm;* ***(b)*** *Three dimensional plot of (a);* ***(c)*** *5.0µm x 5.0µm height image, z-range 100nm;* ***(d)*** *Three dimensional plot of (c).*

$[Os(bpy)_2(PVP)_{10}Cl]Cl$ is soluble in methanol and is also investigated by TM-AFM in an air environment. Solutions were spin-cast onto solvent-cleaned native oxide covered Si(100). Similar to its ruthenium analogue the films formed are granular in their morphology with the z-range in Figure 3.21 equal to 2nm. The films appear homogeneous across the surface with 'dark' and 'light' areas with the doughnut-like holes similar to the ruthenium films. By the roughness value it is possible to determine alternating height differences better than just by height parameters alone. The osmium polymer films have a higher value of R_{rms} roughness of 0.218nm and 0.208nm, than the ruthenium analogues.

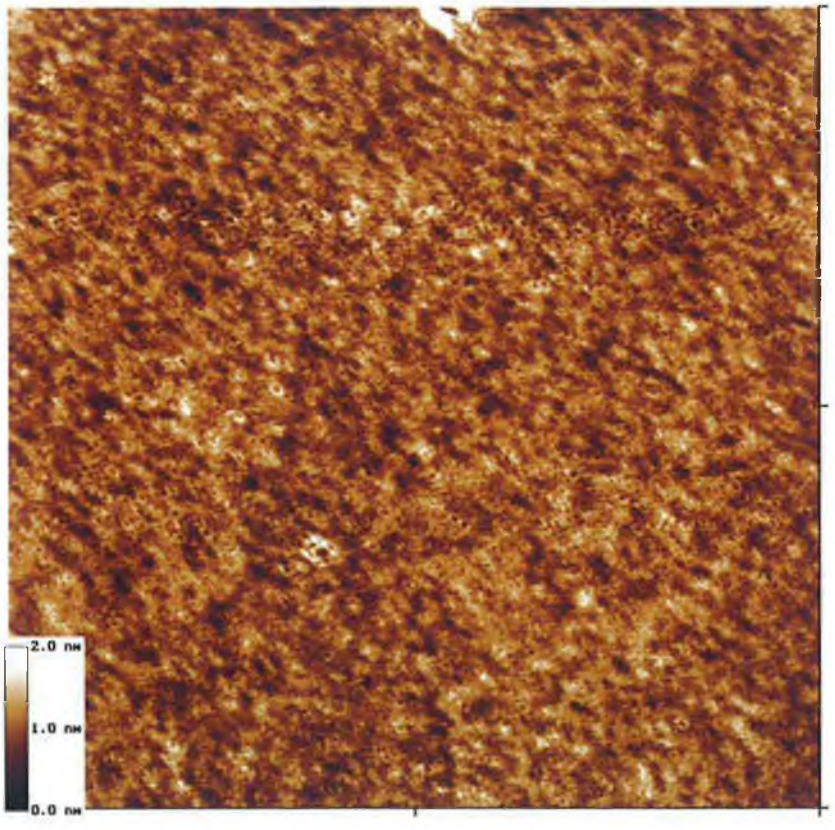

***Figure 3.21** Tapping mode AFM images of $[Os(bpy)_2(PVP)_{10}Cl]Cl$ thin films: 2μm x 2μm height image, z-range 2nm.*

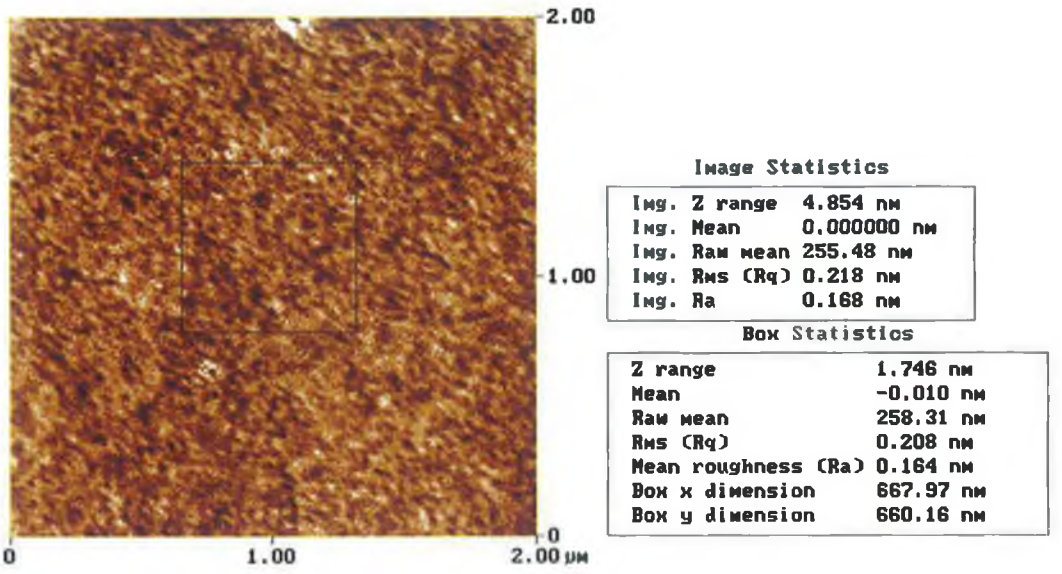

Figure 3.22 *Roughness analysis of of [Os(bpy)$_2$(PVP)$_{10}$Cl]Cl] thin film. The surface topography is characterised by its RMS roughness value*

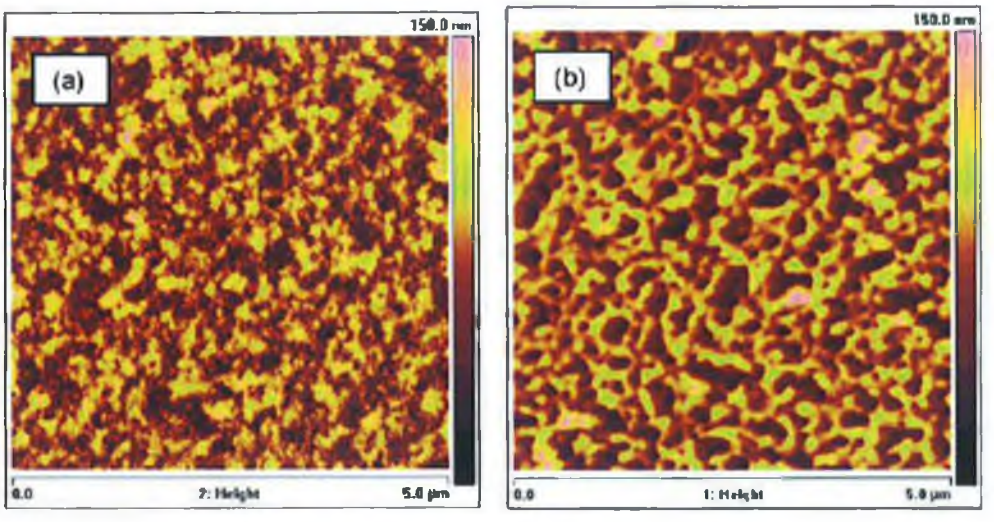

Figure 3.23 *Tapping mode AFM 5µm x 5µm height images, z range 150nm, deposited by spin-casting:* ***(a)*** *[Os(bpy)$_2$(PVP)$_5$Cl]Cl films;* ***(b)*** *[Os(bpy)$_2$(PVP)$_{10}$Cl]Cl films.*

[Os(bpy)$_2$(PVP)$_5$Cl]Cl is also soluble in methanol. Figure 3.23 shows height data of the two osmium polymers when spin-cast from a concentrated solution. The morphology of these polymers indicates that these films have a fairly open, porous structure similar to the more concentrated spin-cast ruthenium polymer films (Figure

3.20). The $[Os(bpy)_2(PVP)_5Cl]Cl$ polymer appears to be more compact and homogeneous that the $[Os(bpy)_2(PVP)_{10}Cl]Cl$ films. Contact mode AFM studies of the osmium polymer films under 0.1M aqueous $LiClO_4$ solution carried out by O'Mullane et al. show that these structures for the concentrated spin-cast polymers are maintained [104].

3.3.3 Photoelectron Spectroscopy Analysis

The key disadvantage of conventional AFM is the inability to carry out detailed chemical analysis. In the next part of this chapter, a complementary technique, photoemission spectroscopy (PES), which is a highly chemically specific technique, is used to investigate the solid-state electronic structure of the $[Ru(bpy)_2PVP_{10}Cl]Cl$ metallopolymer using synchrotron radiation (SR) photoemission. PES may also be a useful tool in the detection of common additives or contaminants in polymer technology – such as detecting elements on 'as-received' samples in quality control operations which involve surface properties. The morphology of the thin films of the polymer used for the SR-based measurements is similar to that in Figure 3.12. The film structure exposes a small amount of the underlying silicon substrate. This coupled with the presence of adventitious carbon on the silicon substrates makes reliable analysis and interpretation of C1s spectra from the film extremely difficult.

Valence band spectra ($h\nu$ = 60eV) taken from a silicon sample with and without an adsorbed polymer layer are shown in Figure 3.24. The overall shape of the spectrum changes only slightly when the polymer layer is present, and is dominated by the substrate valence band structure. However, an additional peak at a binding energy of 2.5eV is observed. This peak originates from the highest occupied molecular orbital (HOMO) of the polymer. With conventional photoemission it is problematic in the absence of *a priori* knowledge to identify the electronic character

of the peaks in a valence band spectrum. Hence the spectrum in Figure 3.25 yields little information beyond the energetic position of the HOMO below the Fermi level.

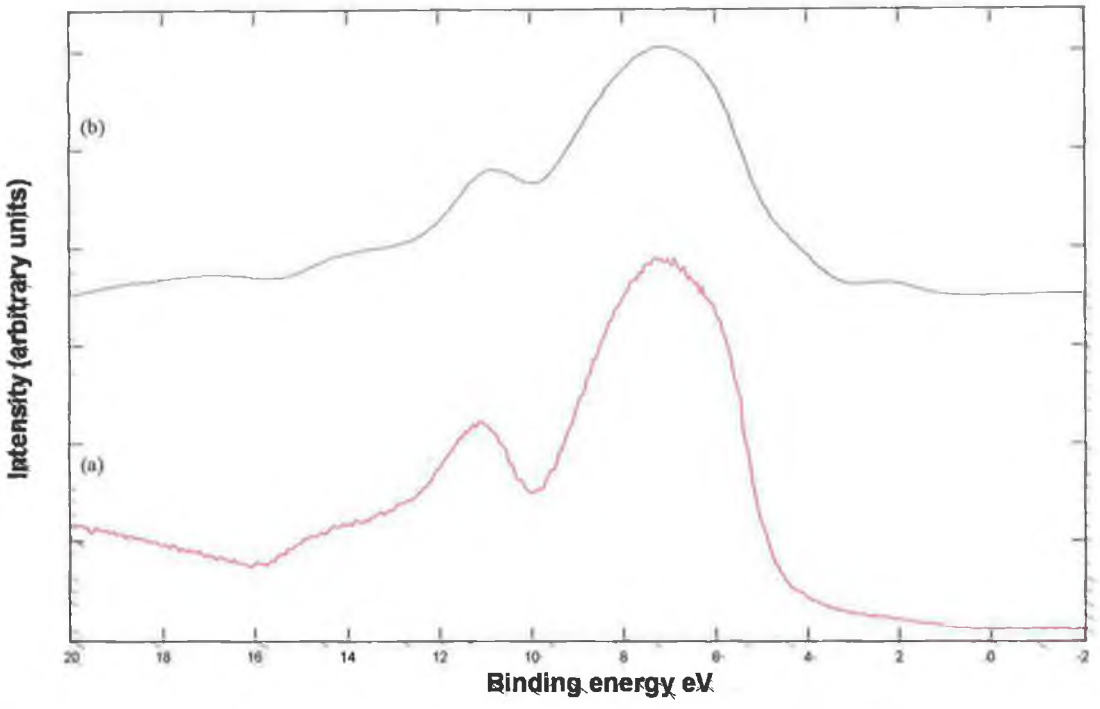

***Figure 3.24** Valence band spectra for **(a)** native oxide-terminated Si(111) substrate; **(b)** a thin $[Ru(bpy)_2PVP_{10}Cl]$ film on the $SiO_2/Si(111)$ substrate.*

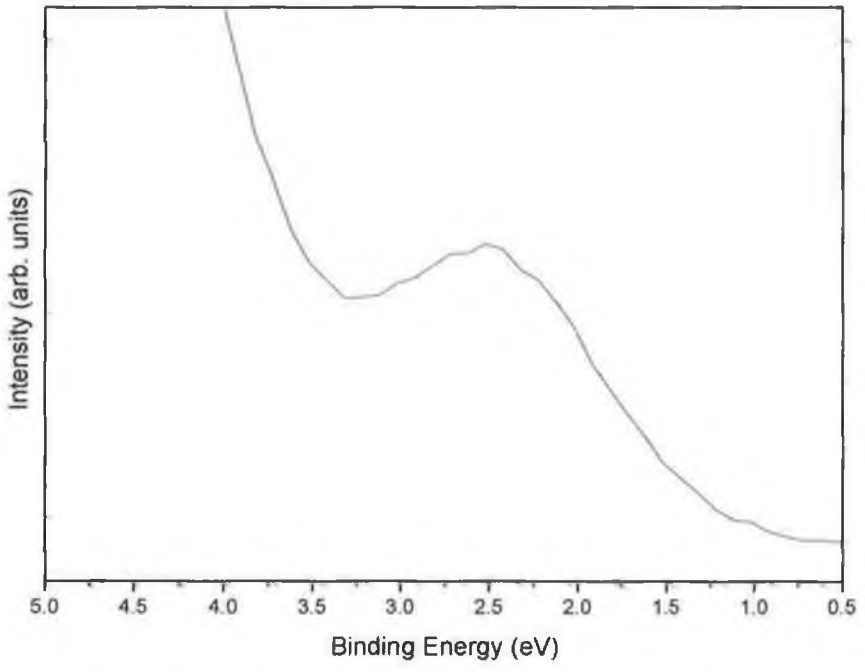

***Figure 3.25** The highest occupied molecular (HOMO)-derived peak of the $[Ru(bpy)_2PVP_{10}Cl]$ film visible from Figure 3.24.*

Figure 3.26 shows the N1s core level photoemission spectrum ($h\nu$ = 400eV) for the $[Ru(bpy)_2PVP_{10}Cl]$ polymer. The spectrum is relatively broad indicating the possible presence of two components. In their XPS studies of organic compounds Beamson and Briggs reported that the polymer poly(4-vinyl)pyridine (PVP), exhibits a single N1s core level peak at 399.34eV [105]. Rensmo at al. have carried out photoemission studies on ruthenium-polypyridine complexes [106]. The main complex studied, $[Ru(dcbpy)_2(NCS)_2]$ {*cis-bis*(4,4'-dicarboxy-2,2'-bipyridine)-*bis*-(isothiocyanato)-ruthenium(II)}, shows two peaks in the N1s spectrum. The N1s peak associated with the negatively charged NCS^- ligand is significantly shifted towards lower binding energy with respect to the pyridine N1s peak (398eV and 399.5eV respectively).

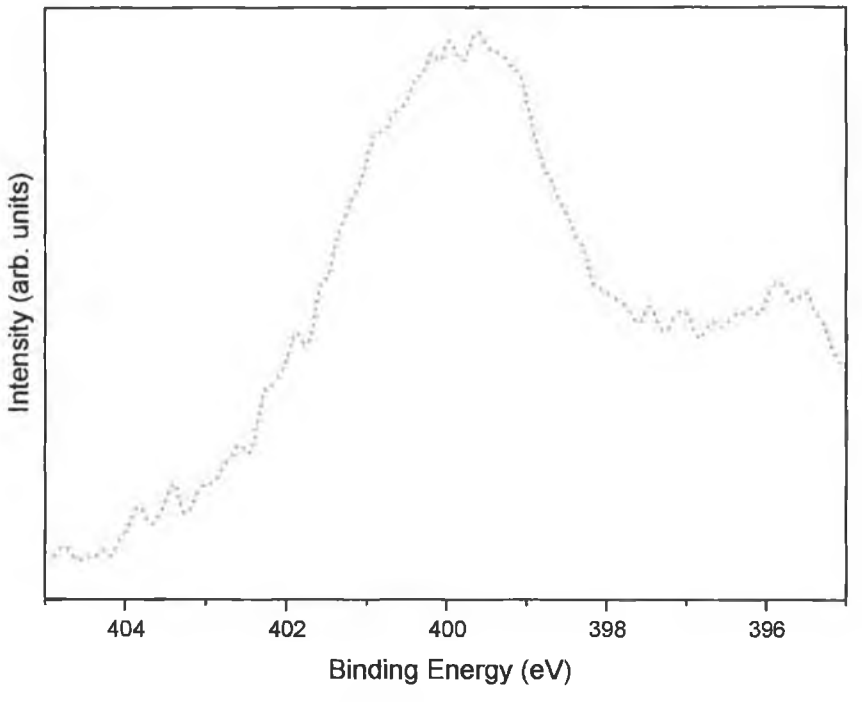

Figure 3.26 *N1s core level spectra for a thin $[Ru(bpy)_2PVP_{10}Cl]$ film on the SiO_2/Si(111) substrate.*

As the two different nitrogen environments (those from the PVP environment and those from the metal centred-bipyridine environments) are unresolved in Figure 3.26, NEXAFS (Near edge X-ray absorption Fine Structure spectroscopy) measurements

were carried out in parallel to the photoemission experiments. In a NEXAFS experiment, unoccupied conduction states are probed by excitation of core electrons to these levels. In this study the lowest unoccupied states for this polymer is expected to be ligand centred. In the N1s NEXAFS spectrum in Figure 3.27 the first resonances reflect the electronic structure of the lowest unoccupied states, i.e. the bipyridine-like environment. In the N1s NEXAFS spectrum obtained for the model complex $Ru(bpy)_3^{2+}.2Cl^-$, reported by Westermark at al., the major resonance for the pyridine nitrogens was observed at 399.8eV, followed by three minor resonances at 1.2, 2.7 and 4.2eV above the major resonance [107]. They report that the effect of introducing a doubly charged central ruthenium ion complexing to the nitrogens is basically twofold. This will lead to a lowering in the electronic energy levels, resulting in higher binding energies of the N1s level. This effect will result in an upward shift in the energy of the NEXAFS spectrum (thus appearing at higher photon energies). The presence of a central ion will also lead to a general shift of electron density toward the nitrogen atom region. This polarisation effect will result in a general appearance of new peaks (i.e. the minor resonances) in the spectrum, since the unoccupied orbitals will gain density on the nitrogens. The first resonance due to the lowest unoccupied states of the bipyridine ligand surrounding the central ruthenium metal environment in Figure 3.27 is indicated at 399.36eV followed by the second nitrogen component from the PVP environment at 400eV.

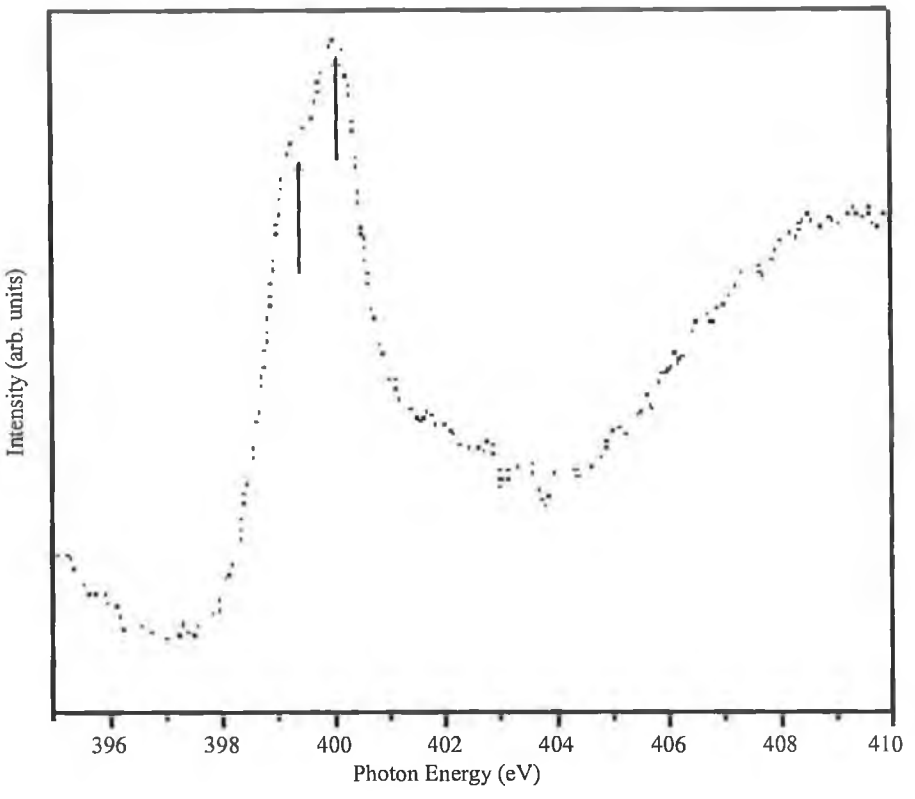

Figure 3.27 *N1s NEXAFS spectrum for a thin [Ru(bpy)$_2$PVP$_{10}$Cl] film on the SiO$_2$/Si(111) substrate.*

Figures 3.28 and 3.29 show the core level spectra for Cl2p ($h\nu$ = 250eV) and Ru3p ($h\nu$ = 550eV) for the [Ru(bpy)$_2$PVP$_{10}$Cl] polymer respectively. The Cl2p spectrum is broad and may be resolved into two peaks corresponding to its spin-orbit components. Cl2p$_{1/2}$ at 199.5eV and Cl2p$_{3/2}$ at 198.3eV. These values are only shifted by ~0.4eV when compared to data obtained for a single crystal of the RuCl$_3$ model complex [108]. Pollini reports two resolved peaks for the Cl2p spectrum at 199.1eV and 197.6eV. This shift is due to a shift of electron density toward the nitrogen atom region due to the presence of the bipyridine ligands. The spectrum in Figure 3.29 shows the ruthenium 3p$_{1/2}$ and 3p$_{3/2}$ spin orbit components at 486.9eV and 472.67eV respectively. There has been detailed photoemission studies of the electronic character of RuCl$_3$, RuO$_2$ and a single Ru crystal [108]. The peak position determined for the Ru3p core levels are outlined in Table 3.5.

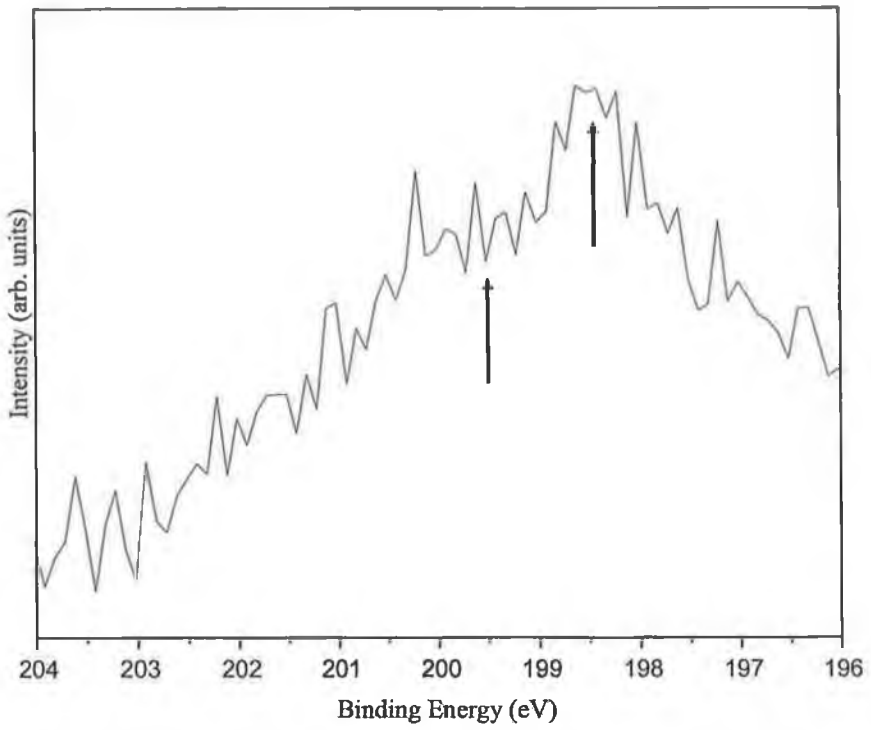

Figure 3.28 *Cl2p core level spectra for a thin $[Ru(bpy)_2PVP_{10}Cl]$ film on the $SiO_2/Si(111)$ substrate.*

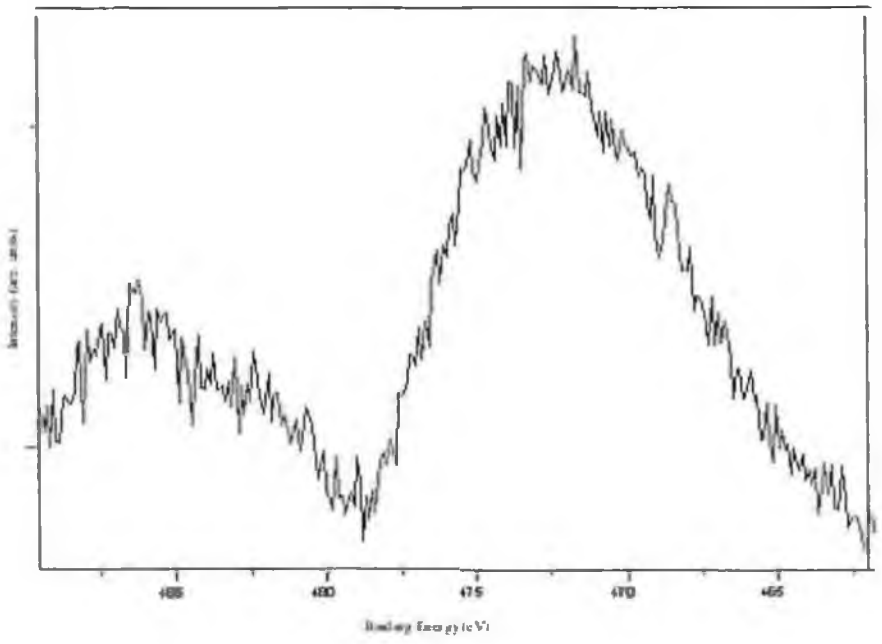

Figure 3.29 *Ru3p core level spectra for a thin $[Ru(bpy)_2PVP_{10}Cl]$ film on the $SiO_2/Si(111)$ substrate.*

	$3p_{3/2}$	$3p_{1/2}$
$RuCl_3$ single crystal [108]	462.5eV	484.8eV
$RuCl_3$ powder [108]	462.3eV	484.6eV
RuO_2 powder [108]	462.3eV	484.7eV
Ru single crystal [108]	461.2eV	483.3eV
$[Ru(bpy)_2PVP_{10}Cl]$	472.67eV	486.9eV

Table 3.5 *Ru3p core level values for some ruthenium based systems.*

A clear shift towards higher binding energy is seen for the Ru $3p_{3/2}$ core level when compared to the $RuCl_3$ model. This difference is attributed to the complexation of ruthenium with the bipyridine ligand. Joseph at al. report a similar shift of the Ru $3p_{3/2}$ core level spectrum by 10eV to 473eV [109]. This shift has been reported to be due to the charge transfer from the ligand to the metal.

3.4 Conclusions

A series of metallopolymers based on PVP containing ruthenium or osmium bis-(2,2'-bipyridyl) centres have been synthesised using microwave radiation as an alternative route to conventional heating. These polymers have been characterised using spectroscopic techniques (UV-VIS, emission) and electrochemical methods. The results compare with those of analogous polymeric compounds reported in the literature [37] and have the structure $[M(bpy)_2PVP_nCl]Cl$ where M is the metal centre and n is either 5 or 10.

The self-assembly and the morphology of $[Ru(bpy)_2PVP_{10}Cl]Cl$ has been investigated using tapping mode AFM, as a function of both the adsorption technique employed, and the concentration of the solution. Drop-cast solutions may be characterised as droplet-like agglomerates which appear to form randomly across the substrate. Spin-cast solutions dewet the substrate via a mechanism which leads to the formation of thin films (~ 1.66nm in height) with a granular nature. Small pin holes

of bare silicon are also observed which represent locations where the polymer film has ruptured via a dewetting mechanism. The morphology of the same polymer deposited at slower spin speeds and higher concentrations highlights the importance of controlling the deposition parameters. The resulting morphology shows an open non-uniform porous structure with the film height fluctuating between 50-100nm.

The self-assembly of $[Os(bpy)_2PVP_nCl]Cl$ (where n is 5 or 10), from solution via spin-coating deposition has also been investigated by tapping mode AFM. The osmium polymers have higher values of rms surface roughness than their ruthenium analogues, and the morphology of these polymers indicates that these polymers also have a fairly open, porous structure similar to the concentrated ruthenium polymer described above. However, the $[Os(bpy)_2PVP_5Cl]Cl$ structure appears to be more compact and homogeneous than the $[Os(bpy)_2PVP_{10}Cl]Cl$ films.

The electronic structure of the polymer $[Ru(bpy)_2PVP_{10}Cl]Cl$ has been investigated with synchrotron radiation photoemission. In the valence band spectra the peak at a binding energy of 2.5eV originates from the highest occupied molecular orbital (HOMO) of the polymer. The N 1s spectrum indicates the presence of two different chemical environments which is shown by the N1s NEXAFS spectrum. The Ru3p core level spectrum shows a shift towards a higher binding energy which is indicative of the presence of the 2,2'-bipyridine ligands when compared to the $RuCl_3$ model compound. More comprehensive photoemission work is needed to elucidate fully the molecular orbital conformation of this polymer.

3.5 References

1. Naarmann H., **1963**, BASF Corp. Germany
2. Chiang C.K., Fincher C.R., Park Y.M., Heeger A.J., Shirakawa H., Louis E.J., Gua S.C., Mac Diarmid A.G., **1977**, *Phys. Rev. Lett.*, 39, 1098.
3. Zhang C., Von Seggern H., Pakbaz K., Kraabel B., Schmidt H.-W., Heeger A.J., **1994**, *Synth. Met.*, 62, 35.
4. Roncali J., **1992**, *Chem. Rev.*, 92, 711.
5. McCullough .D., **1998**, *Adv. Mater.*, 10, 93.
6. Murray R.W., **1984**, *Electroanal. Chem.*, 13, 191.
7. Kaneko M., Wohrle D., **1988**, *Adv. Polym. Sci.*, 84, 141
8. Abruna H.D., **1988**, *Coord. Chem. Rev.*, 86, 135.
9. (a) Heller A., **1990**, *Acc. Chem. Res.*, 23, 128; (b) Gregg B.A., Heller A., **1992**, *J. Phys. Chem.*, 96, 3579.
10. (a) C alvo E .J., B attaglini F ., D anilowicz C ., Wolosiuk A ., O tero M ., **2 000**, *Faraday Discuss. Chem. Soc.*, 116, 47; (b) Calvo E.J., Etchenique R., Pietrasanta L., Wolosiuk A., Danilowicz C., **2001**, *Anal. Chem.*, 73, 1161.
11. Jernigan J.C., Murray R.W., **1987**, *J. Amer. Chem. Soc.*, 109, 1738.
12. Sosnoff C.S., Sullivan M., Murray R.W., **1994**, *J. Phys. Chem.*, 98, 13643.
13. Kaneko M., **2001**, *Prog. Polm. Sci.*, 26, 1101.
14. Forster R.J, Keyes T.E., Bond A.M., **2000**, *J. Phys. Chem. B*, 104, 6389.
15. Paris J.P., Brandt W.W., **1959**, *J. Amer. Chem. Soc.*, 81, 5001.
16. Durham B., Casper J.V., Nagle J. K., Meyer T. J., **1982**, *J. Am. Chem. Soc.*, 104, 4803.
17. Watts R.J., **1983**, *J. Chem. Ed.*, 60, 834.
18. Casper J. V., Meyer T. J., **1983**, *J. Am. Chem. Soc.*, 105, 5583.

19. Damrauer N. H, Cerullo G., Yeh A., Boussie T .R., Shank C. V., McCusker J. K., **1997**, *Science*, 275, 54.

20. Li C., Hoffman M. Z., **1998**, *Inorg. Chem.*, 37, 830.

21. Kober E.M., Meyer T.J., **1984**, *Inorg. Chem.*, 23, 3877.

22. Balzani V., Scandola F., **1996**, *Comp. Supramol. Tech.*, 10, 687.

23. Adamson A. W.,**1983**, *J. Chem. Ed.*, 60, 797.

24. Balzani V., Juris A., **2001**, *Coor. Chem. Rev.* 211, 97.

25. Balzani V., Scandola F., **1983**, *J. Chem. Ed.*, 60, 814.

26. Kalyanasundaramk K., **1992**, In *Photochemistry of Polypyridine and Porphyrin Complexes*, Academic Press Publishers, London.

27. Barigelletti, F., DeCola, L., Balzani, V., Hage, R., Haasnoot, J., Reedijk, J., Vos, J. G., **1991**, *Inorg. Chem.*, 30, 641.

28. Clear J.M., Kelly J.M., Pepper D.C., Vos J.G., **1979**, *Inorg. Chim. Acta.*, 33, L139.

29. Haas O., Kriens M., Vos J.G., **1981**, *J. Amer. Chem. Soc.*, 103, 1318.

30. Forster R. J., Vos J. G., **1992**, *Electrochim. Acta.*, 37, 159.

31. Forster R. J., Vos J. G., **1994**, *Langmuir*, 10, 4330.

32. Doherty A. P., Vos J. G., **1997**, *Anal. Chim. Acta.*, 344, 159.

33. Hogan C. F., Forster R. J., **1999**, *Anal. Chim. Acta.*, 396, 13.

34. Forster R. J., Figgemeir E., Lees A. C., Hjelm J., Vos J. G., **2000**, *Langmuir*, 16, 7867.

35. Calvert J.M., Caspar J.V., Binstead R.A., Westmoreland T.D., Meyer T.J., **1982**, *J. Amer. Chem. Soc.*, 104, 6620.

36. Leech D., Forster R.J., Smyth M.R., Vos J.G., **1991**, *J. Mater. Chem.*, 1, 629.

37. Forster R. J., Vos J. G., **1990**, *Macromolecules*, 23, 4372.

38. Samuels G.J, Meyer T.J., **1981**, *J. Amer. Chem. Soc.*, 103, 307.

39. Calvert J.M., Meyer T.J., **1981**, *Inorg. Chem.*, 20, 27.

40. Calvert J.M., Meyer T.J., **1982**, *Inorg. Chem.*, 21, 3978.

41. Haas O., Vos J.G., **1980**, *J. Electroanal. Chem.*, 113, 139.

42. Haas O., Muller N., Gerischer H., **1982**, *Electrochim. Acta.*, 27, 991.

43. Haas O., Zumbrunnem H.R., Vos J.G., **1985**, *Electrochim Acta.*, 30, 1551.

44. Clear J.M., Kelly J.M., Vos J.G., **1983**, *Makromol. Chem.*, 184, 613.

45. Clear J.M., Kelly J.M., O'Connell C.M., Vos J.G., **1981**, *J. Chem. Res.*, m, 3039.

46. Geraty S.M., Vos J.G., **1987**, *J. Chem. Soc. Dalton Trans.*, 3037.

47. Geraty S.M., Vos J.G., **1984**, *J. Electroanal. Chem.*, 176, 389.

48. White H.S., Leddy J., Bard A.J., **1982**, *J. Amer. Chem. Soc.*, 104, 4811.

49. Oyama N., Ohsaka T., Ushirogouchi T., Sapei S., Nakamura S., **1988**, *Bull. Chem.Soc. Jpn.*, 61, 3103.

50. Tsou Y.M., Anson F.C., **1984**, *J. Electrochem. Soc.*, 131, 595.

51. Jones E.T.T., Faulkner L.R., **1987**, *J. Electroanal. Chem.*, 222, 201.

52. Majda M., Faulkner L.R., **1984**, *J. Electroanal. Chem.*, 169, 77.

53. Chen X., He P., Faulkner L.R., **1987**, *J. Electroanal. Chem.*, 222, 223.

54. Sharp M., Lindholm B., Lind E.L., **1989**, *J. Electroanal.Chem.*, 274, 35.

55. Anson F.C., Tsou Y.M., Saveant J.M., **1984**, *J. Electroanal. Chem.*, 178, 113.

56. Leddy J., Bard A.J., **1985**, *J. Electroanal. Chem.*, 189, 203.

57. Sullivan B.P., Salmon D.J., Meyer T.J., **1978**, *Inorg. Chem.*, 17, 3334.

58. Kober E.M., Casper J.V., Lumpkin R.S., Meyer T.J., **1986**, *J. Phys. Chem.*, 90, 3722.

59. Calvert J. M., Schmehl R. H., Sullivan B. P., Facci J. S., Meyer T. J., Murray R. W., *1983*, *Inorg. Chem.*, 22, 2151.

60. Schmehl R. H., Murray R. W., **1983**, *J. Electroanal. Chem.*, 152, 97.

61. Facci J .S., Schmehl R. H., Murray R. W., **1982**, *J. Amer. Chem. Soc.*, 104, 4959.

62. Forster R.J., Vos J.G., **1991**, *J. Electroanal. Chem.*, 314, 135.

63. Forster R.J., Vos J.G., **1992**, *Electrochim. Acta.*, 37, 159.

64. Forster R.J., Vos J.G., Lyons M.E.G., **1991**, *J. Chem. Soc. Faraday Trans.*, 87, 3761.

65. Forster R.J., Vos J.G., Lyons M.E.G., **1991**, *J. Chem. Soc. Faraday Trans.*, 87, 3769.

66. Andrieux C.P., Haas O., Saveant J.M., **1986**, *J. Amer. Chem. Soc.*, 108, 8175.

67. Forster R.J., Kelly A.J., Vos J.G., **1989**, *J. Electroanal. Chem.*,270, 365.

68. Forster R.J., Vos J.G., **1991**, *J. Inorganic and Organometallic Polymers*, 1, 67.

69. Buttry D. A., Anson F. C., **1981**, *J. Electroanal. Chem.*, 130, 333.

70. Sabatani R., Anson F.C. **1993**, *J. Phys. Chem.*, 97, 10158

71. Buck R. P., **1988**, *J. Phys. Chem.*, 92, 4196.

72. Buck R. P., Madaras M. B., **1993**, *J. Electroanal. Chem.*, 362, 33

73. Kelly A.J., Ohsaka T., Oyama N., Forster R.J., Vos J.G., **1990**, *J. Electroanal. Chem.*, 287, 185

74. Brown N. M. D., You H. X., Forster R. J., Vos J. G., **1991**, *J. Mater. Chem.*, 1, 517.

75. Lay P., Sargeson A.M., Taube H., Chou M.H., Creutz C., **1986**, *Inorg. Synth.*, 24, John Wiley and Sons (Publishers).

76. Kolthoff I. M., Coetzee J .F., **1957**, *J. Amer. Chem. Soc.*, 79, 1852.

77. Buckingham D.A., Dwyer F.P., Goodwin H.A., Sargeson A.M., **1964**, *Aust. J. Chem.*, 17, 325.

78. Shimidzu T., Izaki K., Akai Y., Iyoda T., **1981**, *J. Chem. Soc., Chem. Commun.*, 793.

79. Lyons M.E.G., Fay H.G., Vos J.G., Kelly A.J., **1988,** *J. Electroanal. Chem.*, 250, 207.

80. Johnson E.C., Sullivan B.P., Salmon P.J., Adeyemi S.A., Meyer T.J., **1964**, *Aust. J. Chem.*, 17, 325.

81. Mallakpour S. E., Majipour A. R., Zamanlou M. R., **2001**, *J. Polymer Science A.*, 39, 177.

82. Jones J.R., Lockley W.J.S., Lu S.Y., Thompson S.P., **2001**, *Tet. Lett.*, 42, 331.

83. Elander N., Jones J.R., Lu S.Y., Stone-Elandor S., **2000**, *Chem. Soc. Rev.*, 29, 239.

84. Erb W.T., Jones J.R., Lu S.Y., **1999**, *J. Chem. Res.*, (S), 728.

85. Anto S., Getvoldsen G.S., Harding J.R., Jones J.R., Lu S.Y., Russell J.C., **2000**, *J. Chem. Soc., Perkin Trans.*, 2, 2208.

86. Lockley, W.J.S., **1982**, Tet. Lett., 23, 3819.

87. Kober E.M., Caspar J.V., Sullivan B.P., Meyer T.J., **1988**, *Inorg. Chem.*, 27, 4587.

88. Goldsby K.A., Meyer T.J., **1984**, *Inorg. Chem.*, 23, 3002

89. Albrecht T. R., Dovek M. M., Lang C. A., Grutter P., Quate C. F., Kuan S. N. J., Frank C. W., **1988**, *J. Appl. Phys.*,64, 1178.

90. Geoghegan M., Krausch G., **2003**, *Prog. Polym. Sci.*, 28, 261.

91. (a) Young T., **1805**, *Philos. Trans. Roy. Soc. London*, 5, 65; (b) Cooper W.F., Nutall W.H., **1915**, *J. Agric. Sci.*, 7, 219.

92. Frehill F., Schulte K.H.G., Martin C.P., Wang L., Patel S., Purton J.A., Vos J.G., Moriarty P., **2004**, *Langmuir*, 108, 9787.

93. Poler J.C., McKay K.K., Irene E.A., **1994**, *J. Vac. Sci. Technol B.*, 12, 88.

94. Lawrence C.J., **1988**, *Phys. Fluids.*, 31, 2786.

95. Emslie A.G., Bonner F.T., Peek L.G., **1958**, *J. Appl. Phys.*, 29, 858.

96. Meyerhofer D., 1978, *J. Appl. Phys.*, 49, 3393.

97. Daughton W.J., Givens F.L., **1982**, *J. Electrochem. Soc.*, 129, 173.

98. Chen B.T., **1983**, *Polymer Eng. Sci.*, 23, 399.

99. (a) Reiter G., **1993**, *Langmuir*, 9, 1344. (b) Reiter G., **1992**, *Phys. Rev. Lett.*, 68, 75.

100. Barnes K.A., Douglas J.F., Liu D.-L., Karim A., **2001**, *Adv. Colloid & Interface Science A.*, 94, 83.

101. Bico J., Thiele U., Quere D., **2002**, *Colloids & Surfaces A.*, 206, 41.

102. Thermo Micro Web page http://thermomicro.com/spmguide/1-2-0.htm (03/00 Edition)

103. © Digital Instruments, **1998**, *Scanning Probe Microscopy Training Manual*, 40.

104. O'Mullane, Macpherson J.V., Unwin P.R., Cervera-Montesinos J., Manzanares J.A., Frehill F., Vos J.G., **2004**, *J. Phys. Chem. B.*, 108, 7219.

105. Beamson G., Briggs D., **1992**, in *High Resolution XPS on Organic Compounds*, p 84, Wiley, Chichester, U.K.

106. Rensmo H., Westermark K., Sodergren S., Kohle O., Persson P., Lunell S., Siegbahn H., **1999**, *J. Chem. Phys.*, 111, 2744.

107. Westermark K., Rensmo H., Schnadt J., PerssonP., Sodergren S., Bruhwiler P.A., Lunell S., Siegbahn H., **2002**, *Chem. Phys.*, 285, 167.

108. Pollini I., **1994**, *Phys. Rev. B.*, 50, 2095.

109. Joseph T., Sawant D.P., Gopinath C.S., Halligudi S.B., **2002**, *J. Molecular Cat. A.*, 184, 289.

Chapter 4

Studies of a Functionalised Carbon Nanotube System

Chapter 4 details the modification of multi-walled carbon nanotubes with an inorganic ruthenium complex. The reasons for this modification are outlined at the beginning of the chapter, where an introduction to carbon nanotubes is given, followed by a discussion on some of their possible applications. The linkage is carried out by forming of an amide group and the resulting ruthenium-functionalised carbon nanotube assembly is characterised using spectroscopic and scanning probe microscopy techniques. The techniques suggest that the reaction is successful. The final section of the chapter briefly describes the reaction of a ^{13}C-labelled molecule with multi-walled carbon nanotubes.

"We find comfort among those who agree with us – growth among those who don't"

Frank A. Clark

4.1 Introduction to Carbon Nanotubes

Carbon nanotubes were first discovered by Sumio Iijima of the NEC Corporation in 1991 [1]. When voltage was applied between two carbon electrodes contained within an argon environment, carbon needles were observed on the negative electrode and examined by transmission electron microscopy (TEM). These appeared to be microtubules of graphitic carbon, most containing multiple shells, like concentric hollow cylinders. These macromolecules became known as carbon nanotubes (CNTs). Since their discovery, CNTs have excited scientists and engineers with their wide range of unusual physical properties. These outstanding physical properties are a direct result of the near-perfect microstructure of the CNT which, at the atomic scale, may be thought of as a hexagonal sheet of carbon atoms rolled into a seamless, quasi-one-dimensional cylindrical shape. It has been suggested that CNTs have tensile strengths twenty times that of high strength steel alloys, are half as dense as aluminium, have current carrying capacities 1000 times that of copper, and transmit heat twice as well as pure diamond [2].

4.2 Properties of Carbon Nanotubes

Like graphite, CNTs are comprised of interconnected six-member rings, or hexagons of carbon atoms. These hexagons of carbon span the entire surface of a nanotube and are the source of the many impressive qualities of CNT. The spatial orientation of the hexagon with respect to the length of the nanotube is not fixed, resulting in three chirality classifications for nanotubes – armchair, zigzag and chiral. The geometry of a particular nanotube is best described in terms of the unit cell of the CNT, as shown in Figure 4.1. The atomic arrangement of the CNT is described by the chiral vector which is defined by:

$$\mathbf{c} = n\mathbf{a_1} + m\mathbf{a_2} \tag{4.1}$$

where $\mathbf{a_1}$ and $\mathbf{a_2}$ are unit vectors on the 2-D hexagonal lattice, and n and m are integers. Using this description [3], the chiral angle (θ) and diameters (d_t) of the CNT are given as:

$$\theta = \tan^{-1}\left(\frac{\sqrt{3}n}{2m+n}\right) \tag{4.2}$$

$$d_t = \frac{\sqrt{3}}{\pi} a_{c-c}\sqrt{m^2 + mn + n^2} \tag{4.3}$$

where a_{c-c} is the distance between neighbouring carbon atoms in a flat graphene sheet (approx 0.142nm).

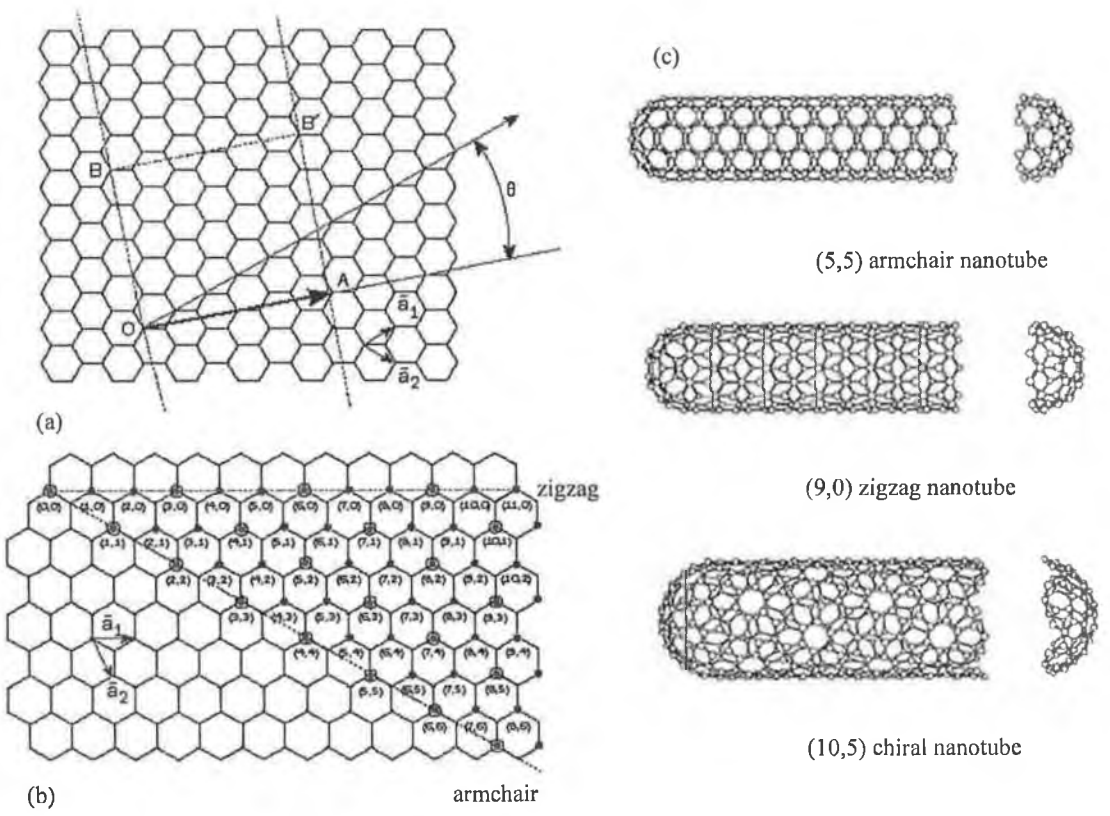

Figure 4.1 (a) *The relationship between the graphite lattice basis vectors and the chiral vectors used to characterise nanotubes;* ***(b)*** *The limiting cases are shown: (n, 0) indices are associated with zigzag tubes whereas (n, n) indices are associated with armchair tubes. All other tubes are chiral.* ***(c)*** *Diagrams of examples of the three types of nanotube [3].*

Armchair nanotubes are formed when $n = m$. Zigzag nanotubes are formed when either n or m is zero and the chiral angle is 0°. All other nanotubes with chiral angle intermediate between 0° and 30° are known as chiral nanotubes. CNTs with different chiral vectors (n, m) will have different atomic configurations. The electronic properties have been found to be strongly dependent on the chirality of the CNT. By changing the tube diameter or its helicity, the electronic properties may be changed between metallic or semiconducting [4,5]. For example, a CNT will be metallic when the chiral vector satisfies the relationship $n-m=3l$, where l is an integer, while all other nanotubes will be semiconducting. A theoretical prediction is that armchair nanotubes are metallic.

CNTs may be further classified into three broad categories: single-walled nanotubes (SWNTs), multi-walled nanotubes (MWNTs) and nanotube bundles or ropes. SWNTs consist of a single layer of carbon atoms wrapped into a cylindrical shape, which may or may not be capped on each end by one half of a fullerene molecule (see Figure 4.1(c)). Typical diameters for SWNT are on the order of 1nm, while lengths are often on the order of μm. Both this diameter and the length are typically dependent on the particular technique used to create the nanotubes. MWNTs consist of several concentric layers (or shells) of individual carbon nanotubes that are weakly coupled to each other through Van der Waals forces. The diameter and number of shells comprising a MWNT is again dependent on the fabrication process, although diameters on the order of 30nm have been routinely reported [6,7]. Nanotube bundles or ropes consist of several to hundreds of SWNTs or MWNTs arranged in a closest-packed two-dimensional lattice [8,9]. Within these bundles, the nanotubes normally display a mono-disperse range of diameters, with adjacent tubes weakly coupled via Van der Waals interactions.

An in-depth discussion of nanotube fabrication techniques and characterisation methods is beyond the scope of this chapter. Due to experimental conditions, the first nanotubes observed were predominantly MWCTs [1]. A year later (1992), two independent research groups found that by adding small amounts of transition metals, namely cobalt, nickel, or iron, growth would favour SWNT [10,11]. Called the arc-discharge method, this type of production resulted in nanotubes with few structural defects and is still widely used in the field of nanotube production. Other fabrication methods used to date include: chemical vapour deposition (CVD) [2,12]; laser ablation [8]; and high-pressure carbon-monoxide conversion (HiPco) techniques [13]. A great deal of research is focused on both limiting the defects within the nanotubes and increasing the production yields from nanotube processing techniques. As interest from the scientific community continues to expand, it is expected that nanotube fabrication techniques will continue to develop.

4.3 Device Applications of Carbon Nanotubes

CNTs are a contender for device elements in the next evolution of computers because of their impressive electronic properties. As previously discussed, theoretical work has predicted that nanotubes may be metallic or semiconducting depending on their chirality [4,14]. Experimental work involving STM and tunnelling spectroscopy has already confirmed these electronic properties [15,16]. Conductivity measurements for individual SWNT have been made [17], and an effective field-effect transistor has been successfully engineered and demonstrated [18]. In that case, a SWNT that was 1.6nm in diameter was manipulated into place using a tip of an atomic force microscope. Once placed on the metal contacts, the semiconducting tube behaved like the channel in a field-effect transistor, turning on or off depending on the applied gate voltage. Electronic transport in metallic CNTs occurs without backscattering of

electrons, therefore they are able to carry a large current without heat building up [19,20]. The high conductivity is the result of the unmodified bond structure running the length of the nanotube. The conductivity is reduced as more scattering sites are introduced, either through physical or chemical means [21].

The development of electronic devices based on nanotubes is hampered by the inability to produce CNTs with the exact desired electronic properties. Only one third of all CNTs produced in fabrication techniques are truly metallic. The remaining two thirds are semiconductors. Tubes are normally produced as random mixtures of metallic and semiconducting tubes with a different range of band gaps. While it is possible to measure the electronic properties of single tubes and then choose the right one for a given experimental set-up, any large scale application would depend on selective synthesis or efficient separation. A huge research effort is currently focused on finding the optimal ways of growing nanotubes in specific locations, orientations, shape and sizes [22]. Other recent demonstrations of nanotubes as diodes [23,24], transistors [25], and as three- and four-terminal devices [26] further support the possibility of using CNTs as building blocks for nanometre-sized electronic devices.

In this chapter, the attempted covalent linkage of a ruthenium poly(pyridyl) complex to amino-functionalised MWNTs will be described. The objective of this work is the fabrication of interconnected carbon nanotubes with potential application as components in nanoscale devices. The inclusion of a ruthenium complex is not essential for creating CNT interconnects. However, due to their rich range of photochemical and photophysical properties (as discussed in section 3.1.2) [27,28,29] ruthenium complexes, acting as nanotube linkers, could be essential in sensing applications through electrochemical monitoring of the change in redox potential, or in transistor applications, through photophysical and electrochemical

switching of the contact between MWNTs. A schematic representation of a possible interconnected carbon nanotube junction is shown in Figure 4.2. This junction is backgated through an underlying silicon gate or by metal contacted MWNT 2.

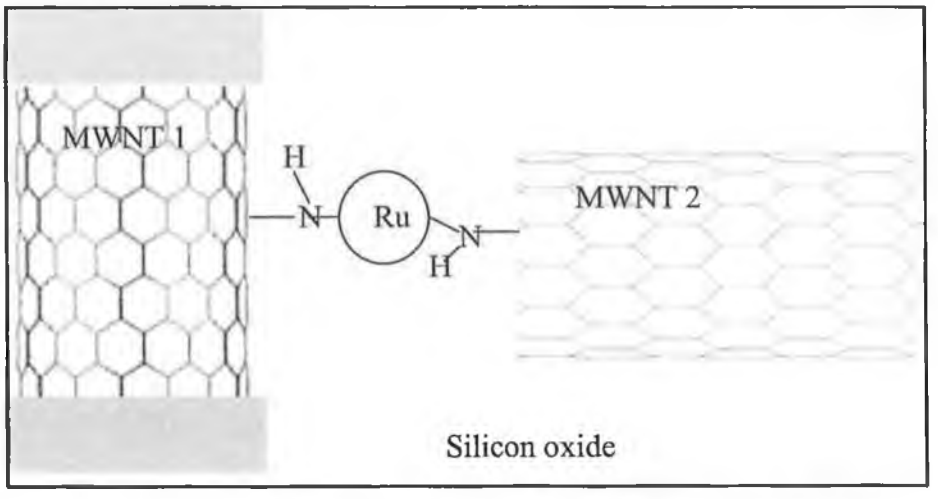

Figure 4.2 *Schematic of metal contacted interconnected MWNT junction on a SiO_2 wafer.*

4.4 Experimental

[Ruthenium (4, 4'-dicarboxy-2,2'-bipyridyl) (2,2'-bipyridine)$_2$](PF$_6$)$_2$ **{1}**

This was synthesised and characterised using the procedure reported in reference [30] by Dr. W. Browne.

Amino-functionalised MWNTs **{3}**

The amino-functionalised MWNTs were produced by catalytic chemical vapour deposition and obtained from Nanocyl S.A (Namur, Belgium) [31].

Ruthenium-functionalised MWNT assembly **{4}**

10 mg (0.011 mmol) **1** was dissolved in 15 ml thionyl chloride. The reaction mixture was refluxed under an argon atmosphere for 5 h. The thionyl chloride was removed by vacuum distillation. The remaining solid **2** was partially dissolved in dichloromethane (DCM). 2 mg of **3** were sonicated in 5 ml DCM for 2 min, and then

added to the refluxed mixture **2**. 10 ml of triethylamine was added. The solution reaction mixture was stirred at room temperature under an argon atmosphere for 72 h. To remove the solvent, the reaction mixture was filtered, and then washed with DCM. The reaction product was placed in 20 ml DCM and sonicated for 2 min. The solution was then allowed to settle for 24 h. Excess **3** settled at the bottom, while the 'Ru-functionalised MWNT' product(s) are solubilised. A colour change from dark red-orange (**2**) to dark brown-green (**product 4**) was observed after the reaction was completed.

Atomic Force Microscopy

A set of $1cm^2$ SiO_2 pieces of wafer were cleaned by sonication in acetone and ethanol for 5 min each, and then gently boiled in H_2O_2:NH_4:H_2O (1:1:5) solution for 25 min. The wafer pieces were rinsed with Milli-Q water and dried under argon. A 1% (v/v in Milli-Q water) solution of 3-(aminopropyl)triethoxysilane (APS, Aldrich), was dropped onto a cleaned wafer piece and allowed to react for up to 10 min. The wafer pieces were rinsed with Milli-Q water and dried under argon.

i). A sample of the amino-silanised silicon oxide wafer was imaged using TM-AFM.

ii). 2 mg MWNT-NH_2 were sonicated in 5mls Milli-Q water. This nanotube suspension was drop-cast onto a silanised wafer, and allowed to stand for 10 min. The wafer was then rinsed with Milli-Q water and dried under argon. TM-AFM analysis was carried out.

iii). Homogeneous solutions of **4** were obtained. This Ru functionalised-nanotube containing solution was drop-cast onto a piece of silanised wafer, and allowed to stand for up to 10 min. The wafer pieces were rinsed with Milli-Q water and dried under argon. TM-AFM analysis was carried out.

Absorption and Emission Spectroscopy

Emission and UV/Vis absorption spectra of **1, 2** and **4** were recorded in dichloromethane using the instruments described in section 3.2.1

MWNT-NH_2 {3} reaction with ^{13} C-labelled molecule {A}

50mg (0.3mmol) ^{13}C-labelled bridge molecule, terephthalic-carboxy-$^{13}C_2$ acid (Aldrich) {**A**} was dissolved in 15ml thionyl chloride. The reaction mixture was refluxed under an argon atmosphere for 5 hours. The thionyl chloride was removed by vacuum distillation. The remaining solid **B** was dissolved in dichloromethane (DCM). 2mg of amino-functionalised MWNTs {**3**} were sonicated in 5ml DCM for 2min, and then added to the refluxed mixture **B**. 10ml of triethylamine was added. The solution reaction mixture was stirred at room temperature under an argon atmosphere for 72 hours. All solvents were removed by vacuum distillation. The reaction products were placed in 5mls DCM. The solution was sonicated and allowed to settle for 48 hours. Excess **3** settled at the bottom, leaving chemically modified carbon nanotubes in solution {**Products C, D, E**}.

4.5 Results and Discussion

4.5.1 Introduction

Carbon nanotubes are a good platform for functionalisation, especially with a view to applications in molecular electronic devices. Attachment of functional groups, such as aliphatic carbon chains to CNT may dramatically increase the solubility of nanotube material. Chemical modified nanotubes may be fixed on a surface via chemical bonds from the surface to the nanotube. Organic molecules like dyes, proteins or nucleic acids may be coupled with functionalised nanotubes for sensor applications. Side-wall functional groups react with polymers and improve the

mechanical properties of nanocomposites [32]. Tubes interconnected by chemical bonds will have a reduced contact resistance in conducting and transparent layers [33]. Furthermore, even for interconnection purposes in nanoscale circuits, suitable functionalisation provides an attractive method to link individual tubes to form more complex networks.

A wide range of approaches toward organic nanotube chemistry has been developed. These include: defect functionalisation [34]; covalent functionalisation [35]; and non-covalent functionalisation [36] (for example, formation of supramolecular adducts with surfactants and polymers). Covalent sidewall functionalisation has been carried out on SWNTs. This has been achieved through: electrochemical reduction of aryl diazonium salts [37]; a co-ordinately unsaturated Vaska's compound [38]; and using 1,3-dipolar cyclo-additions [39,40]. The 1,3-dipolar cyclo-addition of azomethine ylides generated *in-situ* by thermal condensation of aldehydes and α-amino acids gives rise to soluble functionalised-CNT materials [33]. Azomethine ylides are very reactive intermediates and attack efficiently the vast π-system of the CNT, both at the tips and the sidewalls. Using this type of chemistry, a large number of pyrrolodine rings fused to the carbon-carbon bonds of CNTs are produced. End-to-end and end-to-side SWNT interconnects were formed by reacting chloride terminated SWNTs with aliphatic diamine [25].

The proposed synthetic route for the linkage of the ruthenium complex with MWNTs is shown in Figure 4.3 [50]. Covalent attachment of functional groups to CNT has almost exclusively been achieved using ester or amide linkages. Amides have been the primary linkage for nanotube interconnects [25], the covalent attachment of proteins [41,42], DNA [43,44], nanocrystals [45,46], and metal containing complexes [36,47]. Amide connections are produced by a chemical

reaction between starting products with carboxylic acid and free amino groups. The starting ruthenium complex **1** is first converted into its acyl chloride **2**. This is achieved by heating the acid at reflux in thionyl chloride giving the acyl chloride, which is extremely reactive and must be used immediately. The CNTs used in this work are open-ended MWNT functionalised with amino ($-NH_2$) groups. [Ruthenium (4,4'-dicarboxy-2,2'-bipyridyl) (2,2'-bipyridine)$_2$].$(PF_6)_2$ is a very suitable ruthenium moiety as it contains two carboxylic acid groups which are available for reaction. In addition the photophysical/photochemical properties of this complex are well understood [28].

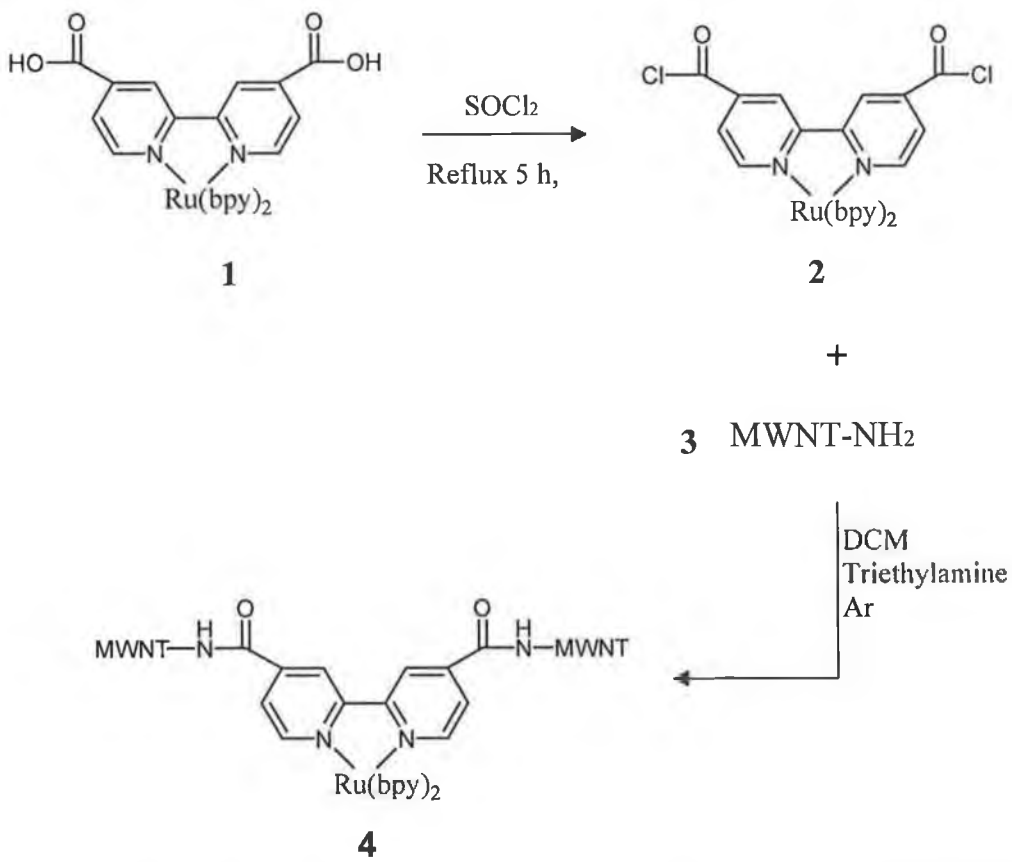

Figure 4.3 *The proposed synthetic route for the linkage of the ruthenium complex with MWNT. 1[Ru (4,4'-dicarboxy-2,2'-bipyridyl) (2,2'-bipyridine)$_2$].$(PF_6)_2$; 2 Corresponding acid chloride of 1; 3 Amino-functionalised open-ended MWNTs.; 4 Reaction product 'ruthenium-functionalised MWNT'.*

In general it is very difficult to obtain unambiguous analytical data of functionalised-CNTs allowing for a satisfying structure interpretation. This is related to the fact that the CNT used as starting materials: a) aggregate as rather insoluble bundles of different diameters making a selective chemistry difficult; b) vary greatly in length and diameter; and c) possess a range of helicities and defects both at the tube ends and on the sidewalls [48]. Moreover, it is difficult to obtain CNTs that are free from impurities such as amorphous carbon and metal catalyst particles. As a consequence, functionalised-CNTs represent an extremely poly-disperse mixture of compounds, in most cases, undefined or difficult to define purity [49]. The characterisation of functionalised CNTs relies on UV/Vis, Raman, and FT-IR spectroscopy. Standard techniques for molecular structure characterisation such as liquid nuclear magnetic resonance (NMR) spectroscopy or mass spectroscopy are of limited use or cannot be applied because of the poor solubility. Transmission electron and atomic force microscopy are routinely employed.

4.5.2 Characterisation of Starting Amino-functionalised MWNTs

The amino-functionalised MWNTs contain the free amino groups for reaction with the ruthenium complex **1.** The NH_2-MWNTs were fully characterised using techniques that include XPS, IR spectroscopy and STM by Kónya et al. [31,50]. They are open-ended and 200-300nm in length. In the IR spectra, characteristic bands due to C-NH_2 (1400cm^{-1}) are observed. Their STM analysis suggests that the amino groups organise in islands. This is shown in the topographic images in Figure 4.4. Kónya et al. report that the nanotubes were ultrasonicated in toluene and droplets of suspension placed on highly oriented pyrolytic graphite (HOPG) [31]. Small islands of functional groups which are bound to defects were observed with STM on the nanotube surface. Due to the presence of the functionalised islands, the exterior

wall of the CNT cannot come close enough to the HOPG surface to establish strong Van der Waals interaction which would fix the nanotube to the support. This allows the functionalised MWNTs to be moved with the tip of a STM for example to certain 'markers' on the support, and has proved useful in further characterisation [31]. The MWNT-NH_2 do not dissolve in dichloromethane or any aqueous/non-aqueous solvent. Suspensions of MWNT-NH_2 may be formed by ultrasonication. However, the tubes tend to fall to the bottom of the solvent when allowed to settle.

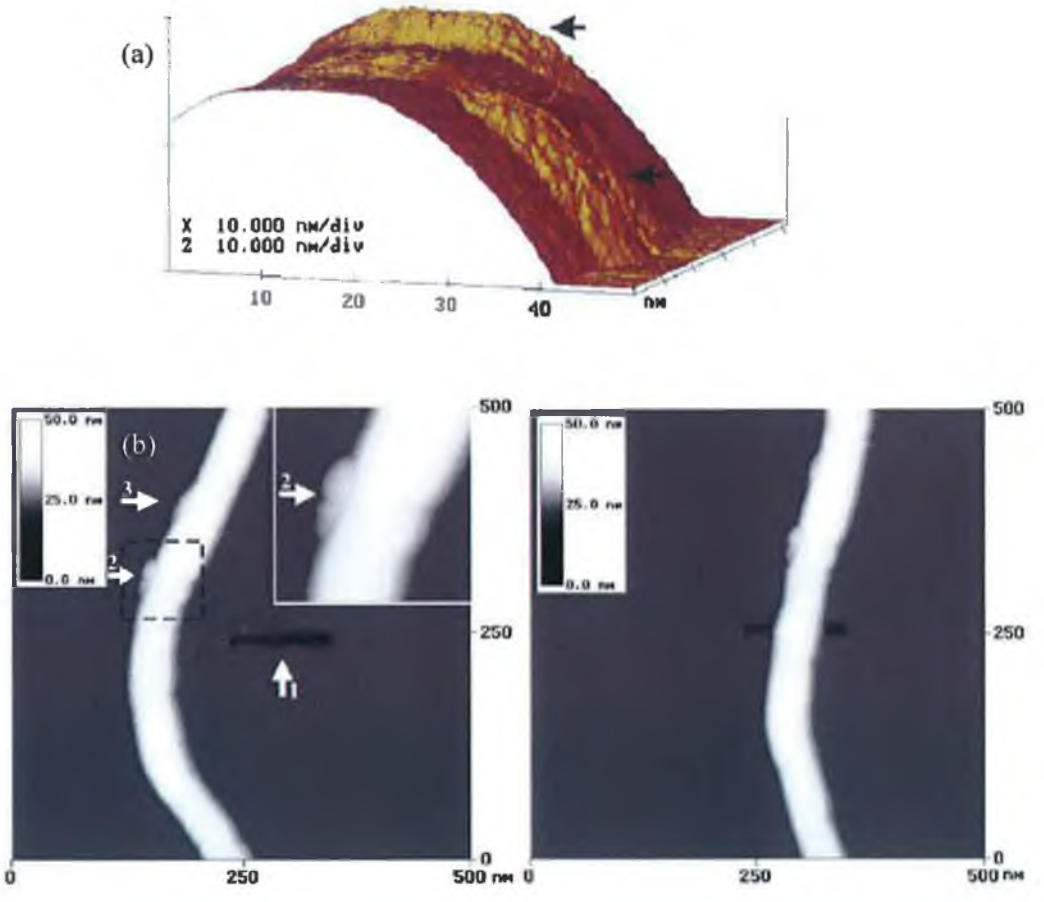

Figure 4.4 ***(a)*** *3D constant current topographic STM image showing amino island (black arrows) on surface of MWNT;* ***(b)*** *Top view topographic consecutive STM images of individual amino-functionalised MWNT shifted by the scanning tip on HOPG. Horizontal arrows indicate amino islands, vertical arrow indicates marker cut in HOPG [31,50].*

4.5.3 Absorption and Emission Spectroscopy of Modified Nanotubes

UV/Visible absorption spectroscopy was carried out in dichloromethane for the starting ruthenium complex **1**, the corresponding acid chloride **2**, and the Ru-functionalised MWNT assembly **4**. As already mentioned, MWNT-NH_2 does not dissolve in dichloromethane, however homogeneous solutions of **4** were obtained. As described in section 3.1.2 ruthenium poly(pyridyl) complexes are typically dominated by two intense bands in the visible region of the spectrum. Strong π-π^* bands appear in the region of ~ 285nm due to the pyridine rings. The bands in the visible part of the spectrum have been assigned to metal-to-ligand-charge transfer (^{1}MLCT) transitions from the metal localised orbital Ru ($d\pi$) to the ligand localised orbital, bpy(π^*) orbitals [29,30]. The characteristic $d\pi^*$ MLCT band typically appears in the region of ~ 450 - 500nm.

The starting ruthenium complex **1** has characteristic absorption bands at 285nm and 454nm. The corresponding acid chloride **2** exhibits a red shift to 286nm and 498nm. For the final product **4** bands at 290nm and 459nm are observed. The exact λ_{max} for **1** and **4** varies only slightly and are very similar. Therefore these cannot give a precise answer to whether the reaction scheme in Figure 4.4 was successful. However, this is the first indicator of any differences in the properties of the ruthenium centres brought about by the introduction of a different functional group on one of the bpy ligands.

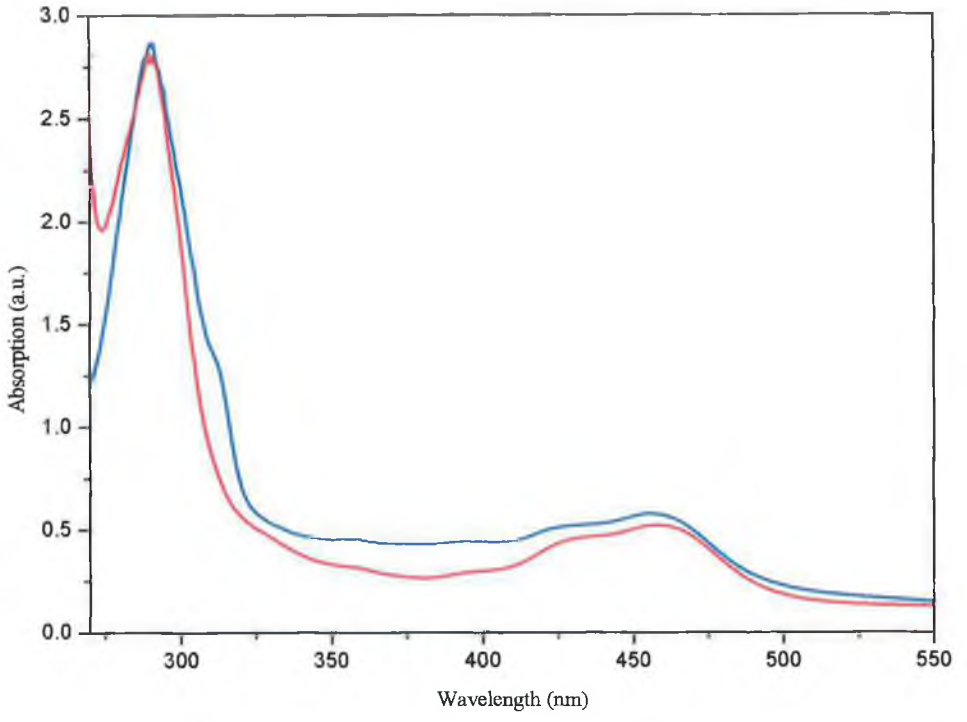

Figure 4.5 *The UV/Vis absorption spectra of [Ru(4,4'-dcbpy)(bpy)$_2$](PF$_6$) **1** (blue), and Ru-functionalised MWNT assembly **4** (red) in dichloromethane.*

Figure 4.6 shows the emission spectra obtained for the starting ruthenium complex **1**, the corresponding acid chloride **2**, and the Ru-functionalised MWNT assembly **4**. All materials exhibited room temperature emission in dichloromethane. The emission spectrum for **1** shows a characteristic maximum at 629nm. The corresponding acid chloride **2** results in a red shift to 719nm. It has been shown that the introduction of an electron withdrawing substituent into a bpy ring shifts the emission maximum to lower energy (the electronegative chlorine substituent) [51]. The red shift of the emission here is an indicator that the excited state is located on the substituted bpy ligand. Emission occurs from the lowest energy level to the ground state. This is the result of a reduction in the t_{2g} ^{3}MLCT energy gap, resulting in lower emission energy. These shifts are as expected [30]. The Ru-functionalised MWNT assembly **4**

has a maximum at 609nm, a blue shift of 108nm compared with **2** and 20nm compared with **1**. These changes in the peak maxima suggest that a reaction has occurred between **2** and **3** [29,30].

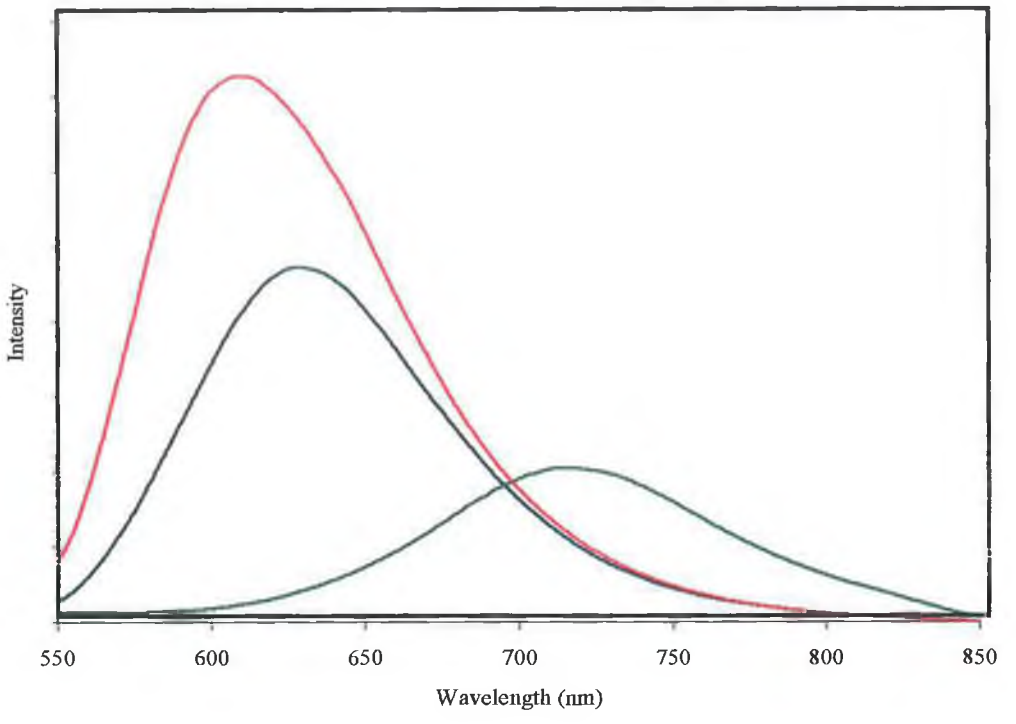

***Figure 4.6** Emission Spectra of starting ruthenium complex **1** (blue), chlorinated product **2** (green), and Ru-functionalised MWNT assembly **4** (red) in dichloromethane.*

Compound	$\lambda_{max}^{(absorption)}$ nm	$\lambda_{max}^{(emission)}$ 298K, nm
1	285, 454	629
2	286, 498	719
4	290, 459	609

***Table 4.1** Absorption and emission spectroscopy results.*

The absorption and emission spectra do not provide the necessary proof that the ruthenium complex was successfully attached to the MWNT. A non-covalent attachment may lead to a shift in the peak maxima of absorption and emission

spectra as well. The colour change from dark red-orange to dark brown-green observed after the reaction product was placed in fresh dichloromethane may be a result of Ru^{III} complexes which can be a side product of the reaction [29,30].

4.5.4 Atomic Force Microscopy of Modified Nanotubes

The sp^2 hybridisation of carbon makes possible a large variety of tubular carbon based nanostructures such as multiwalled and singlewalled carbon nanotube Y-, T-, L- and H-junctions, as well as simple and multiple coiled nanotubes [52]. Experimental observation of spontaneously branched MWNTs produced by the arc-discharge method was first reported by Zhou et al. in 1995 [53]. L-, Y-, and T-junctions were observed by TEM. The formation of these junctions was totally random. To date L-, Y-, T-, H-junctions, and three dimensional CNT webs are either achieved during nanotube growth [31,50,54], or by later processing steps such as functionalisation and interconnecting through bonds [55].

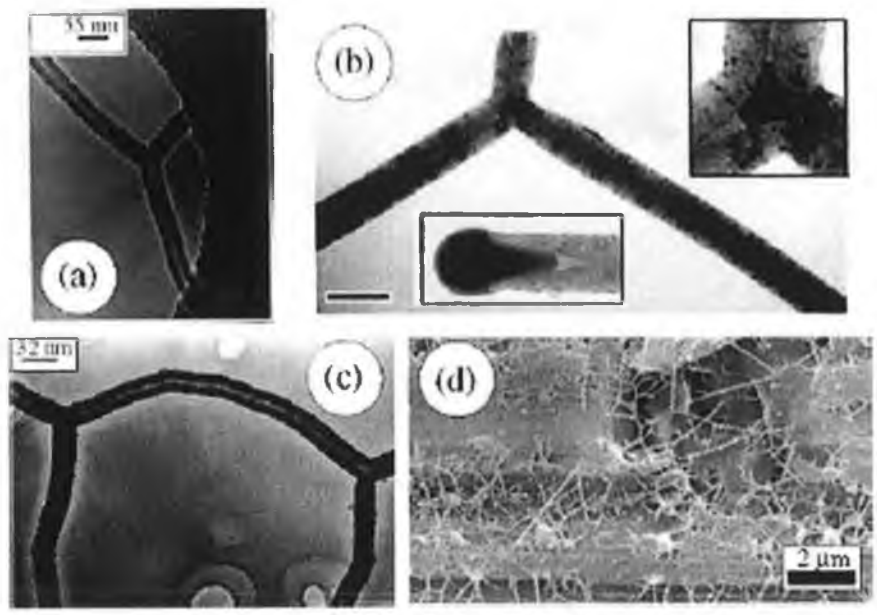

Figure 4.7 ***(a)*** *Multiwall, symmetric Y junctions with well developed central hollow;* ***(b)*** *Y junction with the triangular amorphous particle at the joining of the branches (scale bar 100 nm);* ***(c)*** *double Y junction;* ***(d)*** *SEM image of an area showing several multi-junction tubes [56].*

The interest in these junctions lies primarily in the development of CNT-based circuits. To construct a network, the simplest basic building elements one can use are Y- or T-junctions. Nanodevice elements including junctions in transistors, p-n junctions in diodes, and metal-oxide-semiconductor junctions all need such connections [57]. AFM may be a useful technique for characterisation of chemically modified CNTs. Chiu at al. reports the chemical modification of CNTs by attaching chemical functional groups to the sidewalls and open ends which can be used to interconnect nanotubes [24]. In their study they report that statistical analysis from the AFM images shows that around 30% of the functionalised nanotubes form the intermolecular T- and Y-junctions, whereas less than 2% of the pristine nanotubes show similar junctions [58].

Figure 4.8 shows TM-AFM height and amplitude images of the amino-silanised silicon oxide wafer. These are used as a reference prior to deposition of nanotube containing solutions. The uniform flatness of the substrate is shown using a height range of 5nm. Figures 4.9 and 4.10 show typical images of the MWNT-NH_2 on the amino-salinised silicon oxide wafer.

***Figure 4.8** 3μm x 3μm TM-AFM height (left) and amplitude (right) images of the amino-silanized silicon oxide wafer. Left: height z = 5nm, right: amplitude data z = 90mV.*

Figure 4.9 *7.436μm x 7.436μm TM-AFM height (left) and amplitude (right) images of MWNT-NH_2 Left: height z = 75nm, Right: Amplitude z=90mV.*

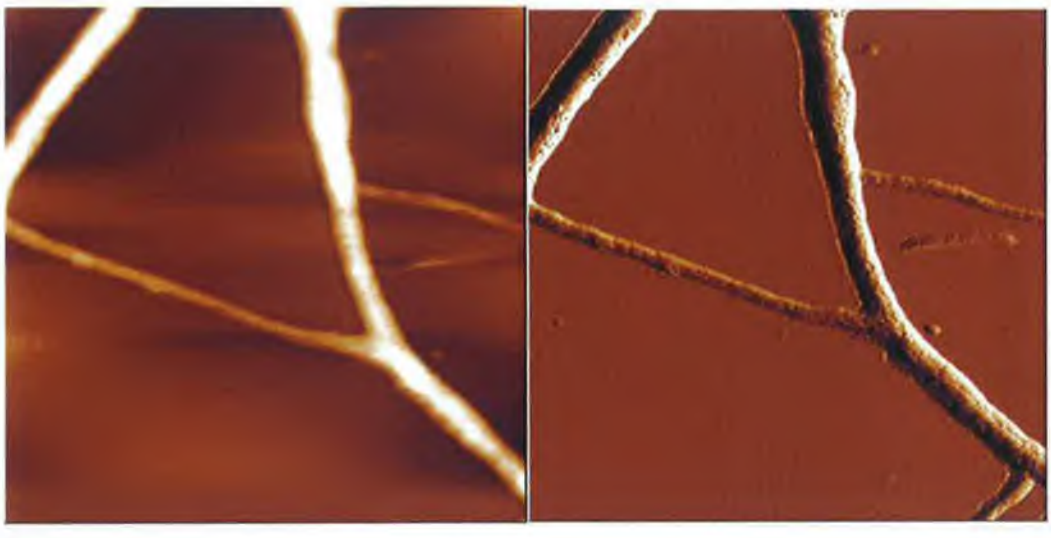

Figure 4.10 *2.623μm x 2.623μm TM-AFM height (left) and amplitude (right) images of MWNT-NH_2 Left: height z = 50nm, right: amplitude Z=50mV.*

The tubes were sonicated in solvent to form a suspension is solution, which was drop-cast immediately onto the wafer. TM-AFM of MWNTs was achieved by drop-casting the nanotube suspension onto an amino-silanised silicon oxide wafer after treatment with 3-(aminopropyl)triethoxysilane solution. The silanisation treatment allows for washing of the wafer without removal of nanotubes as they stick to the functionalised surface through non-covalent interactions. Amplitude data

complements the height data as it shows the edges of the nanotube features more clearly.

Homogeneous solutions of **4** were obtained. As the ruthenium-functionalised MWNT assembly **4** is drop-cast from a DCM solution, some residual solvent may stick to the surface, resulting in AFM images that are not as clean as reported images using aqueous nanotube containing solution [59]. A TM-AFM image is shown in Figure 4.11. MWNTs are indicated in these images by the white lines. Multiple junctions are observed distinct from naturally occurring splitting of MWNT ropes which are observed in Figure 4.9.

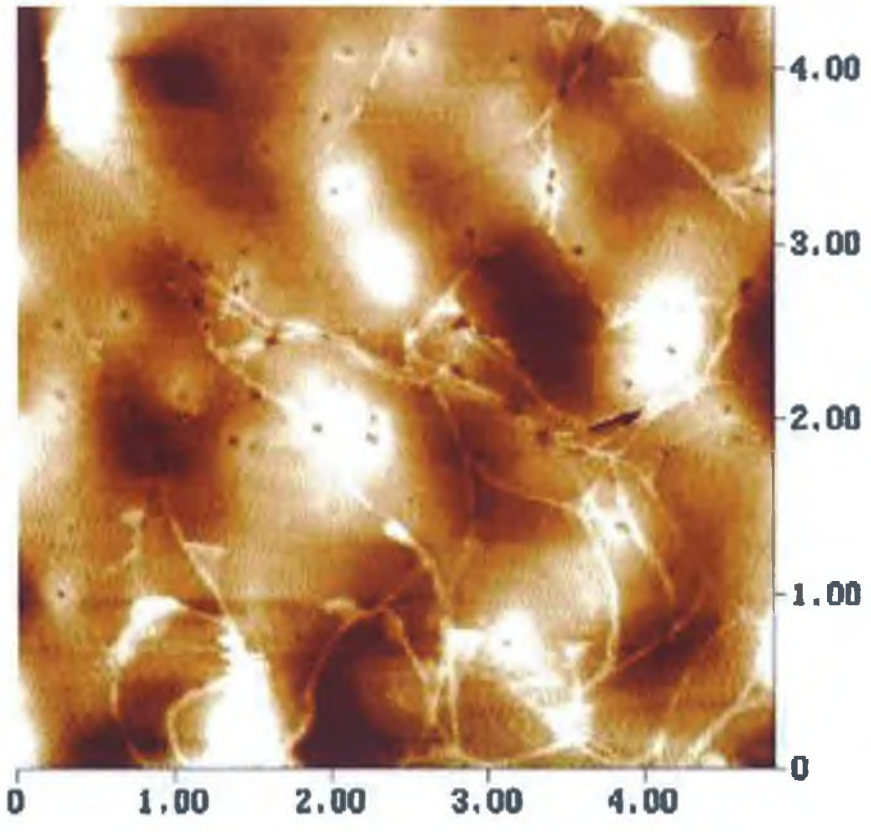

Figure 4.11 *TM-AFM image of amide linked MWNT interconnects.*

As the amino functionalisation occurs in islands, it is expected that MWNTs are interconnected through more than one ruthenium complex. The AFM images present strong evidence that the reaction scheme in Figure 4.3 was successful and a linkage

between MWNTs and the ruthenium complex was achieved due in the increase in the number of T- and Y-junctions after the reaction.

A close up of a typical T- and Y-junction is shown in Figure 4.12. To verify that the tubes are not just overlapping, height analysis was carried out. Nanotube 1 has an approximate height of 7.5nm above and below the junction. Nanotube 2 is 5.6nm along its entire tube. The Y-junction has a height 9.3nm both parallel and perpendicular to either nanotube 1 or 2. This indicates that nanotube 1 and 2 are not overlapping which if occurring would result in a height in excess of 13nm. A similar observation may be made at the T-junction between nanotube 3 and 4. Tube 3 at a height 10nm above and below the junction and tube 4 varied between 7nm and 9nm along its length. The T-junction has a height of 12nm, far less than the 17nm expected for overlapping tubes.

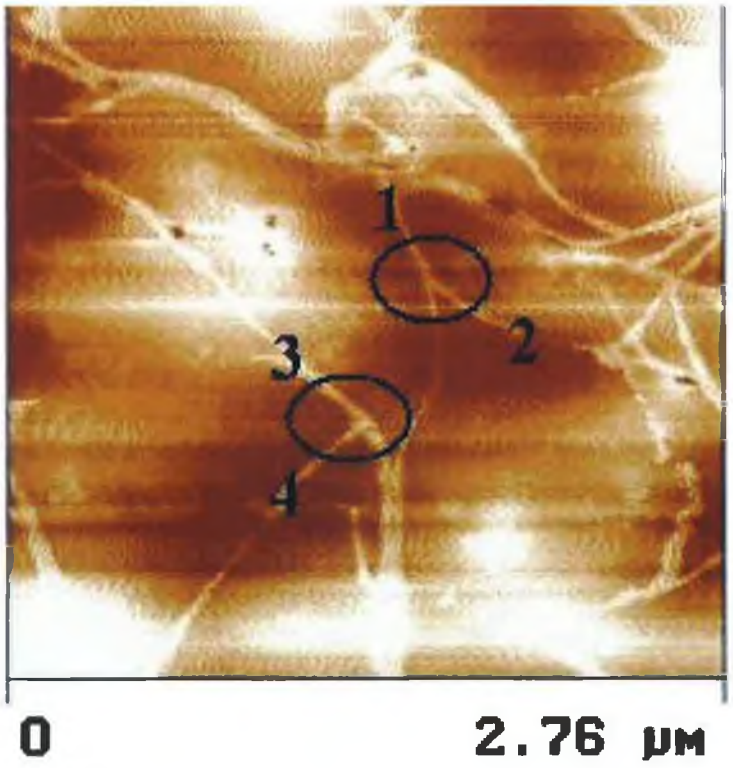

Nanotube	Height nm
1	7.5
2	5.6
Y-junction	9.3

Nanotube	Height nm
3	10
4	7-9
T-junction	12

***Figure 4.12** Close up of T- and Y-MWCT junction, indicated by circles.*

4.5.5 Modification of MWNT-NH_2 using a ^{13}C-labelled Bridge Molecule.

STM, IR, NMR and XPS are routinely employed to characterise CNTs that have been functionalised with small groups such as amino (-NH_2) and carboxylic acid groups (-COOH) [31,42-46,60]. When large molecular moieties are attached to the functional groups of the CNTs, characterisation methods become increasingly difficult to interpret. The work presented so far uses UV/Vis and emission spectroscopy along with AFM imaging and height analysis to investigate such a modification. Attempts have also been made to use NMR spectroscopy to characterise covalent bonding to CNTs. For example, Goze-Bac at al., [61] use ^{13}C NMR to investigate covalent functionalisation of ^{13}C enriched CNTs. In that work, the NMR data originates from the carbon atoms in the nanotubes.

In this study the ^{13}C-labelled bridge, terephthalic-carboxy-$^{13}C_2$ acid, is used as the starting material for reaction with amino-functionalised MWNTs. The carboxy groups of terephthalic acid are 100% labelled with ^{13}C. This allows ^{13}C NMR spectroscopy to be carried out where emphasis in on the carbon in the attached molecules. As a result non-labelled positions will show only weak signals due to the low natural ^{13}C abundance. Figure 4.13 shows the reaction scheme for the covalent attachment of the ^{13}C-labelled molecule with the amino-functionalised MWNTs. The labelled molecule was heated at reflux in thionyl chloride to form the corresponding acid chloride. This was immediately reacted with the MWNT-NH_2 to allow the formation of amide linkages. Having carried out the reaction detailed in Figure 4.13 NMR spectroscopy was carried out [62].

Rüther at al. reports that signals for the amide linkage between terephthalic acid and MWNTs could be assigned using ^{1}H NMR, ^{13}C NMR spectra, and the corresponding 2D HMBC (heteronuclear multiple bond connectivity) correlation spectrum [61]. NMR correlation regions are attributed to amide linkages (product **C**)

and acyl chloride parts of product **D** (Figure 4.13). This is very strong evidence for the covalent attachment of the labelled molecule to the nanotubes. In addition, signals originating from non-covalent functionalisation of MWNT (product **E**) with **B** were also assigned.

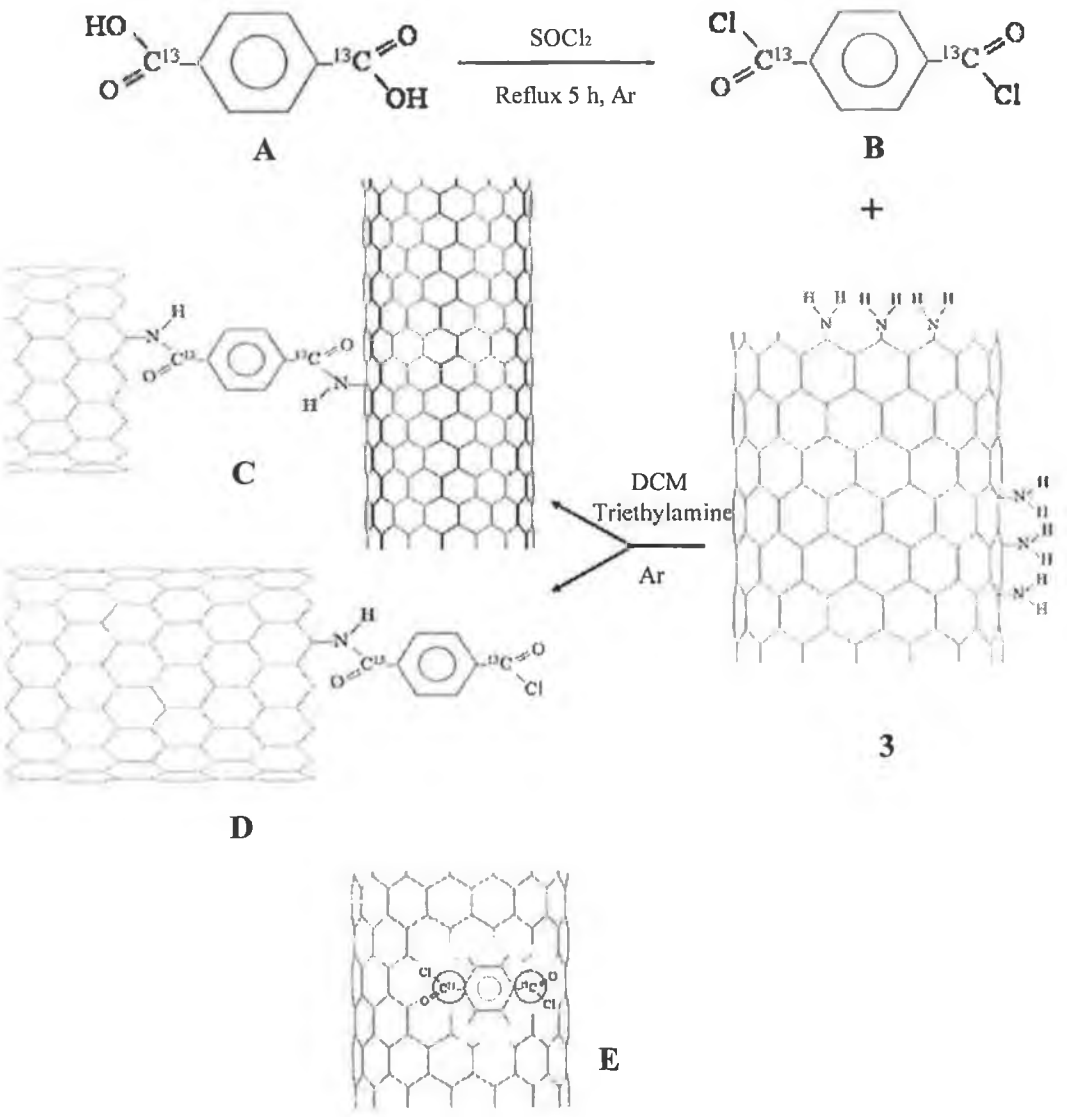

Figure 4.13 *The reaction scheme for the linkage of the ^{13}C-labelled bridge molecule with MWNT.* ***A****: Terephthalic-carboxy-$^{13}C_2$ acid;* ***B****: Corresponding acid chloride of* ***A****;* ***3****; Amino-functionalised open-ended MWNTs;* ***C, D****: Represent products of all forms of covalent functionalisation at the nanotube sidewalls and ends;* ***E*** *Product of non-covalent functionalisation.*

4.6 Conclusions

Amino-functionalized MWNTs were reacted with the acid chloride of a ruthenium complex. There is evidence that an amide group was formed and the nanotubes are linked together through the ruthenium complex. MWNT-NH_2 does not dissolve in dichloromethane, however, homogeneous solutions of the ruthenium-functionalised MWNT product were obtained. Absorption and emission spectroscopy show changes in the spectra between the starting materials and formed ruthenium-functionalised MWNT assembly, suggesting that a chemical reaction has occurred. T- and Y-nanotube interconnects were visualized through AFM imaging of this homogeneous solution, showing that the solubility of the tubes has changed. These images also show an increase in T- and Y-junctions after the reaction which strongly suggests that the reaction between amino functionalized MWNT and the acid chloride of the ruthenium complex was successful.

In a parallel experiment a ^{13}C labelled molecule was converted to its acid chloride and reacted with amino-functionalised MWNTs. Using ^{1}H NMR, ^{13}C NMR, and the 2D (HMBC) correlation spectrum, signals which can be assigned to an amide linkage between the labelled terephthalic acid molecule and MWNTs were identified, this showing that a combination of NMR experiments are a useful tool in the characterization of chemical bonds between carbon nanotubes and molecular entities, leading to advances in molecular sensing and electronics.

4.7 References

1. Iijima S., **1991**, *Nature*, 354, 56.
2. Collins P.G., Avouris P., **2000**, *Scientific American*, Dec, 38.
3. Dresselhaus M.S., Dresslhaus G., Eklund P.C., **1996**, In *Science of Fullerenes and Carbon Nanotubes*, Academic Press (Publishers)
4. Hamada N., Sawada S-I., Oshiyama A., **1992**, *Phys. Rev. Lett.*, 68, 1579.
5. Mintmire J.W., Dunlap B.I., White C.T., **1992**, *Phys. Rev. Lett.*, 68, 631.
6. Pan Z.W., Xie S.S., Lu L., Chang B.H., Sun L.F., Zhou W.Y., Wang G., Zhang D.L., **1999**, *Appl. Phys. Lett.*, 74, 3152.
7. Qian, D., Dickey E.C., Andrews R., Rantell T., **2000**, *Appl. Phys. Lett.*, 76, 2868.
8. Thess A., Lee R., Nikolaev P., Dia H., Petit P., Robert J., Xu C., Lee Y.H., Kim S.G., Rinzler A.G., Colbert D.T., Scuseria G.E., Tománek D., Fischer J.E., Smalley R.E., **1996**, *Science*, 273, 483.
9. López M.J., Rubio A., Alonso J. A., Qin L.C-., Iijima S., **2001**, *Phys. Rev. Letts.*, 86, 3056.
10. Bethune D.S., Kiang C.H., de Veries M.S., Gorman G., Savoy R., Vasques J., Beyers R., **1993**, *Nature*, 363, 605.
11. Ebbesen T.W., Ajayan P.M., **1992**, *Nature*, 358, 220.
12. Endo M., **1988**, *Chemtech.*, 18, 568.
13. Bronikowski M.J., Willis P.A., Colbert D.T., Smith K.A., Smalley R.E., **2001**, *J. Vac. Sci. Tech. A.*, 19, 1800.
14. Saito R., Fujita M., Dresselhaus G., Dresselhaus M.S., **1992**, *Appl. Phys. Letts.*, 60, 22004.
15. Odom T.W., Huang J., Kim P., Lieber C.M., **1998**, *Nature*, 391, 62.

16. Wildoer J.W.G., Venema L.C., Rinzler A.G., Smalley R.E., Dekker C., **1998**, *Nature*, 391, 59.

17. Tans S.J., Devoret H.H., Dai H., Thess A., Smalley R.E, Geerligs L.J., Dekker C., **1997**, *Nature*, 386, 474.

18. Martel R., Schmidt T., Shea H.R., Hertel T., Avouris P., **1998**, *Appl. Phys. Letts.*, 73, 2447.

19. Liang W., Bockrath M., Bozovic D., Hafner J.H., Tinkham M., Park H., **2001**, *Nature*, 411, 665.

20. Frank S.P., Poncharal P., Wang Z.L., de Heer W.A., **1998**, *Science*, 280, 1744.

21. Saito R., Dresselhaus G., Dresselhaus M.S., **1998**, In *Physical Properties of Carbon Nanotubes*, Imperial College Press (Publishers), London.

22. Gross M., **2003**, *Chemistry in Britain*, 39, 16.

23. Yao Z., Postma H.Ch., Balents L., Dekker C., **1999**, *Nature,* 402, 273.

24. Chiu P.W., Duesberg G.S., Dettlaff-Wegikowska U., Roth S., **2002**, *Appl. Phys. Lett.,* 80, 3811.

25. Rueckos T., Kim K., Joselevich E., Tseng G.Y., Cheung C.-L., Lieber C.M., **2000**, *Science,* 289, 94.

26. Fuhrer M.S., Nygard J., Shih L., Forero M., Yoon Y.-G., Zettle A., McEuen P.L., **2000**, *Science*, 288, 494.

27. Durham B., Casper J.V., Nagle J. K., Meyer T. J., **1982**, *J. Amer. Chem. Soc.*, 104, 4803.

28. Damrauer N. H, Cerullo G., Yeh A., Boussie T .R., Shank C. V., McCusker J. K., **1997**, *Science*, 275, 54

29. Li C., Hoffman M. Z., **1998**, *Inorg. Chem.*, 37, 830.

30. (a) Ferguson J., Mau A.W.H., Sasse W.H.F., **1979**, *Chem. Phys. Lett.*, 68, 21. (b) Nazeeruddin Md.K., Kalyanasundaram K., **1989**, *Inorg. Chem.*, 28, 4251. (c) Vos J.G., **1992**, *Polyhedron*, 11, 2285. (d) Giordano P.J., Bock C.R., Wrighton M.S., Interrante L.V., Williams R.F.C., **1977**, *J. Amer. Chem. Soc.*, 99, 3187. (d) Shimidzu T., Iyoda T., Izaki K., **1985**, *J. Phys. Chem.*, 89, 642.

31. Konya Z., Vesselenyi I., Niesz K., Kukovecz A., Demortier A., Fonseca A., Delhalle J., Mekhalif Z., Nagy J.B., Koos A.A., Osvath Z., Kocsonya A., Biro L.P., Kiriscsi I., **2002**, *Chem. Phys. Lett.*, 360, 429.

32. Curran A.S., Ajayan P.M., Blau W.J., Carroll D.L., Coleman J.N., Dalton A.B., Davey A.P., Drury A., McCathy B., Maier S., **1998**, *Adv. Mater.*, 10, 1091.

33. Dettlaff-Wegikowska U., Benoit J.M., Chiu P.-W., Graupner R., Lebedkin S., Roth S., **2002**, *Curr. Appl. Phys.*, 2, 497.

34. (a) Chen J., Hamon M.A., Hu H., Chen Y., Rao A.M., Eklund P.C., Haddon R.C., **1998**, *Science*, 282, 95. (b) Chen J., Rao A.M., Lyuksyutov S., Itkis M.E., Hamon M.A., Hu H., Cohn R.W., Eklund P.C., Colbert D.T., Smalley R.E., Haddon R.C., **2001**, *J. Phys. Chem. B.*, 105, 2525.

35. (a) Georgakilas V., Voulgaris D., Vazquez E., Prato M., Guldi D.M., Kukovecz A., Kuzmany H., **2002**, *J. Amer. Chem. Soc.*, 124, 14318. (b) Georgakilas V., Kordatos K., Prato M., Guldi D.M., Holzinger M., Hirsch A., **2002**, *J. Amer. Chem. Soc.*, 124, 760. (c) Holzinger M., Vostrowsky O., Hirsch A., Hennrich F., Kappes M., Weiss R., Jellen F., **2001**, *Angew. Chem. Int. Ed.*, 40, 4002.

36. (a) Chen R.J., Zhang Y., Wang D., Dai H., **2001**, *J. Amer. Chem. Soc.*, 123, 3838. (b) Kong J., Dai H., **2001**, *J. Phys. Chem. B.*, 105, 2890. (c) Star A.,

Steuerman D.W., Heath J.R., Stoddart J.F., **2002**, *Angew. Chem. Int. Ed.*,41, 2508.

37. Georgakilas V., Kordatos K., Prato M., Guldi D.M., Holzinger M., Hirsch A., **2002**, *J. Amer. Chem. Soc.,* 124, 760.
38. Banerjee S., Wong S.S., **2002**, *Nano. Lett.,* 2, 49.
39. Bahr J.L., Yang J., **2001**, *J. Amer. Chem. Soc.,* 123, 6536.
40. Tagmatarchis N., Prato M., **2004**, *J. Mater. Chem.,* 14, 437.
41. Huang W., Taylor S., Fu K., Lin Y., Zhang D., Hanks T.W., Rao A.M., Sun Y.-P, **2002**, *Nano. Lett.,* 2, 311.
42. Fu K., Huang W., Lin Y., Zhang D., Hanks T.W., Roa A.M., Sun Y.-P., **2002**, *Nanosci.. Nanotech.,* 2, 457.
43. Baker S.E., Cia W., Lasseter T.L., Weidkamp K.P., Hamen R.J., **2002**, *Nano Lett.,* 2, 1417.
44. Williams K.A., Veebhuizen P.T.M., de la Torre B.G., Entja R., Dekker C., **2002**, *Nature*, 420, 761.
45. Banerjee S., Wong S.S., **2002**, *Nano Lett.,* 2, 195.
46. Haremza J.M., Hahn M.A., Krauss T.D., Chen S., **2002**, *Nano Lett.,* 2, 1253.
47. Banerjee S., Wong S.S., **2002**, *J. Amer. Chem. Soc.,* 124, 8940.
48. Hirsch A., **2002**, *Angew. Chem. Int. Ed.,* 41, 1853.
49. Holzinger M., Abraham J., Whelan P., Graupner R., Ley L., Hennrich F., Kappes M., Hirsch A., **2003**, *J. Amer. Chem. Soc.*,125, 8566.
50. Frehill F., Vos J.G., Benrezzak S., Koos A.A., Konya Z., Ruther M.G., Blau W.J., Fonseca A., Nagy J.B., Biro L.P., Minett A.I., in het Panhuis M., **2002**, *J. Amer. Chem. Soc.,* 124, 13694.
51. O' Connor C.M., **1999**, *Ph.D. Thesis*, Dublin City University.

52. (a) Li J., Papadopoulos Ch., Xu J., **1999**, *Nature,* 402, 253; (b) Nagy P., Ehlich R., Biro L.P., Gyulai G., **2000**, *Appl. Phys. A.*, 70, 481; (c) Amelinckx S., Zhang X.B., Bernaerts D., Zhang X.F., Ivanov V., Nagy J.B., **1994**, *Science,* 265, 635; (d) Biro L.P., Mark G.I., Koos A.A., Nagy J.B., Lambin Ph., **2002**, *Phys. Rev. B*, 66, 165405. (e) Ding D.Y., Wang J.N., Cao Z.L., Dai J.H., Yu F., **2003**, *Chem. Phys. Lett.,* 371, 333.

53. Zhou D., Serapin S., **1995**, *Chem. Phys. Lett.,* 238, 286.

54. Biro L.P., Ehlich R., Osvath Z., **2002**, *Mater. Sci. Eng. C,* 19, 3.

55. Satishkumar B.C., Thomas P.J., Govindaraj A., Rao C.N.R., **2000**, *Appl. Phys. Lett.*, 77, 2530.

56. Biro L.P., Horvath Z.E., Mark G.I., Osvath Z., Koos A.A., Benito A.M., Maser W., Lambin Ph., **2004**, *Diam. and Related Mater.*, 13, 241.

57. Ming Ting J., Chang C.C., **2002**, *Appl. Phys. Lett.*, 80, 324.

58. Chu P.W., Duesburg G.S., Dettlaff-Wegiikowska U., Roth S., **2002**, *Appl. Phys. Lett.,* 80, 3811.

59. Burghard M., Duesbrug G., Phillipp G., Muster J., Roth S., **1998**, *Adv. Mat.,* 10, 584.

60. Chen J., Hamon M.A., Hu H., Chen Y., Rao A.M., Eklund P.C., Haddon R.C., **1998**, *Science, 282*, 95.

61. Goze Bac C., Bernier P., Latil S., Jourdain V., Rubio A., Jhang S.H., Lee S.W., Park Y.W., Holzinger M., Hirsch A., **2001**, *Curr. Appl. Phys.,* 1, 149.

62. Rüther M.G., Frehill F., O'Brien J.E., Minett A.I., Blau W.J., Vos J.G., In het Panhuis M., **2004**, *J. Phys. Chem. B.*, 108, 9665.

Chapter 5

Iron Wheels on Silicon: Wetting Behaviour and Electronic Structure of Adsorbed Organostannoxane Clusters

Chapter 5 describes the morphology observed when an organostannoxane cluster is deposited onto SiO_2. Atomic force microscopy imaging with subsequent statistical crystallography analysis shows that these structures form random cellular networks when deposited from toluene. AFM and synchrotron radiation spectroscopy have also been used to study the wetting behaviour and electronic structure of thin films of the cluster on silicon substrates. Advanced image analysis techniques based on Minkowski functionals are used to provide a detailed quantitative analysis of the morphology of the organostannoxane overlayers. This analysis shows that the dewetting patterns are rather far removed from those expected to arise from a simple Poisson distribution of centres, and the implications of this finding in terms of nucleated and spinodal dewetting are discussed.

"Exhilaration is that feeling you get just after a great idea hits you, and just before you realise what's wrong with it" ***Unknown***

5.1 Introduction

Self-assembly may be defined as the '*autonomous organisation of components into patterns or structures without human intervention*' [1]. Self-assembly processes include the non-covalent association of organic molecules in solution, to the folding of globular proteins. Self-assembly also provides an alternative strategy for constructing ensembles of nanostructures, for example the growth of semiconductor quantum dots on solid substrates [1]. A key motivation underlying the work described in this chapter relates to the possibility of ultimately translating crystal engineering combined with supramolecular chemistry to the self-assembly of organostannoxane and other organometallic clusters on a solid surface.

This is a goal that has parallels in many areas of state-of-the art nanoscale science. For example, alongside the development of synthetic procedures that impart device-related functionality to single molecules, there has been a drive toward the integration of molecular electronics with more conventional silicon technology [2]. There are many scientific issues to address in this area with some of the more fundamental questions related to the manner in which the molecular units interact with a substrate. Although considerable effort has been expended in studying the interaction of a range of small organic molecules with atomically clean, reconstructed silicon surfaces under ultrahigh vacuum (UHV) conditions [3,4,5] many applications necessitate an understanding of the self-organization, interactions, and morphology of molecular and polymeric systems deposited from solution. It is important to establish therefore if the resulting spin-cast or drop-deposited thin film is stable, unstable, or metastable and the extent to which it will dewet the underlying substrate/electrode surface. The issue of wettability is also of vital importance when considering the possibility of hydrogen-bonding mediated self-assembly of 2D organostannoxane or other organometallic overlayers

Organometallic chemistry underlies the synthesis and functionality of a wide variety of molecular and polymeric systems. Metallocenes, and ferrocene [6] in particular, have been exploited as central elements of a family of emerging molecular electronics devices. These prototype systems include components whose structure or conformation is switchable via variations in redox state [7], and a variety of switching methods have been envisaged. For example, magnetic control of the activity of (bio)electrocatalytic systems has recently been demonstrated by Katz et al. [8]. Photoisomerization has been exploited by a number of groups [9,10,11] to generate redox-active states, and variations in pH are commonly used to reversibly modify molecular properties. Novel cluster-type molecules based on organometallic compounds, structures such as ladder, cube, butterfly and drum, have also been assembled and structurally characterised in recent years [12].

The synthesis of the organometallic molecule, $[BuSn(O)OC(O)Fc]_6$ (where "Fc") ferrocenyl), was first reported by Chandrasekhar et al.[13]. The molecule comprises six ferrocene units which are attached to a central stannoxane core. As discussed in ref 13, this represents a rather novel cyclic interconnection of ferrocenyl elements. In more recent work, Chandrasekhar et al. have shown that it is possible to generate supramolecular "grids" of the stannoxane cluster through the formation of intermolecular C-H--O bonds between the ferrocenyl C-H and the carboxylate oxygen. This is an exciting development as it provides a relatively simple route, via the formation of hydrogen bonds, to the self-assembly of ferrocene-stannoxane clusters into a predefined pattern in the solid state.

The structures formed by the clusters after deposition need to be studied and the interactions with the substrate need to investigated so that this structure may be controlled. Atomic force microscopy and synchrotron radiation spectroscopy have been used in this chapter to study the wetting behaviour and the electronic structure

of thin films of the organometallic cluster $[BuSn(O)OC(O)Fc]_6$ mentioned above, on silicon substrates.

5.2 Experimental

5.2.1 Equipment and Materials

The grade of solvent and the equipment used for the ^1H NMR spectroscopy, the UV-Visible absorption spectroscopy, and the electrochemical analysis used throughout this chapter are described in detail in section 3.2.1.

Measurements of ^1H NMR spectra were recorded in d_3-chloroform. Cyclic voltammetric studies used in the characterisation of the organostannoxane cluster at the synthetic stage were carried out using 0.1M tetrabutylammonium hexafluorophosphate in dichloromethane as electrolyte. A three-electrode configuration of a platinum working electrode, a platinum mesh counter electrode and a saturated calomel electrode (SCE) as the reference electrode was used.

Elemental analysis on C, H, N, Sn and Fe was carried out at the Microanalytical Laboratory of University College Dublin (UCD). The analyser used is an Exador analytical CE440.

All Tapping Mode AFM analysis were carried out on a Digital Instruments Nanoscope IIIa AFM and a Digital Instruments Multimode AFM as described in detail in sections 2.3.5 and 3.2.1

Synchrotron core-level and valence band photoemission and resonant photoemission spectroscopy measurements were taken on Beamline 5U1 of the UK Synchrotron Radiation Source (SRS) at Daresbury.

5.2.2 Synthesis of the Organostannoxane Cluster

0.208g (1.0 mmol) of *n*-butylstannonic acid and 0.23g (1.0 mmol) of ferrocene monocarboxylic acid were heated under reflux for 6 h in 120ml toluene using a Dean-Stark apparatus. The reaction mixture was filtered and the solvent removed from the filtrate in vacuo to afford an orange powder, which was found to be analytically pure. Diamond-shaped, shining crystals were obtained in chloroform at 5°C. Yield 0.35g (0.14 mmol, 83%) m.p. 244°C

^{1}H NMR (400MHz) (in $CDCl_3$): 4.82 (2H, m), 4.30 (2H, m), 4.14 (5H, s), 1.91 (2H, m), 1.54 (4H, m), 1.0 (3H, t).

Elemental analysis for $C_{90}H_{108}Fe_6O_{18}Sn_6$: Found (Calculated) C 42.73 (42.81), H 4.25 (4.31), N 0.0 (0.0), Sn 28.56 (28.20), Fe 13.50 (13.27).

5.2.3 Surface Preparation and Analysis of the Organostannoxane Cluster

5.2.3.1 Morphology at different concentrations and solvents.

Solutions of the organostannoxane cluster have been applied to substrates of native-oxide covered silicon (100) or silicon (111) wafers 1cm^2 in area. The silicon substrates were solvent rinsed by sonication in four stages with: a) ethyl lactate; b) acetone; c) methanol; and d) isopropyl alcohol, and then blow-dried with N_2 before sample deposition. The solvents employed and the deposition parameters have been varied systematically. A film-coated wafer surface was achieved by using spin-casting as the adsorption technique. The two solvents employed were dichloromethane and toluene. Unless otherwise stated 15µl of a 0.25mmol solution of the organostannoxane cluster in either dichloromethane or in toluene was placed on the substrate. The samples were then rotated at speeds which ranged between 2500rpm and 4500rpm for 30 seconds. The dried films prepared by the different routes have been studied by tapping mode AFM in an air environment.

5.2.3.2 Statistical Crystallography.

Statistical crystallography was carried out on the organostannoxane cluster AFM height data using a Matlab program written by Dr. Dave Keeling (University of Nottingham). The Matlab algorithm was used to select the coordinates of the cell centres. These coordinates return the vertices of the polygons comprising the Voronoi tessellation. The program then draws the tessellation and calculates the relevant statistical quantities. This is described in more detail in the results and discussion section of this chapter.

5.2.3.3 Dewetting Properties

Thin films of the organostannoxane cluster in toluene were prepared by spin-coating at 4000rpm 15μL of a 0.25mmol solution. Two types of silicon samples were used:

i). Samples which were solvent rinsed as described in section 5.2.3.1 and blow dried with N_2 before spin-coating.

ii). Samples which were solvent rinsed as described in section 5.2.3.1 and then further cleaned with a 1:1 mixture of H_2SO_4:H_2O_2 (30%) for 1 h. These were then thoroughly rinsed with deionised water and blow-dried with N_2 before spin-coating.

The dried films prepared by the different routes have been observed by tapping mode AFM in an air environment. The different samples were then annealed within a range of annealing times (30 min to 60 h), and annealing temperatures (75°C and 125°C). When a specific period of annealing time was complete the samples were quenched to room temperature for tapping mode AFM observations and analysis, and then placed back in the vacuum oven for further annealing. Samples were annealed for

periods of 30 min up to 12 hours, then for periods of 1 h up to 20 hours and finally for periods of 4 h up to 60 hours annealing time.

5.2.3.4 Photoemission Spectroscopy

For all photoemission spectroscopy samples, 15μL of a 0.25mmol solution of the organostannoxane cluster in toluene was spin-cast at 4000rpm onto a solvent rinsed 0.7cm^2 piece of native oxide-covered Silicon (111) sample. Synchrotron radiation (SR) photoemission and SR resonant photoemission spectroscopy (RESPES) measurements were taken on Beamline 5U1 of the UK Synchrotron Radiation Source (SRS) at Daresbury. The photon energy range of the undulator beam is 60eV to 1keV. Photon energies were calibrated using Ti L_2 X-ray absorption spectra from a TiO_2 thin film (which could be moved in to and out of the beam upstream from the sample), and the Si $L_{2,3}$ edge spectra from the silicon substrate. A VSW HA100 hemispherical electron energy analyser with single channel detection was used for all photoemission and RESPES measurements. All photoelectron binding energies were calibrated by referencing to the Si 2p photoemission peak (at a binding energy of 99.5eV) of the native oxide-terminated Silicon (111) substrate.

5.2.3.5 Current-Voltage (I-V) Measurements.

For the electrical measurements the substrate used was a 2-inch Si(100) wafer with a 200nm thermally grown SiO_2 surface layer. This was scribed in a clean-room using a Dynapert-premicia scriber, into a 1cm^2 sample. 15 μl of a 0.25mmol solution of the organostannoxane cluster in toluene was spin-coated (4000rpm) onto this substrate. Gold contacts were then deposited on to the sample by using a shadow masking technique. The shadow masking technique consists of a bronze mask with 200μm wide strips cut out of it. 5μm and 10μm lengths of tungsten wire were attached

across these gaps. The organostannoxane cluster sample was then secured face down on to the bronze mask. The mask was then mounted into an Edwards Auto 306 evaporator which was evacuated down to a pressure of $3*10^{-7}$ atm. Gold was evaporated onto the sample through the mask by electrically heating a small piece of gold held below the sample (see Figure 5.1). The room temperature electrical measurements were carried out on an in-house (Nanoscience group, School of Physics and Astronomy, Nottingham University) built electrical measuring rig controlled by a Labview program. The rig consists of a 1MΩ resistor connected in series with the sample, the voltage over the resistor is measured from which the current flowing through the circuit is calculated. The computer program controls allows the choice of starting and stopping voltages, the number of data points to record and the voltage ramp speed (See Figure 5.2). The organostannoxane cluster thin films were measured between -20V and +20V, collecting 200 data points and with a ramp speed of 0.1V/sec. The contact to the sample electrodes is made with needlepoint wires controlled with micro-positioners.

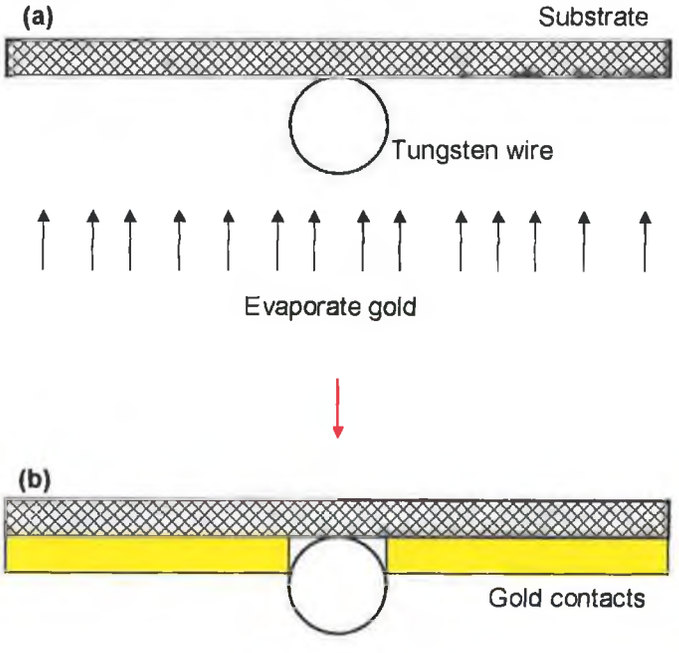

Figure 5.1 *Schematic of shadow masking technique used for producing 5μm and 10μm spaced microelectrodes on the surface.*

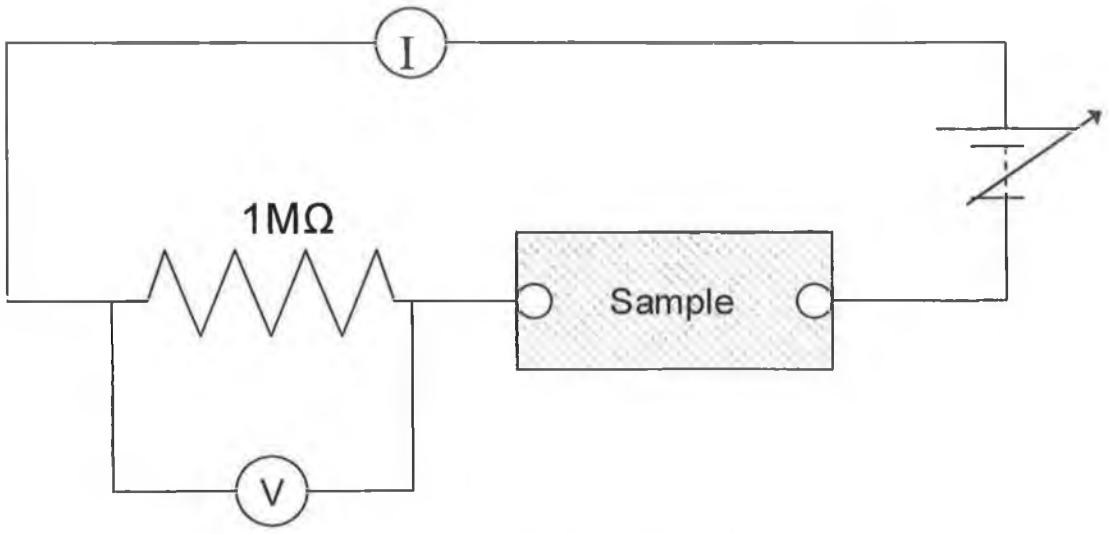

Figure 5.2 *Schematic of electric circuit diagram.*

5.3 Results and Discussion

5.3.1 Characterisation of the Organostannoxane Cluster molecule.

The synthesis of the organometallic molecule $[BuSn(O)OC(O)Fc]_6$ where Fc is ferrocenyl was first reported by Chandrasekhar et al. in 2000 [13]. The molecule comprises six ferrocene units which are attached to a central stannoxane core. There is a cyclic connectivity of the six ferrocene units established through the linking tin atoms which represents a rather novel cyclic interconnection of ferrocenyl elements. As discussed in ref 13 the central stannoxane cluster in the molecule is made up of two hexameric Sn_3O_3 rings, each present in a puckered chair-like conformation [13]. These rings are joined to each other to afford six Sn_2O_2 distannoxane units as the side faces of the cluster. This represents the signature structural feature of stannoxane clusters as discussed by Chandrasekhar at al. [14,15,16].

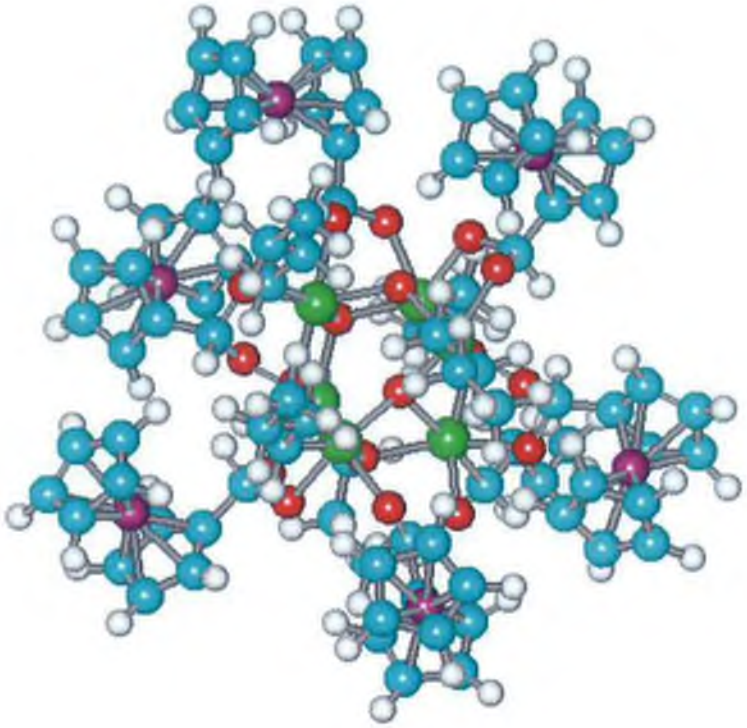

Figure 5.3 *[BuSn(O)OC(O)Fe]$_6$ Bu = butyl, Fe =ferrocenyl, O; C; Sn; Fe; and H.*

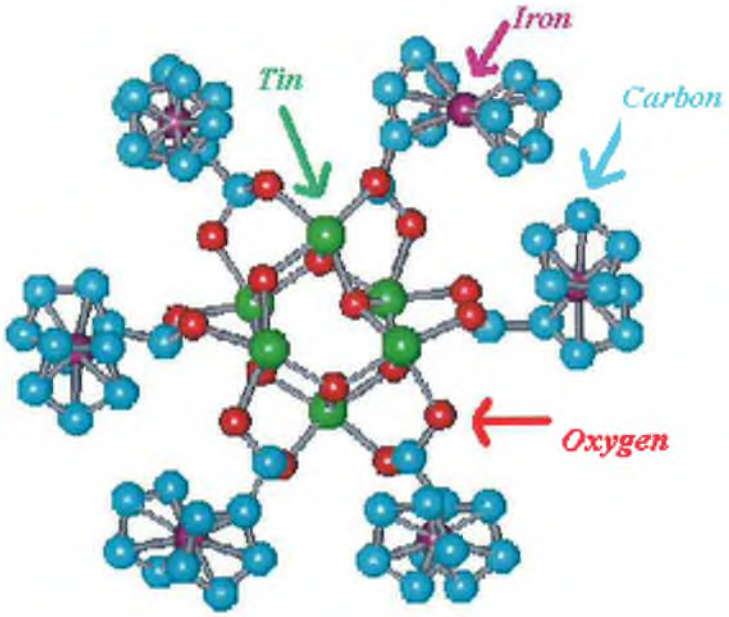

***Figure 5.4** Schematic of [BuSn(O)OC(O)Fc]$_6$ with all hydrogen atoms omitted.*

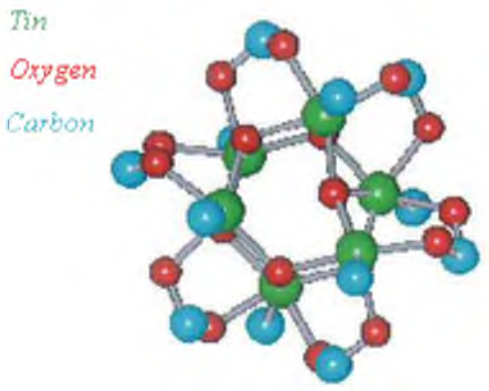

Figure 5.5 *$[BuSn(O)OC(O)Fc]_6$ central core (all hydrogen atoms omitted)*

The synthetic characterisation of the molecule $[BuSn(O)OC(O)Fc]_6$ will be described briefly in the next section as the results are compared with those obtained in the literature in ref 13. Figure 5.6 shows the absorption spectrum of $[BuSn(O)OC(O)Fc]_6$ in dichloromethane. The band in the visible region with λ_{max} equal to 443nm is characteristic of similar ferrocene compounds [17], which show λ_{max} between 425 and 500nm. It is ascribed to the lowest energy spin-allowed d-d band of the ferrocene unit.

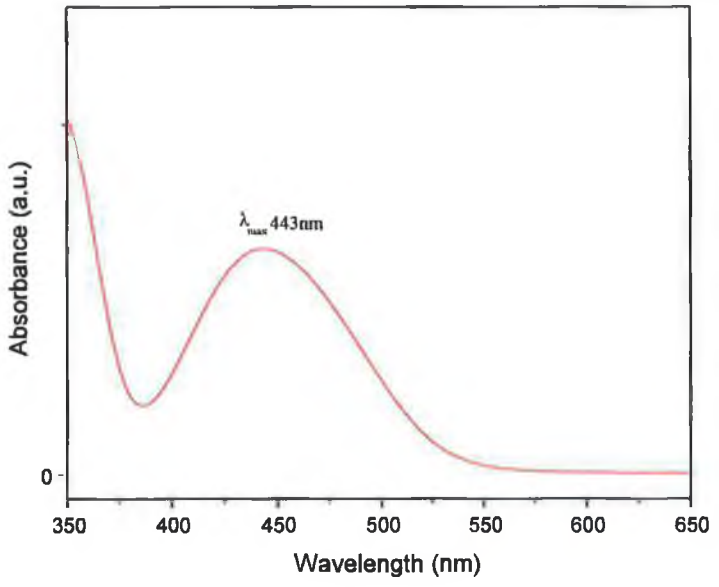

Figure 5.6 *The UV-Visible absorption spectra of $[BuSn(O)OC(O)Fc]_6$ in dichloromethane.*

Cyclic voltammetric studies show a single quasireversible peak with an $E_{1/2}$ value of 0.73 V (vs. SCE). This agrees with the values obtained by Chandrasekhar et al. in ref 13. Here it is suggested that all six ferrocene units are oxidised at the same potential. Another feature of the electrochemical behaviour reported in ref 13 is the reversibility of the voltammogram even after several cycles. Experimentally this has been verified up to ten cycles. This indicates that the cluster is robust and does not decompose upon oxidation.

The spectroscopic and electrochemical behaviour of this molecule is consistent with that described in ref 13. Chandrasekhar et al. also point out, that not only is the synthetic reaction to form $[BuSn(O)OC(O)Fc]_6$ important in that it produces a hexaferrocene compound in high yield (as compared to the modest yields of multiferrocene compounds produced via other synthetic routes), but the resulting organostannoxane cluster is robust and thermally stable up to a temperature of 244°C.

5.3.2 Surface Analysis

5.3.2.1 Cellular Networks

As discussed in the atomic force microscopic analysis of the polymer $[Ru(bpy)_2PVP_{10}Cl]Cl$ (in section 3.3.2), optimisation of the tapping mode scan parameters is essential in order to follow the surface topography as closely and as accurately as possible. Not only are AFM images susceptible to artefacts due to the condition of the tip, but also scan instabilities such as noise, drift and scanner hysteresis. For this reason all the evaluations and results that are presented in the next sections have been carried out quantitatively and averaged over a large number of samples. The calibration surface (Figures 2.14 and 2.15) and a reference solvent-rinsed native oxide-covered silicon (111) or (100) substrates, were also routinely investigated as described in section 3.3.2. For the solvent-rinsed silicon substrates the contact angle was 45° ± 5°.

The assembly and the morphology of the organostannoxane cluster molecules have been investigated on a solvent-cleaned native oxide-covered silicon substrate as a function of the adsorption technique and the solvent employed. The cluster molecules exhibit good solubility in toluene. This allows the formation of free-standing films by spin-coating deposition. The initial goal was to observe the self-organisation of the cluster molecules when deposited from solution, and to establish if the resulting film is stable, unstable, or metastable. The results from this analysis have lead to a more detailed investigation to determine if the films dewet the underlying silicon substrate and the dewetting mechanism.

Figure 5.7 shows an AFM height image of the organostannoxane cluster spin-cast onto a solvent-rinsed silicon substrate at 4000rpm from toluene. Under these conditions the organostannoxane cluster overlayers adopt a cellular morphology. This cellular morphology bears a striking resemblance to images of random, space-

filling foams or cellular networks previously found in nature and reported in the literature [18,19]

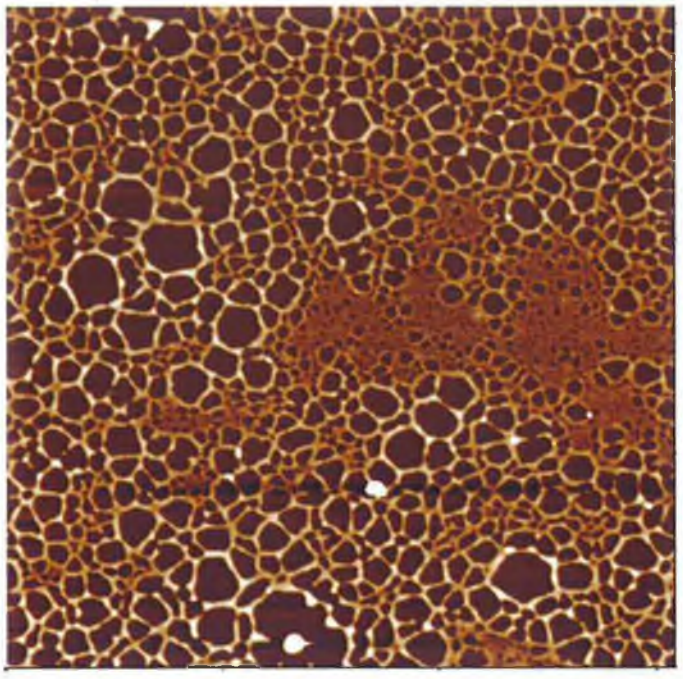

*Figure 5.7 Tapping Mode AFM height data of $[BuSn(O)OC(O)Fc]_6$ deposited by spin-coating from toluene; 7.715μm * 7.715μm z-range 15nm.*

What are Random Cellular Networks?

Many materials occurring in nature possess the form of a cellular network, which means they are composed of domains divided by sharp boundaries. The domains outlined by these boundaries are generally polygonal in shape with three boundaries meeting at every intersection or vertex, for example soap froths, foams, biological tissues and grains in metal [19,20,21,22]. Froths, as a typical class of cellular structure have been the focus of considerable interest over recent decades, and have stimulated numerous attempts to model cellular networks and to describe their properties [23,24,25]. The froth is an almost ideal system, with all boundaries equivalent and with motion of bubble boundaries driven by a transfer of gas between neighbouring bubbles, i.e. surface-energy-driven diffusion. A balance of forces at

each vertex yields an angle of 120° between boundaries, where this constraint can be satisfied only if the boundaries are curved [19,26,27]. The fact that the initial system is intrinsically in a state of non-equilibrium leads the system to evolve over time to seek a stable equilibrium through reduction in interfacial area. In the process, froth bubbles shrink or vanish, resulting in a self-similar structure, on a larger scale that the original, i.e. the system has coarsened. Natural froth networks exhibit the characteristic of randomness and disorder (non-uniform)[19,28,26].

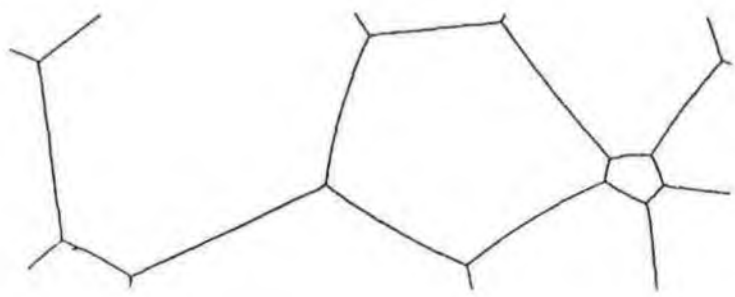

Figure 5.8 *A dry froth where the cell sides meet at 120° [29].*

Other examples of random space-filling cellular structures includes biological tissues like cucumber, and on scales greater than molecular dimensions the largest example being the galactic structure of the Universe [19]. All of these networks have huge differences in length scale yet disorder is inherent in each system. That such a similarity appears in the presence of very different formation mechanisms points to a universal behaviour that may be applied to all systems exhibiting these properties. The study of these cellular systems has led to the development of statistical techniques used to analyse their formation and evolution, and which may also be used to quantifiably characterise a cellular network [18,19,24]. In the next section AFM height data of the organostannoxane cluster thin film networks will be analysed

using these techniques of statistical crystallography. The aim is to determine to what extent the cluster networks conform to the laws of statistical crystallography, and to identify where deviations from ideal cellular network behaviour occurs. Figure 5.9 shows the network morphology of the organostannoxane cluster thin film (from toluene). Line sections through the networks show that they are 4.2 ± 0.5nm in height. The widths of the network branches fall within the range 45 ± 15nm. Roughness analysis shows an R_{rms} value of 1.936nm.

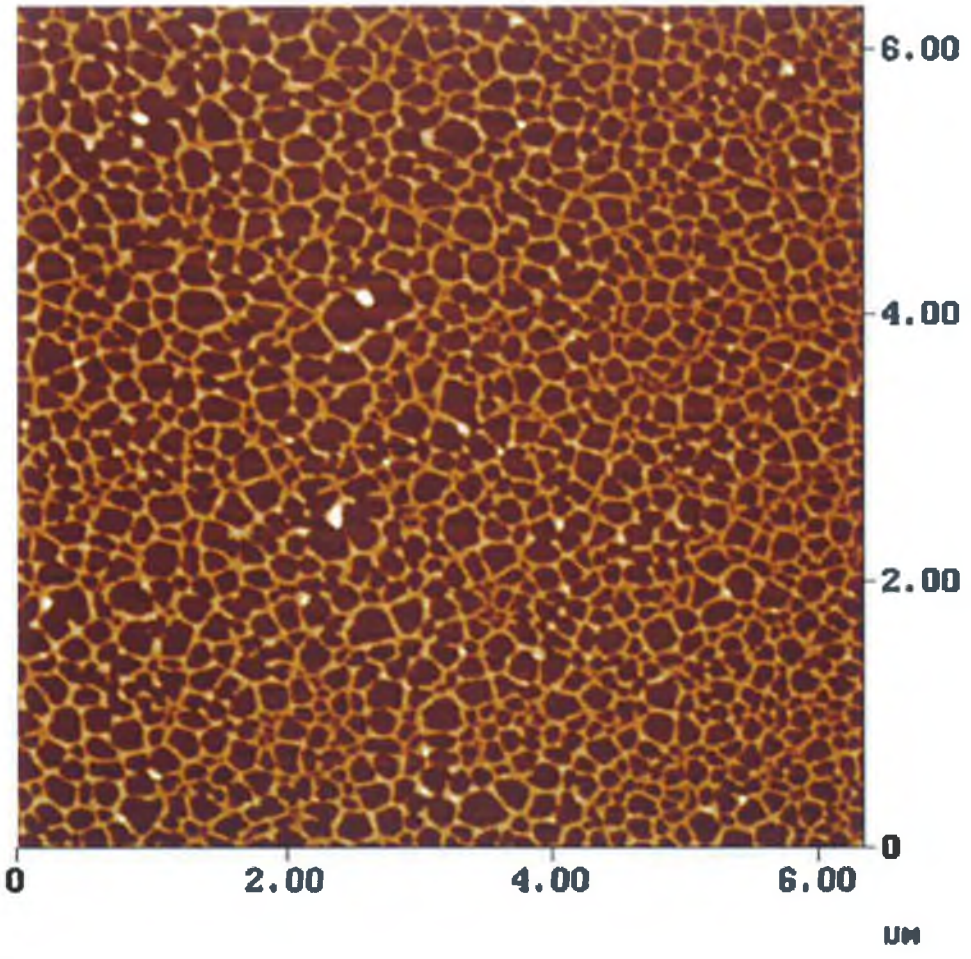

Figure 5.9 *Tapping Mode AFM image of typical network resulting from spin-coating $[BuSn(O)OC(O)Fc]_6$ from toluene onto a native oxide- covered silicon substrate ; 6.328μm x 6.328μm z-range 15nm.*

Voronoi Constructions

The starting point in the analysis of the cellular network shown in Figure 5.9 uses the technique of Voronoi constructions. This is based on the counting and classification of polygons and is used to define the correlations between neighbouring points on a surface. In a typical construction an array of cell centres is first defined. These may be completely random or correlated in some way. Each cell centre is then assigned a cell containing all points which are nearest to it. A Matlab program was used to select the coordinates of the cell centres. These coordinates then returned the vertices of the polygons comprising the Voronoi tessellation. Specifically the Matlab program locates the cell centres, and the lines joining the nearest neighbours are bisected to give a straight line representation of the cellular structure. The smallest convex polygon surrounding a given centre contains all points in space closest to this centre. The Matlab program then draws the tessellation and calculates the relevant statistical quantities. Figure 5.11 shows the Voronoi constructions for the feature wall height data from Figure 5.9.

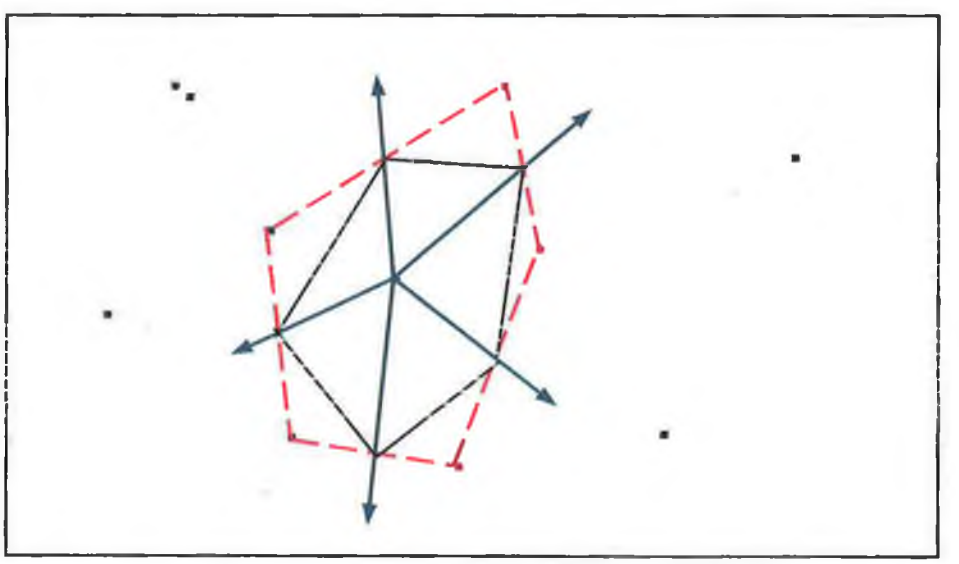

Figure 5.10 (a) *A Voronoi Cell. Red lines indicate lines joining nearest neighbours. Blue arrows indicate bisectors from cell centre resulting in new Voronoi construction.*

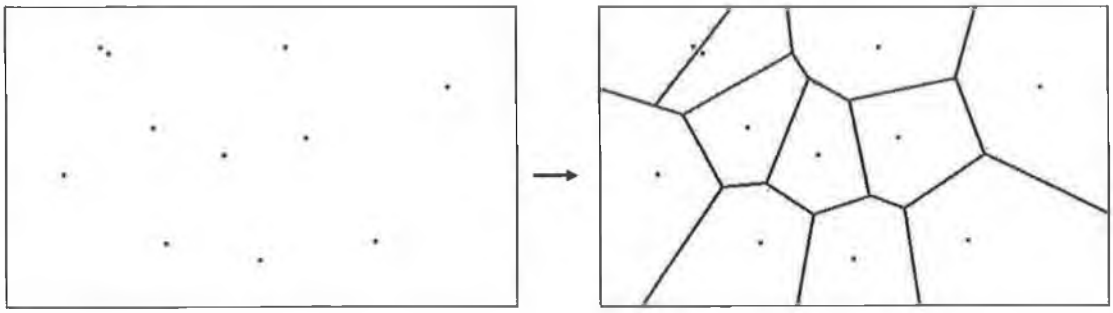

Figure 5.10 (b) *Completed Voronoi construction for the set of cell centres on the left.*

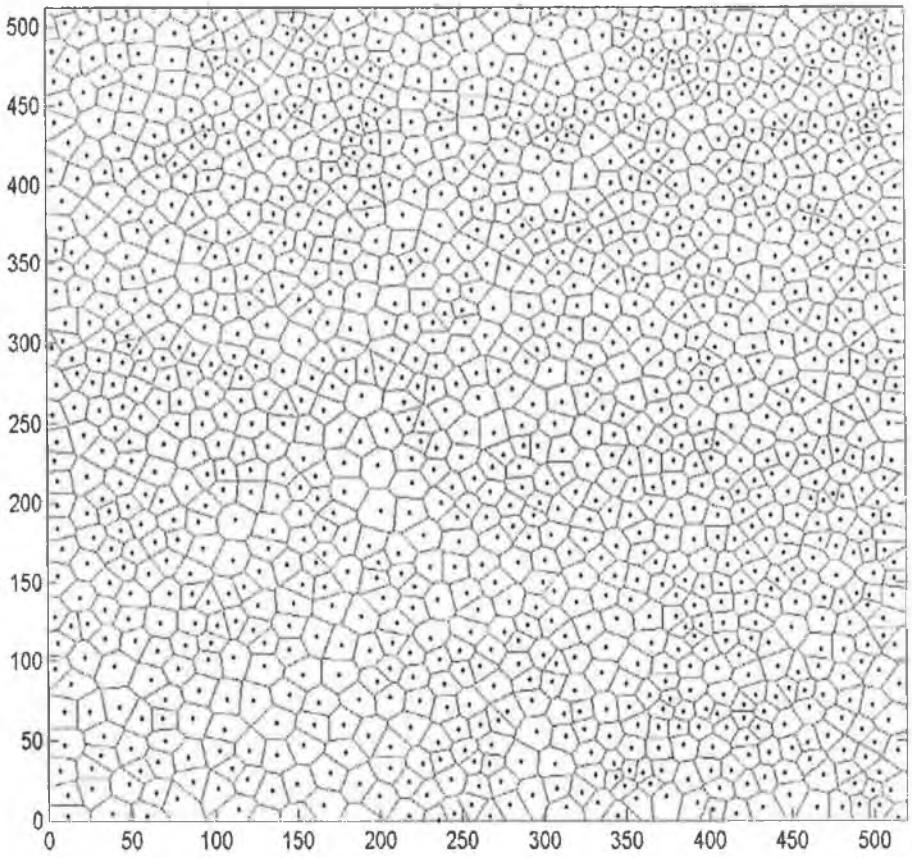

Figure 5.11 *The Voronoi construction for the height network data in Figure 5.9. The scale refers to the number of data points (i.e. pixels per images is 512 x 512)*

Quantitative measures may be determined from the analysis of the distribution of polygon sidedness from the histogram in Figure 5.12. The total number of cells included is 1071. Cells with less than 4 sides are not observed. 9- and 10-sided cells

are present but their number is very small ~ 1%. The mean value of the number of polygon sides, $\langle n \rangle$, is 5.99. Euler's theorem gives the relationship between the number of faces F, edges E, and vertices V of a polygon domain, and may be expressed as:

$$F - E + V = \chi \tag{5.1}$$

where χ is the Euler characteristic which is a topological measure describing the connectivity of a pattern. Rivier derived Euler's relation and the valence relations between incident edges, vertices, and faces and determined that for a random froth in two dimensions in an infinite network $\langle n \rangle = 6$ [30]. The value of $\langle n \rangle = 5.99$ calculated from the histogram in Figure 5.12 is extremely close to this value of $\langle n \rangle = 6$, which is determined in the limit of an infinite network expected from Euler's theorem. A value of $\langle n \rangle = 5.99$ also indicates that the data are not statistically skewed through sampling of an insufficient number of cells.

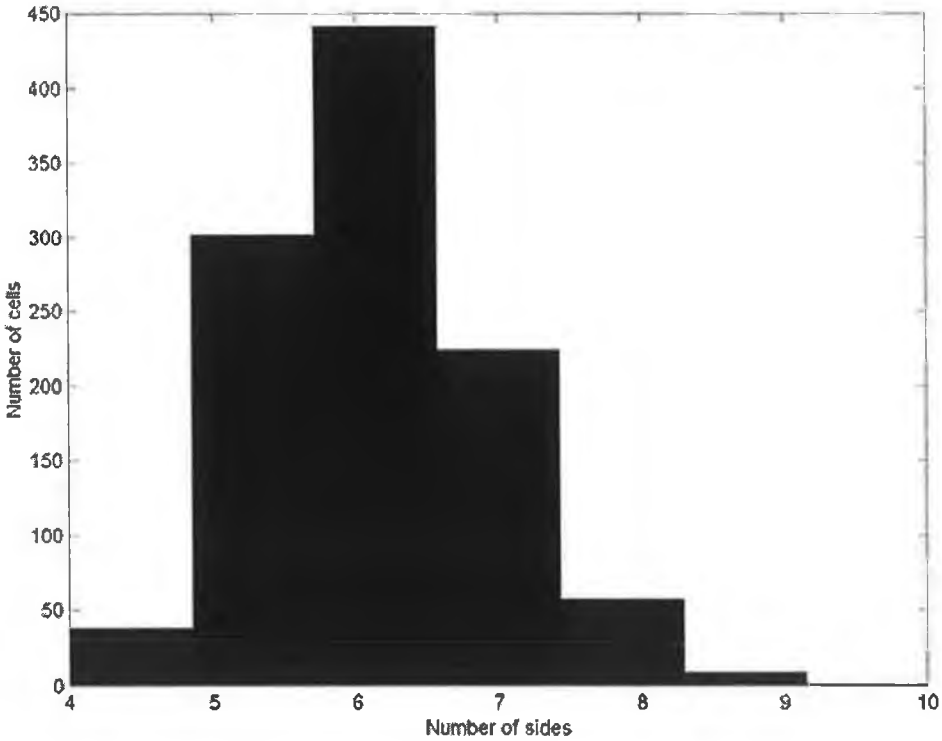

Figure 5.12 *Histogram of polygon side distribution.*

A random cellular network or froth may also be characterised in terms of its side distribution function and second moment. The topological or side distribution function *p(n)* is the set of probabilities for cells in the structure with *n* sides, $n = 3, 4, 5, \ldots$ with topological moments of side distribution defined by:

$$\mu_m = \sum_{n=2}^{\infty} p(n)(n - < n >)^m \tag{5.2}$$

The second moment μ_2 measures the dispersion or variance of a distribution and so to some extent may characterise the amount of disorder of a network. In equation 5.2 $m = 2$ for the second moment, and <n> = 5.99, so equation 5.2 is rewritten as:

$$\mu_2 = \sum_n P(n)(n - < 5.99 >)^2 \tag{5.3}$$

where *P(n)* is the normalised distribution function. The prototypical-quenched froth, the two-dimensional Poisson Voronoi tessellation, has a μ_2 value of 1.78 [31].The network in Figure 5.9 has a μ_2 value of 0.93. This value indicates that the network is not derived from a Poisson distribution of points, and so may not arise from nucleation or dewetting events that are spatially uncorrelated. Large values of μ_2 indicate greater disorder and deviation from a perfect hexagonal structure [32]. Low values of μ_2 are associated with 'young' systems that are far from statistical equilibrium. This may also be quantifiably confirmed from a measure of the networks entropy *S*, where:

$$S = -\sum P_n \ln P_n \tag{5.4}$$

By maximising the entropy of the system, the most probable distribution of cells can be found when in statistical equilibrium. For all network foams studied in the literature *S* is ~ 1.4, which is smaller than the value of 1.71 expected for a purely

random 2D set of points [33]. The value of S from this analysis is 1.37. This means that the cell distribution is constrained by external forces, and thus is not driven by entropy maximisation only.

Lewis, Aboav-Weaire and Desch Laws: Correlations in Cells

A linear correlation function may be defined between the average area of an n-sided cell A_n and the number of sides [34]:

$$<A_n> = an + b \tag{5.5}$$

where $<A_n>$ is the normalised area; a and b are network constants which are dependent on cell pattern and the average area of all cells. This law, termed Lewis' law, holds for an ideal random froth and is described by Rivier as '*representing an equation of state of an ideal cellular structure*' [34].

The law results from entropy maximisation. Figure 5.13 shows a graph of the data in the present work for the Lewis law. A quadratic curve would provide a better fit than a linear relationship indicating failure of this law for the organostannoxane cluster networks. If the cellular network has perfect agreement with this law it implies that the structure of the network is determined solely by the mathematics of space-filling. Deviations however, indicate that physical and/or chemical forces, in addition to topological constraints must be considered; as previously shown by the measurement of the entropy S of the system. In other work deviations from the Lewis law have been observed in thiol-stabilised gold clusters which form cellular networks when deposited on SiO_2 [33], and metallurgical grains [35]. This deviation has been reported to be due in part to the energy stored in the cell boundaries. One type of system which does obey this law is Voronoi froths generated from Poisson-distributed centres.

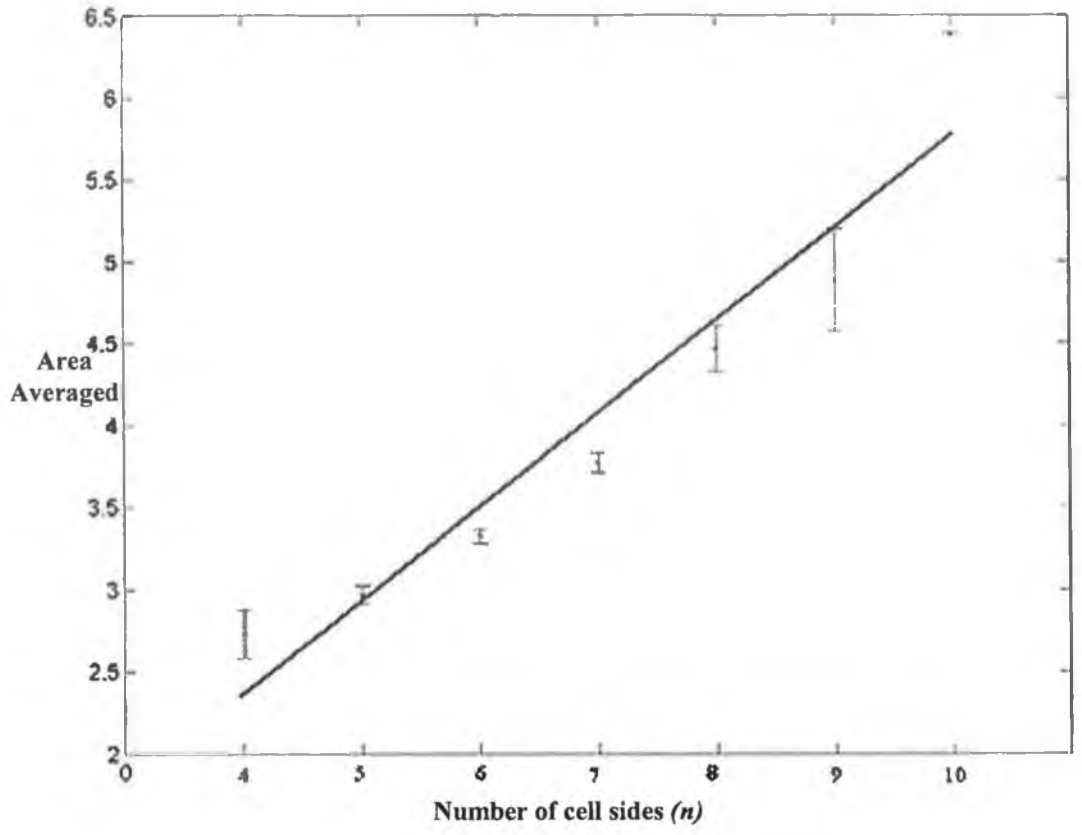

Figure 5.13 *Lewis Law; Plot of the normalised average area of an n-sided cell vs. n.*

The second correlation function to measure is the average number of sides of the neighbours of an *n*-sided cell, *m(n)*:

$$m(n) = (6 - a) + \left(\frac{6a + \mu_2}{n} \right) \tag{5.6}$$

where a is a network parameter generally within [0,1] (but values outside this range have also been reported [36]), and *m(n)* is the average number of sides of the neighbours of an *n*-sided cell, with μ_2 the second moment of *p(n)*. This is known as the Aboav law, and for the case of a = 1 is usually called the Aboav-Weaire law [37,38,39]. This law describes inter-cellular correlations and puts forward that '*the product of a cell's sidedness n, and its neighbours' average sidedness, m, is linear in n*'. All known random cellular networks obey this law [40]. Figure 5.14 shows the

plot of $m(n)$ as a function of n for the networks studied. This plot conceals small deviations in the relationship [41], therefore the correlation between $m(n)$ and $1/n$ is plotted in Figure 5.15. This illustrates a linear relationship which shows that the Aboav-Weaire law holds for the organostannoxane cluster networks. The only value of $m(n)$ that is independent of a is $m(6)$, and is given by the Weaire relationship $m(6) = \langle n \rangle + \mu_2/6$ [19].

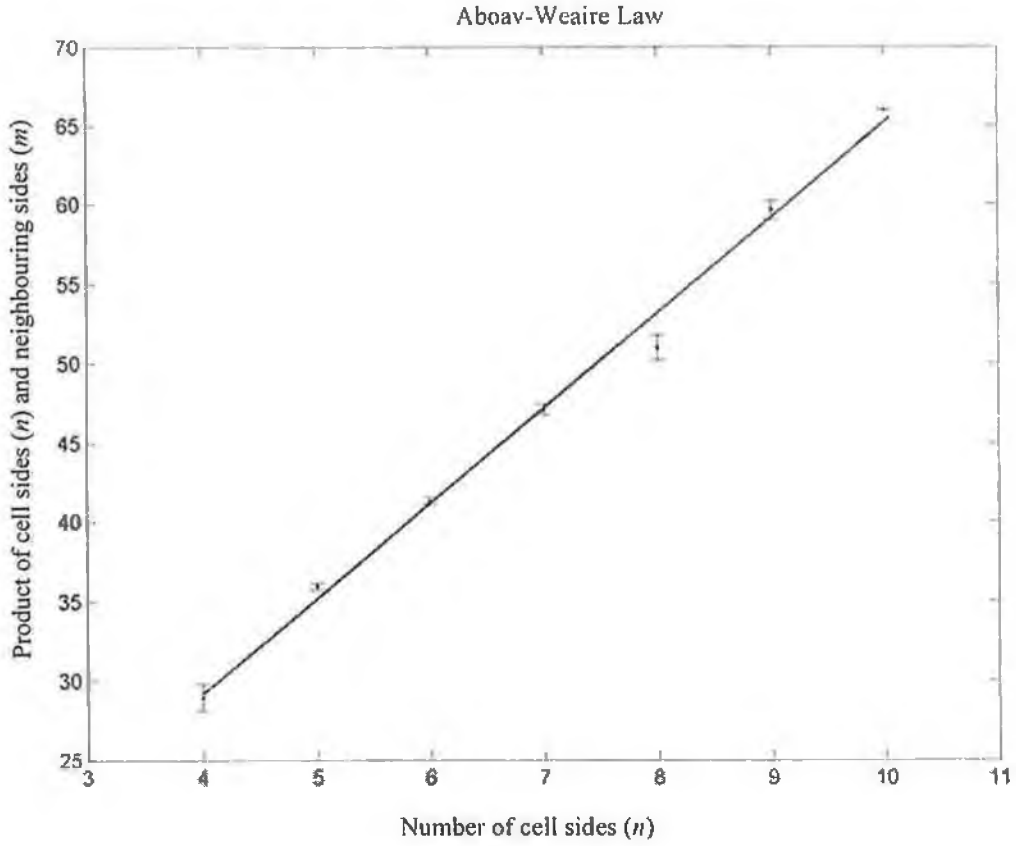

Figure 5.14 Plot of m(n) as a function of n for organostannoxane cluster network.

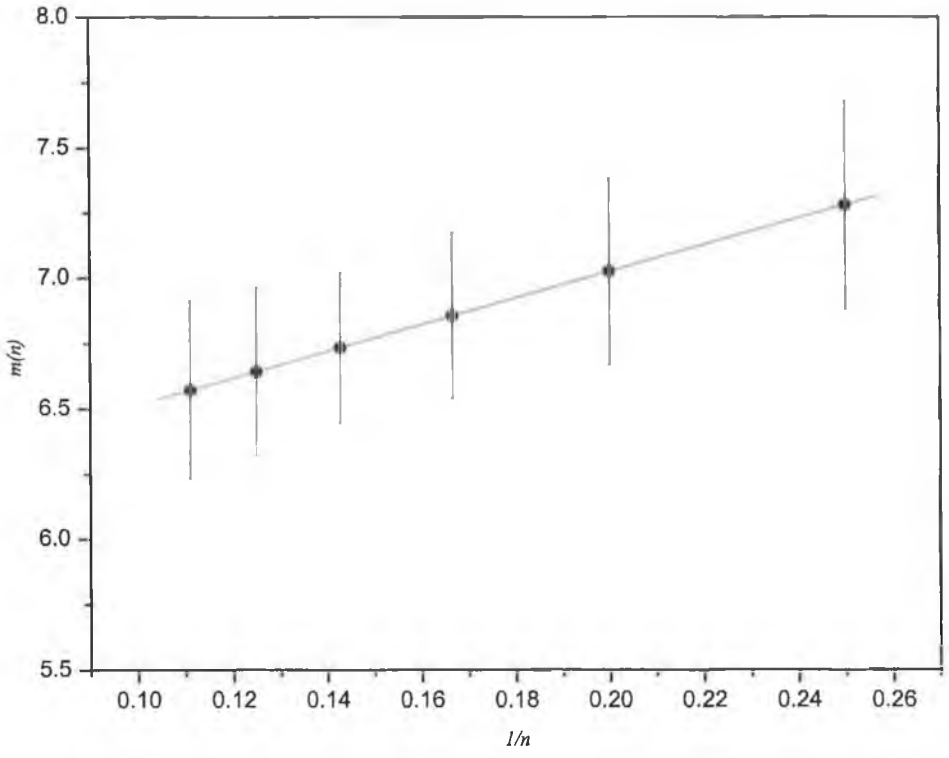

Figure 5.15 *Plot of m(n), the average number of sides of the neighbours of an n-sided polygon as a function of 1/n for the organostannoxane cluster network.*

The third and final cell-cell distribution function, derived by Desch is known as the perimeter law. It states that '*the average perimeter of an n-sided cell should vary linearly with the number of its sides*';

$$\langle P_n \rangle = cn + d \tag{5.7}$$

where c and d are network parameters. This law provides information on the distribution of energy to the cell borders. The data for the organostannoxane cluster network is plotted in Figure 5.18. A linear relationship is observed. Deviations from the law do occur for cells with 4, 9 and 10 sides. This is due to the fact that these cells make up such a small proportion of the total number of cells studied. For the

previous data the Matlab algorithm uses the POLYVAL function to calculate the error estimates which represent one standard deviation.

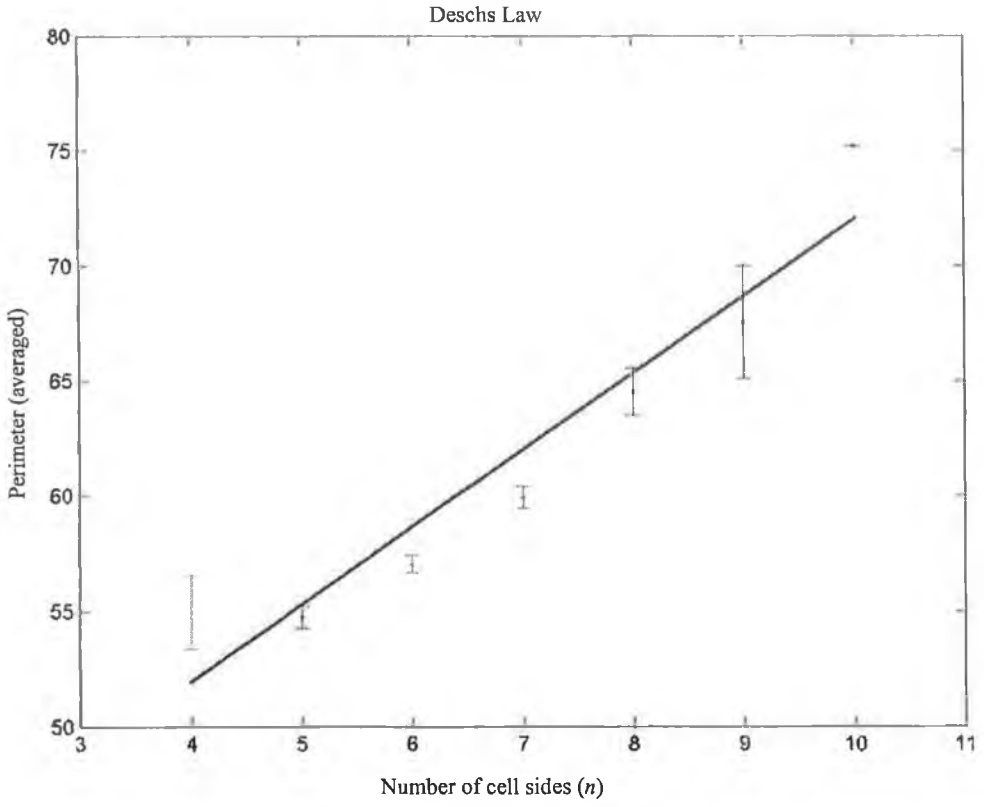

Figure 5.16 *Desch's Law.*

Figure 5.17 highlights the formation of secondary networks, with smaller intercellular spacing, within the primary networks observed for the organostannoxane cluster thin film spin-cast from toluene. Statistical crystallography shows that the laws for random cellular networks are also obeyed for these types of networks. Statistical analysis has been carried out on these and a range of tapping mode height data for the organostannoxane cluster networks. Table 5.1 shows the results. The relative height data, Voronoi constructions and cell-cell correlation functions may be found in Appendix B. These networks also obey the laws of statistical crystallography and may be described as random cellular networks.

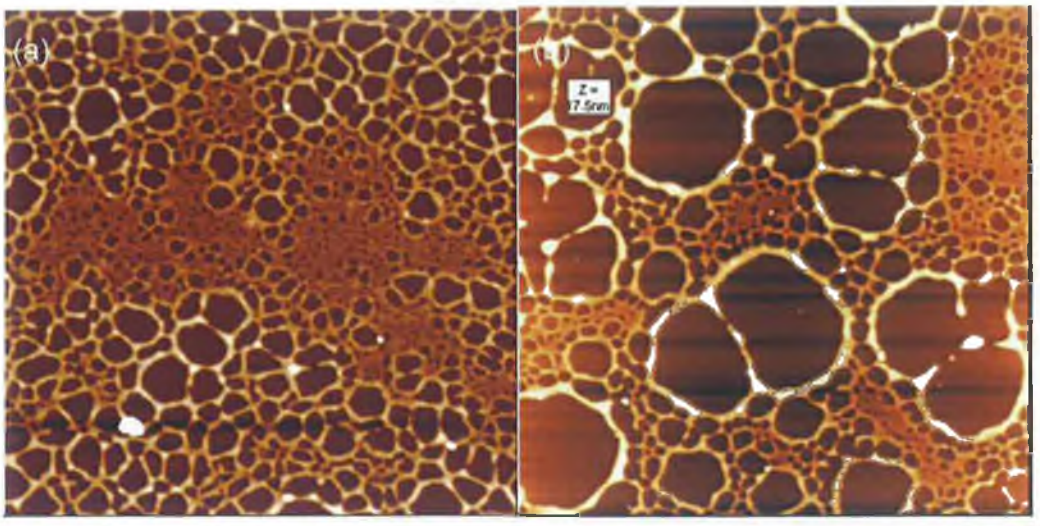

Figure 5.17 *Tapping mode AFM height data showing foam networks within other networks;* ***(a)*** *5.020μm x 5.020μm z range 15nm;* ***(b)*** *10μm x 10μm z range 17.5nm.*

Sample	Polygon Number	<n>	μ_2	S	a
A	1208	6.0	0.94	1.37	0.99
B	795	5.99	1.1	1.43	0.98
C	1121	6.0	1.0	1.44	1.00

Table 5.1 *Statistical Crystallography data for organostannoxane cluster network data in Appendix B.*

5.3.2.2 Morphology as a Function of Concentration

The organostannoxane cluster deposition from solution has also been investigated as a function of the concentration of cluster molecules in toluene. In Figures 5.18 and 19 a systematic increase in the concentration of solution has been employed. In Figures 5.18 (a-b) the solution is very dilute and the cellular networks described above are not observed. These images may be compared with Figures 5.18(c-d),

where as the concentration of the solution increases the thin film morphology begins to resemble the cellular networks observed in Figure 5.9.

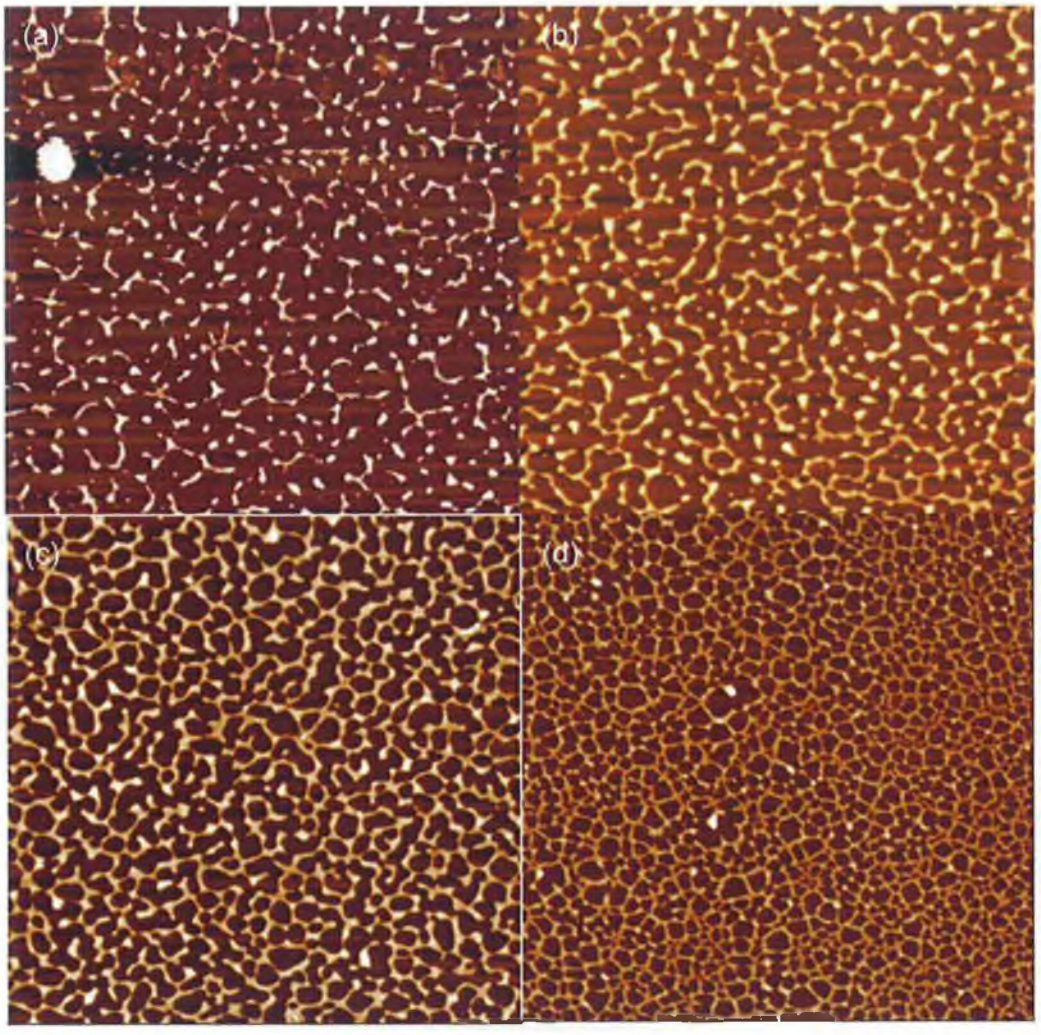

Figure 5.18 *Tapping Mode AFM height data of* $[BuSn(O)OC(O)Fc]_6$ *deposited by spin-coating from toluene;* ***(a)*** *10μm x 10μm z-range 25nm;* ***(b)*** *6μm x 6μm z-range 11.27nm;* ***(c)*** *10μm x10μm z-range 17.5nm;* ***(d)*** *6.328μm x 6.328μm z-range 15nm.*

Figure 5.19 shows height data of the organostannoxane cluster thin films obtained by using increasingly more concentrated solution; in these cases the intercellular separation decreases to such a point that as shown in Figure 5.19 (d) more and more areas with nearly complete coverage are observed. Figure 5.20 shows AFM height

data for films deposited from solution employing a spin-speed of 2500rpm and using a very concentrated solution of molecules. The resulting images show films that do not form cellular networks and are up to 650nm in thickness. Also the thick films of the organostannoxane cluster do not dewet the underlying silicon substrate. This dewetting phenomenon (which is observed for the thin spin cast films) will be discussed and explained in section 5.3.2.4. These data highlight the dependence of the self-assembly of the organostannoxane cluster on the parameters employed to deposit the molecules from solution.

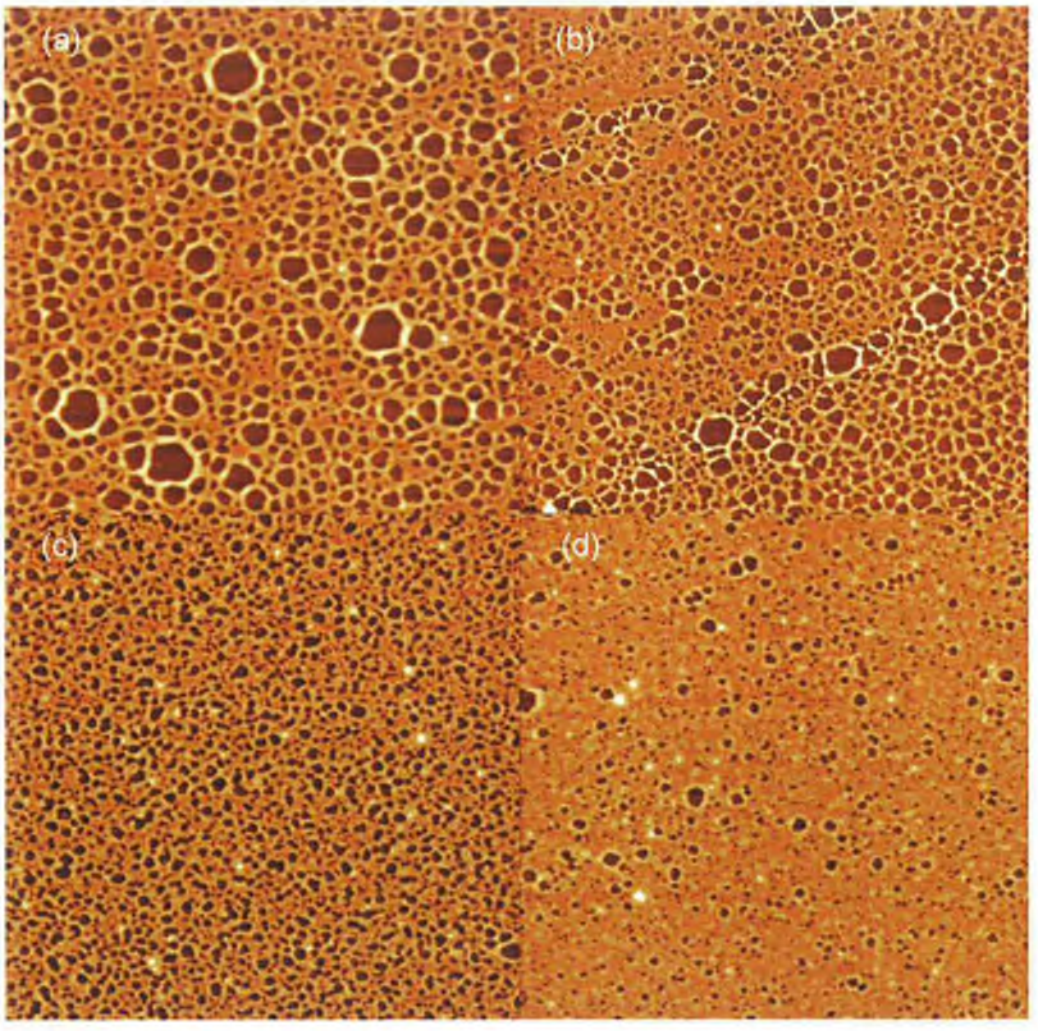

Figure 5.19 *Tapping Mode AFM height data of $[BuSn(O)OC(O)Fc]_6$ deposited by spin-coating from toluene;* ***(a)*** *6μm x 6μm z-range 13.759nm;* ***(b)*** *8μm x 8μm z-range 10.606nm;* ***(c)*** *8μm x 8μm z-range 10.905nm;* ***(d)*** *8μm x 8μm z-range 7.175nm*

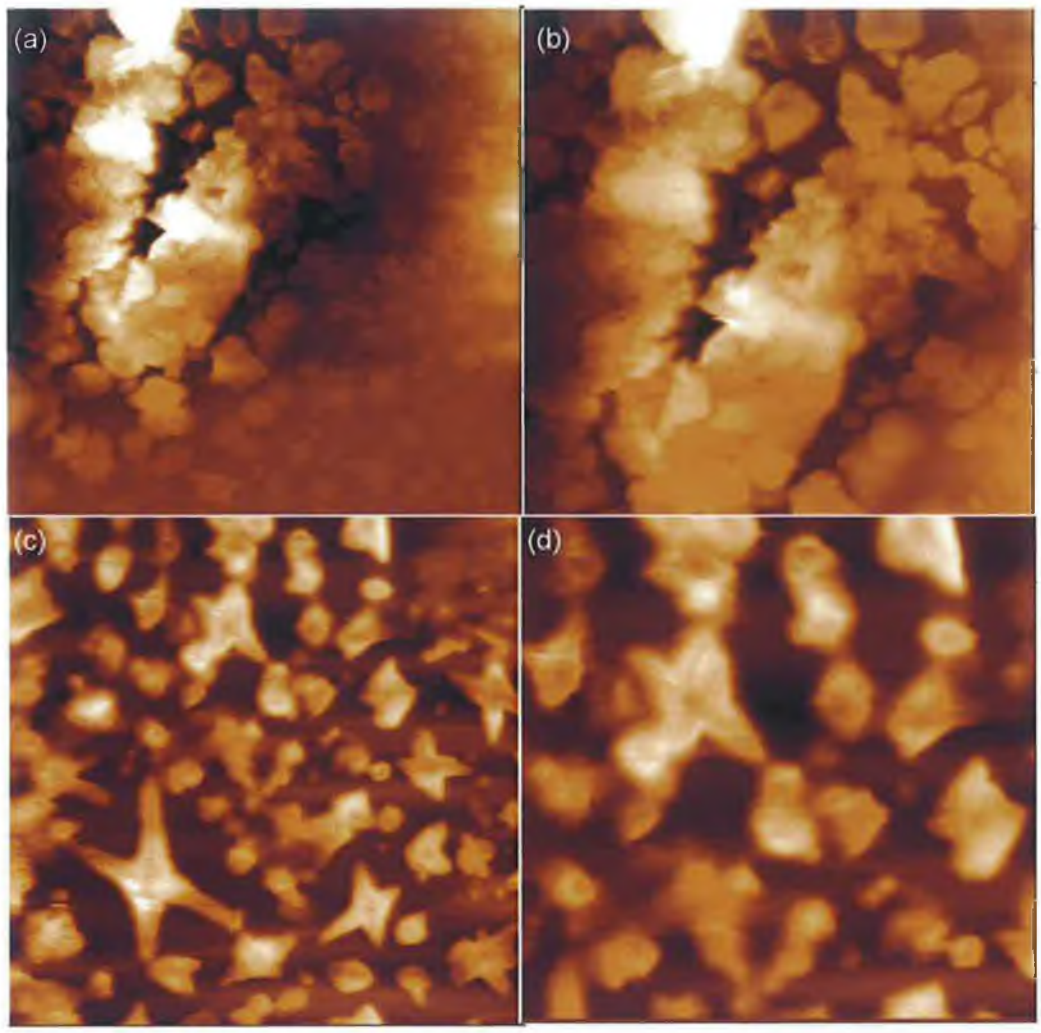

Figure 5.20 *Tapping Mode AFM height data of $[BuSn(O)OC(O)Fc]_6$ deposited by spin-coating from toluene;* ***(a)*** *10μm x 10μm z-range 650nm;* ***(b)*** *7.051μm x 7.051μm z-range 1μm;* ***(c)*** *10μm x 10μm z-range 125nm;* ***(d)*** *5.767μm x 5.767μm z-range 125nm .*

5.3.2.3 Morphology as a Function of Solvent

The cellular networks described so far result from the spin-coating of the organostannoxane cluster molecules from toluene. When identical sample preparation conditions were employed with the exception that dichloromethane was used as the solvent, cellular networks are not observed. Figure 5.23 shows the tapping mode AFM height data. The clusters aggregate in the presence of this solvent. The aggregates have an average height of 45nm ± 10nm. Roughness analysis of the aggregates shows an R_{rms} value of 12.53nm.

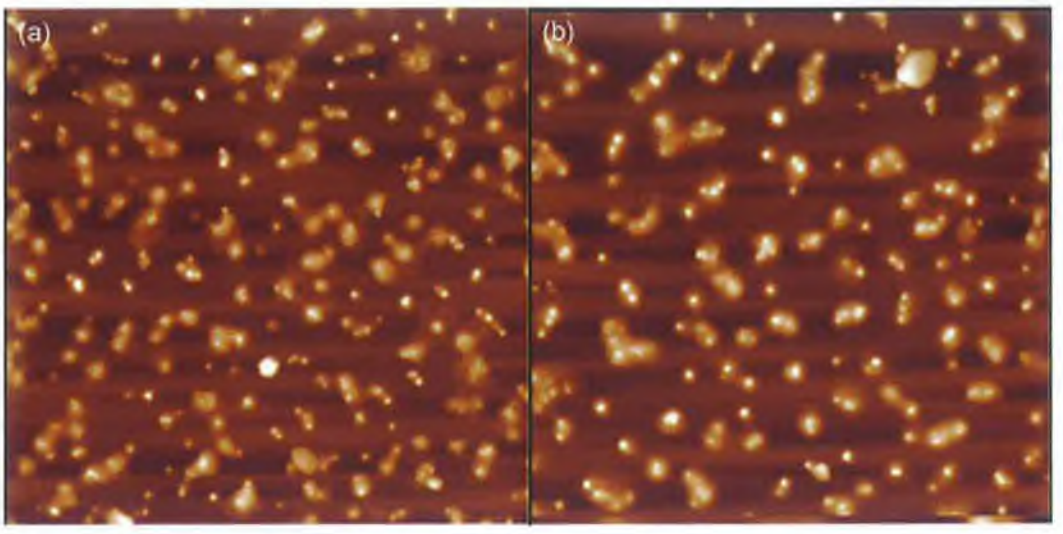

Figure 5.21 *Tapping Mode AFM height data of* $[BuSn(O)OC(O)Fc]_6$ *deposited by spin-coating from dichloromethane;* ***(a)*** *6μm x 6μm z-range 125nm;* ***(b)*** *2.748μm x 2.748μm z-range 150nm.*

The morphology observed from toluene and from dichloromethane suggests that the structures formed are strongly solvent dependent. One solvent parameter that plays an important role in spin-coating is the vapour pressure. At room temperature toluene has a much lower vapour pressure than dichloromethane (28.5Torr vs. 350Torr). This plays a role in the structure of the films as the high solvent evaporation rate of dichloromethane suppresses cellular network formation. If the simplified three-step model of the spinning process described in section 3.3.2 is applied to this process; first a solution is dropped onto the substrate which is then started spinning. During this step most of the solution is centrifuged off, leaving a thin layer on the substrate. In the second step the layer thins due to fluid flow until the evaporation of the solvent becomes important. The evaporation increases the viscosity of the solution and slows the shear thinning of the film. During the third step, solvent is lost only by evaporation, freezing in a thin film. The resulting thickness is controlled by the initial concentration used for the spin coating, and the surface topography is determined by the solvent used [42]. Heterogeneously nucleated holes may grow and cover the

substrate before the solvent is thin enough for the mechanisms that cause network formation to set in.

Moriarty at al. report a similar study where gold nanocrystals spin-coated onto silicon from toluene form cellular networks. When the crystals are deposited from hexane, however, networks do not form [33]. Instead, structures described as '*isolated droplets*' and *'labyrinthine patterns*' are reported. Ge at al. also reports similar patterns which have been produced via a spinodal phase separation mechanism involving spinodal decomposition [43]. It seems a necessity therefore to establish if the resulting spin-cast organostannoxane cluster films from toluene are stable, unstable or metastable. Other questions which also follow include; do the films dewet the silicon substrate? What is the dewetting mechanism? Is it related to conventional nucleation and spreading of holes or is a spinodal process involved? These questions are investigated in the next section.

5.3.2.4 Wetting and Dewetting of Organostannoxane Cluster Thin Films

Thin adsorbed films play a central role in processes and applications ranging from protective/lubricating coatings, to optoelectronic device technology, to the functionalisation of solid surfaces for biomedical applications. Thin film stability is therefore an issue of scientific significance. If a liquid completely wets a surface it forms a perfectly homogeneous coating. Liquids that do not naturally wet a substrate may be forced to form a continuous uniform film using different coating techniques such as the formation of the cellular networks in this work by deposition via spin coating. Films produced in this way are generally not stable and if permitted to reach their thermodynamic equilibrium the films may become more unstable and eventually break up or rupture. This rupturing process is termed 'dewetting', and may lead to different types of film patterns, depending on the mechanism involved.

Understanding the causes of dewetting opens routes to improve the stability of such films [44], and in some cases may be controlled to produce technologically interesting structures [45]. Stange at al. report the dewetting of polystyrene films from non-wetting silicon substrates [46]. Four stages of dewetting of a thin liquid film are described (Figure 5.22):

i). Dewetting begins with the nucleation of dry patches or holes in a film.

ii). This is followed by the growth of these holes. A narrow size distribution of holes is typically observed. As the holes begin to grow they impinge on each other forming a ribbon of material between them.

iii). The onset of hole coalescence distinguishes advanced dewetting from the early stages in which growing holes remain isolated from each other.

iv). Complete dewetting results in the formation of cellular patterns composed of liquid droplets. This pattern is formed by coalescence of holes followed by the break-up of the ribbons into isolated droplets.

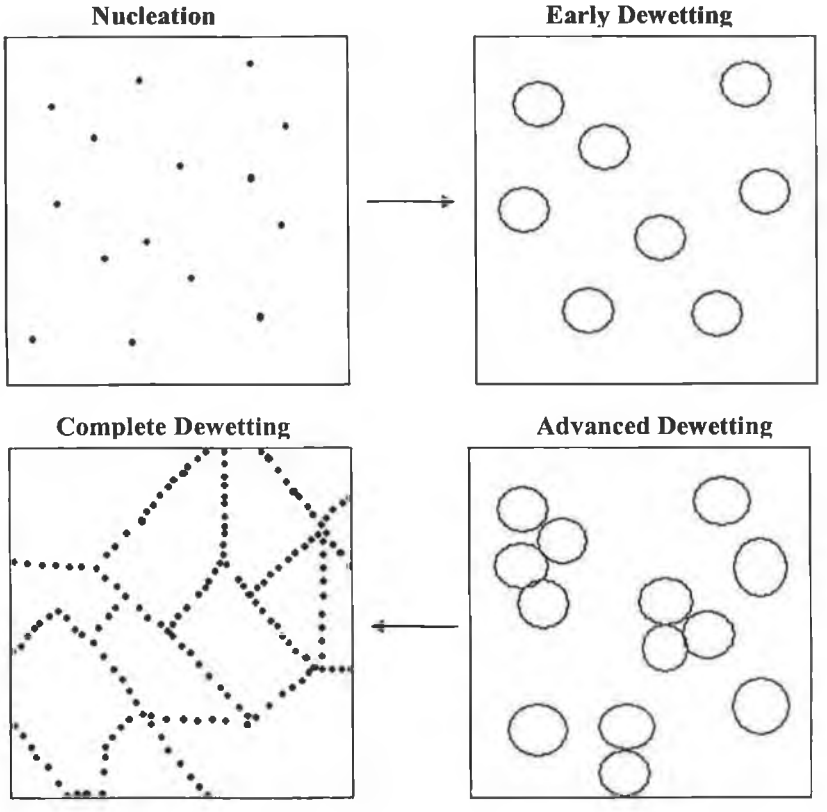

Figure 5.22 *The stages of dewetting of a thin liquid film as described by Stange at al. [46].*

In a thin film, dewetting may be characterised by the occurrence of dry spots and their growth. There are different modes of dewetting which cause various patterns. The aim of this work is to determine whether the cellular network structure, which arises from the coalescence of the rims of expanding dewetting holes [47,48], occurs from a dewetting process derived from an intrinsic surface instability (i.e. a process termed spinodal dewetting), or from a heterogeneous or thermal nucleation mechanism.

The spinodal dewetting process has been reported to drive the break-up of liquid crystals, homopolymer, and copolymer films on silicon substrates [46,49,50]. Described in the literature by Brochard-Wyart and Daillinat, and Reiter, spinodal dewetting involves the amplification of thin film thickness fluctuations via long range Van der Waals forces, which lead to the break-up an adsorbed molecular film [48,51]. Spinodal dewetting may be termed an 'intrinsic rupture mechanism'. This process is analogous to spinodal decomposition in fluid mixtures, where the thickness fluctuations correspond to composition fluctuations in the fluid system. Spinodal dewetting is distinctly different from the thermal or heterogeneous nucleation of holes in a metastable film. Dewetting in the latter mode is typically initiated by nuclei in the form of, for instance dust particles, or other surface heterogeneities, and may also be described as an 'extrinsic rupture mechanism'.

A more detailed AFM study of as-prepared spin cast thin films that results in a cellular morphology similar to that in Figure 5.9 and, annealed spin-cast thin films has been carried out to address these issues and will be presented next. The important characteristic of spinodal dewetting and spinodal decomposition which is investigated, is the presence of a preferred length scale in the film rupture/phase separation process. This presence of a dominant length scale has significant implications for controlled self-assembly.

For the network thin films it is useful to know which wavelength imparts the greatest influence to the surface topography. In a dynamical instability process such as spinodal dewetting there exists a critical wavelength, the corresponding amplitude of which grows the fastest, and thus determines the dominant wavelength (q). An important characteristic of spinodal dewetting is that the positions of the dewetting holes should be strongly spatially correlated as a result of this critical wavevector associated with the instability [48]. For a nucleation mechanism, the spatial correlation is absent, and the hole positions should follow a Poisson distribution.

As a first step in the determination of the degree of interhole correlation, the in-plane correlation length of the surface undulations ($\Lambda(t)$) is obtained from the radial average of the two-dimensional Fourier transform (FT) where;

$$\Lambda(t) = \frac{2\pi}{q} \tag{5.8}$$

The Fourier transfrom of the network image in Figure 5.23 may be examined for the presence of a preferred wavevector. As shown in the inset of Figure 5.24, a distinct ring is observed in the two-dimensional FT. Similarly a clear peak appears in the radially averaged transform. This is strong evidence for spatial correlations in the hole positions. The presence of a peak in the radial average of the 2D-FT at a wavevector, q, of $\sim 25\mu m^{-1}$, suggests the presence of an intercell correlation length of $\sim 2\pi/25$ μm i.e., ~ 250nm.

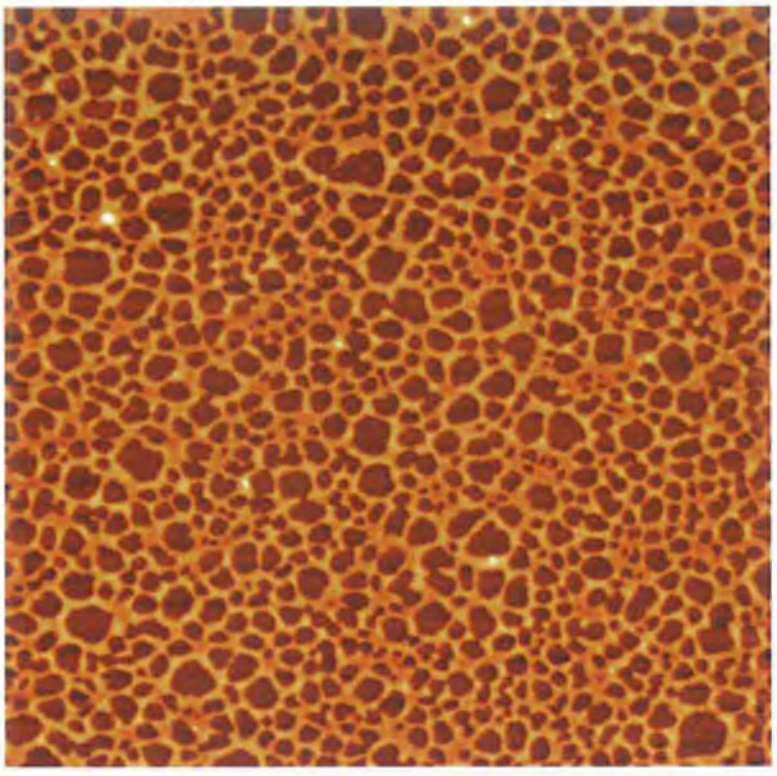

Figure 5.23 *Tapping Mode AFM height data of $[BuSn(O)OC(O)Fc]_6$ deposited by spin-coating from toluene; 8μm x 8μm z-range 15nm.*

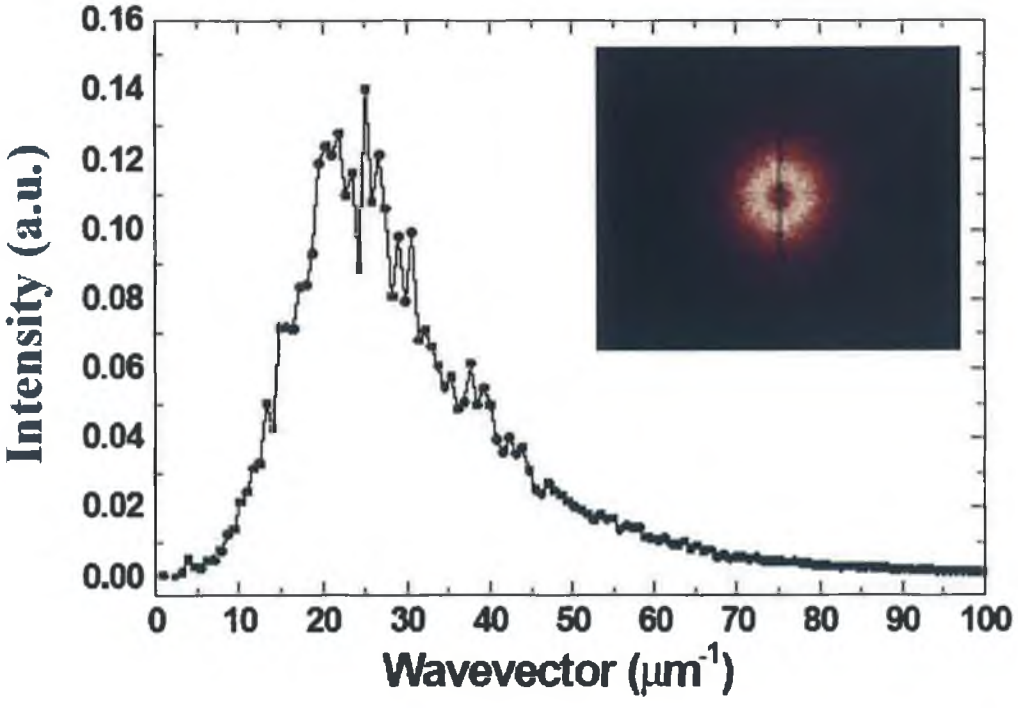

Figure 5.24 *A radial average of a 2D FT of the image shown in Figure 5.23. The 2D FT is shown in the inset.*

To provide a more quantitative distinction between correlated and uncorrelated dewetting centres, a powerful statistical geometry technique based on Minkowski functions may be employed. [52]. Jacobs at al. reports the analysis of thin film dewetting patterns using Minkowski functionals in two dimensions [53]. Minkowski functionals are related to important morphological measures. In two dimensions, these are the covered area F, boundary length U, and Euler characteristic χ, of the pattern of interest [54]. While the covered area and perimeter length are easy-to-visualize geometrical quantities, the third Minkowski measure - the Euler characteristic, χ - is a key topological measure describing the connectivity of a pattern. In two dimensions - and on a binary image consisting of black and white pixels-the Euler characteristic is the number of separate objects comprising interconnected black pixels minus the number of enclosed white regions [52]. These functionals provide statistically unbiased descriptors which contain features of n-point correlation functions at any order n [54].

Using an efficient algorithm based on that put forward by Michielsen and Raedt, [54], the behaviour of the morphological Minkowski measures for a 2D distribution of points whose coordinates are given by the centres of the cells shown in Figure 5.23 [55]. Specifically, to determine the degree to which the cell centres in Figure 5.23 deviate from the Poisson distribution of points expected from a conventional nucleation-driven dewetting scenario, the following procedure was adopted: To each "germ" (i.e., cell centre - see inset to Figure 5.25 (a)) which has an edge length of 1, a square "grain" of edge length $2r + 1$ (where r is a positive integer whose initial value is 1) was attached. Consequently, and as described in detail by Michielsen and Raedt, [54] the point pattern arising from the cell centres is transformed into a pattern of square grains. The grain size r - or, as in Figure 5.25,

the "normalized" quantity $x = \frac{r}{L}$, where L is the mean germ separation - was systematically varied and the changes in the three Minkowski functionals (see Figure 5.25) were compared to those expected for a Poisson distribution. Essentially the scale-dependent morphological features of the network coverage are explored by varying the radius of the disk and calculating the Minkowski measures of the coverage as a function of r.

Considering first the x-dependent variation in Minkowski functionals for a Poisson distribution of points (represented by the solid lines in Figure 5.25a-c), for small x, the grains are isolated. This produces a small covered area, a small boundary length, and a positive Euler characteristic. As the grain size is increased, the degree of overlap rises in a characteristic manner until the entire 2D plane is covered with black pixels producing a "saturated" covered area. The boundary length curve exhibits a clear peak at intermediate values of x, while the Euler characteristic turns negative. The minimum in the Euler characteristic curve (Figure 5.25 (c)) arises from the highly interconnected and "void-ridden" structure present at intermediate x values. The x-dependent behaviour of the Minkowski functionals for the distribution of points with coordinates given by the cell centres in Figure 5.23 is markedly different. In each case - area, perimeter, and Euler characteristic – the curve for the organostannoxane cluster film centres (open circles-solid lines in Figure 5.25a-c) deviates significantly from that for the Poisson distribution. It is particularly interesting to note that the Euler characteristic decreases much more rapidly for a Poisson distribution at low values of x than for the distribution of points derived from the dewetting centres in the organostannoxane cluster film. To highlight more clearly the deviations from a Poisson distribution, Figure 5.25d-f shows graphs of the organostannoxane cluster film-related Minkowski functionals minus the

corresponding Poisson-derived functional. That the distribution of dewetting centres in the organostannoxane cluster film is far removed from that expected for a Poisson distribution of points is clear from these graphs. One might now argue that as the spatial distribution of the dewetting centres does not follow a Poisson distribution, there is clear evidence for spinodal dewetting of the organostannoxane film.

However, a number of groups [56,57] have recently pointed out that for the "inverse" problem of droplet (rather than hole) growth on a substrate, deviation from a non-random spatial distribution of domains can occur simply by the coalescence of close pairs of droplets. Coalescence "wipes out" the clustering inherent in a Poisson point distribution and introduces a minimum nearest-neighbour distance. This, in turn, produces a spatial correlation length in the droplet - or, in this case, hole-distribution. More detailed morphological comparisons of dewetting centre distributions, coupled with simulation studies, are required to address this issue.

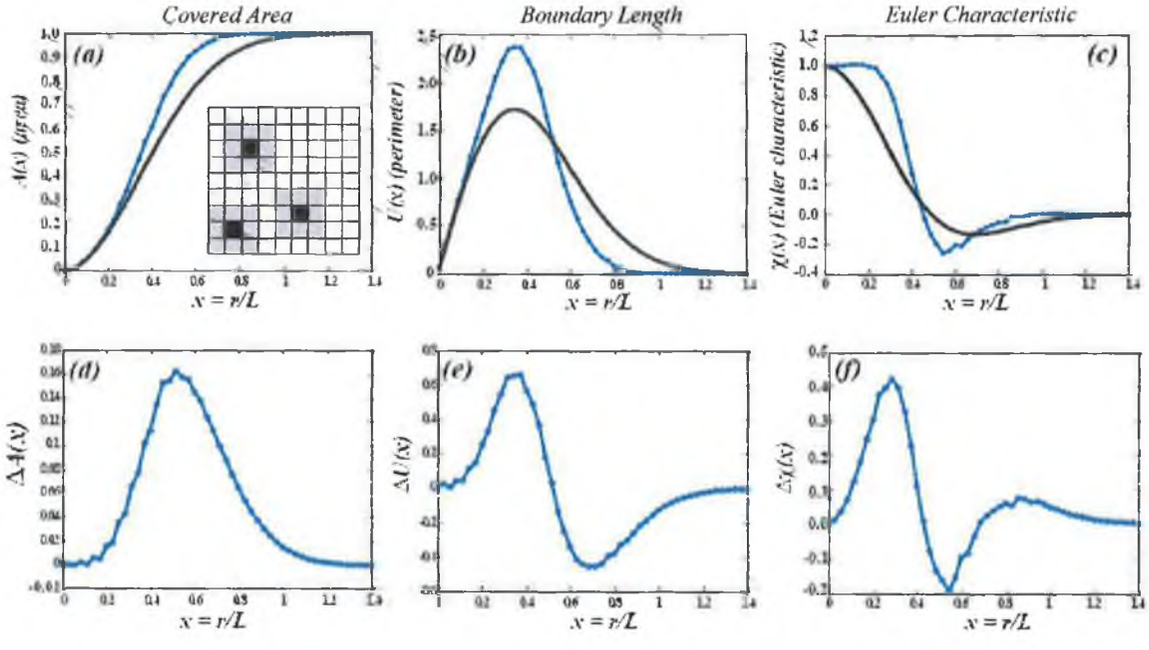

***Figure 5.25 (a-c)**; Minkowski functionals for a Poisson distribution of points and a point set based on the coordinates of the dewetting cell centres for the image shown in Figure 5.23 (solid lines and filled circles/solid lines, respectively). In each case, the functionals are plotted as a function of x, the normalized grain size. The inset to (a) depicts the difference between germs (the black pixels) and grains (grey pixels) centred on the germs. **(d-f)**; Difference between the organostannoxane - and Poisson-derived result for each 2D Minkowski functional.*

It is important to highlight at this point that the organostannoxane cluster films studied have been produced via spin-coating. This is an exceptionally complicated, far-from-equilibrium process that has been considered by Lawrence [58] to comprise three consecutive phases. Previously discussed in section 3.3.2 following the initial transient phase where fluid inertia, the Coriolis force, and surface tension are the dominant effects, the second phase of the process involves a balance between viscous and centrifugal forces. In this secondary phase, the dynamics are driven by fluid flow, whereas in the final phase (phase III), the fluid viscosity is so high the evolution of the film is largely driven by solvent evaporation. Unfortunately, the AFM measurements in this study - which provide little or no information on the film growth dynamics-cannot address the question of whether the viscosity of the fluid plays a large role in defining the final film morphology observed. While one might speculate that the absence of macroscopic spatial uniformity in the organostannoxane cluster films suggests that phase II dynamics are important, a "star-like" pattern which has previously been identified as the signature of hydrodynamic instabilities [59] are not observed at the centre of rotation. An optical scattering study may provide some insight into the influence of the spin-coating process on the film morphology.

Having quantitatively ascertained that the morphology of as-cast organostannoxane cluster films on native oxide-terminated Si(111) substrates is primarily determined by the presence of a well-defined correlation (but not necessarily spinodal) wavelength, the dynamics of dewetting is now considered. A comprehensive series of annealing studies of organostannoxane cluster thin films on (both H_2SO_4:H_2O_2- treated and "out of the box" solvent-rinsed) silicon samples has been carried out to probe whether the evolution of the film morphology is consistent with models of spinodal dewetting.

Brochard and Dalliant [51] have put forward a variant of Vrij's [60] original capillary wave instability model to treat spinodal dewetting of thin liquid films from solid substrates. Both the Brochard and Dalliant and the Vrij models predict that thickness fluctuations of the film can be approximated by the following expression:

$$z(x,t) = h + \delta h e^{iqx} \tag{5.9}$$

Here, the fluctuation amplitude, δh, is given by:

$$\delta h = \delta h_0 e^{t/\tau} \tag{5.10}$$

Where τ is the relaxation time and $1/\tau$ is the growth rate, and δh_0 is the initial fluctuation amplitude. The x coordinate is associated with displacements parallel to the surface, and q denotes the wavevector associated with the wave instability. In this model, thermally driven thickness fluctuations are exponentially amplified if their associated wavevector q, is less than some critical wavevector, q_c, but are attenuated if $q > q_c$. Importantly, if one now monitors the distribution of wavevectors by, for example, plotting the radially averaged Fourier transform of AFM images of the thin film taken as a function of annealing time, then it is possible to determine a value for q_c by identifying a "crossover" wavevector in the Fourier spectra. Furthermore, the position of the peak in the radially averaged transform shifts to lower wave-numbers as a function of annealing time according to a power law whose exponent yields information on the type of underlying destabilization kinetics. These types of analyses have been successfully adopted by Xie et al. [61] in the analysis of dewetting of polymer films from silicon substrates.

Figure 5.26 is a series of representative tapping mode AFM height images (H_2SO_4:H_2O_2-treated) for the organostannoxane cluster film annealed for progressively longer times at a temperature of 75 °C. Figure 5.26 (a) illustrates the

morphology of the film directly following spin-casting with no annealing. Figures 5.26 b-d are AFM height images taken following annealing periods of 1, 6, and 12h, respectively. These images are largely representative of the macroscopic morphology of the film. The in-plane peak wavevector as a function of annealing time is measured by acquiring similar AFM images at a number of well separated regions (spaced by millimetres) on the organostannoxane film and subsequently calculating the radially averaged Fourier transform. Figure 5.27 shows the corresponding radially averaged Fourier transforms for Figure 26a-d. From the Fourier transforms of the AFM data, it is extremely problematic to systematically and reproducibly define a crossover wavevector (q_c) above (below) which thickness fluctuations decay (grow) in time.

Figure 5.28 shows the evolution of the surface roughness as a function of the annealing time. The error bars represent ± 1 standard deviation for a set of 30 measurements taken at macroscopically separated regions of the film. Although it is possible to fit the early stage annealing data with an exponential function, as expected on the basis of the spinodal dewetting theory, the magnitude of the error bars means that a number of other functional forms may also be used as a fit to the data. The inset of Figure 5.28 shows a plot of the peak wavevector as a function of the annealing time. Representative error bars for a number of points are shown. Within these error limits no systematic change of the peak wavevector is observed. Within the range of annealing times and error limits associated with this study we do not recover the power-law dependence of wavevector on annealing time (i.e. there is a lack of power law dependence). This is different to results reported in studies of polymer dewetting from silicon substrates in which power law dependence has been observed [50,61].

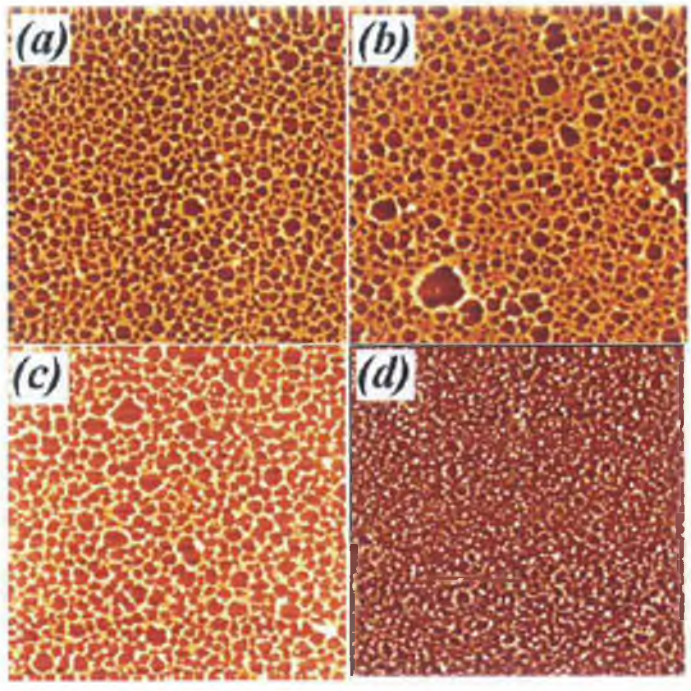

Figure 5.26 *8μm x 8μm tapping mode AFM height data for the organostannoxane cluster thin film annealed for progressively longer times at a temperature of 75°C;* ***(a)*** *No annealing:* ***(b-d)*** *AFM images taken following annealing periods of 1, 6, and 12 h, respectively.*

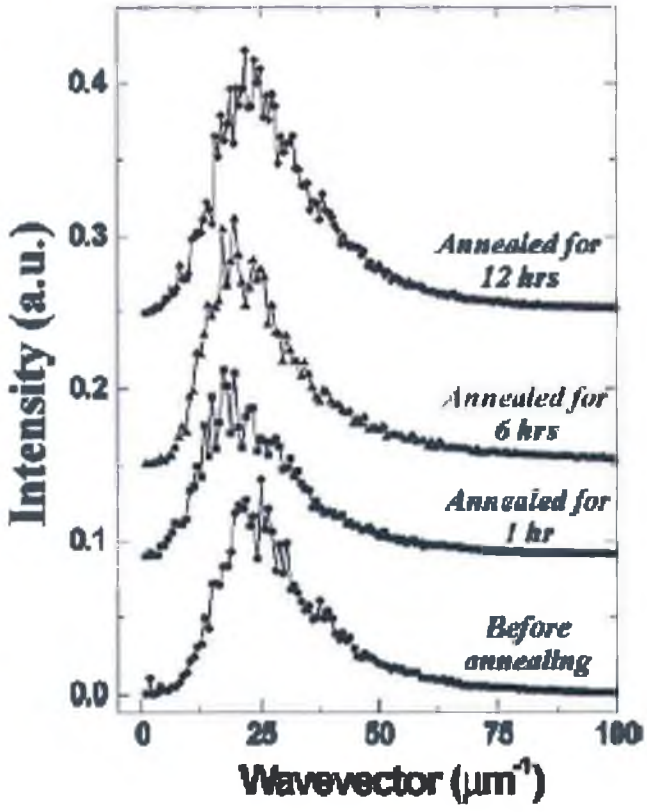

Figure 5.27 *Radially averaged 2D Fourier transforms for the images shown in Figure 5.26.*

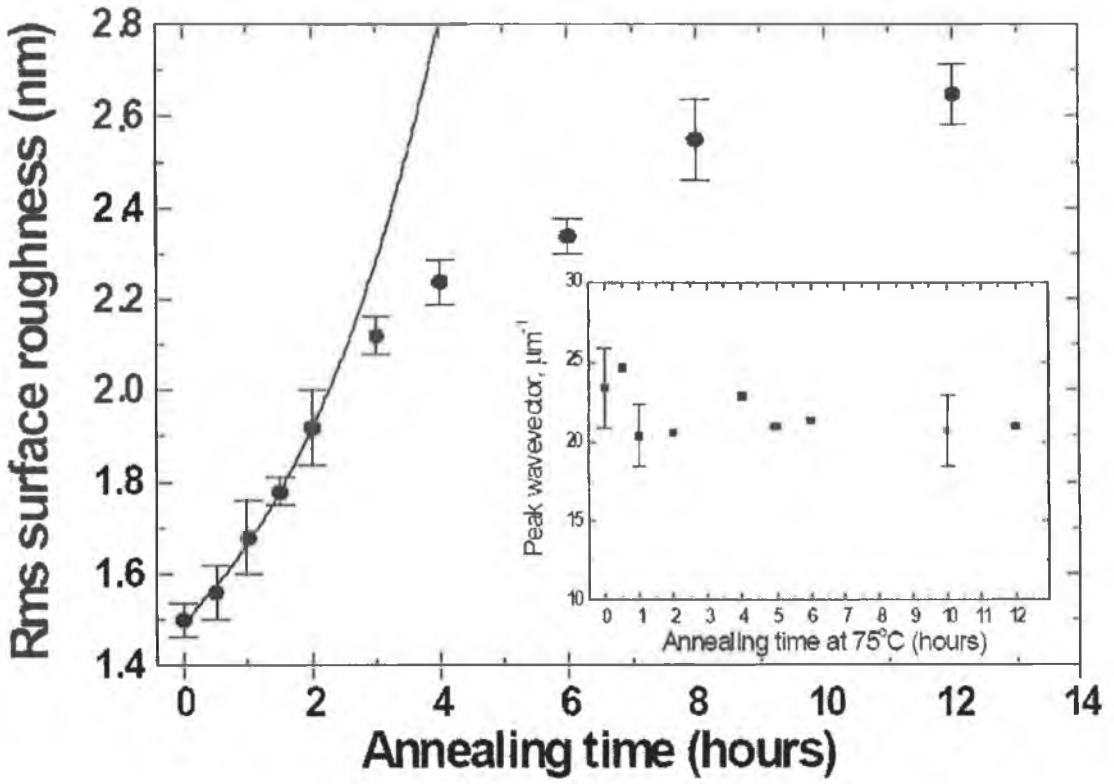

Figure 5.28 *Evolution of surface roughness as a function of annealing time. Inset: Plot of the peak wavevector as a function of annealing time.*

These difficulties in interpreting the experimental data in terms of spinodal dewetting theory arise in part from variations in organostannoxane cluster film structure from region to region across the substrate sample. Morphological variations across the film substantially increase the magnitude of the error bars (shown as 1 standard deviation) on the data points and render detailed comparison with theory difficult. The experiment was repeated many times (See Appendix C for images) with a number of samples in an identical manner. The morphological variations observed as a function of position on the sample were comparable from sample to sample for H_2SO_4:H_2O_2-treated silicon substrates. Substantially higher levels of film inhomogeneity and sample irreproducibility were observed for substrates that were simply solvent-rinsed. Dynamic contact angle measurements show that the wetting properties of the silicon substrate were dramatically affected by the H_2SO_4:H_2O_2

treatment. For solvent-rinsed samples, the contact angle was 45° ± 5°, whereas the sulphuric acid-peroxide treatment reduces the hydrophobicity of the surface so that the contact angle was 5° ± 5°.

However, it is also important to note that the initial (i.e., preannealed) film is associated with a morphology where the dewetting holes already expose the underlying silicon substrate and the film roughness is rather close to one half the mean film thickness (2.1 nm). These initial conditions are somewhat different from, for example, previous studies of polymer dewetting from silicon [50], where the latter criterion was not met until the sample was annealed for some time. As already mentioned, Figure 5.28 shows the change in surface roughness as a function of annealing time for the organostannoxane sample shown in Figures 26(a). While it is possible to fit the early stage annealing data (up to~3h) with an exponential function - as expected on the basis of spinodal dewetting theory-note again that the error bars are relatively large (and derive once more from morphological variations as a function of lateral position on the sample surface).When coupled with the lack of systematic wavevector variation and the difficulties associated with defining the critical wavevector (q_c) discussed previously, it is clear that, although there is a strong spatial correlation in the positions of the dewetting centres (an important result in itself, given the recent uncertainty regarding spinodal dewetting for adsorbed polymer films on silicon [48]), a quantitative understanding of the dewetting dynamics of the organostannoxane film as a function of annealing time is currently lacking.

Further elucidation of the dewetting mechanism will necessitate extremely careful control of substrate heterogeneity and surface chemistry. In particular, substrate surface treatment plays a central role in controlling the dewetting dynamics. Figure 5.29 shows the evolution of morphology for a film of thickness comparable to

that discussed above but spin-cast onto a silicon substrate that was simply solvent treated. It is clear that, although the initial morphology is comparable to that of the H_2SO_4: H_2O_2-treated samples (compare Figure 5.26(a) with Figure 5.29(a)), the dependence of film morphology on annealing time is dramatically different. In particular, the break-up of the film into droplets via the Rayleigh instability [48,61] occurs on much shorter time scales for the untreated silicon substrate. In addition, sample-to-sample reproducibility and film homogeneity were substantially poorer for the untreated silicon substrates. The organostannoxane-substrate interaction potential is clearly particularly sensitive to minor modifications in silicon surface chemistry.

In conclusion, within the range of annealing times and annealing temperatures used in this study (30 min to 60 h, 75-125 °C) and for organostannoxane films ranging in thickness from ~4 to 10 nm, there is no consistent evidence for the evolution of surface wavevector expected from the theory of spinodal dewetting.

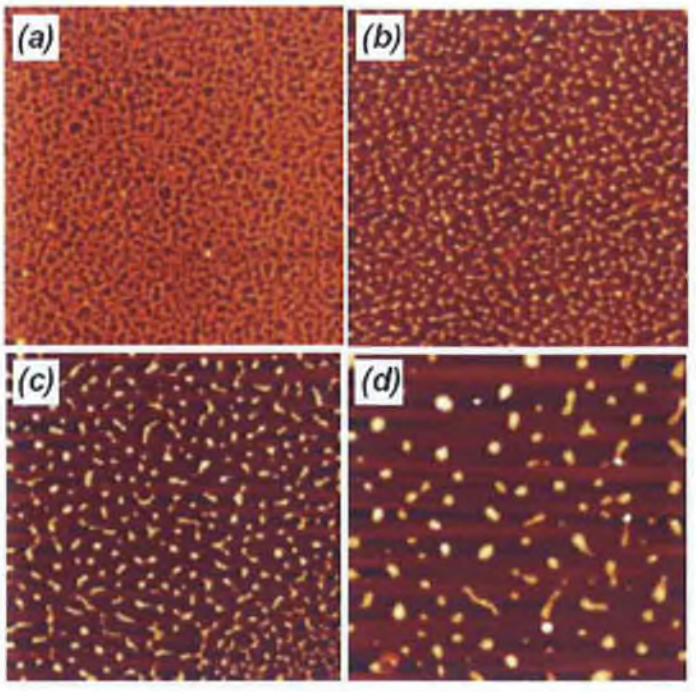

Figure 5.29 *8μm x 8μm tapping mode AFM height data for the organostannoxane cluster thin film on a silicon substrate which was simply solvent rinsed before spin coating, annealed for progressively longer times at a temperature of 75°C;* ***(a)*** *No annealing:* ***(b-d)*** *AFM images taken following annealing periods of 2, 4, and 8 h, respectively.*

5.3.3 Photoemission Spectroscopy Analysis.

In the next part of this chapter, a complementary technique, photoemission spectroscopy (PES), which is a highly chemically specific technique, investigates the solid-state electronic structure of the organostannoxane cluster using synchrotron radiation (SR) photoemission and resonant photoemission (RESPES). Resonant photoemission, particularly, is a sensitive probe of the density of states associated with the Fe and Sn atoms at the core of the organostannoxane and ferrocenyl units.

The morphology of the organostannoxane thin film used for the SR-based measurements is similar to the cellular networks described so far in this chapter (For example in Figure 5.9) and is shown in Figure 5.30. Note that, as for the dewetting studies described previously, the film structure is cellular in nature and thus exposes a substantial amount of the underlying silicon substrate. This coupled with the presence of adventitious carbon on the silicon substrates and the strong oxygen-derived photoemission signal from the SiO_2 layer make reliable analysis and interpretation of C 1s and O 1s spectra from the organostannoxane film extremely difficult. (These may still be found in Appendix D) Therefore, attention is focused on the acquisition of Fe- and Sn-derived core-level photoemission and RESPES spectra as these signals arise solely from the adsorbed organostannoxane clusters.

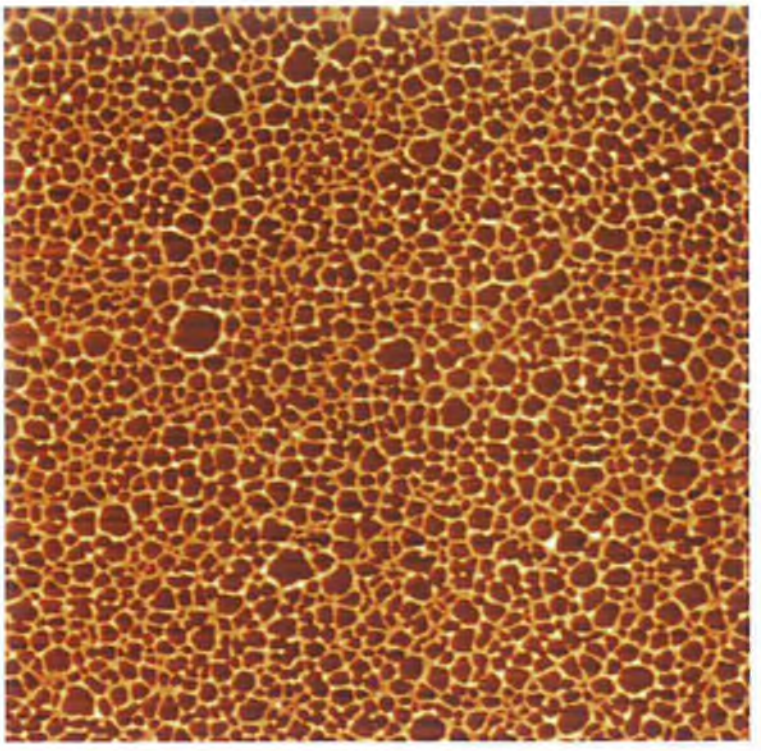

Figure 5.30 *Tapping mode AFM height image of organostannoxane cluster film used for photoemission. 8μm x 8μm, z-range =10.5nm.*

Valence band spectra ($h\nu$ = 60 eV) taken from a silicon sample with and without an adsorbed organostannoxane layer are shown in Figure 5.31. Although it is clear that the overall shape of the spectrum changes little when the organostannoxane overlayer is present and is dominated by the substrate valence band structure, an additional peak at a binding energy of 2 eV is observed. While this peak derives from the highest occupied molecular orbital (HOMO) of the organostannoxane cluster, the spectrum shown in Figure 5.32 yields little information beyond the energetic position of the HOMO below the Fermi level. This is because with conventional photoemission it is extremely difficult (in the absence of *a priori* knowledge) to identify the electronic character of the peaks in a valence band spectrum. Therefore, RESPES is used to probe the contribution of Fe and Sn to the frontier orbitals of the adsorbed organostannoxane cluster.

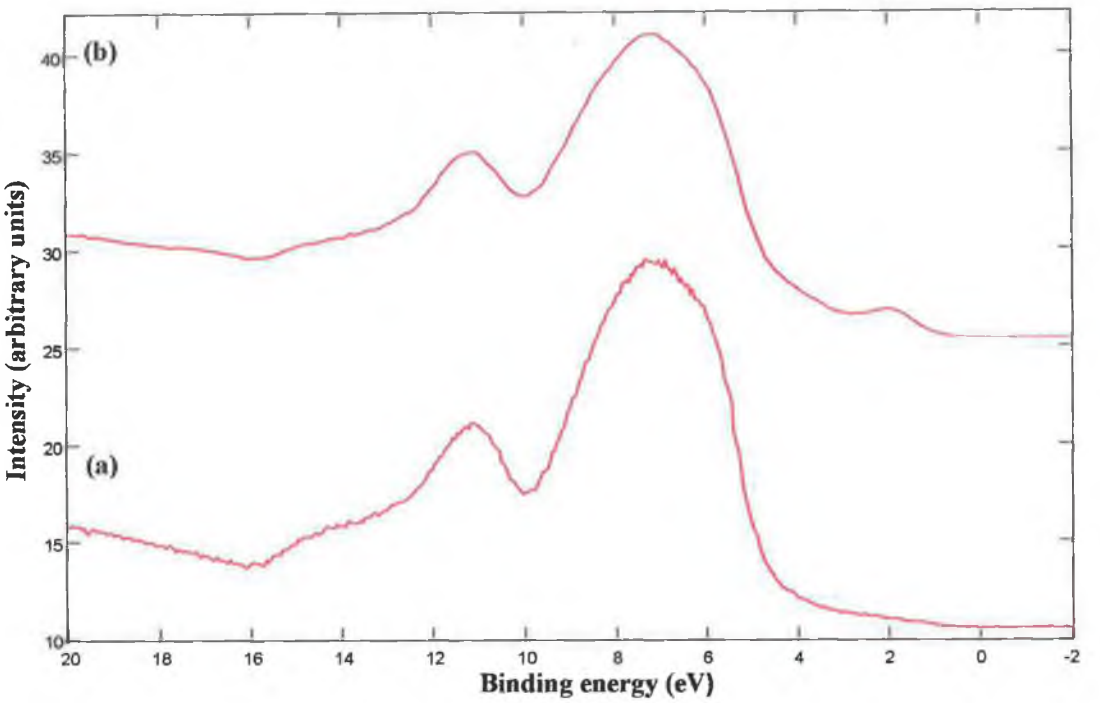

Figure 5.31 *Valence band spectra for* ***(a)*** *native oxide-terminated Si(111) substrate;* ***(b)*** *a thin organostannoxane film on the SiO_2/Si(111) substrate.*

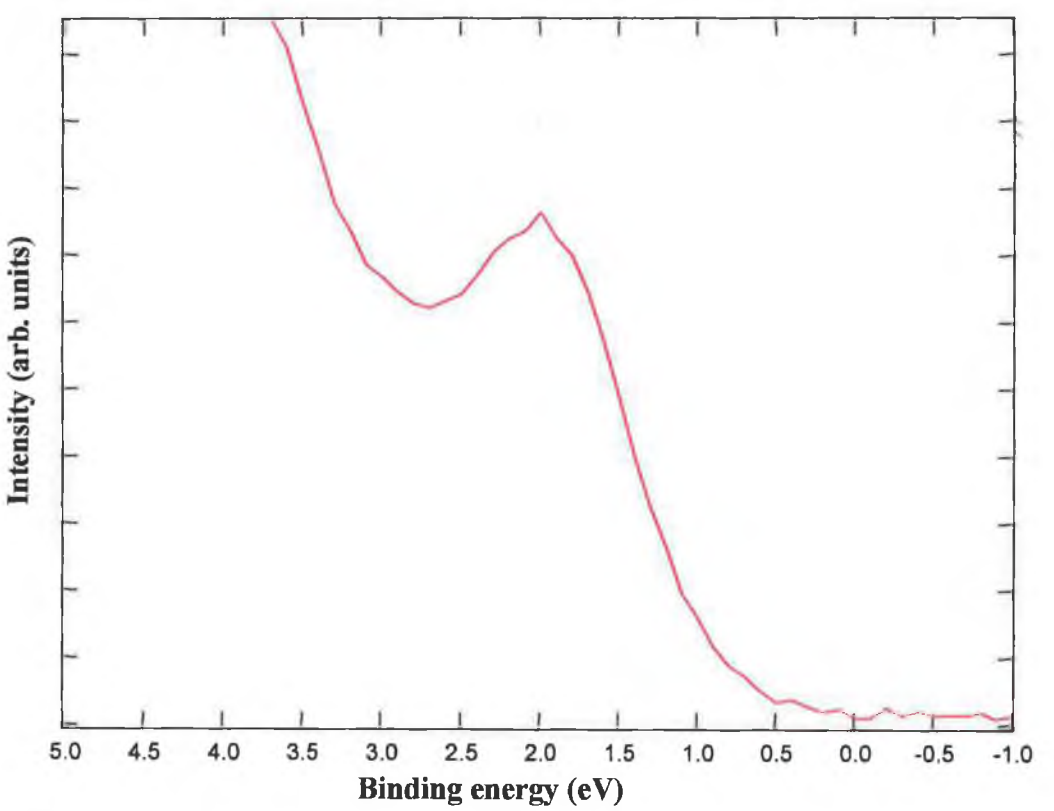

Figure 5.32 *The highest occupied molecular orbital (HOMO)-derived peak of the organostannoxane film visible from Figure 5.30.*

RESPES [62] exploits the resonant enhancement of the spectral intensity of valence states associated with a particular chemical element. This occurs when the incoming photon energy is tuned to the absorption threshold of a more strongly bound core-level of that element. In this way, one gains insight into the partial density of states. This process is sketched in Figure 5.33 (a). Following threshold excitation of a core-level electron, in this case, from an Fe 2p level into the unoccupied Fe 3d-derived density of states, non-radiant decay of an Fe 3d valence electron to the Fe 2p core-hole is accompanied by the emission of the originally excited core-level electron. Importantly, this process produces a single hole final state that is identical to that associated with direct valence band photoemission (as depicted in Figure 5.33(b)). Constructive interference between the two excitation channels leads to resonant enhancement of the spectral intensity of Fe 3d-related features in the valence band. RESPES therefore acts as an element-specific, localized probe.

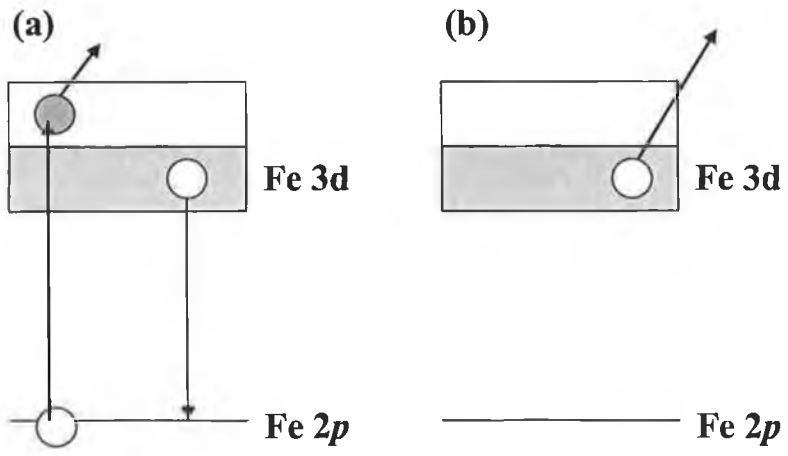

Figure 5.33 *Schematic illustration of the resonant photoemission process for Fe 2p → 3d RESPES*

Valence band spectra from the organostannoxane-SiO_2/Si sample for photon energies from 702 to 711 eV are shown in Figure 5.34. Below the Fe 2p threshold ($h\nu$ = 702 eV), the spectra are dominated by photoemission from the SiO_2/Si substrate. As the photon energy is increased toward the Fe 2p threshold, the Fe 3d states are enhanced in the photoemission spectrum. By subtracting the off-resonance spectrum from the

on-resonance spectrum, as shown in Figure 5.37, the Fe 3d-derived partial density of states may be extracted. Three broad features are identified in the difference spectrum shown in Figure 5.35: a shoulder at a binding energy of approximately 4 eV, an intense peak at 7.0 eV, and another shoulder at ~11 eV. (Note that the combined photon and electron energy resolution for the Fe 2p $\rightarrow$3d RESPES measurements was rather poor (>1 eV) due largely to the use of an analyzer pass energy of 90 eV to ensure sufficiently high electron count rates.)

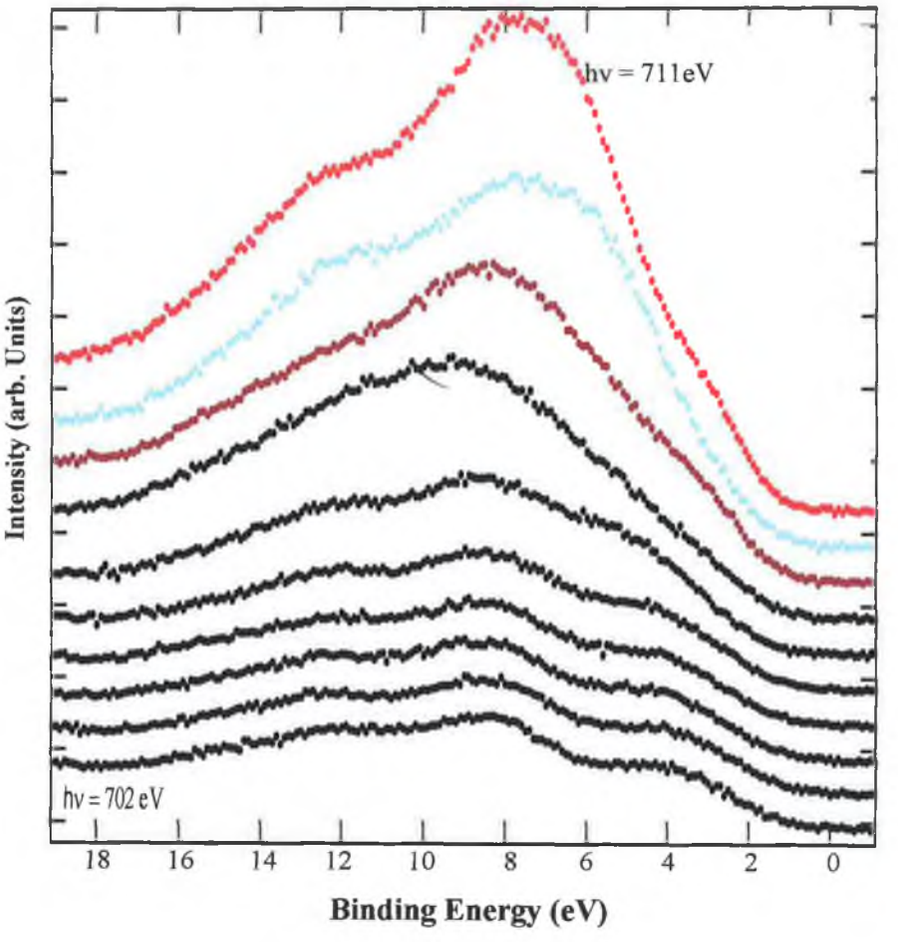

Figure 5.34 *On- resonance (upper spectrum at 711eV) and off-resonance (lower spectrum at 702eV) valence band spectra.*

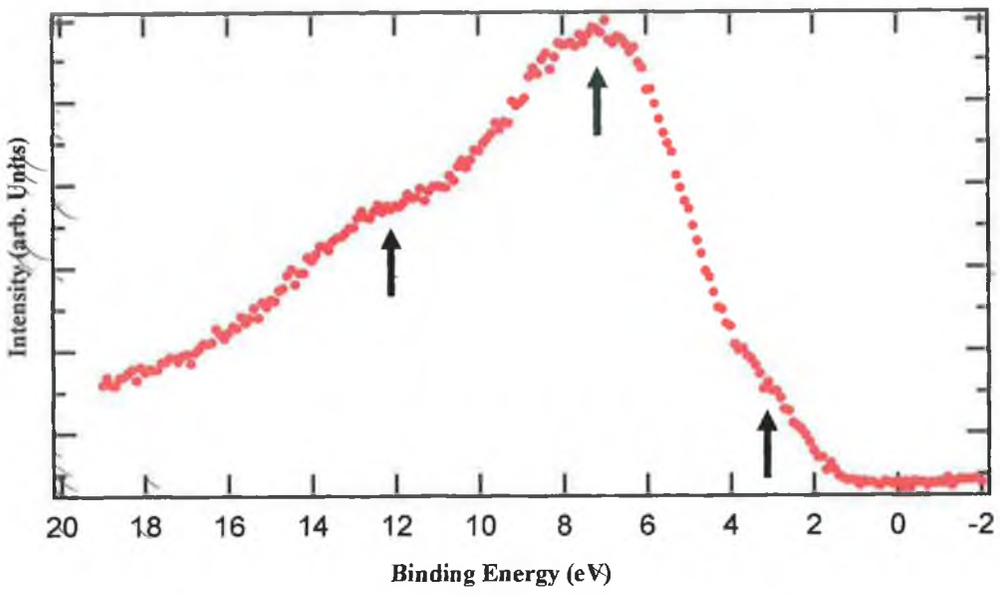

Figure 5.35 *On- resonance-off-resonance difference spectrum for data in Figure 5.30..*

It is now instructive to compare the Fe 2p→3d RESPES difference spectrum shown in Figure 5.34 with the calculated and experimentally measured density of states of ferrocene, the "parent" molecule of the ferrocenyl groups at the periphery of the organostannoxane cluster. A previous photoemission study reported by Driscoll at al. [63] on adsorbed ferrocene identified a series of peaks at energies of ~2.3, 4.4, 7.9, 12.3, and 17.2 eV, with respect to the Fermi level. Through comparison with ground-state theoretical calculations for ferrocene, the various peaks are assigned to their corresponding orbitals. Of particular relevance to the present study, however, Dowben et al. [64] have discussed the enhancement of the ferrocene molecular orbital- derived photoemission features in RESPES. They point out that the $4e_{1g}$, $7a_{1g}$, $6e_{1u}$, and $2e_{1g}$ features at binding energies of ~7.0, 10.9, and ~13 eV derive from molecular orbitals which have the highest level of π-Cp ligand orbital hybridization with Fe d states. The $8a_{1g}$ and $4e_{2g}$ molecular orbitals with binding energies of 4-5 eV and ~4 eV, respectively, have strong localized Fe 3d character.

Specifically, the $8a_{1g}$ and $4e_{2g}$ features arise from d_{z^2} and d_{xy},$d_{x^2-y^2}$ orbitals, respectively.

In Fe 2p→3d RESPES, it may be expected to observe strong enhancement of the photoemission features which arise from molecular orbitals having a large component of localized Fe 3d character. That intense resonances at ~4 and ~7 eV are observed in the difference spectrum shown in Figure 5.35 is strongly suggestive that these peaks derive from molecular orbitals with Fe 3d content similar to that of the $8a_{1g}$, $4e_{2g}$, and $4e_{1g}$ orbitals of the "parent" ferrocene molecule. The shoulder observed at an energy of ~11 eV in Figure 5.32 must also arise from orbitals with a high degree of Fe d character, and a family of orbitals ($3e_{2u}$, $3e_{2g}$, $3e_{1g}$, $5e_{1u}$, and $7a_{1g}$) have previously been identified as contributing to this spectral feature in studies of ferrocene adsorption on Ag(100) [65].

It therefore appears that the ferrocenyl groups at the periphery of the organostannoxane cluster retain a high degree of the electronic character of the ferrocene molecule. What is particularly interesting, however, is that with Fe 2p→3d RESPES no evidence is observed for a strong resonant enhancement of the HOMO-derived peak centred at ~2 eV below the Fermi edge (see Figure 5.31(b)). This suggests that the highest occupied orbital is associated with very little (localized) Fe 3d character.

A RESPES measurement involving photon energies crossing the Sn 3d edge was therefore carried out to probe whether Sn 5p states make a significant contribution to the HOMO of the organostannoxane cluster. The Sn 3d core-level photoemission spectrum is shown in Figure 5.36. Note that a less intense resonant enhancement for the Sn3d→5p RESPES than for the Fe 3d-related RESPES measurements is expected, as the electric dipole transition from a state of orbital angular momentum l to an l - 1 state is much weaker than $l \rightarrow l + 1$. It is clear from

Figure 5.37 that there is measurable resonant enhancement of the valence band in the near- Fermi level region when the photon energy is tuned to the Sn 3d threshold (*hv* = 488 eV). The apparent very high density of states at the Fermi level (0 binding energy) is a consequence of the poor energy resolution of the measurement and the associated high degree of broadening of the resonance structure.

Not withstanding the low energy resolution, however, the stronger contribution of the Sn partial density of states to the highest-lying molecular orbitals of the organostannoxane complex is readily apparent from Figure 5.37. In addition, a strong (and trivial) resonant enhancement of the HOMO feature - and the entire valence band spectrum - was observed for photon energies comparable to that of the C K edge (285 eV).

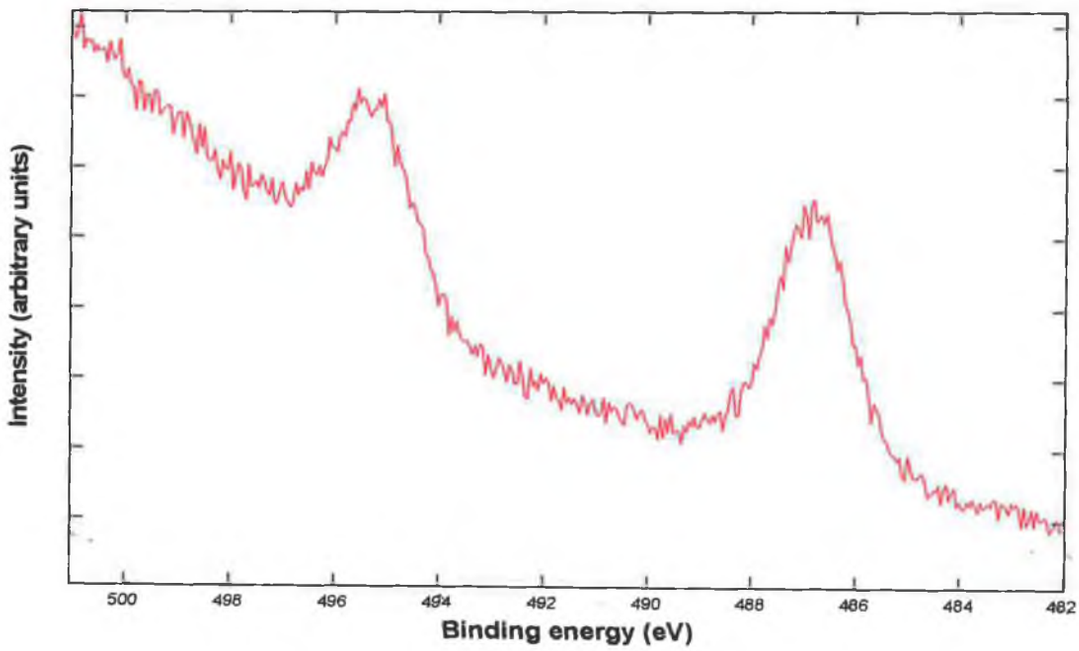

Figure 5.36 *Sn 3d core –level photoemission spectrum (hv = 550eV)*

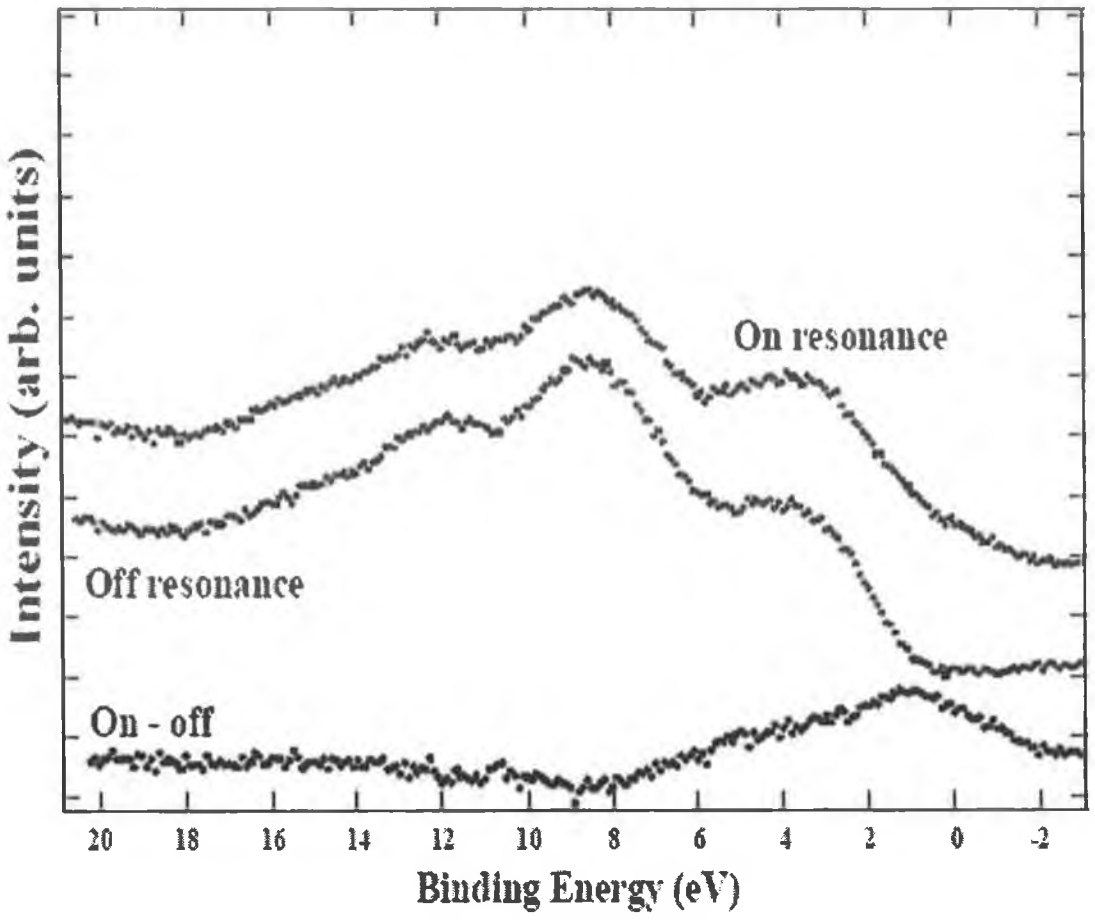

Figure 5.37 Sn3d → 5p RESPES spectra. The 'on-resonance' and 'off-resonance' spectra were taken at photon energies of 488 and 480 eV respectively.

5.3.4 Current-Voltage (I-V) measurement of the cellular networks on SiO_2

Current-Voltage measurements of the organostannoxane cluster networks were carried out at room temperature. The aim of this experiment is to probe the conductivity of the networks by interfacing them to gold microelectrodes. It is important to ensure that if any conduction does occur that it is from the networks only and not the substrate. Samples of the cellular network type structures were produced on SiO_2. The choice of SiO_2 as the substrate arises from the need to electrically insulate the networks from the bulk of the substrate. Thus when the gold contacts were deposited on the sample any possible conduction is through the networks only. Tapping mode AFM is used to visualise the gold electrode and the

size of the gap which is covered in network films (Figure 5.38). The measurements show that for $|V| \leq 30$volts the conductivity of this non-doped network is in the range of an insulating material (i.e. there is no conduction).

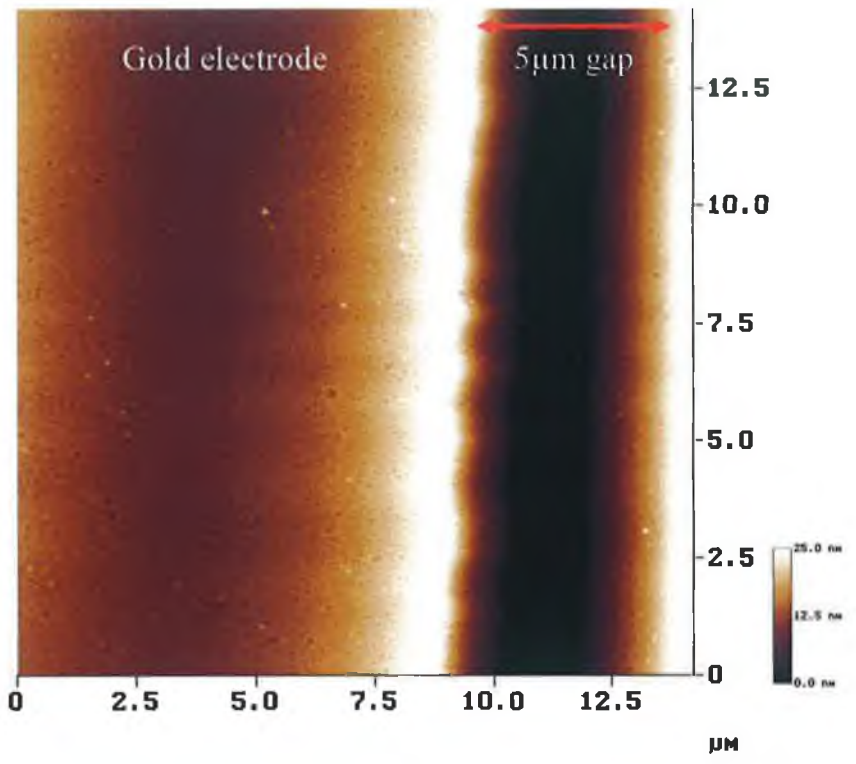

Figure 5.38 *Tapping mode AFM height image of the organostannoxane cluster sample for electrical measurements.*

5.4 Conclusions

In this chapter some of the factors controlling the self-assembly of an organostannoxane cluster molecule on native oxide-terminated silicon substrates were discussed. The clusters dewet the substrate via a mechanism which leads to the formation of a cellular network having a high degree of spatial correlation in the dewetting centres when spin coated from toluene. No such patterns are observed when spin-coated from dichloromethane. For the cluster deposited from toluene,

while the lack of film stability has important implications for the synthesis of high-quality organostannoxane layers on silicon substrates, the influence of a dewetting process with a well-defined correlation length opens up a number of possibilities related to patterning stannoxane and other organometallic thin films at the submicron and nanometer scale levels.

In addition, given that a previous application of Minkowski functionals to polymer film stability called into question the presence of spatially correlated dewetting centres, the quantitative analysis presented, represents an important confirmation of morphological deviations from Poisson statistics in a molecular, non-polymeric thin film. However, although it is tempting to associate the spatial correlations observed with spinodal dewetting, it must be stressed that early stage coalescence of Poisson-distributed dewetting holes may also yield a spatial correlation length.

Synchrotron radiation RESPES measurements have shown that the ferrocenyl groups at the periphery of the organostannoxane cluster retain a high degree of ferrocene-like electronic character but that there is little Fe 3d contribution to the highest occupied molecular orbital. Instead, Sn 3d$\rightarrow$5p RESPES data highlight the role of Sn-derived states in determining the character of the higher-lying occupied frontier orbitals. Although the RESPES data provide a first insight into the electronic structure of this novel and complex organometallic cluster, a detailed theoretical study combined with more comprehensive photoemission work is required to elucidate fully the molecular orbital configuration. Electrical conductivity measurements of this non-doped cellular network show that it is insulating.

5.5 References

1. Whitesides G.M., Grzybowski B., **2002**, *Science,* 295, 2418.
2. Fang L.A., Liu J.M., Coulter S., Cao X.P., Schwartz M.P., Hacker C., Hammers R.J., **2002**, *Surf. Sci.,* 514, 362.
3. Schwartz M.P., Hamers R.J., **2002**, *Surf. Sci.,* 515, 75.
4. Cao X.P., Hamers R.J., **2001**, *J. Amer. Chem. Soc.,* 123, 10988.
5. Lopinski G.P., Wayner D.D.M., Wolkow R.A, **2000**, *Nature*, 406, 48.
6. Special edition on ferrocene chemistry. **2001**, *J. Organomet. Chem.,* 637 -639.
7. Plenio H., Aberle C., **2001**, *Chem,-Eur. J.,* 7, 4438..
8. Katz E., Sheenye-Haj-Ichia L., Willner I., **2002**, *Chem,-Eur. J.,* 8, 4138
9. Tsivgoulis G.M., Lehn J.-M., **1997**, *Adv. Mater.,* 9, 39.
10. Takeshita M., Choi C. N., Irie M., **1997**, *Chem., Commun.,* 2265.
11. Bissell R.A., Cordova E., KeiferA.E., Stoddard J.F., **1994**, *Nature*, 369, 133.
12. Chandrasekhar V., Boomoshankar R., Singh S., Steiner A., Zacchini S., **2002**, *Organometallics*, 21, 4575.
13. Chandrasekhar V., Nagendran S., Bsal S., Kozec M.A., Powell D.R., **2000**, *Angew. Chem. Int. Ed.,* 39, 1833.
14. Chandrasekhar V., Schmid C.G., Burton S.D., Holmes J.M., Day R.O., Holmes R.R., **1987**, *Inorg. Chem.,* 26, 1050.
15. Holmes R.R., Schmid C.G., Chandrasekhar V., Day r.o., Holmes J.M., **1987**, *J. Amer. Chem. Soc.,* 109, 1408.
16. Kumaraswamy S., Nagabrahmanandrachari S., **1992**, *Phosphorus Sulphur Silicon Retat. Elem.,* 65, 9.
17. Sato M., Fukui K., Sakamoto M., Kashiwagi S., Hiroi M., **2001**, *Thin Solid Films.,* 393, 210.
18. Rivier N., **1985**, *Phil. Mag.,* 52, 795.

19. Weaire D., Rivier N., **1984**, *Contemp. Phys.*, 25, 59.

20. Glazier J.A., Weaire D., **1992**, *J. Phys. Condens. Mater.*, 4, 1867.

21. Aste T., Rivier N., **1997**, *Shape Modelling and Application (IEEE Computer Society Press)*, 2.

22. Graner F., Jiang Y., Janiaud E., Flament C., **2000**, *Phys. Rev. E.*, 63, 011402.

23. Grest G.S., Anderson M.P., Srolovitz D.J., **1988**, *Phys. Rev. B*, 38, 4752.

24. Weaire D., Kermode J.P., **1983**, *Phil. Mag. B,* 47, L29.

25. Weaire D., Kermode J.P., **1983**, *Phil. Mag* B., 48, 245.

26. Ruskin H.J., Feng Y., **1995**, *J. Phys. Cond. Mater.*, 7, L553.

27. Ruskin H.J., Feng Y., Zhu B., **2001**, *Physica A,* 293, 315.

28. Stavans J., **1999**, *Foams and Emulsions; NATO ASI Series*, 91-101.

29. Weaire D., Coughlan S., Fortes A.M., **1995**, *J. Mater. Process. Tech.*, 55, 178.

30. Rivier N., **1986**, *Physica*, 23D, 129.

31. Kumar S., Kurtz S.K., **1993**, *Mater. Char.*, 31, 55.

32. Noever D.A.,**1995**, *J. Coll. Int. Sci.*, 174, 92.

33. Moriarty P., Taylor M.D.R., Brust M., **2002**, *Phys. Rev. Letts.*, 89, 248303.

34. Lewis F.T., **1928**, *Anat. Rec.*, 38, 341.

35. Earnshaw J.C., Robinson D.J., **1994**, *Phys. Rev. Lett.*, 72, 3682.

36. Fortes MA. Pina P., **1993**, *Phil. Mag. B.*, 67, 263.

37. Aboav D.A., **1974**, *Metallography*, 3, 383.

38. Weaire D., **1974**, *Metallography*, 7,157.

39. Aboav D.A., **1980**, *Metallography*, 13, 43.

40. Lambert C.J., Weaire D., **1983**, *Phil. Mag.* B., 47, 445.

41. Earnshaw J.C., Robinson D.J., **1994**, *Phys. Rev. Lett.*, 72, 3682.

42. Strawhecker K.E., Kumar S.K., Douglas J.F., Karim A., **2001**, *Macromolecules*, 34, 4669.

43. Ge G., Brus L., **2000**, *J. Phys. Chem. B.,* 104, 9573.

44. Yerushalmi-Rosen R., Klein J., Fetters L., **1994**, *Science,* 263, 793.

45. Higgins A.M., Jones R..A.L., **2000**, *Nature*, 404, 476.

46. Stange T.G., Evans D.F., **1997**, *Langmuir*, 13, 4459.

47. Thiele U., Velarde M.G., Neuffer K., **2001**, *Phys. Rev. Lett.,* 87, 016104.

48. Reiter G., **1992**, *Phys. Rev. Lett.,* 68, 75.

49. Herminghaus S., Jacobs K., Mecke K., Bischof J., Fery A., Ibn-Elhaj M., Schlagowski S., **1998**, *Science*, 282, 916.

50. Muller-Buschbaum P., Wolkenhauer M., Wunnicke O., Stamm M., Cubitt R., Petry W., **2001**, *Langmuir,* 17, 5567.

51. Brochart-Wyatt F., Dalliant J., **1990**, *Can. J. Phys.,* 68, 1084.

52. Stoyan D., Kendall W.S., Mecke J., **1989**, *Stochastic Geometry and its Applications;* Akademie Verlag,: Berlin.

53. Jacobs K., Herminghaus S., Mecke K.R., **1998**, *Langmuir*, 14, 965.

54. Michielsen K., De Raedt H., **2000**, *Comput. Phys. Commun.,* 132, 94.

55. The code to numerically calculate the 2D Minkowski functionals was written in Matlab by C.P. Martin of the University of Nottingham and the analysis was carried out by Dr. Philip Moriarty.

56. Brinkmann M., **2002**, *Phys. Rev. B.,* 66, 165430.

57. Ruckenstein E., Dadyburjor D.B., **1978**, *This Solid Films*, 55, 89.

58. Lawrence C.J., **1988**, *J. Phys. Fluids*, 31, 2786.

59. Muller-Buschbaum P., Gutmann J.S., Wolkenhauer M., Kraus J., Stamm M., Smilgies D., Petry W., **2001**, *Macromolecules*, 34, 1369

60. Vrij A., **1966**, *Discuss. Faraday Soc.,* 42, 23.

61. Xie R., Karim A., Douglas J.F., Han C.C., Weiss R.A., **1998**, *Phys. Rev. Lett.,* 81, 1251.

62. Nilsson A., **2002**, *J. Electron Spectrosc. Relat. Phenom.*, 126, 3.

63. Driscoll D.C., Dowben P.A., Boag N.M., Grade M., Barfuss S., **1986**, *J. Chem. Phys.*, 85, 4802.

64. Dowben P.A., Waldfried C., Komesu T., Welipitiya D., McAvoy T., Vescovo E., **1998**, *Chem. Phys. Lett.*, 283, 44.

65. Welipitiya D., Dowben P.A., Zhang J., Pai W.W., Wendelken J.F., **1996**, *Surf. Sci.*, 367, 20.

Chapter 6

Conclusions and Future Work

"Today's greatest labour-saving device is tomorrow"

Tom Wilson

6.1 Conclusions

The studies described in this thesis cover a varied range of topics. These include: polymeric systems, carbon nanotubes and an organostannoxane cluster system. The common thread within these studies is in improving understanding of the fundamental processes that may occur in the self-assembly of these systems on substrates, with the possibility of the development of their functionality in nanotechnological systems.

Chapter 1 provides a broad introduction to the concept of nanotechnology, some of its origins and possible applications. The area of self-assembly is also introduced with examples of some applications in the field of nanoelectronics. Self-assembly is an important technique as it relates to the majority of the experimental studies carried out in this thesis; the self-assembly of the systems when deposited from solution are investigated.

Chapter 2 extends on the techniques introduced in chapter one. Atomic force microscopy and photoemission spectroscopy are useful probes as many of the important properties of materials depend on their surface structure and how the material interacts with its environment. AFM and PES are described in detail. They are used as probes throughout this thesis. AFM is particularly important as it allows the morphology of conducting and insulating samples to be investigated in detail.

The rest of the thesis may be separated into three separate projects. The first (Chapter 3) and second projects (Chapter 4) are based on ruthenium systems containing bis(2,2'-bipyridly) centres. In Chapter 3 the "parent" complex of those systems investigated, $[Ru(bpy)_3]^{2+}$ is introduced, and its importance to the area of inorganic chemistry is highlighted. The first project involves the synthesis and characterisation of a range of polymers containing poly(pyridyl) complexes of ruthenium^{II} and osmium^{II}. The self-assembly and the morphology of

$[Ru(bpy)_2PVP_{10}Cl]Cl$ is investigated when deposited from a methanol solution. Drop deposition represents adsorption in nearly-equilibrated conditions and the resulting films on a native oxide-terminated silicon substrate may be characterised as droplet-like agglomerates which appear to form randomly across the substrate. Spin-cast depositions represents the opposite adsorption technique; where the system is in a far-from-equilibrium state. Polymer solutions dewet the substrate via a mechanism which leads to the formation of thin granular films. Small pin holes of bare silicon are also observed which represent locations where the polymer film has ruptured via a dewetting mechanism. Deposition parameters (solvent type, concentration, adsorption technique employed etc.) play an important role in controlling the resulting morphology and stability of the redox polymers and hence in their use in polymer applications. The electronic structure of the polymer $[Ru(bpy)_2PVP_{10}Cl]Cl$ has been investigated with synchrotron radiation photoemission. In the valence band spectra the peak at a binding energy of 2.5eV originates from the highest occupied molecular orbital (HOMO) of the polymer. The N1s spectrum indicates the presence of two different chemical environments which is shown by the N1s NEXAFS spectrum. The Ru3p core level spectrum shows a shift towards a higher binding energy which is indicative of the presence of the 2,2'-bipyridine ligands when compared to the $RuCl_3$ model compound. More comprehensive photoemission work is needed to elucidate fully the molecular orbital conformation of this polymer.

The self-assembly of $[Os(bpy)_2PVP_nCl]Cl$ (where n is 5 or 10), from solution via spin-coating deposition is also investigated. The osmium polymers have higher values of R_{rms} surface roughness than their ruthenium analogues, and the morphology of these polymers indicates that these polymers have a fairly open, porous structure. However, the $[Os(bpy)_2PVP_5Cl]Cl$ structure appears to be more compact and homogeneous than the $[Os(bpy)_2PVP_{10}Cl]Cl$ films.

Chapter 4 of this thesis details the second project. Amino-functionalised multi-wall carbon nanotubes are reacted with the acid chloride complex of bis-(2,2'-bipyridine)-(4,4'-dicarboxy-2,2'bipyrine)-ruthenium^{II}. Absorption and emission spectroscopy show evidence that an amide linkage is formed between the nanotubes and the ruthenium complex. A detailed AFM analysis allows us to visualise T- and Y-junction interconnects, showing that the solubility of the tubes has changed. In a parallel experiment carried out with collaborators to this project [1], a ^{13}C labelled molecule is converted to its acid chloride and reacted with the amino-functionalised multiwall nanotubes. ^{1}H NMR and ^{13}C NMR identify signals assigned to an amide linkage between the labelled terephthalic acid molecule and the MWNTs. More work on these systems needs to be done however and this will be discussed in section 6.2.

The third project in Chapter 5 probes some of the factors that control the self-assembly of the organostannoxane cluster molecule $[BuSn(O)OC(O)Fc]_6$ (where "Fc") ferrocenyl) on native oxide-terminated silicon substrates. The clusters dewet the substrate via a mechanism which leads to the formation of cellular networks having a high degree of spatial correlation in the dewetting centres when spin coated from toluene. No such patterns are observed when spin coated from dichloromethane. For the cluster deposited from toluene, while the lack of film stability has important implications for the synthesis of high-quality organostannoxane layers on silicon substrates, the influence of a dewetting process with a well-defined correlation length opens up a number of possibilities related to patterning stannoxane and other organometallic thin films at the submicron and nanometre scale levels.

In addition, given that a previous application of Minkowski functionals to polymer film stability called into question the presence of spatially correlated dewetting centres, the quantitative analysis presented in Chapter 5, represents an

important confirmation of morphological deviations from Poisson statistics in a molecular, non-polymeric thin film. Although it is tempting to associate the spatial correlations observed with spinodal dewetting, it must be stressed that early stage coalescence of Poisson-distributed dewetting holes may also yield a spatial correlation length.

Synchrotron radiation RESPES measurements show that the ferrocenyl groups at the periphery of the organostannoxane cluster retain a high degree of ferrocene-like electronic character but that there is little Fe 3d contribution to the highest occupied molecular orbital. Instead, Sn 3d→5p RESPES data highlight the role of Sn-derived states in determining the character of the higher-lying occupied frontier orbitals.

6.2 Future Work

Interconnected Carbon Nanotubes

There is at present an enormous interest in the potential of carbon nanotubes as components in molecular electronics. However, although carbon nanotubes promise a wide range of potential applications a number of fundamental and fabrication problems need to be solved before a technology based on these materials may be developed; (a) methods for producing either semiconducting or metallic tubes, (b) methods for chemical modification of nanotubes for creating interconnects and (c) methods for addressing a single nanotubes electronic component, such as interconnects.

The initial observation of the linkage between a ruthenium complex and amino-functionalised MWNTs in Chapter 4 needs to be investigated in further detail. Some other potential interconnects are shown in Figure 6.1. These compounds would allow the investigation of a number of the fundamental questions. For example, the

effect of redox potential on the conductivity and tunnelling properties of interconnected MWNTs may be investigated by comparing ruthenium and osmium compounds as linkers. With the terpyridine type linkers (compound b) the geometry of the links may be modified. Also with an introduction of heterdinuclear compounds (compound c) it would be possible to determine how the photophysical properties of the dinuclear unit may be affected by its attachment to the nanotubes. Depending on the number of 4,4'-dicarboxy-2,2'bipyridyl (dcbpy) groupings present the dinuclear compounds may be able to form different types of linkages: via one or two metal centres.

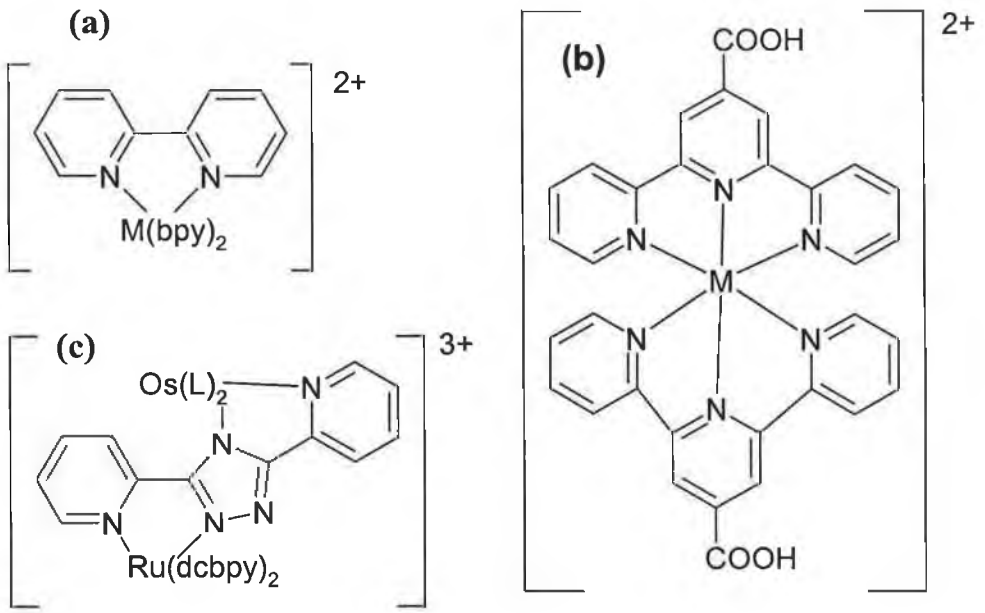

Figure 6.1 *Potential molecular interconnects.*

In Chapter 4 the modified linkage was investigated using UV-VIS and emission spectroscopy and AFM analysis. ^{13}C NMR also shows potential as a characterisation tool for the chemical bond between carbon nanotubes and molecular entities. The linkers proposed above have well-defined electrochemical and photophysical properties which need to be investigated for the further development of these interconnected carbon nanotubes as components in molecular devices. The

investigations in Chapter 4 show that the ruthenium-modified MWNTs do emit in solution. This is a very interesting observation, which may yield information concerning the electronic coupling between the molecular component and the nanotubes. However, more extensive emission studies on the modified tubes, both in solution and as thin films, are needed to fully understand and characterise this observation. This type of study would include transient absorption spectroscopy, solvent and temperature dependent emission studies, and excited state lifetime studies on nano- and femto- second timescales. The electrical characterisation of covalently interconnected carbon nanotubes has not been studied so far and would be another area in which the linkers would need to be investigated in detail.

Metallopolymer Carbon Nanotube Composites

There is also interest in the non-covalent functionalisation of carbon nanotubes. This has been achieved, for example with biological entities [2], surfactants [3], and conjugated polymers [4]. Tahhan et al. reports stable dispersions of carbon nanotubes in sulfonated polyaniline, which has potential applications as carbon nanotubes mats. The polyaniline may be used to solubilise SWNTs via formation of donor-acceptor complexes [5,6]. Carbon nanotubes have also been introduced into matrices of conjugated polymers for preparation of composites for optoelectronic applications [7,8]. For example, photovoltaic devices have been fabricated from carbon nanotubes/poly (*p*-phenylenevinylene) (PPV) composites by using carbon nanotubes as a hole collecting electrode [9].

The polymers studied in Chapter 3 $[M(bpy)_2PVP_nCl]Cl$ where M is either ruthenium^{II} or osmium^{II} would be ideal candidates for the formation of carbon nanotubes-redox polymer composites. This may be a promising approach for the effective incorporation of carbon nanotubes into redox-active polymer based devices.

Preliminary studies being carried out in collaboration with Dr. Marc in Het Panhuis suggest that the redox polymers act as host materials by wrapping around the carbon nanotubes, and act as an efficient dispersant for nanotubes. Initial TEM data (Figure 6.2) show intercalation of the polymer into carbon nanotubes bundles. This work is in very early stages and will be ongoing.

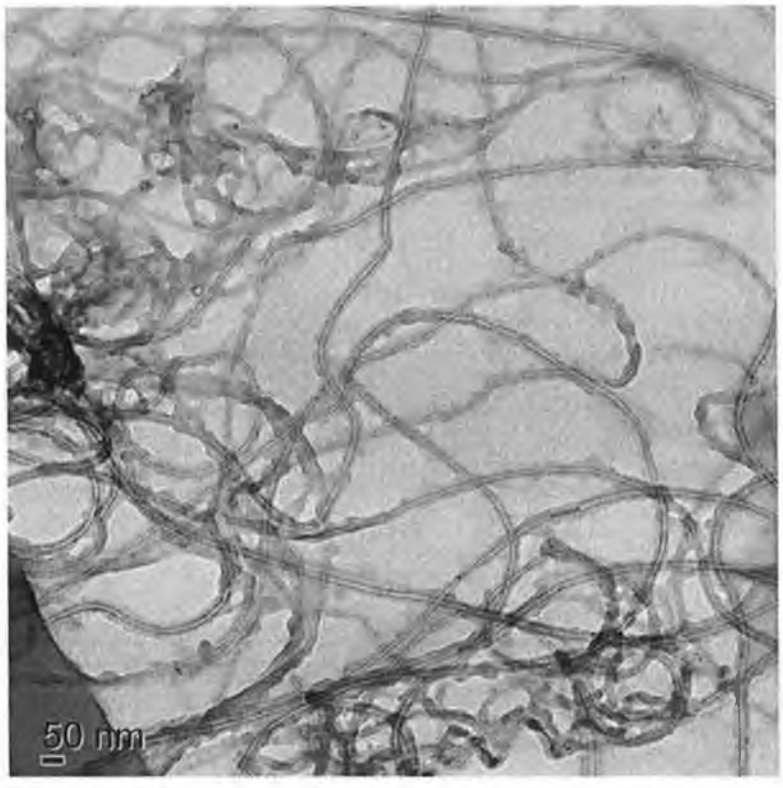

Figure 6.2 *Preliminary transmission electron microscopy (TEM) image showing thick multiwall nanotubes coated with* $[Ru(bpy)_2PVP_{10}Cl]Cl$.

Organostannoxane Cluster Molecule

Preliminary voltammetric studies (described in Appenix E) of this organometallic molecule adsorbed as monolayers on single crystal gold electrodes have been carried out a with a view to extending the studies of the monolayers formed to *in situ* STM analysis. Electrochemical scanning tunneling microscope allows real-time *in situ* STM imaging with atomic and molecular resolution of the electrode surface in solution under electrochemical control. Also the RESPES data provides a first insight

into the electronic structure of this novel and complex organometallic cluster. However, a detailed theoretical study combined with more comprehensive photoemission work is required to elucidate fully the molecular orbital configuration.

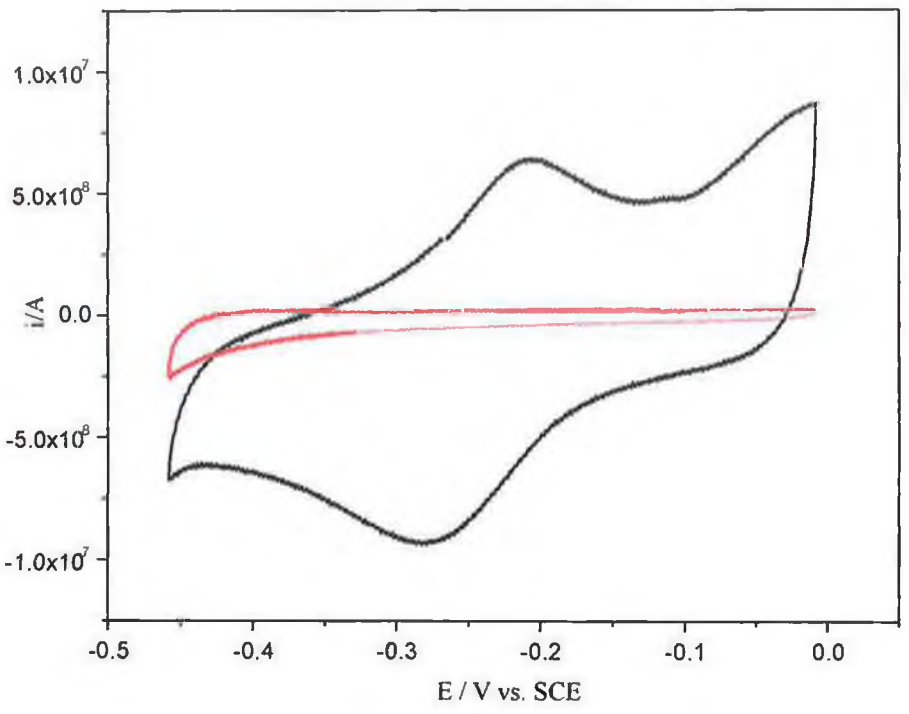

***Figure 6.3** Initial CV results for organostannoxane cluster (black) and toluene (red) adsorbed onto a single crystal gold electrode in 0.1mmol perchloric acid (pH 3.0). Scan rate 20mVs^{-1}.*

6.3 References

1. R üther M., Frehill F., O 'Brien J., M inett A .I., Blau W .J., V os J. G., In h et Panhuis M., **2004**, *J. Phys. Chem. B*, 108, 9665.
2. In het Panhuis M., Salvador-Morales C., Franklin E., Chambers G., Fonseca A., Nagy J.B., Blau W.J., Minett A.I., **2003**, *J. Nanosci. Nanotech.,* 3, 209.
3. Richard C., Balavoine F., Schultz P., Ebbesen T.W., Mioskowski C., **2003**, *Science*, 300, 775.
4. Dalton A.B., Stephan C., Coleman J.N., McCarthy B., Ajayan P.M., Lefrant S., Bernier P., Blau W.J., Byrne H.J., **2000**, *J. Phys. Chem. B.,* 104, 10012.
5. Tahhan M., Barisci J.N., Wallace G.G., **2004,** *J. Nanosci. Nanotech.* (submitted).
6 Huang J-E., Xiao-Hong L., J-Chuan X., Hu-Lin L., **2003**, *Carbon*, 41, 2731.
7. Star A., Stoddart J.F., Steuerman D., **2001**, *Angew. Chem. Int. Ed.,* 40, 1721.
8. Curran S.A., Ajayan P.M., Strevens A., **1998**, *Adv. Mater.,* 11, 1281.
9. Ago H., Petritsch K., Shaffer M.S.P., **1999**, *Adv. Mater.,* 11, 1281.

Appendix A

Matlab Algorithm

The following Matlab algorithm was written by Dr. Dave Keeling, Nanoscience Group, University of Nottingham, May 2002, as a script file for analysing random cellular networks (RCN) including implementation of Desch's law, Lewis's law and the Aboav-Waeire law.

```
% To use - you need the RCN picture in bitmap form and to measure the conversion
factor in distance per pixel.
%
% The name of the bitmap image and the AREA factor (i.e. the conversion factor of
distance per pixel ^2)
% need to be inserted just below this comment where it says "Change here" (type
"edit Nottcell" to edit the data).
% The image also needs to be in the same folder as this analysis file
% or the whole path needs to be entered.
%
% To run the program just type Nottcell at the MATLAB command prompt
%
% To analyse the RCN :-
% 1)Left click the centre of every cell in the image (or as much as you want to
analyse).
% 2)To finish this stage, right click once.
% 3)Define a box on the image (left click each of two opposite corners of the box)
that encompasses
%   the centres of all the cells you wish to include in the calculations of the three
laws.  Any cell
%   with a centre outside will be disregarded.
% 4)If the box is in the right place type "1" followed by return in the main MATLAB
window
%   if you want to redefine the box, type "0".
%
%   The script will then carry out analysis of the voronoi diagram
%
% 5)Specify the name of a datafile into which the array carrying data for number of
sides,area and perimeter
%   of each cell is to be stored in ASCII text N.B. File extension is NOT
automatically added.
%
% Any other paramters that you want to save have to be done by hand.
%
% Information for lewis's law:-
%    lewis2              - contains raw sorted data
%    lcount              - array containing number of points in each column
%    lewis3(1,fmd(lcount))  - contains averaged points that are plotted on the graph
(lewis3=sum(lewis2)./lcount)
%    errorl              - contains standard errors as calculated from lewis2
%    Yl                  - points from polynomial fit (type "help polyfit" for more info.)
%    deltal              - errors from polynomial fit
%
%
% Information for Desch's law:-
%    desch2              - contains raw sorted data
```

```
%    dcount              - array containing number of points in each column
%    desch3(1,find(dcount))  - contains averaged points that are plotted on the graph
(desch3=sum(desch2)./dcount)
%    errord              - contains standard errors as calculated from desch2
%    Yd                  - points from polynomial fit (type "help polyfit" for more info.)
%    deltad              - errors from polynomial fit
%
%
% Information for Aboav-Waeire law:-
%    AV3                 - contains raw sorted data
%    AVcount             - array containing number of points in each column
%    AV3(3,find(AVcount))    - contains averaged points that are plotted on the
graph (AV3(3,:)=AV3(1,:)./AV3(2,:))
%    errorAV             - contains standard errors as calculated from AV3
%    YAV                 - points from polynomial fit (type "help polyfit" for more
info.)
%    deltaAV             - errors from polynomial fit
%
% DLK 27/05/2002




close all
clear all
clc

% Change here
fname = 'd62204b.bmp';
areafactor = 36.14;     %e.g. (10,000 Angstroms or in my case it will be
nanometres./512 pixels).^2;


a = imread(fname,'bmp'); %imread - command to read files (filename, filetype)
image(a);
axis equal
x=[];
y=[];

button = 1;
while(button~=3)
   [xtemp ytemp button] = ginput(1);   %This loop takes in the X,Y data of the
centres of each cell
   if button==1                  %loop ends on a right click
      x = [x; xtemp];
      y = [y; ytemp];
      image(a)
      hold on
      plot(x,y,'c+')
      hold off
      axis equal
```

```
   end
end

ask=0;
hold on
voronoi(x,y,'c')                %'Voronoi' is the command to draw a voronoi diagram
hold off;
axis([0 max(size(a)) 0 max(size(a))]);



while ask==0
   [xbox(1) ybox(1)]=ginput(1);                %This loop asks you to draw a box, only
cells with centres inside
   image(a)                                    %the box are used in subsequent calculations.
Loop ends when you pass a
   axis equal                                  %'1' to the variable 'ask' to say the box is OK.
   hold on
   voronoi(x,y,'c')
   plot(x,y,'c+')
   line([xbox(1) xbox(1)],[-max(size(a)) max(size(a))])
   line([-max(size(a)) max(size(a))],[ybox(1) ybox(1)])
   hold off
   axis([0 max(size(a)) 0 max(size(a))]);

   [xbox(2) ybox(2)]=ginput(1);
   image(a)
   axis equal
   hold on
   voronoi(x,y,'c')
   plot(x,y,'c+')
   line([xbox(1) xbox(1) xbox(2) xbox(2) xbox(1)],[ybox(1) ybox(2) ybox(2)
ybox(1) ybox(1)]);
   hold off
   axis([0 max(size(a)) 0 max(size(a))]);



   ask=input('Is the box OK? (1=yes, 0=no)')
end


index_clip = find(x>min(xbox) & x<max(xbox) & y>min(ybox) & y<max(ybox));


figure
voronoi(x,y)
[v,c]=voronoin([x(:) y(:)]);       %'Voronoin' is the voronoi analysis function -
vertices are stored in the variable array v
                                   %array c stores indices into the vertex aray to define the cells
sides=[];
areas=[];
```

```
for i = rot90(index_clip)
   ind = c{i};
   areas = [areas; polyarea(v(ind,1),v(ind,2))];
   sides = [sides; length(ind)];

end

areas = areas*areafactor;

figure
hist(sides,(max(sides)-min(sides))+1)
xlabel('Number of sides')
ylabel('Number of cells')
s = [sides areas];              %s is an array that stores the number of sides of each cell
and its area and its perimeter
                        %- this array is saved out as an ASCII text file later on


%**********************************
%* implementation of Lewis's Law *
%**********************************

s(:,3)=s(:,2)./s(:,1);
s=sortrows(s,1);

lewis=[];
lcount=ones(1,max(s(:,1)));
currentside=0;
count=1;
lewis(1,count)=s(1,2);
lewis(2,count)=1;
lewis(3,count)=s(1,1);
lewis2=[];

%this loop goes through s and compiles a new array 'lewis' which contains the
appropriate data
%to plot Lewis's law

for i=2:length(s)
   if s(i,1)>s(i-1,1)
      count=count+1
      lewis(1,count)=0;
      lewis(2,count)=0;
      lewis(3,count)=0;
   end

   if isfinite(s(i,2))==1
      %lewis(1,count)=lewis(1,count)+s(i,2);
      %lewis(2,count)=lewis(2,count)+1;
      %lewis(3,count)=s(i,1);
      lewis2(lcount(count),count)=s(i,2); %lewis2 is an array used subsequently for
```

```
generating error bars
      lcount(count)=lcount(count)+1;
   end
end

lcount=lcount-1;

lewis3(1,:)=sum(lewis2)./sum(lewis2>0);
count=0;
for i=find(lcount)
   count=count+1;
   errorl(count)=std(lewis2(1:lcount(i),i))./sqrt(lcount(i)); %generating errors
end

figure
[Pl,Sl]=polyfit(find(lcount),lewis3(1,find(lcount)),1); %this does a straight line fit of
lewis's law data
[Yl,deltal]=polyval(Pl,find(lcount),Sl);

errorbar(find(lcount),lewis3(1,find(lcount)),errorl,'.')
hold on
plot(find(lcount),Yl)
hold off
title('Lewiss Law')
xlabel('Number of cell sides (n)')
ylabel('Area (averaged)')


%*********************************
%* implementation of desch's law *
%*********************************


desch=zeros(3,max(s(:,1)));
dcount=ones(1,max(s(:,1)));
desch(1,count)=s(1,2);
desch(2,count)=1;
desch(3,count)=s(1,1);
counter2=1;
desch2=[];
count=1;

%this loop compiles a new array 'Desch' storing the appropriate data to plot desch's
law
for i=rot90(index_clip)
   ind=c{i};
   perimeter=0;
   for j=1:length(ind)-1
      x1=v(ind(j),1);
      y1=v(ind(j),2);
      x2=v(ind(j+1),1);
      y2=v(ind(j+1),2);
```

```
      perimeter=perimeter+sqrt(((x2-x1).^2) + ((y2-y1).^2));
   end
   x1=v(ind(1),1);
   y1=v(ind(1),2);
   perimeter=perimeter+sqrt(((x2-x1).^2) + ((y2-y1).^2));
   s(count,3)=perimeter;

   %desch(1,length(ind))=desch(2,length(ind))+1;
   desch2(dcount(length(ind)),length(ind))=perimeter; %desch2 is used for
generating error bars
   dcount(length(ind))=dcount(length(ind))+1;
end
dcount=dcount-1;
desch3=sum(desch2)./dcount;

count=0;
for i=find(dcount)
   count=count+1;
   errord(count)=std(desch2(1:dcount(i),i))./sqrt(dcount(i)); %generating errors
end

figure
errorbar(find(dcount),desch3(1,find(dcount)),errord,'.');
[Pd,Sd]=polyfit(find(dcount),desch3(1,find(dcount)),1);
[Yd,deltad]=polyval(Pd,find(dcount),Sd);
hold on
plot(find(dcount),Yd);
hold off
title('Deschs Law')
xlabel('Number of cell sides (n)')
ylabel('Perimeter (averaged)')


%****************************************
%* implementation of the Aboav-Weaire Law *
%****************************************
AVcount=ones(1,max(s(:,1)));
AV1=zeros(length(index_clip),max(s(:,1)));
AV2=zeros(1,length(index_clip));
for i = 1:length(index_clip)
   ind=(c{index_clip(i)});              %This puts all the useful indices into a big
array padded by zeros
   AV1(i,1:length(ind))=ind;
end


for i=1:length(index_clip)             %This loop uses some nifty logic operations to
discover the nearest neighbours
   test=AV1(i,1)==AV1;                 %for a given cell. For those unfamiliar with
MATLAB array operations:
   for j=2:(length(c{index_clip(i)}))          % the op. Array1==Array2 gives an
array3 with '1's where the cells match and zeros
```

```
      test=test | (AV1(i,j)==AV1);       %everywhere else - the |=logical OR which
makes sure all vertices are counted
   end
   cells=find(sum(test,2));              %This line tells you which cells are nearest
neighbours - 'find' returns the index
                                         %of all non-zero elements
   for j=rot90(cells)
      AV2(i)=AV2(i)+ length(c{index_clip(j)});       %This loop goes throgh the
array 'cells' and compiles the
   end                                   %Aboav-Weaire data

end
AV3=zeros(2,max(s(:,1)));

for i=1:length(index_clip)
   AVlarge(AVcount(length(c{index_clip(i)})),length(c{index_clip(i)}))=AV2(i);
   AVcount(length(c{index_clip(i)}))=AVcount(length(c{index_clip(i)}))+1;
   AV3(1,length(c{index_clip(i)}))=AV3(1,length(c{index_clip(i)}))+AV2(i);
   AV3(2,length(c{index_clip(i)}))=AV3(2,length(c{index_clip(i)}))+1;
end

AV3(3,:)=AV3(1,:)./AV3(2,:);

AVcount=AVcount-1;
count=0;

for i=find(AVcount)
   count=count+1;
   errorAV(count)=std(AVlarge(1:AVcount(i),i))./sqrt(AVcount(i)); %generating
errors
end


figure
errorbar(find(AVcount),AV3(3,find(AVcount)),errorAV,'.');
[PAV,SAV]=polyfit(find(AVcount),AV3(3,find(AVcount)),1);
[YAV, deltaAV]=polyval(PAV,find(AVcount),SAV);
hold on
plot(find(AVcount),YAV)
title('Aboave-Waeire Law')
xlabel('Number of cell sides (n)')
ylabel('Product of cell sides(n) and neighbouring sides(m)')

[filename, pathname] = uiputfile('*.dat', 'Data file for [sides, area, perimeter] array');
save([pathname filename], 's', '-ascii')
```

Appendix B

Statistical Crystallography Data

The following data is for the analysis of the organostannoxane cluster networks described in section 5.3.2. The statistical crystallography results include:

i). The TM-AFM Image.

ii). The Voronoi Construction.

iii). Histogram.

iv). Plots for the Aboav-Weaire Law and the Lewis Law.

Tapping mode AFM height images of the organostannoxane cluster networks.

Sample A

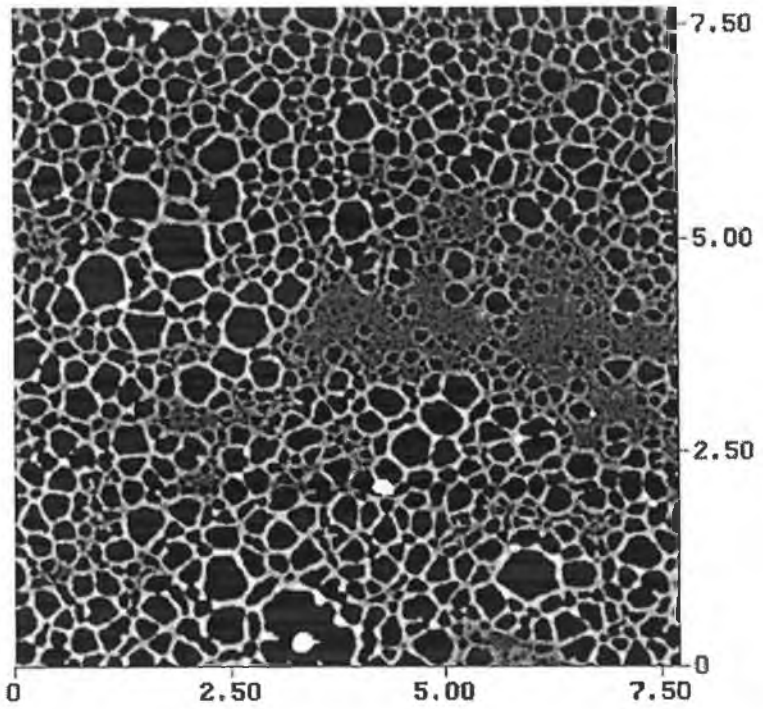

Figure B1 *Tapping mode AFM height data of* $[BuSn(O)OC(O)Fc]_6$ *spin-coated from toluene. 7.6μm x 7.6μm, z-range 15nm..*

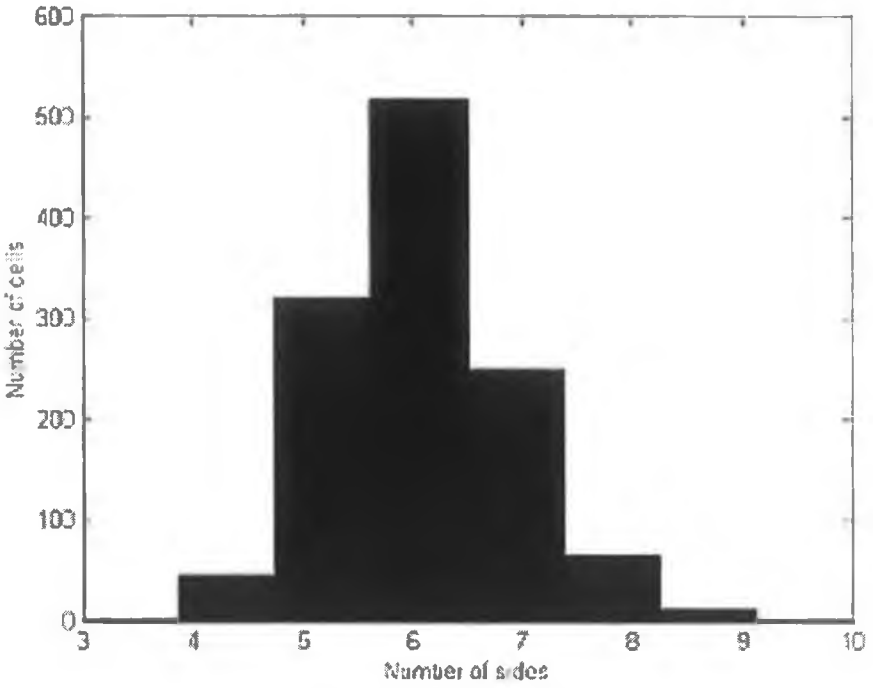

Figure B2 *Histogram 1208 polygons.*

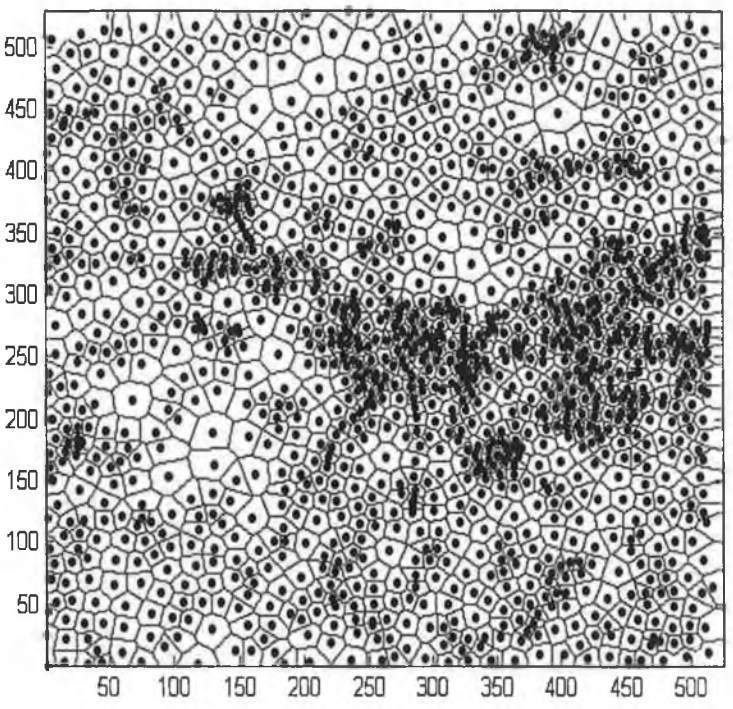

Figure B3 *The Voronoi construction for the height network data in Figure B1. The scale refers to the number of data points (i.e. pixels per image is 512 x 512)*

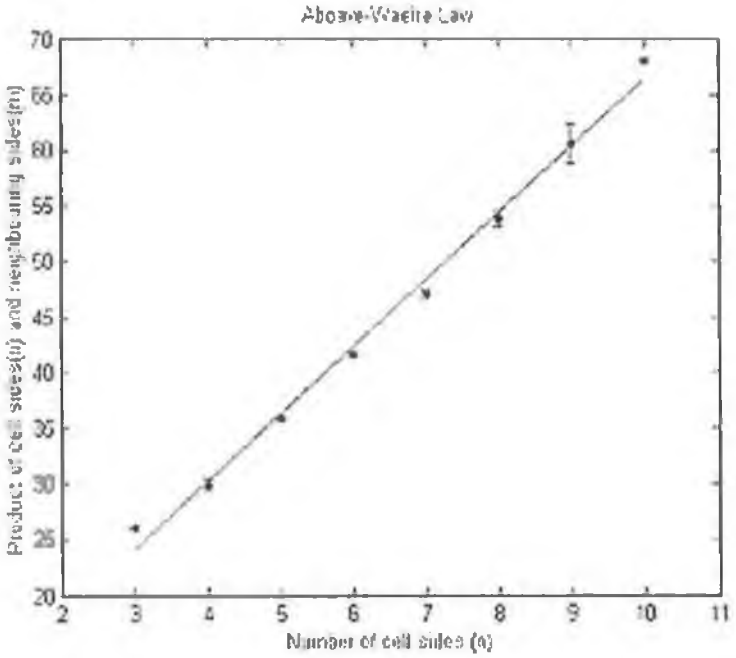

***Figure B4** Aboav-Weaire Law – In agreement*

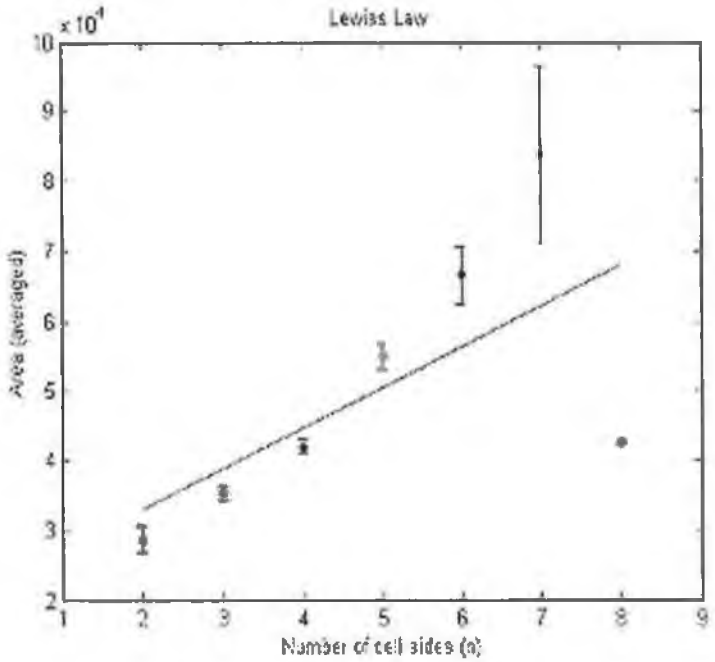

Figure B5 Lewis Law –Not in agreement

Sample B

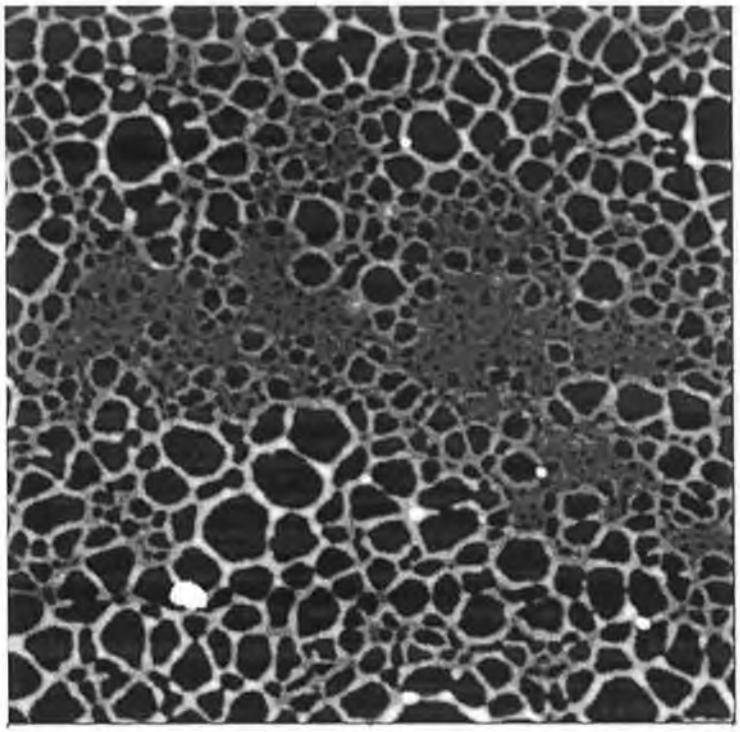

Figure B6 *5.020μm x 5.020μm Tapping mode AFM height data of organostannoxane cluster networks, z = 15nm.*

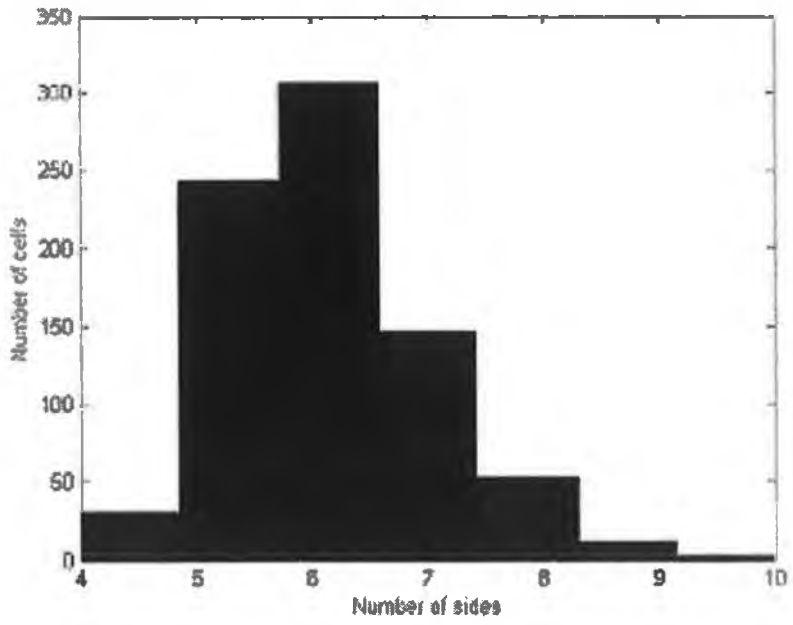

Figure B7 *Histogram 795 polygons*

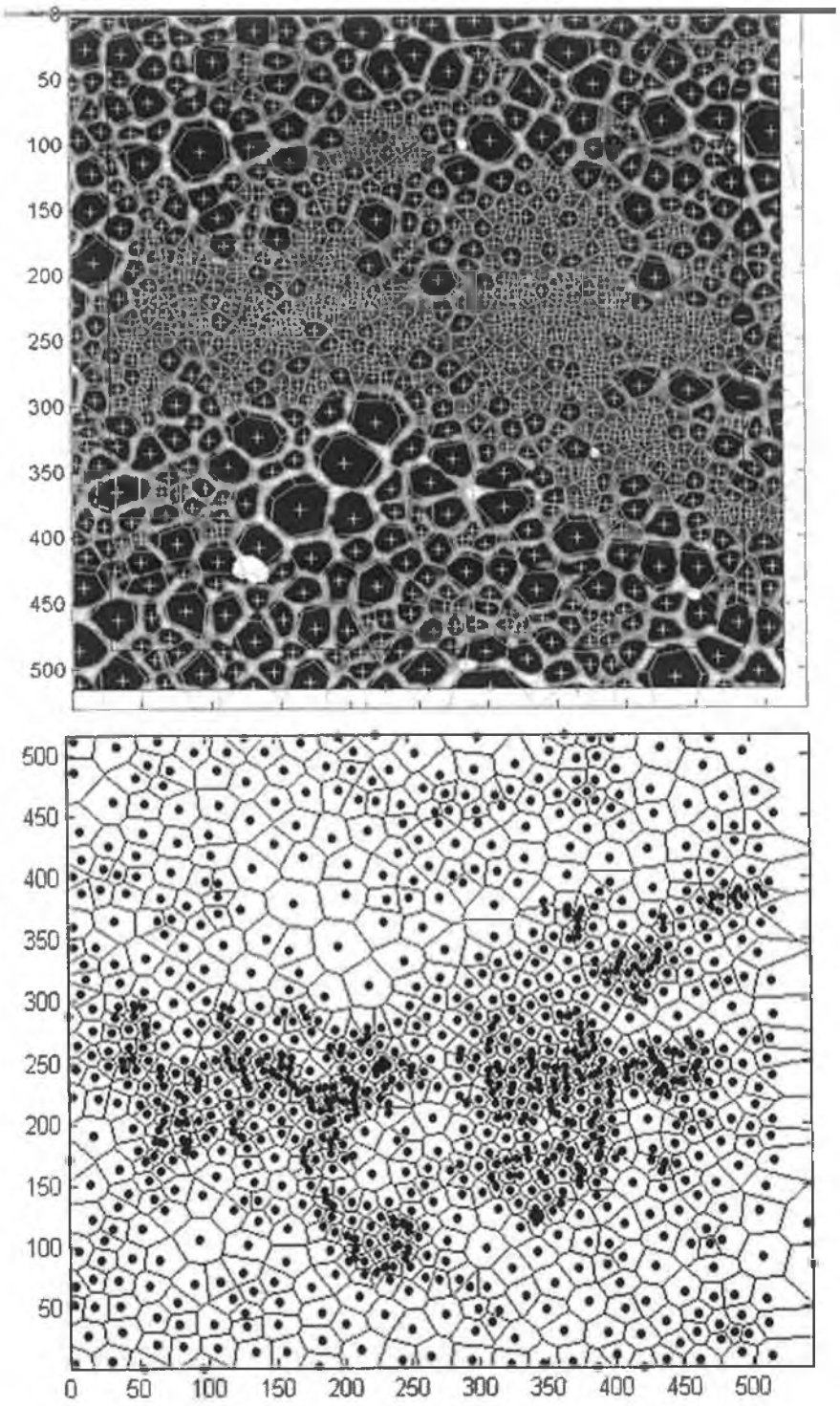

Figure B8 *The Voronoi construction for the height network data in Figure B6. The scale refers to the number of data points (i.e. pixels per image is 512 x 512*

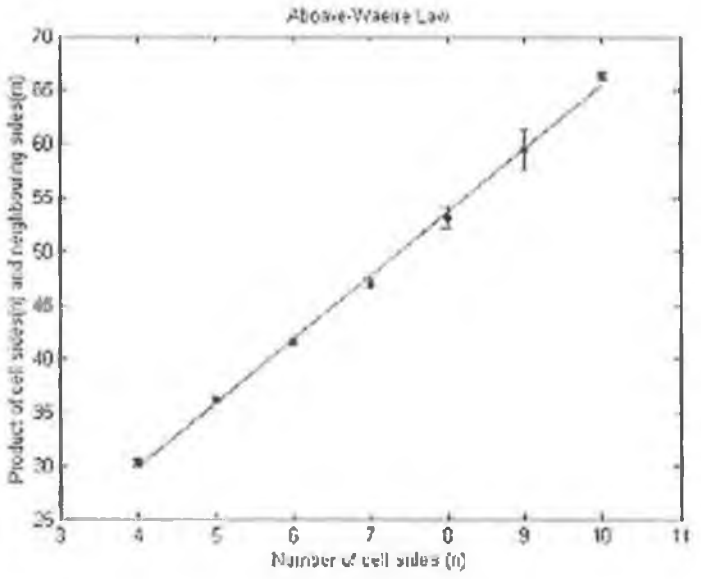

Figure B9 *Aboav-Weaire Law – In agreement*

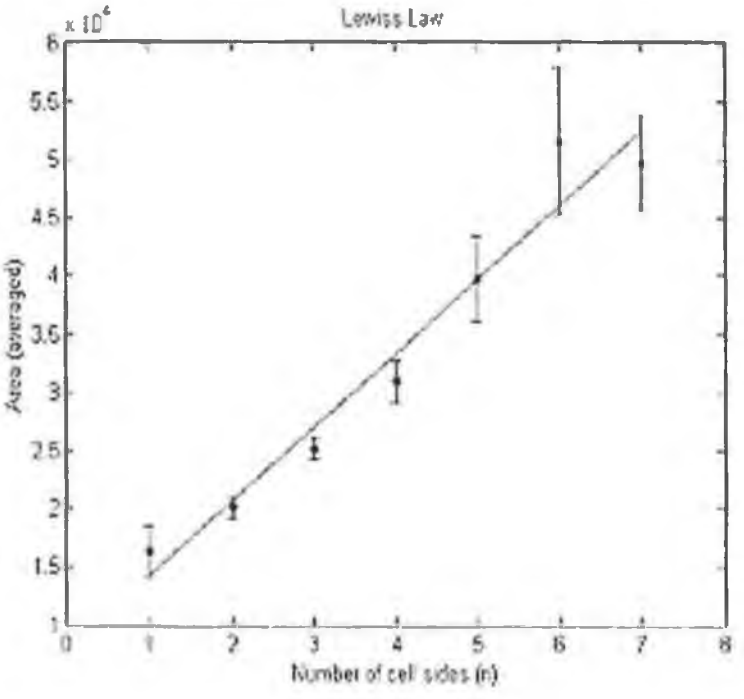

Figure B10 *Lewis Law –Not in agreement*

Sample C

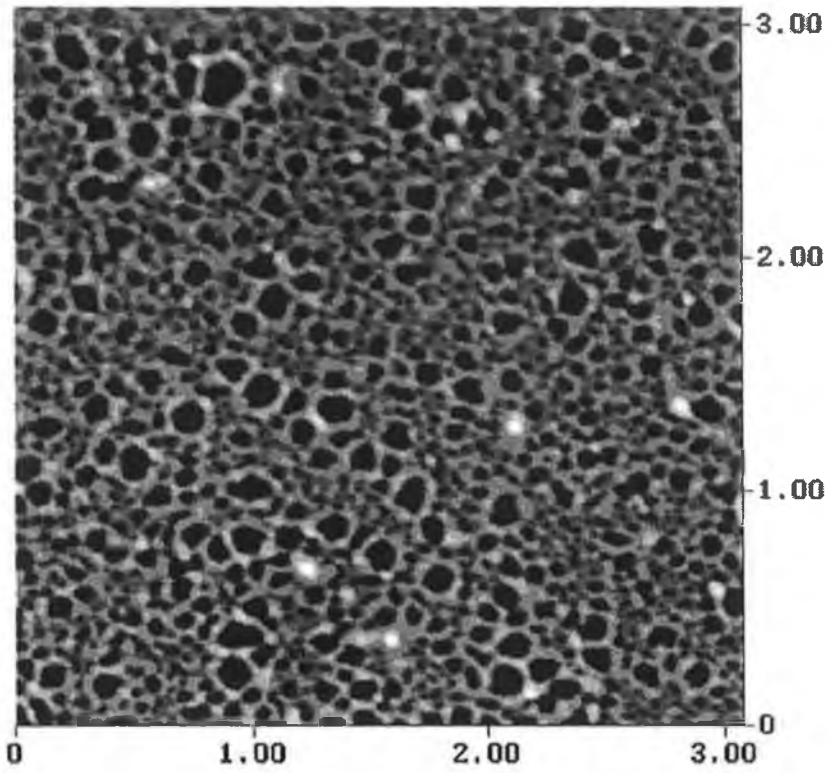

Figure B11 *Tapping mode AFM height data of organostannoxane cluster networks; 6μm x 6μm, z-range 12.5nm.*

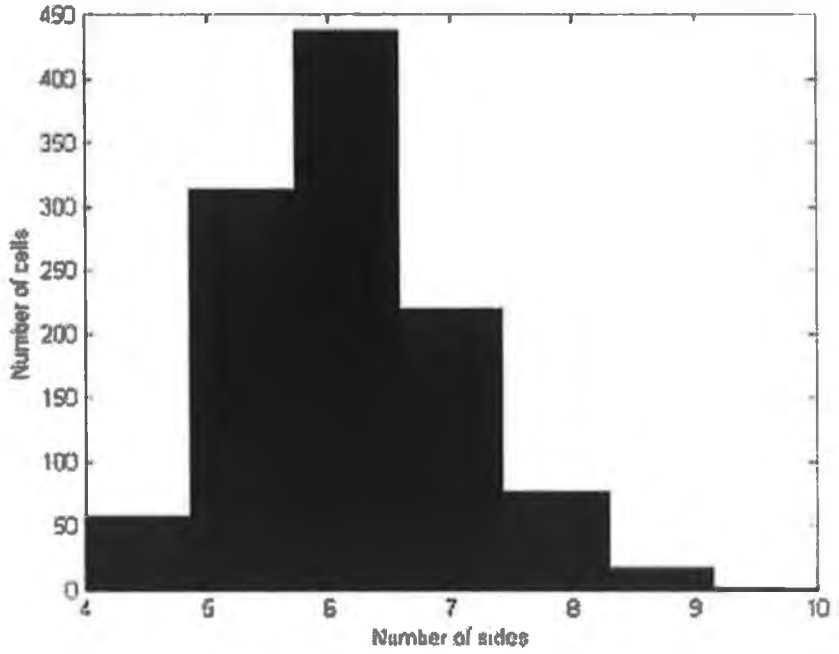

Figure B12 *Histogram 1121 polygons.*

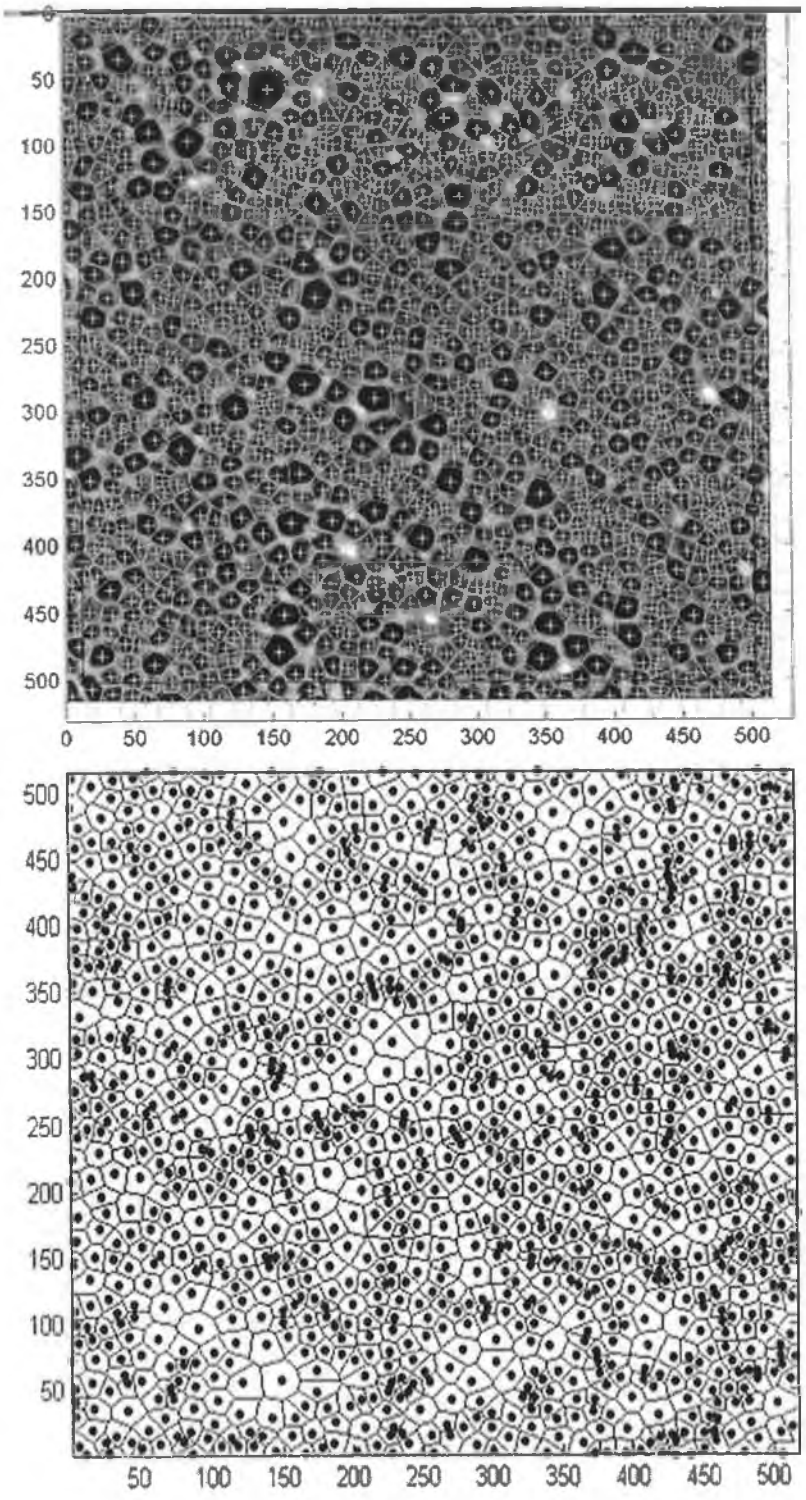

Figure B13 *The Voronoi construction for the height network data in Figure B1. The scale refers to the number of data points (i.e. pixels per image is 512 x 512*

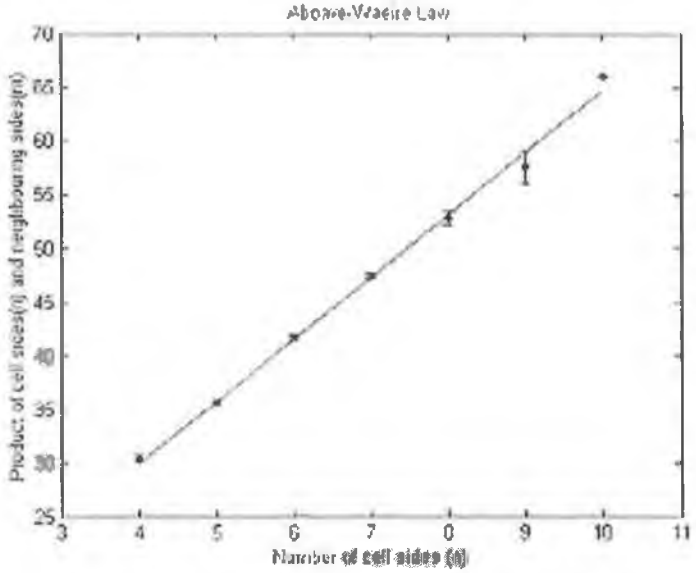

Figure B14 *Aboav-Weaire Law – In agreement*

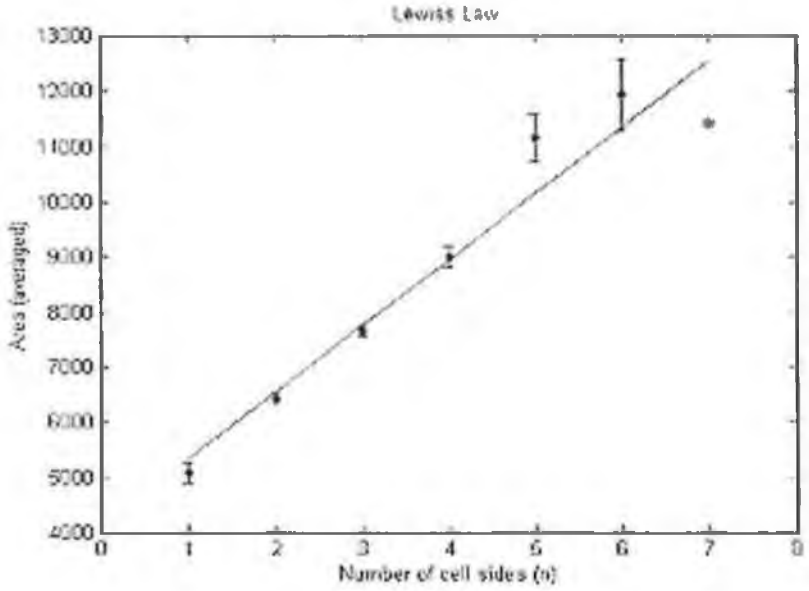

Figure B15 *Lewis' Law –Not in agreement*

Appendix C

Annealing Data for the Organostannoxane Cluster Molecule

Sample spin-cast on a solvent rinsed silicon substrate and annealed at 75°C

25 μL of a 0.25mmol solution of the organostannoxane cluster molecules in toluene was spin-coated onto a 1cm^2 solvent-rinsed native-oxide covered Si(111) wafer. The sample was annealed at 75°C for different times (0 h up to 60 h) and quenched to room temperature for AFM observations. Tapping mode AFM was carried out using a Digital Instruments Multimode AFM system.

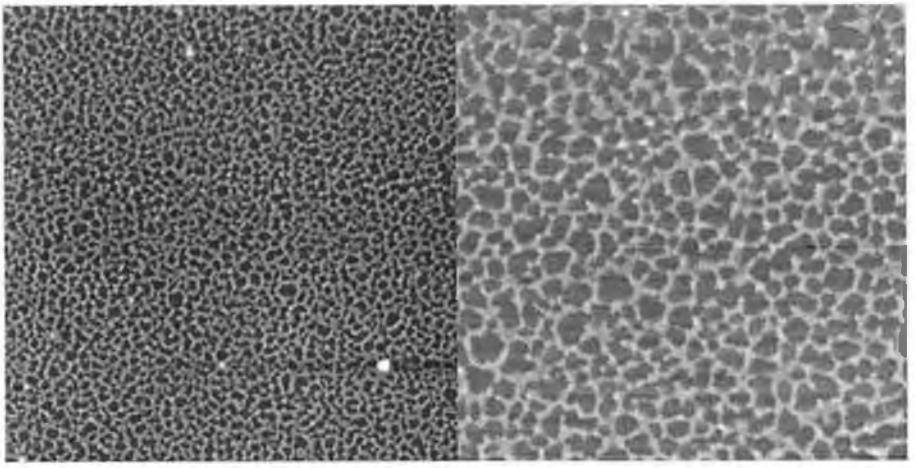

Figure C1. *AFM topographies prior to annealing. Left: 5.0 * 5.0μm^2 Z-range =10nm; Right: 3.2 * 3.2μm^2 Z-range = 12.5nm.*

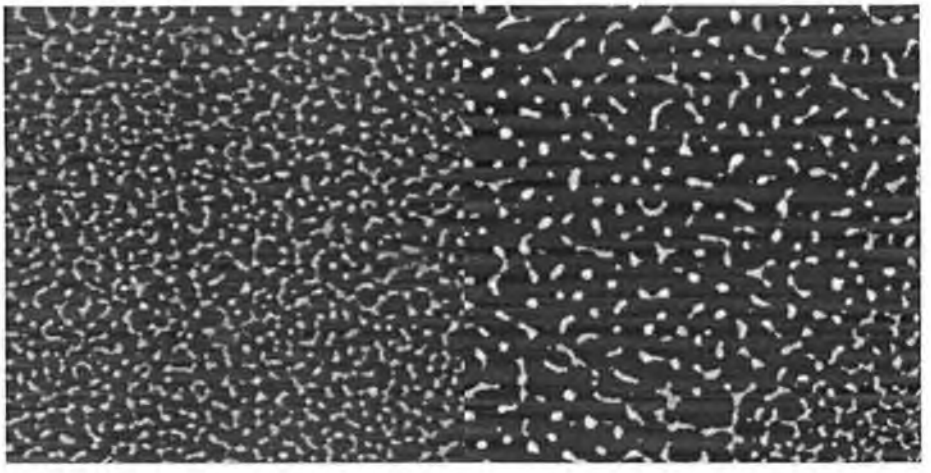

Figure C2. *AFM topographies for a range of annealing times. Left: 4 hours, 8*8μm^2 15nm; Right: 8 hours, 8*8μm^2 15nm.*

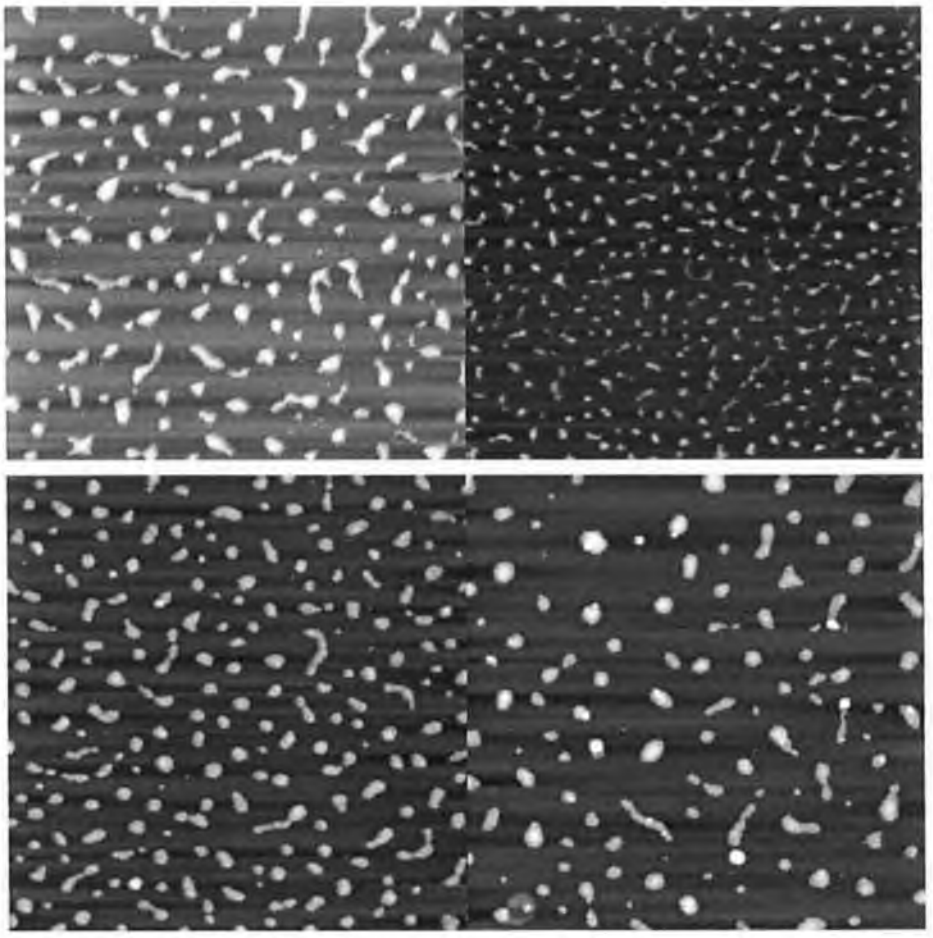

Figure C3. *AFM topographies for a range of annealing times. Top left: 12 hours, 6*6μm^2 Z-range 17.5nm; Top right: 16 hours, 6*6μm^2 Z-range 17.5nm; Bottom left: 24 hours, 6*6μm^2 Z-range 22.5nm; Bottom right: 24 hours, 8*8μm^2 Z-range 25nm.*

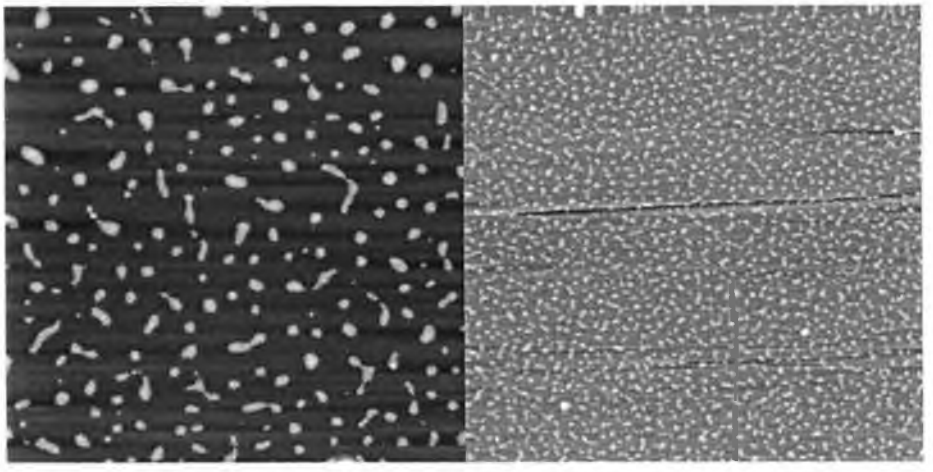

Figure C4. *AFM topographies for a range of annealing times. Left: 64.5 h, 10*10μm^2 Z-range 25nm; Right: 64.5 h, 14.3*14.3μm^2 Z-range 25nm.*

The in-plane correlation length of the surface undulations, $\Lambda(t)$, is obtained from a radial average of a 2-dimensional fast Fourier transform of the AFM image. Figure C5 shows the 2D-FFT of the films prior to annealing and the radial average of this 2D-FFT spinodal ring image is shown.

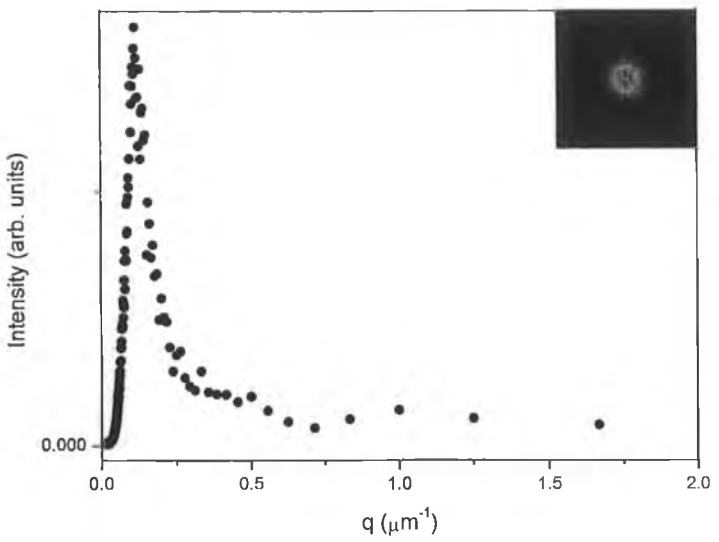

Figure C5 *Plot of the relative intensity versus wave vector q. Both wavelength and power are logarithmic scales. Inset: 2D-fast Fourier transform.*

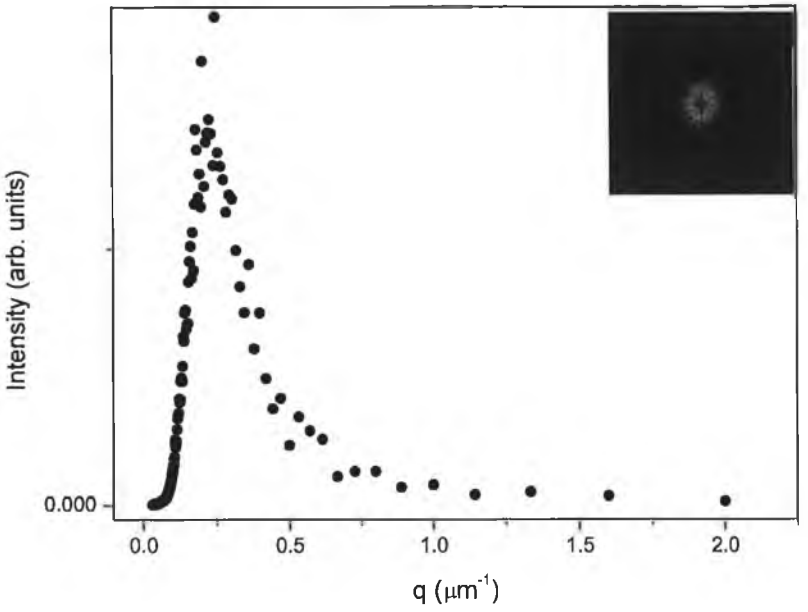

Figure C6 *shows the radial average of 2D-FFT plot of the 60-hours annealed AFM image, the inset shows the 2-D fast-Fourier transform.*

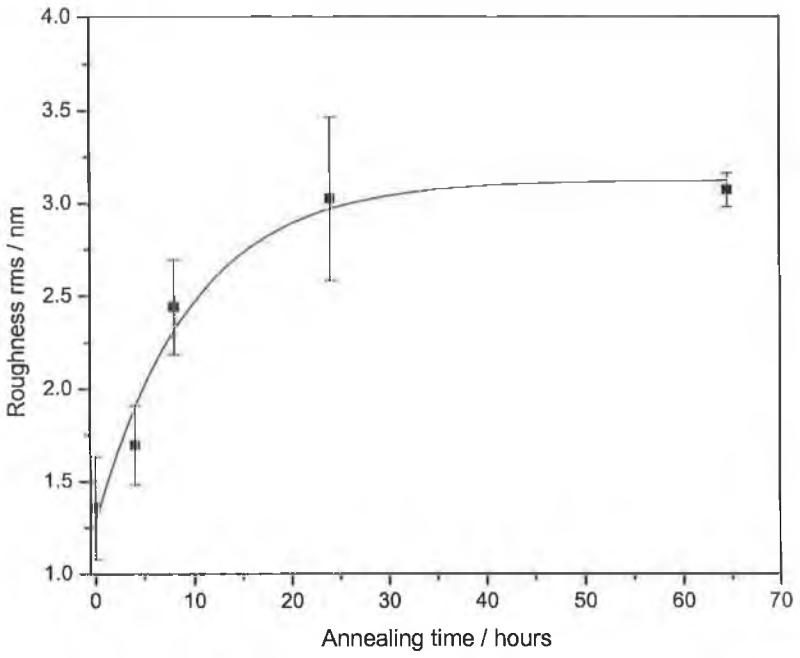

Figure C7 *Plot of the average roughness, rms, as a function of the annealing time at 75 °C.*

Figure C7 shows the average surface roughness rms, plotted as a function of the annealing time. It is a non-linear curve fit with rms standard deviations used as error bars. For all annealing images a sample number of six values of rms were determined, giving on average a data sample of thirty for each annealing time. The average rms values were then calculated.

Sample spin-cast on a solvent rinsed silicon substrate and annealed at 125°C

25 μL of a 0.25mmol solution of the organostannoxane cluster molecules in toluene was spin-coated onto a 1cm^2 solvent-rinsed native-oxide covered Si(111) wafer. The sample was annealed at 125°C for different times (0 h up to 60 h) and quenched to room temperature for AFM observations. Tapping mode AFM was carried out using a Digital Instruments Multimode AFM system. The annealing data is represented by two tapping mode AFM height images for each annealing time. The images range in scan size between 6μm and 8μm, with height variations between 10-20nm.

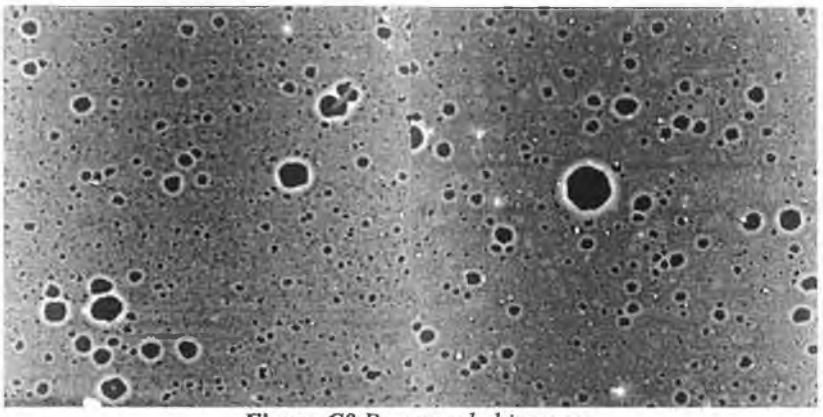

Figure C8 *Preannealed images*

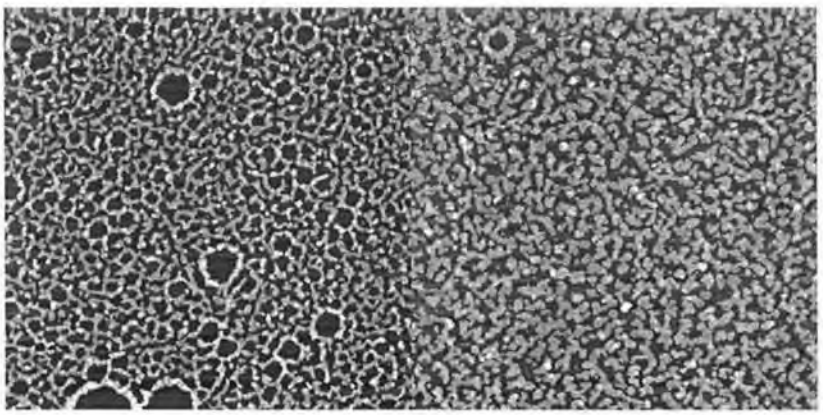

Figure C9 *4 h aneealing*

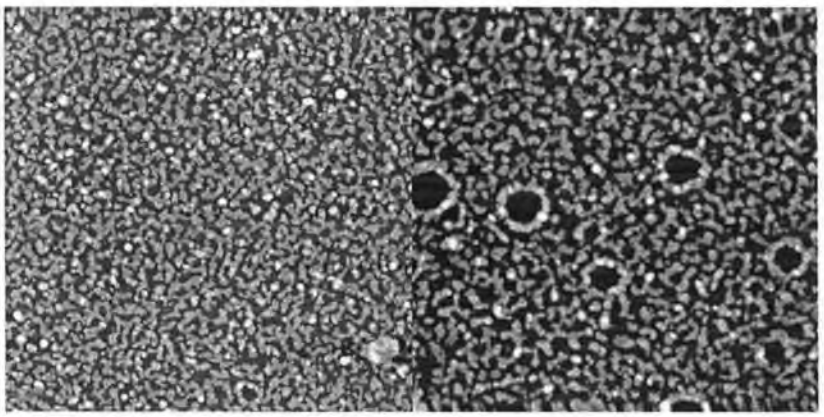

Figure C10 *8 h annealing*

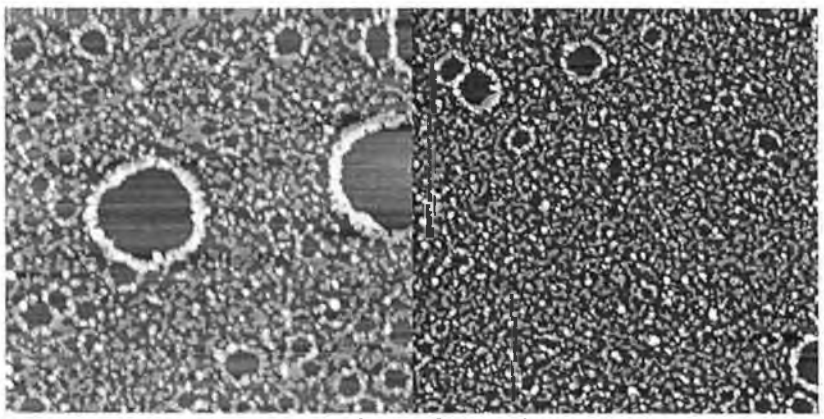

Figure C11 *12 h annealing*

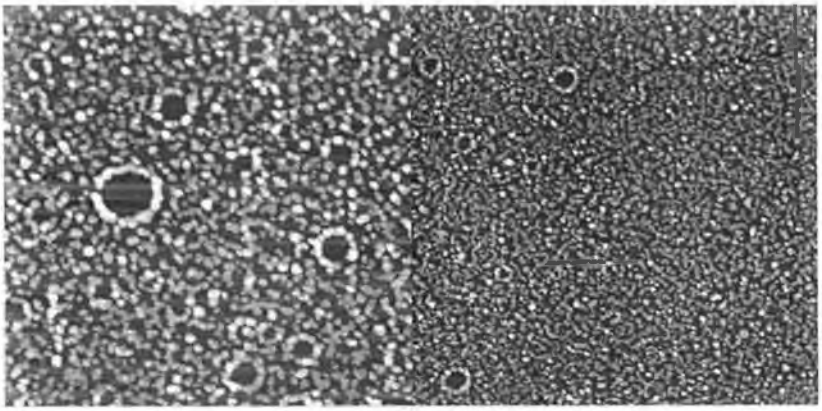

Figure C12 *16 h annealing*

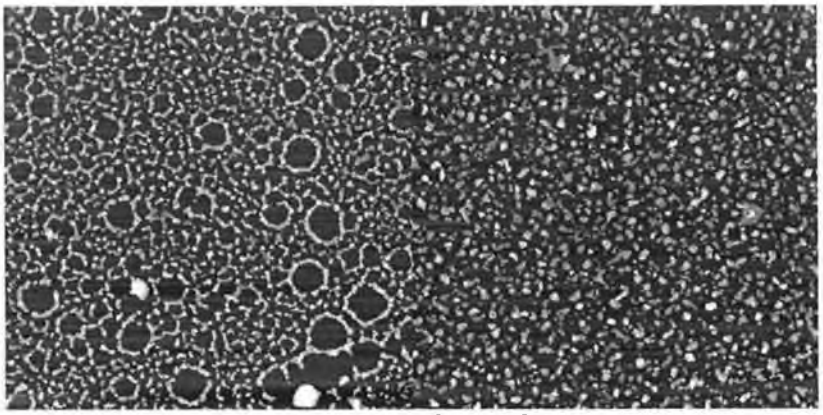

Figure C13 *20 h annealing*

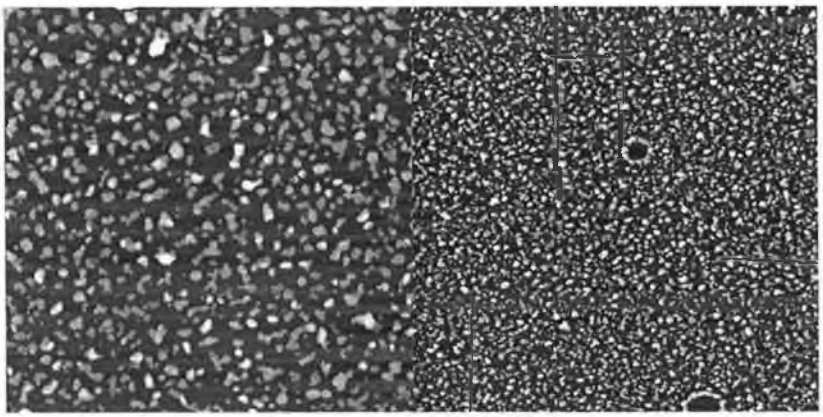

Figure C14 *24 h annealing*

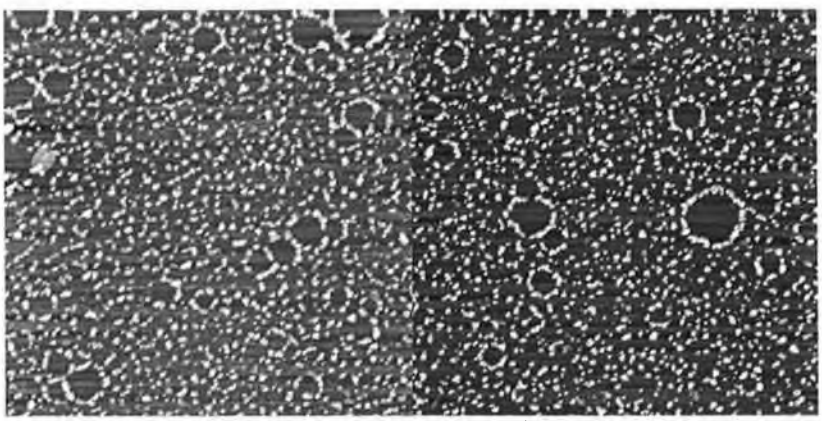

Figure C15 *40 h annealing*

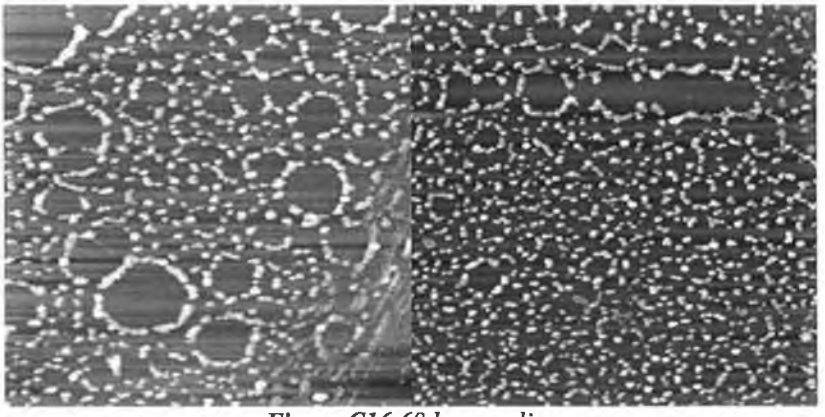

Figure C16 *60 h annealing*

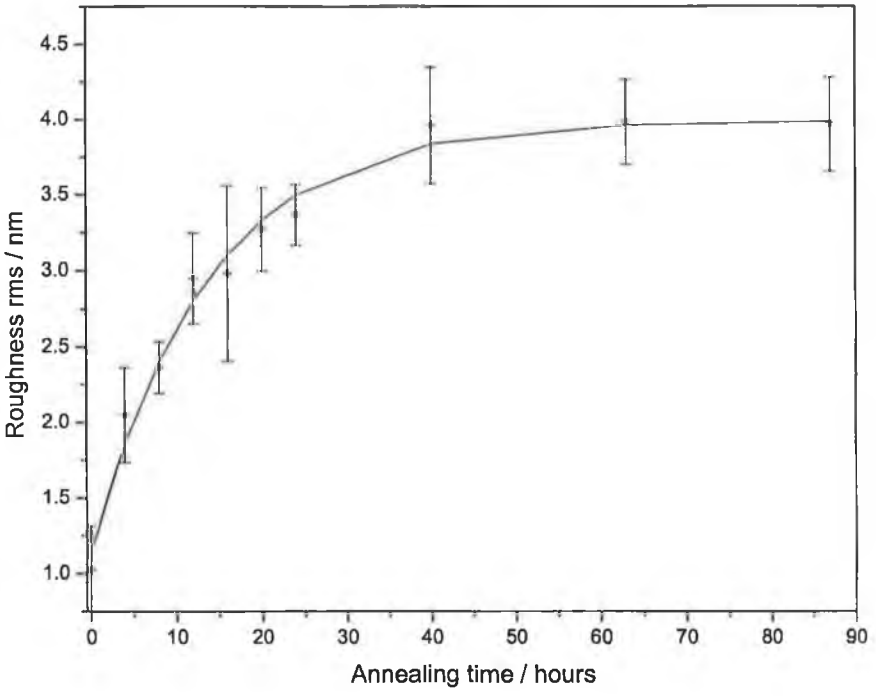

Figure C17 *Plot of the average roughness, R_{rms}, as a function of the annealing time at 125 °C.*

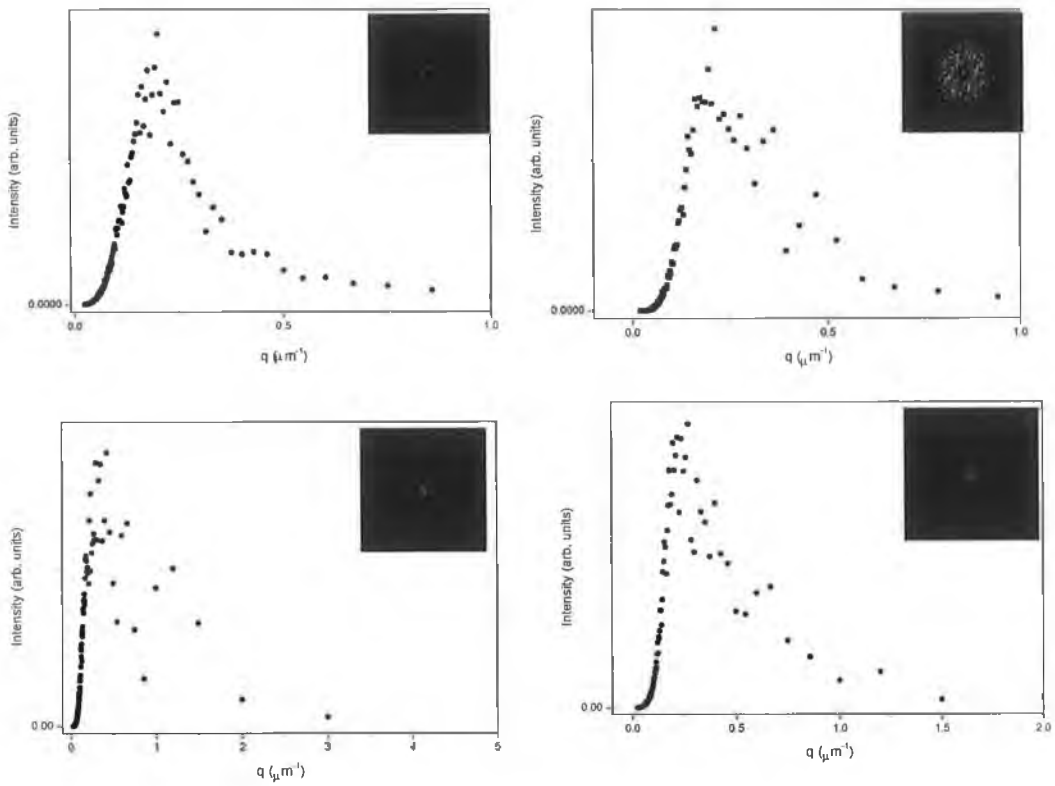

Figure C18 *shows plots of the radial averages of the 2D- FFT on the insets for 4 h, 8h, 12 h and 16 h respectively.*

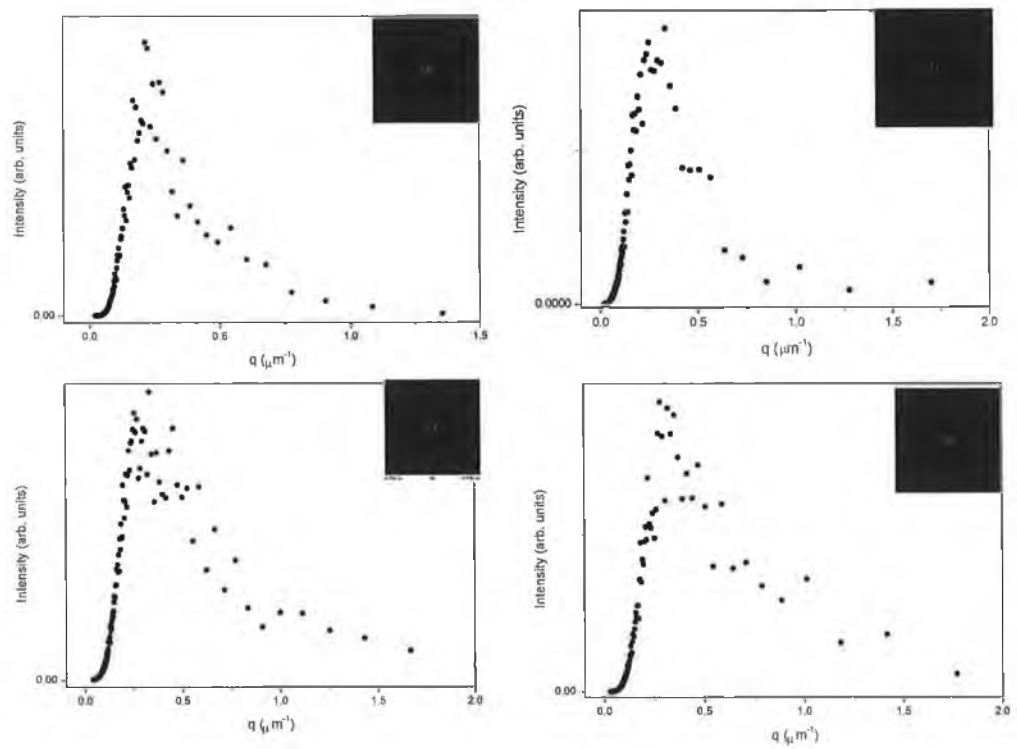

Figure C19 *shows plots of the radial averages of the 2D- FFT on the insets for 20 h, 24 h, 40 h and 60 h respectively.*

Appendix D

Photoemission Data for the Organostannoxane Cluster Molecule

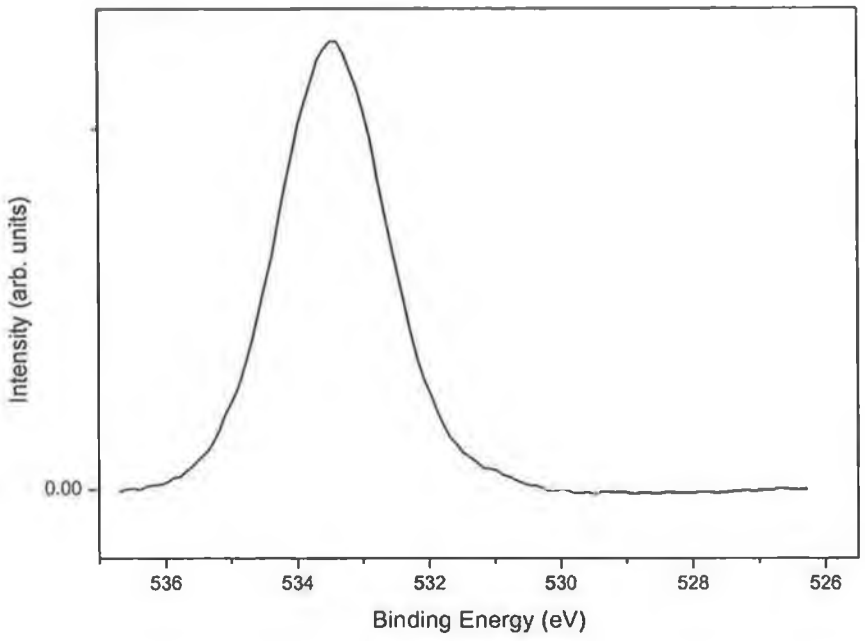

Figure D.1 *O1s core level photoemission spectrum of the organostannoxane cluster thin films (hν = 570.16eV).*

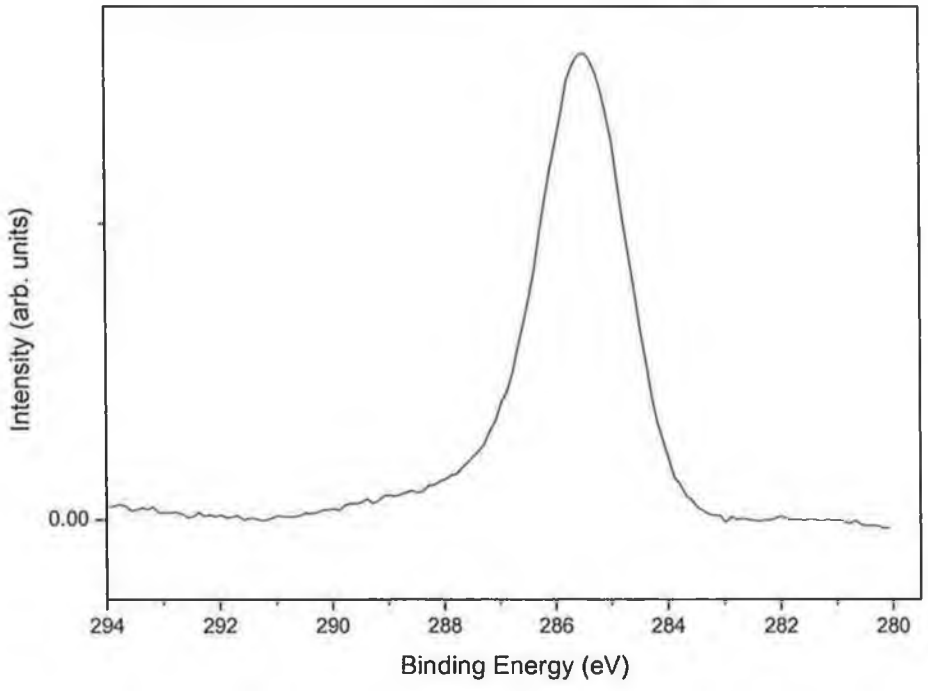

Figure D.2 *C1s core level photoemission spectrum of the organostannoxane cluster thin films (hν = 350eV).*

Appendix E

Electrochemical Studies of the Organostannoxane Cluster on Single Crystal Gold Electrodes

E.1 Experimental

For the electrochemical measurements carried out in DTU the set-up consists of an Autolab Pgstat 10 potentiostat (EcoChemie) using an in-house built electrochemical glass cell. All measurements were carried out using General Purpose Electrochemical System (GPES) version 4.9 software. The electrochemical glass cell is placed in a Faraday cage (Cypress systems) to reduce electronic noise. The glass cell houses three electrodes. The working electrode is a Au(111) bead electrode. The counter electrode is a platinum net on a platinum wire. The reference electrode is a reversible hydrogen electrode (RHE). The working electrode is operated in the meniscus mode so only the Au(111) facet is in contact with the solution.

The Reference Electrode:

For each new electrochemical set-up a new reversible hydrogen electrode was made. In each case a 1mm diameter flame-annealed platinum wire is inserted in to a clean 10cm Pyrex glass tube. The tube is subsequently melted onto the platinum wire by heating it in a hydrogen flame for 5 – 10 sec. The heating is performed from several directions to make the tube fit the wire closely. Electrolyte is added to the tube from a cleaned glass pipette once the tube has cooled down. A stream of H_2 is bubbled through a solution of electrolyte. The tube is then immersed in the solution and H_2 bubbles are allowed to enter the tube. The H_2 gas should cover approximately half the platinum wire inside the tube. The potential follows the equation:

$$E = -59.3mV * pH \text{ at } 25° C \qquad (E.1)$$

All data is plotted vs. a saturated calomel electrode by measuring the RHE vs. SCE, which was measured to be -0.408V.

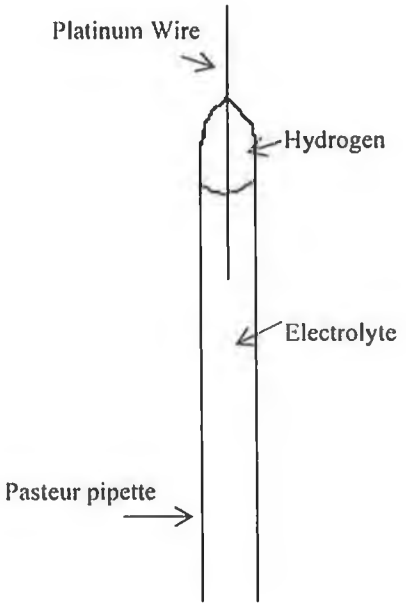

***Figure E.1** Schematic of the Reversible Hydrogen Electrode.*

The Counter Electrode:

A platinum-net on a platinum wire was used as a counter electrode in all measurements. The Pt-net was cleaned in a H_2 flame, rinsed with Millipore water and then transferred to the cell. A counter electrode is essential in electrochemical measurements to minimise any current flow through the reference electrode, since this may destabilise the reference electrode.

The Working Electrode:

All working electrodes were single crystal Au(111) prepared within the group of Prof. Jens Ulstrup (DTU) by the method of A. Hamelin [1,2,]

Prior to electrochemical measurements the electrodes were electro-polished to remove the outer layer of Au-atoms. This is important because the outer layer is disordered

due to adsorption or other molecular contamination. The Au electrode was then placed in a beaker with 0.1M H_2SO_4 and a Pt wire counter electrode. The Au electrode was connected to the (+) pole and the counter electrode to the (-) pole of a power supply. The voltage was then set to ca. 10 V, constant current. The Au (111) bead turns red because of gold oxide formation. The Au (111) bead is slowly lifted to make a hanging meniscus to ensure that the Au (111) surface is oxidised. After the oxidation the gold bead was lifted so that it is no longer in contact with the H_2SO_4. The reaction in H_2SO_4 is:

$$2Au + 3H_2O \rightarrow Au_2O_3 + 6H^+ + 6e^- \qquad (E.2)$$

The electrode was then placed in a beaker with 1M HCl. The chloride ions form a complex with gold oxide and after 10-20 sec the gold will have the usual colour again. The electrode was then washed with Millipore water and placed in an oven at 850° C to anneal for 8 h. Upon removal from the oven the electrode was allowed to cool. The electrode was then annealed in H_2 gas and deposited in a 0.0032M solution of the organostannoxane cluster molecule in toluene. The electrode was soaked in this solution for 6 h and on removal rinsed with a small amount (1-2 ml) of toluene. The electrode was then placed in the electrochemical cell operated in the meniscus mode so only the Au(111) facet is in contact with the solution.

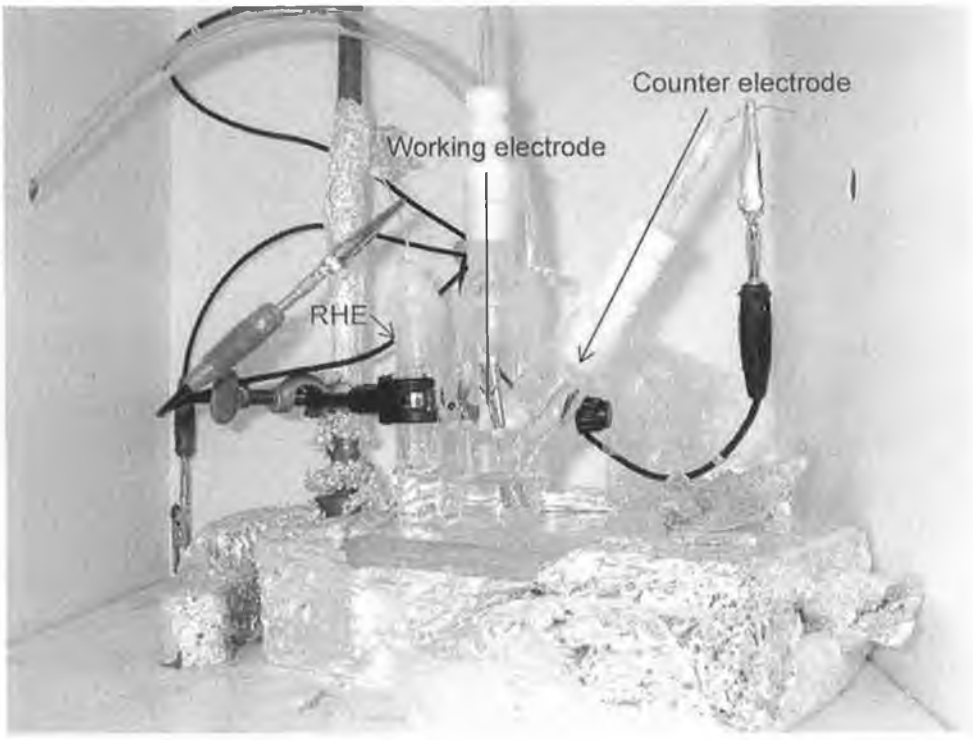

Figure E.2 *Electrochemical cell showing (left) the Reversible Hydrogen Electrode (RHE); (middle) the working Au(111) electrode; and (right) the counter electrode.*

Ultrapure Conditions:

The experiments were conducted under ultrapure conditions. All glassware was cleaned by boiling in 15% nitric acid followed by the procedure of rinsing in Millipore water, then sonicating in Millipore water and finally rinsing three times with Millipore water. The platinum wire for the counter electrode was annealed in a H_2 flame and then rinsed in Millipore water. All chemicals used were of ultrapure grade. The Au (111) working electrodes were electro-polished and annealed for 6 h before each experiment as described previously.

Removal of Oxygen:

Oxygen constitutes a major problem in all electrochemical experiments, mainly because it is reduced to water at low potentials. Dioxygen reduction is suppressed by

flowing a stream of wetted highly pure (99.999%) argon through the electrolyte solution for at least 45 min before the measurement. An overpressure of argon was also maintained above the electrolyte solution during measurement. The argon is guaranteed to contain less than 2 ppm of oxygen. The argon gas was further cleaned by passing through a Chrompack-Gas clean filter system (Varian). The oxygen concentration at the outlet of this filter is guaranteed 0.05ppm.

Electrolyte:

The electrolyte used through out these measurements was a solution of sodium perchlorate in $1x10^{-4}$M perchloric acid. This had a pH of 3.

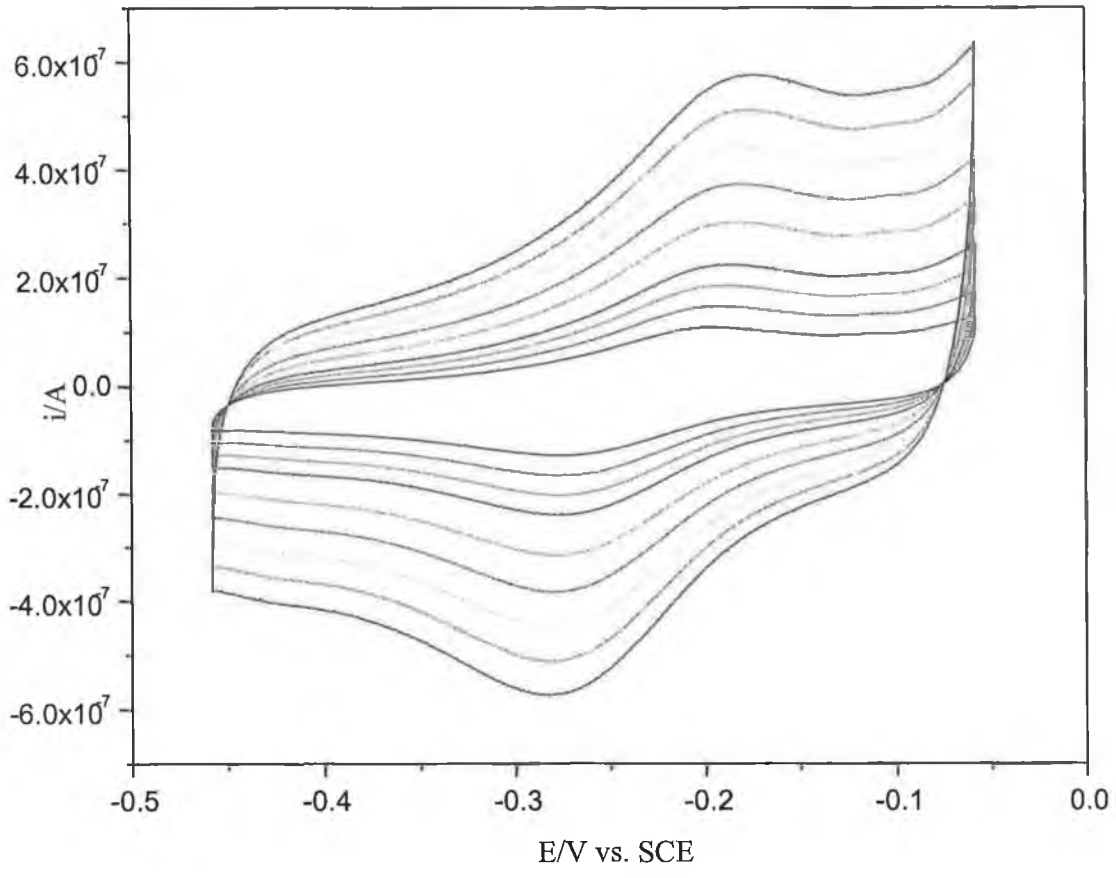

Figure E.1 *Initial CV results in the study of the organostannoxane cluster adsorbed on a single crystal Au (111) electrode in 0.1mmol perchloric acid (pH 3.0). Scan rate 20mVs^{-1} to 180mVs^{-1}..*

E.3 References

1. Hamelin A., **1996**, *J. Electroanal. Chem.*, 407, 1.

2. Hamelin A., Martins A.M., **1996**, *J. Electroanal. Chem.*, 407, 13.

Appendix F

Publications

List of Publications

1. *Interconnecting Carbon Nanotubes with an Inorganic Metal Complex,*
   Frehill F., Vos J.G., Benrezzak S., Koos A.A., Konya K., Rüther M.G., Blau W.J., Fonseca A., Nagy J.B., Biro L.P., Minett A., In het Panhuis A.,
   Journal of the American Chemical Society, **2002**, 124, 13694-13695.

Highlighted in Science/Technology Concentrates, *Chemical & Engineering News,* 2002, 80, 36.

2. *Covalent attachment of a Ruthenium complex to multi wall carbon nanotubes,*
   Benrezzak S., Frehill F., Rüther M.G., Fonseca A., Nagy J.B., Minett A.I., Blau W.J., Vos J.G., and In het Panhuis M.,
   SPIE Conference Proceedings, **2002**, 4876, 770-775.

3. *Characterization of covalent functionalized carbon nanotubes,*
   Rüther M.G., Frehill F., O'Brien J.E., Minett A.I., Blau W.J., Vos J.G., In het Panhuis M.,
   Journal of Physical Chemistry B, **2004**, 108, 9665-9668.

4. *Iron Wheels on Silicon: Wetting Behaviour and Electronic Structure of Adsorbed Organostannoxane Clusters,*
   Frehill F., Schulte K.H.G., Martin C.P., Wang L., Patel S., Purton J.A., Vos J.G., Moriarty P.,
   Langmuir, **2004**, 20, 6421-6429.

5. *Measurement of lateral charge propagation in $[Os(bipy)_2(PVP)_nCl]Cl$ thin films: a scanning electrochemical microscopy (SECM) approach,*
   O'Mullane A.P., Macpherson J.V., Unwin P.R., Cervera-Montesinos J., Manzanares J.A., Frehill F., Vos J.G.,
   Journal of Physical Chemistry B, **2004**, 108, 7219-7227.

J|A|C|S
COMMUNICATIONS

Published on Web 10/26/2002

Interconnecting Carbon Nanotubes with an Inorganic Metal Complex

Fiona Frehill,† Johannes G. Vos,† Sakina Benrezzak,‡ Antal A. Koós,|| Zoltan Kónya,§ Manuel G. Rüther,‡ Werner J. Blau,‡ Antonio Fonseca,§ Janos B. Nagy,§ Laszlo P. Biró,|| Andrew I. Minett,‡ and Marc in het Panhuis*,‡

National Centre for Sensor Research, School of Chemical Sciences, Dublin City University, Dublin 9, Ireland, Department of Physics, Trinity College Dublin, Dublin 2, Ireland, Facultes Universitaires Notre-Dame de la Paix, Laboratoire de RMN, 61 Rue de Bruxelles, B-5000 Namur, Belgium, and Hungarian Academy of Sciences, Research Institute for Technical Physics and Materials Science, H1525 Budapest, P.O. Box 49, Hungary

Received August 13, 2002

Carbon nanotubes have been shown to exhibit phenomenal physical properties. In addition, carbon nanotubes are an excellent platform for functionalization. Noncovalent sidewall functionalization of single and multiwall carbon nanotubes has been achieved by others and ourselves.[1−6] Covalent sidewall functionalization, however, has almost exclusively been carried out on single wall carbon nanotubes (SWNT). Chemical (covalent) functionalization has been achieved through electrochemical reduction of aryl diazonium salts,[7] ultrasonication with organic materials,[8] a coordinatively unsaturated Vaska's compound,[9] a diimide-activated amidation,[10] and by 1,3-dipolar cyclo additions.[11] End-to-end and end-to-side SWNT interconnects were formed by reacting chloride terminated SWNT with aliphatic diamine.[12]

In this paper, we report our approach to covalent attachment of an inorganic metal complex, [ruthenium(4,4′-dicarboxy-2,2′-bipyridine)(2,2′-bipyridyl)$_2$](PF$_6$)$_2$, ([Ru(dcbpy)(bpy)$_2$](PF$_6$)$_2$),[13−15] to amino functionalized multiwall carbon nanotubes.

To the best of our knowledge, this is the first report of multiwall carbon nanotube (MWNT) interconnects.

MWNT were produced by the catalytic chemical vapor deposition (CCVD) of acetylene (30 mL/min) as carbon source under 300 mL/min of N_2. The reaction temperature was 973 K, and the reaction time was 1 h using CoFe/alumina. To dissolve the support and metal particles, NaOH and HCl solution were used. The tubes were ball milled in a stainless steel drum for 100 h in a NH_3 atmosphere, resulting in shortened (200−300 nm) and open-ended MWNT, functionalized with amino (−NH$_2$) groups. In the IR spectra, characteristic bands due to C−NH$_2$ (1400 cm^{-1}) were observed.[16] Spectroscopy measurements showed an altered scanning tunneling spectroscopy (STS) spectrum.[16] The functional groups organized in islands are clearly visible in the topographic scanning tunneling microscopy (STM) images (Figure S1, see the Supporting Information).

The experimental procedure is as follows (see Scheme 1). Ten milligrams (0.011 mmol) of [Ru(dcbpy)(bpy)$_2$](PF$_6$)$_2$ **1A** was dissolved in 15 mL of thionyl chloride. The reaction mixture **1B** was refluxed under argon for 5 h. The thionyl chloride was removed by vacuum distillation. The remaining solid was partially dissolved in dichloromethane (DCM). Two milligrams of the MWNT functionalized with NH_2 (MWNT-NH$_2$) was sonicated in 5 mL of dichloromethane for 2 min and then added to the refluxed mixture. Ten milliliters of triethylamine was added. The solution mixture

Figure 1. Microscopy of amide linked MWNT interconnects. Tapping mode AFM image on glass substrate of resultant T- and Y-MWNT junctions after ruthenium complexation, indicated by circles. White lines indicate MWNT.

Scheme 1

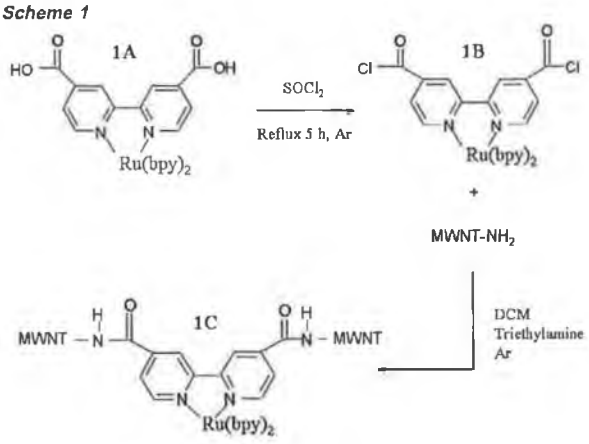

was stirred at room temperature under argon for 72 h. The product was then filtered to remove the solvents and washed with DCM. The product was placed in 20 mL of DCM and sonicated for 2 min. The solution was then allowed to settle for 24 h. Excess MWNT-NH$_2$ settled at the bottom, and the "functionalized ruthenium MWNT" **1C** product was in suspension in solution. A color change from dark red-orange (**1B**) to dark brown-green (**1C**) was observed after the reaction scheme was completed.

MWNT-NH$_2$ do not dissolve in dichloromethane. However, homogeneous solutions of **1C** were easily obtained. This is a good indication that the reaction scheme was successful. Tapping mode atomic force microscopy (AFM) images using a Digital Instruments Nanoscope IIIa are shown in Figure 1 (see also the Supporting Information, Figure S2). MWNT are indicated by the white lines in the figures.

* To whom correspondence should be addressed. E-mail: marc@panhuis.org.
† Dublin City University.
‡ Trinity College Dublin.
§ Facultes Universitaires Notre-Dame de la Paix.
|| Hungarian Academy of Sciences.

10.1021/ja028119q CCC: $22.00

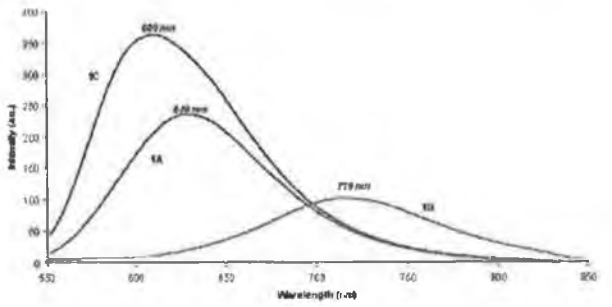

Figure 2. Emission spectroscopy (recorded in dichloromethane) on starting ruthenium complex (**1A**), chlorinated product (**1B**), and ruthenium nanotube complex (**1C**).

It has been reported that less than 2% of pristine tubes show junctions, whereas functionalization of single wall carbon nanotubes (SWNT) can increase this to 30%.[12] Multiple junctions can be observed in Figure S2 (see the Supporting Information) distinct from naturally occurring splitting of MWNT ropes. A close-up of a typical T- and Y-junction is shown in Figure 1. To verify that the tubes are not just overlapping, height analysis was carried out. Nanotube 1 has an approximate height of 7.5 nm above and below the junction. Nanotube 2 is 5.6 nm along its entire observed length. The Y-junction has a height of 9.3 nm both parallel and perpendicular to either nanotube 1 or 2. This indicates that nanotubes 1 and 2 are not overlapping, as this would result in a height in excess of 13 nm. A similar observation can be made at the T-junction between nanotubes 3 and 4. Tube 3 at a height of 10 nm above and below the junction and tube 4 varied between 7 and 9 nm along its length. The T-junction has a height of 12 nm, which is far less than 17 nm as would be expected for overlapping tubes.

As the amino functionalization occurs in islands, it is expected that MWNT are interconnected through more than one ruthenium complex.

UV/vis absorption spectra were carried out in DCM using a Shimadzu UV3100 UV−vis−NIR spectrophotometer. The ruthenium complex **1A** has characteristic absorption bands at 285 and 454 nm. The chlorinated product **1B** exhibits a red shift to 286 and 498 nm, whereas the ruthenium nanotube complex **1C** results in a red shift to 290 nm and a blue shift to 459 nm.

Emission spectra were recorded in DCM using a LS50-B luminescence spectrophotometer, equipped with a red sensitive Hamamatsu R298 PMT detector. Figure 2 shows the emission spectra of the components described in Scheme 1. Using 450 nm excitation wavelength, we found that the emission spectra for **1A** show a characteristic maximum at 628 nm associated with ruthenium complexes. The acid chloride **1B**, on the other hand, emits at 719 nm. The ruthenium nanotube complex **1C** has a maximum at 609 nm, a blue shift of 110 nm as compared with **1B** and 19 nm with **1A**. The observed shifts are expected on the basis of the nature of the modified substituents.

The changes in maxima for absorption and emission spectra observed between starting materials **1A**, **1B**, and product **1C** together with the solubility of **1C** confirmed the chemical modifications. The fact that **1C** emits at a different wavelength to both **1A** and **1B** makes it unlikely that the 609 nm signal is due to unbound starting material (**1A**).

In conclusion, we have presented strong evidence that multiwall carbon nanotube interconnects through amide linkage with a ruthenium complex were successfully created. Interconnects were visualized through AMF imaging, which showed multiple T- and Y-junctions. Absorption and emission spectroscopy showed significant changes between starting components and the resulting ruthenium nanotube complex indicative of a successful chemical modification. Carbon nanotube functionalization is important for sensor applications, as it will allow specific detection of biological entities such as proteins. The inclusion of a ruthenium complex is not essential for creating carbon nanotube interconnects. However, ruthenium complexes could be essential in sensing applications through (electrochemical) monitoring of the change in redox potential or in transistor applications through (photophysical and electrochemical) switching of the contact between MWNT.

Acknowledgment. This work was funded by the European Research Training Network Programs NANOCOMP and COMELCAN. F.F. and J.G.V. thank Enterprise Ireland for financial assistance.

Supporting Information Available: Topographic STM images of individual MWNT-NH_2 and tapping mode AFM image of MWNT junctions (PDF). This material is available free of charge via the Internet at http://pubs.acs.org.

References

(1) Curran, S. A.; Ajayan, P. M.; Blau, W. J.; Carroll, D. L.; Coleman, J. N.; Dalton, A. B.; Davey, A. P.; Drury, A.; McCarthy, B.; Maier, S.; Strevens, A. *Adv. Mater.* **1998**, *10*, 1091−1093.
(2) Coleman, J. N.; Dalton, A. B.; Curran, S. A.; Rubio, A.; Davey, A. P.; Drury, A.; McCarthy, B.; Lahr, B.; Ajayan, P. M.; Roth, S.; Barklie, R. C.; Blau, W. J. *Adv. Mater.* **2000**, *12*, 213−216.
(3) Dalton, A. B.; Stephan, C.; Coleman, J. N.; McCarthy, B.; Ajayan, P. M.; Lefrant, S.; Bernier, P.; Blau, W. J.; Byrne, H. J. *J. Phys. Chem. B* **2000**, *104*, 10012−10016.
(4) Dalton, A. B.; Coleman, J. N.; in het Panhuis, M.; McCarthy, B.; Drury, A.; Blau, W. J.; Paci, B.; Nunzi, J.-M.; Byrne, H. J. *J. Photochem. Photobiol., A: Chem.* **2001**, *144*, 31−41.
(5) Chen, R. J.; Zhang, Y.; Wang, D.; Dai, H. *J. Am. Chem. Soc.* **2001**, *123*, 3838−3839.
(6) O'Connell, M. J.; Boul, P.; Ericson, L. M.; Huffman, C.; Wang, Y.; Haroz, E.; Ausman, K. D.; Smalley, R. E. *Chem. Phys. Lett.* **2001**, *342*, 265−271.
(7) Georgakilas, V.; Kordatos, K.; Prato, M.; Guldi, D. M.; Holzinger, M.; Hirsch, A. *J. Am. Chem. Soc.* **2002**, *124*, 760−761.
(8) Koshio, A.; Yudusaka, M.; Zhang, M.; Iijima, S. *Nano Lett.* **2001**, *1*, 361−363.
(9) Banerjee, S.; Wong, S. S. *Nano Lett.* **2002**, *2*, 49−53.
(10) Huang, W.; Taylor, S.; Fu, K.; Zhang, D.; Hanks, T. W.; Rao, A. M.; Sun, Y.-P. *Nano Lett.* **2002**, *2*, 311−314.
(11) Bahr, J. L.; Yang, J.; Kosynkin, D. V.; Bronikowski, M. J.; Smalley, R. E.; Tour, J. M. *J. Am. Chem. Soc.* **2001**, *123*, 6536−6542.
(12) Chu, P. W.; Duesburg, G. S.; Dettlaff-Weglikowska, U.; Roth, S. *Appl. Phys. Lett.* **2002**, *80*, 3811−3813.
(13) Ferguson, J.; Mau, A. W. H.; Sasse, W. H. F. *Chem. Phys. Lett.* **1979**, *68*, 21−23.
(14) Nazeeruddin, Md. K.; Kalyanasundaram, K. *Inorg. Chem.* **1989**, *28*, 4251−4255.
(15) Vos, J. G. *Polyhedron* **1992**, *11*, 2285−2299.
(16) Kónya, Z.; Vesselenyi, I.; Niesz, K.; Kukovecz, A.; Demortier, A.; Fonseca, A.; Delhalle, J.; Mekhalif, Z.; Nagy, J. B.; Koos, A. A.; Osváth, Z.; Kocsonya, A.; Biró, L. P.; Kiricsi, I. *Chem. Phys. Lett.* **2002**, *360*, 429−435.

JA028119Q

Covalent attachment of a Ruthenium complex to multi wall carbon nanotubes

S. Benrezzak*[a], F. Frehill[b], M.G. Rüther[a], A. Fonseca[c], J. Nagy[c], A.I. Minett[a], W.J. Blau[a], J.G. Vos[b], M. in het Panhuis[a]

[a]Trinity College Dublin (Ireland); [b]Dublin City Univ. (Ireland); [c]Univ. Notre-Dame de la Paix (Belgium)

ABSTRACT

Amino functionalized multi wall carbon nanotubes (MWNT) were reacted with an inorganic Ruthenium complex, $\{[Ru(dcclbpy)(bpy)_2]\cdot(PF_6)_2\}$, in the attempt to covalent attach the Ruthenium complex to the MWNT. The covalent attachment between the Ruthenium complex and the carbon nanotubes is achieved by forming of an amide group. Absorption and emission spectroscopy indicated that a reaction between the amino functionalized MWNT and the Ruthenium complex occurred. Atomic fore microscopy (AFM) images gave further evidence of a successful attachment of the Ruthenium complex to MWNT by showing multiple junctions between MWNT distinct from naturally occurring splitting of MWNT ropes.

Keywords: Carbon nanotubes, Ruthenium complex

1. INTRODUCTION

Carbon nanotubes have been shown to exhibit phenomenal physical properties. In addition, carbon nanotubes are an excellent platform for chemical functionalization. Non-covalent side-wall functionalization has been archived by ourself and other groups.[1-23456] Covalent side-wall functionalization has almost been carried out on single wall carbon nanotubes (SWNT). The covalent functionalization of SWNT has been achieved through electrochemical reduction of aryl diazonium salts[7], a co-ordinately unsaturated Vaska's compound[8] and using 1,3-dipolar cyclo additions.[9] End-to-end and end-to-side SWNT interconnects were formed by reacting chloride terminated SWNT with aliphatic diamine.[10] The characterisation of functionalized carbon nanotubes relies on UV/VIS, Raman, and FT-IR spectroscopy, transmission electron and atomic force microscopy. Liquid NMR spectroscopy is difficult to employ because of the poor solubility of functionalized carbon nanotubes. In this paper we report the approach of a covalent attachment of an inorganic Ruthenium complex, $\{[Ru(dcby)(bpy)_2]\cdot(PF_6)_2\}$,[11-1213] to amino functionalized multi wall carbon nanotubes (MWNT).

2. METHODOLOGY

Emission spectra were recorded in dichloro methane using a LS50-B luminescence spectrometer, equipped with a red sensitive Hamamatsu R298 PMT detector. UV/VIS absorption spectra were carried out in dichloromethane using a Shimadzu UV3100 UV-Vis-NIR spectrometer. Atomic force microscopy (AFM) images were taken with a Digital Instruments Nanoscope IIIa in tapping mode.

* benrezzs@tcd.ie; phone +353 (0)1 608 1469; fax +353 (0)1 671 1759; Materials Ireland, Physics Department, Trinity College, Dublin 2, Ireland

3.RESULTS

3.1 Synthesis

The synthetic route of the attachment of an inorganic Ruthenium complex with multi wall carbon nanotubes (MWNT) is shown in Figure 1. Amino functionalized MWNT **3** used in the synthesis were synthesised in two steps. First, MWNT were produced by chemical vapour deposition (CCVD) using 30 mL/min of acetylene as carbon source and 300 mL/min of nitrogen. The reaction time was kept at 973K for one hour using CoFe/alumina. The support material and metal particles were removed afterwards by treating the MWNT with sodium hydroxide and hydrogen chloride solution. The tubes were then ball milled in a stainless steel drum for 100 hours in an ammoniac atmosphere. The resulting tubes were shortened (200-300nm), open-ended and functionalized with amino ($-NH_2$) groups. The final amino functionalized MWNT can be characterized by IR spectroscopy which shows characteristic bands at 1400 cm^{-1} due to the amino groups.

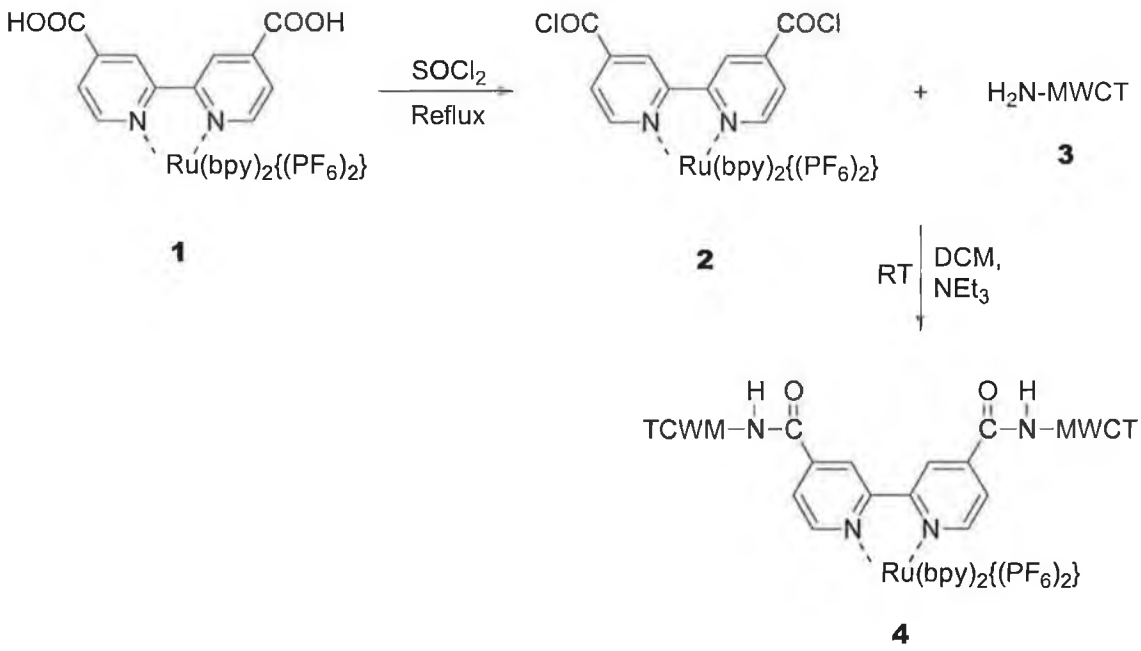

Figure 1: Schematic representation of the synthetic route to form a covalent attachment between amino functionalized MWNT **3** and an inorganic Ruthenium complex **2**.

The synthesis of the ruthenium polypyridyl complex $\{[Ru(4,4'\text{-dcbpy})(bpy)_2]\cdot(PF_6)_2\}$ **1**, where 4,4'-dcbpy is [2,2']-bipyridinyl-4,4'-dicarboxy acid, is described elsewhere.[14] The corresponding acid chloride complex **2** $\{[Ru(4,4'\text{-dcclbpy})(bpy)_2]\cdot(PF_6)_2\}$, where 4,4'dcclbpy is [2,2']-bipyridinyl-4,4'-dicarbolyl dichloride, was synthesised by dissolving 10mg (0.011mmol) of **1** in 15mL of thionyl chloride and refluxing the reaction mixture under argon for 5 hours. The remaining thionyl chloride was removed by vacuum distillation. For the synthesis of **4** 2mg of amino functionalized MWNT (NH_2-MWNT) **3** were sonicated for 5 minutes in dichloromethane and added to a mixture of 10mg of **2** in dichloromethane. 10mL triethylamine were added and the reaction mixture was stirred for three days at room temperature under an argon atmosphere. To remove the solvent the reaction mixture was filtered and washed with dichloromethane. The reaction product on the filter paper was placed in fresh dichloromethane and sonicated for 2 min and allowed to settle for 24 hours where excess MWNT-NH_2 settled at the bottom. At the start of the reaction the reaction mixture had a dark reddish-orange colour. After placing the reaction product in fresh dichloromethane and sonication the colour changed to dark-reddish-green. The colour change from orange to green suggests that a reaction between the MWNT-NH_2 and Ruthenium-complex **2** occurred and a covalent attachment was achieved.

3.2 Absorption and emission spectroscopy

UV/VIS and emission spectra were taken for the initial Ruthenium complex **1**, the corresponding acid chloride **2** and the MWNT-Ruthenium-complex **4**. In the UV/VIS spectrum the Ruthenium complex **1** has characteristic absorption bands at 285 and 454nm. The corresponding acid chloride **2** exhibits a red shift to 286 and 498nm, whereas the MWNT-Ruthenium-complex **4** results in a red shift to 290nm and a blue shift to 459nm. The UV/VIS spectra are all very similar for the initial Ruthenium complex **1** and the MWNT-Ruthenium-complex **4** and thus cannot give a precise answer if the reaction scheme in Figure 1 was successful. On the other hand the emission spectra show significant differences for the initial Ruthenium complex **1** and the MWNT-Ruthenium-complex **4**. In Figure 2 are shown the emission spectra of the initial Ruthenium complex **1**, the corresponding acid chloride **2** and the MWNT-Ruthenium-complex. Using 450nm excitation wavelength the emission spectrum for **1** shows a characteristic maximum at 628.5nm associated with Ruthenium complexes. The corresponding acid chloride **2** results in a red shift of 84.4nm to 716.9nm. The MWNT-Ruthenium-complex **4** has a maximum at 609nm, a blue shift of 107.9nm compared with **2** and 19.5nm with **1**.

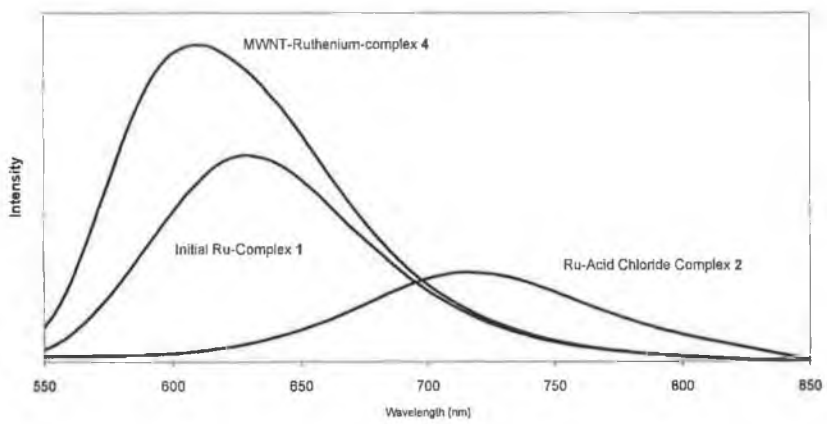

Figure 2: Emission spectra for the compounds **1**, **2** and **4**

The emission spectra suggest that the reaction between **2** and **3** was successful and a covalent attachment of the Ruthenium complex to the MWNT was achieved. In Table 1 is summarized the UV/VIS and emission maxima for the compounds **1**, **2** and **4**. The changes in the peak maxima of the absorption and emission spectra suggest that the chemical modification of amino functionalized MWNT **3** with a chloride acid of the Ruthenium complex **2** was successful.

Table 1: UV/VIS and emission maxima for **1**, **2**, and **4**

Compound	λ_{max} (nm) UV/VIS	$\lambda_{max\ (nm)}$ Emission
Initial Ruthenium Complex **1**	285 ; 454	630
Ruthenium acid chloride complex **2**	286 ; 498	717
MWNT-Ruthenium-complex **4**	290 ; 459	609

However, the absorption and emission spectra do not provide the necessary proof that the Ruthenium complex is covalent attached to the MWNT. A non covalent attachment of the Ruthenium complex may lead to a shift in the peak maxima of absorption and emission spectra as well. The colour change from orange to green observed after the reaction product was placed into fresh dichloromethane may be a result of Ruthenium-(III)-complexes which can be a side product of the reaction and is under further investigation.

3.3 Atomic force microscope images

Further evidence if the reaction scheme shown in Figure 1 was successful can provide atomic force microscopy (AFM). In Figure 3 are shown AFM images of the MWNT-Ruthenium-complex **4** after the reaction with the Ruthenium complex **2**. MWNT are indicated in these images by the white lines. It has been reported that less than 2% of pristine tubes show junction, whereas functionalization of single wall carbon nanotubes (SWNT) can increase this up to 30%.[10] Multiple junctions can be observed in Figure 3 distinct from naturally occurring splitting of MWNT ropes. A close up of a typically T- and Y-junction is shown in Figure 3b. To verify that the tubes are not just overlapping, height analysis was carried out. Nanotube 1 has an approximate height of 7.5 nm above and below the junction. Nanotube 2 is 5.6 nm along its entire tube. The Y-junction has a height of 9.3 nm both parallel and perpendicular to either nanotube 1 or 2. This indicates that nanotube 1 and 2 are not overlapping as this would result in a height in excess of 13 nm. A similar observation can be made at the T-junction between nanotube 3 and 4. Tube 3 at a height of 10 nm above and below the junction and Tube 4 varied between 7 and 9 nm along its length. Whereas, the T-junction has a height of 12 nm, far less than, in excess of 17 nm as would be expected for overlapping tubes.

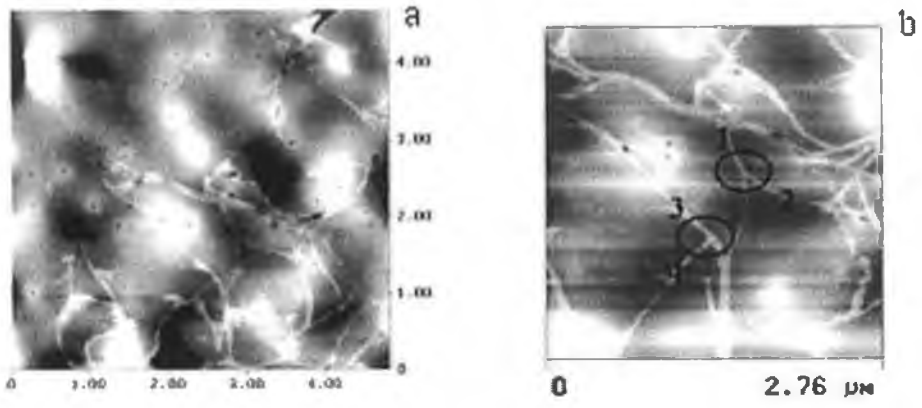

Figure 3: (a) Tapping mode AFM on glass substrate of resultant junctions after reaction with the Ruthenium complex. White lines indicate MWNT. (b) Close up of T- and Y-MWNT junction, indicated by circles.

The AFM images are strong evidence that the reaction scheme shown in Figure 1 was successful and a covalent attachment between MWNT and the Ruthenium complex was achieved because in the increase of T- and Y-junctions after the reaction. In Figure 4 is shown a model for a T-junction formed by two MWNT covalent attached to a Ruthenium complex.

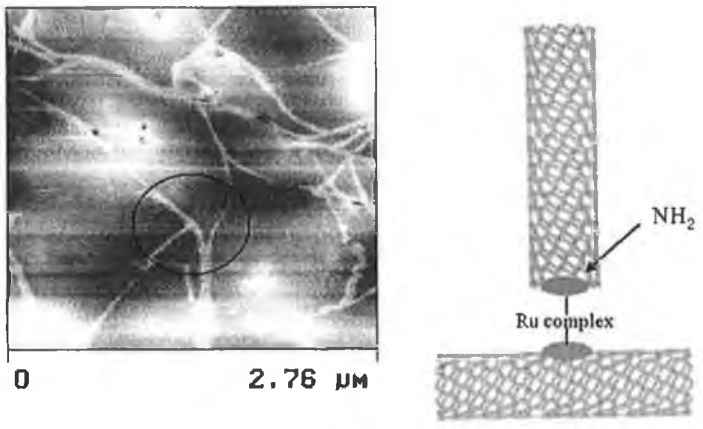

Figure 4: Model of a T-junction formed by two MWNT interconnected by a Ruthenium complex.

4. CONCLUSIONS

We have successfully reacted amino functionalized multi wall carbon nanotubes (MWNT) with an acid chloride of an inorganic Ruthenium complex. There is evidence that an amide group was formed and the nanotubes are linked together through the Ruthenium complex. Absorption and emission spectroscopy showed changes in the spectra between the starting materials and formed MWNT-Ruthenium-complex indicating that a chemical reaction between the amino functionalized MWNT and the acid chloride of the Ruthenium complex occurred. Further evidence for a covalent attachment of the Ruthenium complex to MWNT was found by atomic force microscopy (AFM) images. The images showed an increase in T- and Y-junctions after the reaction what strongly suggests that the reaction between amino functionalized MWNT and the acid chloride of the Ruthenium complex was successful.

ACKNOLEDGMENTS

This work funded by the European Network Programs NANOCOMP and COMELCAN.

REFERENCES

1. A.S. Curran, P.M. Ajayan, W.J. Blau, D.L. Carroll, J.N. Coleman, A.B. Dalton, A.P. Davey, A. Drury, B. McCathy, S. Maier, A. Strevens, "A Composite from Poly(*m*-phenylenevinylene-*co*-2,5-dioctoxy-*p*-phenylenevinylene) and Carbon Nanotubes: A Novel Material for Molecular Optoelectronics ", *Adv. Mater.*, **10**, pp. 1091-1093, 1998.

2. J.N. Coleman, A.B. Dalton, S.A. Curran, A. Rubio, A.P. Davey, A. Drury, M. McCarthy, B. Lahr, P.M. Ajayan, S. Roth, R.C. Barklie, W.J. Blau, "Phase Separation of Carbon Nanotubes and Turbostratic Graphite Using a Functional Organic Polymer", *Adv. Mater.*, **12**, pp. 231-216, 2000.

3. A.B. Dalton, C. Stephan, J.N. Coleman, B. McCarthy, P.M. Ajayan, S. Lefrant, P. Bernier, W.J. Blau, H.J. Byrne, "Selective Interaction of a Semiconjugated Organic Polymer with Single-Wall Nanotubes", **104**, *J. Phys. Chem. B*, pp. 10012-10016, 2000.

4. A.B. Dalton, J.N. Coleman, M. in het Panhuis, B. McCarthy, A. Drury, W.J. Blau, B. Paci, J.-M. Nunzi, H.J. Byrne, " ", **144**, *J. Photochem. Photobio. A:Chem.*, pp. 31-41, 2001.

5. R.J. Chen, Y. Zhang, D. Wang, H. Dai, " Noncovalent Sidewall Functionalization of Single-Walled Carbon Nanotubes for Protein Immobilization ", **123**, *J. Am. Chem. Soc.*, pp. 3838-3839, 2001.

6. M.J. O'Connell, P. Boul, L.M> Ericson, C. Huffman, Y. Wang, E. Haroz, K.D. Ausman, R.E. Smalley, "", **342**, *Chem. Phys. Lett.*, pp. 265-271, 2001.

7. V. Georgakilas, K. Kordatos, M. Prato, D.M. Guldi, M. Holzinger, A. Hirsch, " Organic Functionalization of Carbon Nanotubes ", **124**, *J. Am. Chem. Soc.*, pp. 760-761, 2002.

8. S. Banerjee, S.S. Wong, "Functionalization of Carbon Nanotubes with a Metal-Containing Molecular Complex", **2**, *Nano. Lett.* pp. 49-53, 2002.

9. L.J. Bahr, J. Yang, D.V. Kosynkin, M.J. Bronikowski, R.E. Smalley, J.M. Tour, " Functionalization of Carbon Nanotubes by Electrochemical Reduction of Aryl Diazonium Salts: A Bucky Paper Electrode", **123**, *J. Am. Chem. Soc.*, pp. 6536-6542, 2001.

10. P.W. Chu, G.S. Duesberg, U. Dettlaff-Wegiikowska, S. Roth, "Interconection of carbon nanotubes by chemical functionalization", **80**, *Appl. Phys. Lett.*, pp. 3811-3813, 2002.

11. J. Ferguson, A.W.H. Mau, W.H.F. Sasse, "Localization of electronic excitation energy in Ru(2,2'-bipyridine)$_2$(2,2'-bipyridine-4,4'-dicarboxylic acid)$^{2+}$ and related complexes ", **68**, *Chem. Phys. Lett.*, pp. 21-24, 1979.

12. Md.K. Nazeeruddin, K. Kalyanasundaram, "Acid-base behavior in the ground and excited states of ruthenium(II) complexes containing tetraimines or dicarboxybipyridines as protonatable ligands", **28**, *Inorg. Chem.*, pp. 4251-4259, 1989.

13. J.G. Vos, "Excited-state acid-base properties of inorganic compounds", **11**, *Polyhedron*, pp. 2285-2299, 1992.

14. P.J. Giordano, C.R. Bock, M.S. Wrighton, L.V. Interrante, R.F.C. Williams, "Exited state proton transfer of a metal complex: determination of the acid dissociation constant for a metal-to-ligand charge transfer state of a Ruthenium(II) complex", **99**, *J. Am. Chem. Soc.*, pp. 3187-3189, 1977.

Characterization of Covalent Functionalized Carbon Nanotubes

Manuel G. Rüther,[†] Fiona Frehill,[‡] John E. O'Brien,[§] Andrew I. Minett,[†] Werner J. Blau,[†] Johannes G. Vos,[‡] and Marc in het Panhuis*[,#]

Departments of Physics and Chemistry, Trinity College Dublin, Dublin 2, Ireland, National Centre for Sensor Research, School of Chemical Sciences, Dublin City University, Dublin 9, Ireland, and Department of Physics & NanoTech Institute, the University of Texas at Dallas, 2601 North Floyd Road, Richardson, Texas 75083

Received: March 31, 2004

The characterization of chemically modified carbon nanotubes has been achieved using ^{13}C nuclear magnetic resonance (NMR) spectroscopy. Amino-functionalized multiwall carbon nanotubes (MWNT−NH_2) were reacted with a ^{13}C terephthalic acid. Covalent attachment of the acid to the nanotubes is confirmed by ^{13}C NMR and 2D NMR through the presence of amide grouping resonances.

1. Introduction

Covalent attachment of functional groups to carbon nanotubes has received an increasing amount of attention in the past years. It is thought that covalent coupling of nanotubes to one another or to molecular entities can lead to advances in nanodevice applications such as nanosized electronics and sensing. Coupling has almost exclusively been achieved using ester or amide linkages. Amides have been the primary linkage method for nanotube interconnects,[1,2] the covalent attachment of proteins,[3−5] DNA,[6,7] nanocrystals,[8,9] and metal containing complexes.[1,10−12]

However, the characterization methods employed to confirm the covalent attachment between carbon nanotubes and other entities have so far provided only indirect evidence. For example, in our work on interconnecting multiwall carbon nanotubes (MWNT) using a ruthenium bridging complex,[1] atomic force microscopy (AFM) imaging and height analysis and UV−vis and emission spectroscopy were applied to investigate the reaction.

Characterization of carbon nanotubes before and after functionalization with small groups such as carboxylic acid (−COOH) and amino groups (−NH2) has been carried out using Raman analysis of the nanotube tangential mode,[2] X-ray photoelectron spectroscopy (XPS),[6,13] infrared spectroscopy (IR),[8−10,13,14] scanning tunneling microscopy (STM),[1,13] and nuclear magnetic resonance (NMR).[14,15] Results obtained from these characterization methods become increasingly difficult to interpret when larger molecular entities are attached to the functionalized groups. AFM imaging and height analysis have been employed to verify the presence of interconnected[1,2] and DNA-functionalized[7] carbon nanotubes; however, in itself, AFM only provides a visual suggestion. Attempts have also been made to use nuclear magnetic resonance (NMR) spectroscopy to characterize covalent bonding to carbon nanotubes. Wong et al. carried out ^1H and ^7Li NMR on COO^- NH_3^+ ionically bound organic crown ethers with nanotubes[16] and ^{31}P NMR on Vaska's compound with nanotubes.[10] Sun et al. employed ^1H NMR spectroscopy to study esterification linkages with nanotubes[17] and diimide-activated amidation of nanotubes.[18] Hamers et al. used ^1H NMR to analyze the amide linkage between dodecylamine and nanotubes.[6] These authors report that they have "strong evidence" for ester/amide linkages upon functionalization of carbon nanotubes. In addition, Goze-Bac et al. used ^{13}C NMR to investigate covalent functionalization of ^{13}C-enriched carbon nanotubes.[15,19]

SCHEME 1: Reaction Scheme[a]

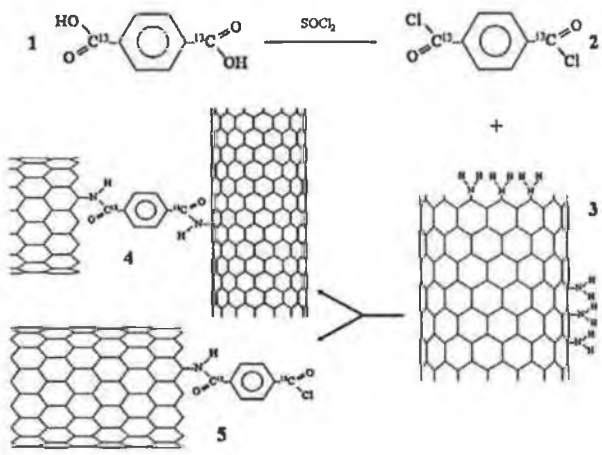

[a] Please note that **4** and **5** represent all forms of covalent functionalization at the nanotube sidewalls and ends.

In this work, ^1H, ^{13}C, and 2D NMR is used for providing evidence of the successful chemical modification of carbon nanotubes using ^{13}C-labeled terephthalic-carboxy-$^{13}C_2$ acid as the modifier (**1**, Scheme 1). It should be noted that the NMR data in ref 19 originates from carbon atoms in the nanotubes, whereas in the present work emphasis is on carbon in the attached molecules.

2. Experimental Details

Amino-functionalized multiwall carbon nanotubes (MWNT−NH_2) were produced by catalytic chemical vapor deposition and obtained from Nanocyl S. A. (Namur, Belgium). Further details of the preparation and analysis of MWNT−NH_2 can be found in refs 1 and 13. Scheme 1 shows the synthesis route taken for

* Corresponding author. E-mail: marc@utdallas.edu.
† Department of Physics, Trinity College Dublin.
‡ Dublin City University.
§ Department of Chemistry, Trinity College Dublin.
# The University of Texas at Dallas.

10.1021/jp040266i CCC: $27.50
Published on Web 06/04/2004

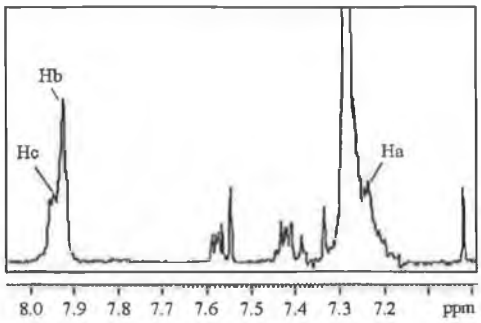

Figure 1. ^{1}H NMR spectrum of the reaction product in $CDCl_3$.

preparing modified nanotubes. Fifty milligrams of **1** was dissolved in 15 mL of thionyl chloride. The mixture was refluxed under argon for 5 h. Thionyl chloride was subsequently removed by vacuum distillation. The compound obtained, **2**, was dissolved in CH_2Cl_2. Two milligrams of MWNT−NH_2, **3**, were sonicated in 5 mL of CH_2Cl_2 for 2 min. This solution was added to the **2** solution. Ten milliliters of triethylamine (TEA) was added to the solution, and the reaction mixture was stirred at room temperature for 72 h under argon. All solvents were removed by vacuum distillation, and the remaining solid was added to 5 mL of CH_2Cl_2. This solution was sonicated and then allowed to settle for 48 h. Unreacted MWNT−NH_2 is obtained as a solid, leaving chemically modified carbon nanotubes in solution.

Subsequently, the top part of the solution was carefully pipetted off, the solvent taken off, and the solid obtained redissolved in $CDCl_3$. ^{1}H and ^{13}C NMR spectroscopy was carried out on this solution using a Bruker Avance DPX 400 MHz spectrometer. To achieve good signal-to-noise ratios the carboxy groups of terephthalic acid were labeled with 100% ^{13}C. As a result nonlabeled positions show only weak signals due to the low natural ^{13}C abundance of 1.1%. All ^{13}C NMR spectra were recorded proton decoupled.

3. Results and Discussion

All NMR spectra were recorded without intensive purification of the reaction mixture. Thus, signals in the NMR spectra that correspond to the starting materials, products, and solvents can be expected. The ^{1}H NMR spectrum of **1** in D_2O/potassium carbonate shows a singlet peak at δ = 7.84 ppm indicative of the four identical hydrogens on the phenyl ring (not shown). **1** is insoluble in $CDCl_3$, and therefore it is not expected to feature in the NMR spectrum of the reaction mixture.

The ^{1}H NMR spectrum of **2** (in $CDCl_3$) shows one peak at δ = 8.04 ppm with a half line width of 2.6 Hz corresponding to the presence of four equivalent aromatic protons (not shown). The ^{1}H NMR spectrum of the reaction mixture (Figure 1 and Figure S1 in the Supporting Information) shows one broad peak at δ = 7.92 ppm (H_b) and two multiplets at δ = 7.95 ppm (H_c) and δ = 7.23 ppm (H_a). The other peaks (in Figure 1) can be attributed to solvent (δ = 7.28 ppm) and vacuum grease contamination which occurred during the drying process in the NMR sample preparation. The appearance of line broadening suggests that a reaction with the amino groups attached on the nanotube surface occurred. The appearance of two signals at δ = 7.95 and δ = 7.23 ppm is indicative of the presence of an asymmetric substituted 1,4-phenylene derivative[20] and is consistent with the presence of **5**. Scheme 2 shows the proposed assignment for the phenylene protons of product **5**. One end of the phenylene ring is connected via an amide group to the

SCHEME 2: Proposed Proton (H_a−H_c, Figure 1) and Carbonyl Carbon (a−g, Figure 2) Assignment in the Reaction Product[a]

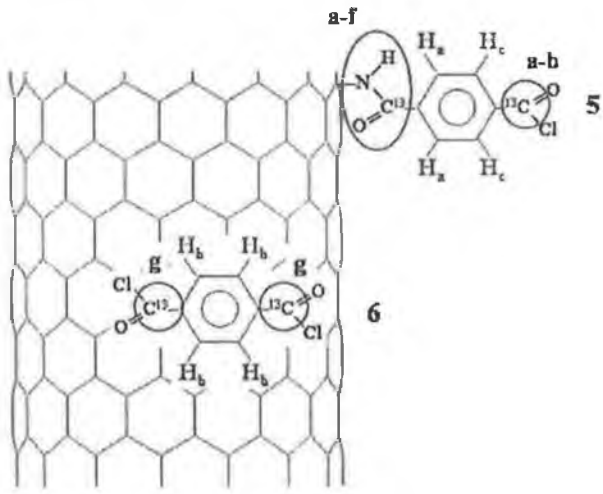

[a] **5** indicates covalent functionalization, whereas **6** indicates noncovalent sidewall functionalization (coating) of MWNT with **2**.

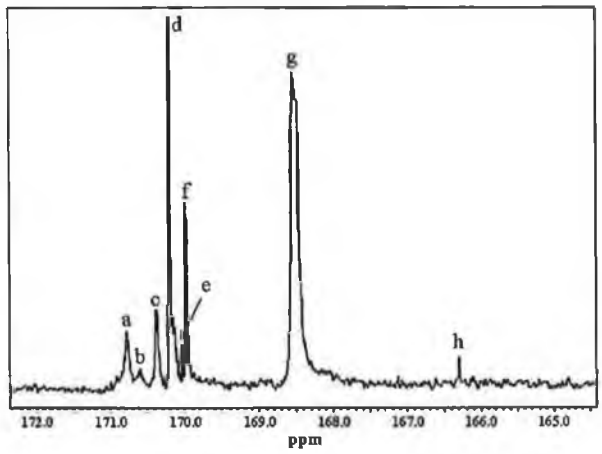

Figure 2. ^{13}C NMR spectrum of the reaction product in $CDCl_3$. Peak positions are indicated by **a**−**h**.

MWNT whereas the other end carries an acyl chloride group (Schemes 1 and 2). The signal at δ = 7.92 ppm (H_b) is indicative of a symmetric arrangement of protons and agrees well with the value obtained for **2** given above.

In the ^{13}C NMR spectrum of the reaction mixture (Figure S2 in the Supporting Information), four large peak areas can be identified around 8, 45, 77, and 170 ppm. These areas are indicative of TEA methyl (−CH_3), TEA alkylamine (−$NHCH_2$−), solvent ($CDCl_3$), and carbon carbonyl (−COX−) groups, respectively. Figure 2 shows the carbonyl region in the ^{13}C NMR spectrum of the reaction product. As noted before, the starting material **1** is insoluble in $CDCl_3$ and is therefore unlikely to feature.[21]

The peaks in Figure 2 correspond to the labeled carbonyl carbons only. It is not straightforward to assign these peaks to a specific nanotube assembly; however, their appearance does confirm covalent bonding. Let us now address which NMR signals could be expected from the reaction product. If both active sides of **2** would react with **3**, then **4** is obtained as the product and only acyl amide type signals are expected. However, if just one active side reacts with the amino-functionalized

nanotubes, giving **5** as product, a carbon signal indicative of acyl chloride should also be detected.

For **2** in $CDCl_3$ a ^{13}C NMR signal at $\delta = 167.50$ ppm was recorded. Therefore, it is reasonable to assume that signal **g** ($\delta = 168.54$) is indicative of acyl chloride (ClCO−phenyl). A more detailed analysis of signal **g** reveals that there are at least three signals together forming one broad signal. The sp^2 nature of the nanotubes has a deshielding effect on the carbonyl carbons, which leads to a downfield shift of the corresponding signal in the ^{13}C NMR. It has been shown that π-conjugated molecules can render nanotubes soluble through noncovalent sidewall functionalization (π-stacking).[22] In Scheme 2, **6** indicates π-stacking of **2** onto MWNT. The (nanotube) sp^2 deshielding effect would result in a downfield shift for **6** (π-stacked component **2**), compared with $\delta = 167.50$ ppm **2** in $CDCl_3$. Therefore, it is assumed that signal **g** could originate from the acyl chloride in **6**.

The carbonyl ^{13}C resonance in dimethyl-substituted amide ($CH_3-NHCO-CH_3$) in $CDCl_3$ has a chemical shift of $\delta = 171.60$ ppm[23] for the carbonyl carbon. Through comparison with other established shifts for amides,[23] it can be deduced that substitution of sp^2 systems results in the following shift changes. Substitution on the nitrogen side (phenyl−NHCO−CH_3) results in a shielding effect which would result in an upfield shift of the signal, whereas substitution on the carbon side (CH_3−NHCO−phenyl) results in a deshielding effect which would result in a downfield shift of the signal. It should be noted that the signal shift caused by deshielding is smaller compared to the signal shift caused by shielding. Thus, an upfield shift (lower ppm) can be expected for MWNT−NHCO−phenyl in comparison with the 171.60 ppm shift recorded for $CH_3-NHCO-CH_3$. We can therefore conclude that the peaks **a**−**f** are indicative of the presence of amide bonds and modified MWNT. The small differences in shifts between peaks **a**−**f** could be indicative of the presence of different local environments in **4** and/or **5**.

2D NMR correlation spectroscopy can provide further useful information about the nature of the signals obtained. The heteronuclear multiple bond connectivity (HMBC) experiment allows the investigation of atoms of long-range coupling between protons and carbons. Figure 3 shows the HMBC spectrum of the reaction mixture in $CDCl_3$.

The correlation regions in the HBMC spectrum can be explained as follows. To identify the correlation regions (CR) the following notation is adopted: (proton peak; carbon peak). The coordinates for the correlation region centers are: CR1 (7.92; 168.5), CR2 (7.23; 170.2), and CR3 (7.95; 171.0). In CR1, the symmetric aromatic proton (H_b) is correlated with carbon in the range of 167.5−169.9 ppm and centered on peak **g**. This is consistent with signals arising from the presence of **6**, as shown in Scheme 2. In CR2, the asymmetric aromatic proton (H_a) is correlated with carbon in the range of 169.5−171.0, corresponding to peaks **a**−**f**. This is consistent with signals arising from the carbon participating in the amide bond of **5** as shown in Scheme 2. In CR3, the asymmetric aromatic proton (H_c) is correlated with carbon in the range of 170.5−171.5 ppm, corresponding to peaks **a** and **b**. This is consistent with signals arising from the carbon in the acyl chloride part of **5** as shown in Scheme 2. The presence of the two correlation regions (CR2 and CR3) is a direct indication that assembly **5** was formed during the reaction. Asymmetric protons are correlated with carbons in different carbonyl environments.

Signals originating from **4** could not be assigned, due most likely to the low concentration of this compound.

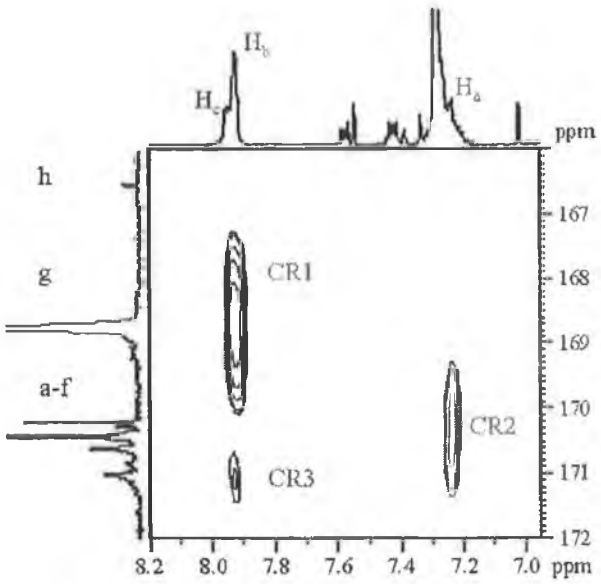

Figure 3. HMBC spectrum of the reaction product in $CDCl_3$. CR1−CR3 indicate correlation regions, whereas H_a−H_c indicate peaks in the ^1H NMR spectrum (see Figure 1) and **a**−**h** indicate peaks in the ^{13}C NMR spectrum (see Figure 2).

4. Conclusions

In conclusion, we have presented evidence of the chemical (covalent) bond formed between carbon nanotubes and a ^{13}C-labeled molecule. With the use of ^1H NMR, ^{13}C NMR, and the 2D (HMBC) correlation spectrum, signals for the (amide) linkage between terephthalic acid (labeled molecule) and MWNT could be assigned.

It was possible to identify (asymmetric) NMR signals originating from labeled molecules bound to MWNT. NMR correlation regions could be attributed to amide linkage and acyl chloride parts of product **5**. In addition, signals originating from **6** (noncovalent functionalization of MWNT with **2**) could be assigned.

We envisage that combination of NMR experiments can become a useful tool in the characterization of chemical bonds between carbon nanotubes and molecular entities, leading to advances in molecular sensing and electronics.

Acknowledgment. F.F. and J.G.V. thank Enterprise Ireland for financial assistance.

Supporting Information Available: ^1H and ^{13}C spectra of the reaction product in $CDCl_3$. This material is available free of charge via the Internet at http://pubs.acs.org.

References and Notes

(1) Frehill, F.; Vos, J. G.; Benrezzak, S.; Koós, A. A.; Kónya, Z.; Rüther, M. G.; Blau, W. J.; Fonseca, A.; Nagy, J. B.; Biró, L. P.; Minett, A. I.; in het Panhuis, M. *J. Am. Chem. Soc.* **2002**, *124*, 13694.

(2) Chiu, P. W.; Duesburg, G. S.; Dettlaff-Wegiikowska, U.; Roth, S. *Appl. Phys. Lett.* **2002**, *80*, 3811.

(3) Huang, W.; Taylor, S.; Fu, K.; Lin, Y.; Zhang, D.; Hanks, T. W.; Rao, A. M.; Sun, Y.-P. *Nano Lett.* **2002**, *2*, 311.

(4) Fu, K.; Huang, W.; Lin, Y.; Zhang, D.; Hanks, T. W.; Rao, A. M.; Sun, Y.-P. *J. Nanosci. Nanotechol.* **2002**, *2*, 457.

(5) Lin, Y.; Taylor, S.; Li, H.; Fernando, K. A. S.; Qu, L.; Wang, W.; Gu, L.; Zhou, B.; Sun, Y.-P. *J. Mater. Chem.* **2004**, *14*, 527.

(6) Baker, S. E.; Cia, W.; Lasseter, T. L.; Weidkamp, K. P.; Hamers, R. J. *Nano Lett.* **2002**, *2*, 1413.

(7) Williams, K. A.; Veenhuizen, P. T. M.; de la Torre, B. G.; Eritja, R.; Dekker, C. *Nature* **2002**, *420*, 761.

(8) Banerjee, S.; Wong, S. S. *Nano Lett.* **2002**, *2*, 195.

(9) Haremza, J. M.; Hahn, M. A.; Krauss, T. D.; Chen, S.; Calcines, J. *Nano Lett.* **2002**, *2*, 1253.

(10) Banerjee, S.; Wong, S. S. *Nano Lett.* **2002**, *2*, 49.

(11) Banerjee, S.; Wong, S. S. *J. Am. Chem. Soc.* **2002**, *124*, 8940.

(12) Ravindran, S.; Chaudhary, S.; Colburn, B.; Ozkan, M.; Ozkan, C. S. *Nano Lett.* **2003**, *3*, 447.

(13) Kónya, Z.; Vesselenyi, I.; Niesz, K.; Kukovecz, A.; Demortier, A.; Fonseca, A.; Delhalle, J.; Mekhalif, Z.; Nagy, J. B.; Koós, A. A.; Osváth, Z.; Kocsonya, A.; Biró, L. P.; Kiricsi, I. *Chem. Phys. Lett.* **2002**, *360*, 429.

(14) Chen, J.; Hamon, M. A.; Hu, H.; Chen, Y.; Rao, A. M.; Eklund, P. C.; Haddon, R. C. *Science* **1998**, *282*, 95.

(15) Goze-Bac, C.; Bernier, P.; Latil, S.; Jourdain, V.; Rubio, A.; Jhang, S. H.; Lee, S. W.; Park, Y. W.; Holzinger, M.; Hirsch, A. *Curr. Appl. Phys.* **2001**, *1*, 149.

(16) Kuhn, M. G. C.; Banerjee, S.; Wong, S. S. *Nano Lett.* **2002**, *2*, 1215.

(17) Fu, K.; Huang, W.; Lin, Y.; Riddle, L. A.; Carroll, D. L.; Sun, Y.-P. *Nano Lett.* **2001**, *1*, 439.

(18) Fu, K.; Kitaygorodskiy, A.; Rao, A. M.; Sun, Y.-P. *Nano Lett.* **2002**, *2*, 1165.

(19) Goze-Bac, C.; Latil, S.; Lauginie, P.; Jourdain, V.; Conard, J.; Duclaux, L.; Rubio, A.; Bernier, P. *Carbon* **2002**, *40*, 1825.

(20) Williams, D. H.; Fleming, I. *Spectroscopic Methods in Organic Chemistry*, 5th ed.; McGraw-Hill: New York; London, 1995.

(21) When the starting product 1 was dissolved in a solvent mixture of D_2O/potassium carbonate, a ^{13}C NMR shift of 174.84 ppm was recorded for the carboxylic acid carbon.

(22) in het Panhuis, M.; Maiti, A.; Dalton, A. B.; van den Noort, A.; Coleman, J. N.; McCarthy, B.; Blau, W. J. *J. Phys. Chem. B* **2003**, *127*, 478.

(23) Levy, G. C.; Lichter, R. L.; Nelson, G. L. *Carbon-13 Nuclear Magnetic Resonance Spectroscopy*, 2nd ed.; John & Sons: New York, 1980.

Iron Wheels on Silicon: Wetting Behavior and Electronic Structure of Adsorbed Organostannoxane Clusters

F. Frehill,[†] K. H. G. Schulte,[‡] C. P. Martin,[‡] L. Wang,[‡] S. Patel,[§] J. A. Purton,[§] J. G. Vos,[†] and P. Moriarty*,[‡]

National Centre for Sensor Research and School of Chemical Sciences, Dublin City University, Glasnevin, Dublin 9, Ireland, School of Physics & Astronomy, University of Nottingham, Nottingham NG7 2RD, UK, and Daresbury Laboratory, Daresbury, Cheshire WXX 4AD, UK

Received December 19, 2003. In Final Form: May 12, 2004

Atomic force microscopy and synchrotron radiation (SR) spectroscopy have been used to study the wetting behavior and electronic structure of thin films of a novel organometallic cluster − $[BuSn(O)OC(O)Fc]_6$ ("Fc" = ferrocenyl) − on silicon substrates. This cluster comprises six ferrocene units connected to a stannoxane central core − "an iron wheel on a tin drum" (V. Chandrasekhar; et al. *Angew. Chem., Int. Ed.* **2000**, *39*, 1833). Thin films spin-cast onto native oxide-terminated silicon readily dewet the substrate. We have utilized advanced image analysis techniques based on Minkowski functionals to provide a detailed quantitative analysis of the morphology of the stannoxane overlayers. This analysis shows that the dewetting patterns are rather far removed from those expected to arise from a simple Poisson distribution of centers, and we discuss the implications of this finding in terms of nucleated and spinodal dewetting. Variations in both the surface roughness and the in-plane correlation length have been followed as a function of annealing time to probe the surface dewetting dynamics. SR valence band photoemission illustrates that the highest occupied molecular orbital (HOMO) of the cluster is found 2 eV below the Fermi level. Fe 2p → 3d and Sn 3d → 5p resonant photoemission spectroscopy have been used to enhance the cross sections of the partial density of states associated with the Fe and Sn atoms. Sn atoms make a large contribution to the HOMO of the cluster, whereas the Fe atoms are associated with an electronic environment seemingly very similar to that in the "parent" ferrocene molecule.

I. Introduction

Organometallic chemistry underlies the synthesis and functionality of a wide variety of molecular and polymeric systems. Metallocenes, and ferrocene[1] in particular, have been exploited as central elements of a family of nascent molecular electronics devices. These prototype systems include components whose structure or conformation is switchable via variations in redox state,[2] and a variety of switching methods have been envisaged. For example, magnetic control of the activity of (bio)electrocatalytic systems has recently been demonstrated by Katz et al.,[3] photoisomerization has been exploited by a number of groups[4,5] to generate redox-active states, and variations in pH are commonly used to reversibly modify molecular properties.[6]

The synthesis of the organometallic molecule of interest in this study, $[BuSn(O)OC(O)Fc]_6$ (where "Fc" = ferrocenyl), was first reported by Chandrasekhar et al. three years ago.[7] The molecule comprises six ferrocene units which are attached to a central stannoxane core. As discussed in ref 7, this represents a rather novel cyclic interconnection of Fc elements. In more recent work,[8] Chandrasekhar et al. have shown that it is possible to generate supramolecular "grids" of the stannoxane cluster through the formation of intermolecular C−H--O bonds between the ferrocenyl C−H and the carboxylate oxygen. This is an exciting development as it provides a relatively simple route, via the formation of hydrogen bonds, to the self-assembly of ferrocene−stannoxane clusters into a predefined pattern in the solid state.

A key motivation underlying the work described in this paper relates to the possibility of ultimately translating the supramolecular chemistry and crystal engineering described above to the self-assembly of organostannoxane (and other organometallic) clusters on a solid surface. This is a goal that has parallels in many areas of state-of-the-art nanoscale science. For example, alongside the development of synthetic procedures that impart device-related functionality to single molecules, there has been a drive toward the integration of molecular electronics with more conventional silicon technology.[9] There are many scientific issues to address in this area with some of the more fundamental questions related to the manner in which the molecular units interact with a substrate. Although considerable effort has been expended in studying the interaction of a range of small organic molecules with atomically clean, reconstructed silicon surfaces under ultrahigh vaccum (UHV) conditions,[10−12] many applications necessitate an understanding of the self-organization, interactions, and morphology of molecular and polymeric systems deposited from solution. It is important

[†] Dublin City University.
[‡] University of Nottingham.
[§] Daresbury Laboratory.

(1) Special edition on ferrocene chemistry. *J. Organomet. Chem.* **2001**, *637−639*.
(2) Plenio, H.; Aberle, C. *Chem.-Eur. J.* **2001**, *7*, 4438.
(3) Katz, E.; Sheeney-Haj-Ichia, L.; Willner, I. *Chem.-Eur. J.* **2002**, *8*, 4138.
(4) Tsivgoulis, G. M.; Lehn, J.-M. *Adv. Mater.* **1997**, *9*, 39.
(5) Takeshita, M.; Choi, C. N.; Irie, M. *Chem. Commun.* **1997**, 2265.
(6) Bissell, R. A.; Cordova, E.; Keifer, A. E.; Stoddard, J. F. *Nature* **1994**, *369*, 133.
(7) Chandrasekhar, V.; Nagendran, S.; Bsal, S.; Kozec, M. A.; Powell, D. R. *Angew. Chem., Int. Ed.* **2000**, *39*, 1833.
(8) Chandrasekhar, V.; Boomishankar, R.; Singh, S.; Steiner, A.; Zacchini, S. *Organometallics* **2002**, *21*, 4575.
(9) Fang, L. A.; Liu, J. M.; Coulter, S.; Cao, X. P.; Schwartz, M. P.; Hacker, C.; Hamers, R. J. *Surf. Sci.* **2002**, *514*, 362.
(10) Schwartz, M. P.; Hamers, R. J. *Surf. Sci.* **2002**, *515*, 75.
(11) Cao, X. P.; Hamers, R. J. *J. Am. Chem. Soc.* **2001**, *123*, 10988.
(12) Lopinski, G. P.; Wayner, D. D. M.; Wolkow, R. A. *Nature* **2000**, *406*, 48.

10.1021/la036414y CCC: $27.50
Published on Web 06/22/2004

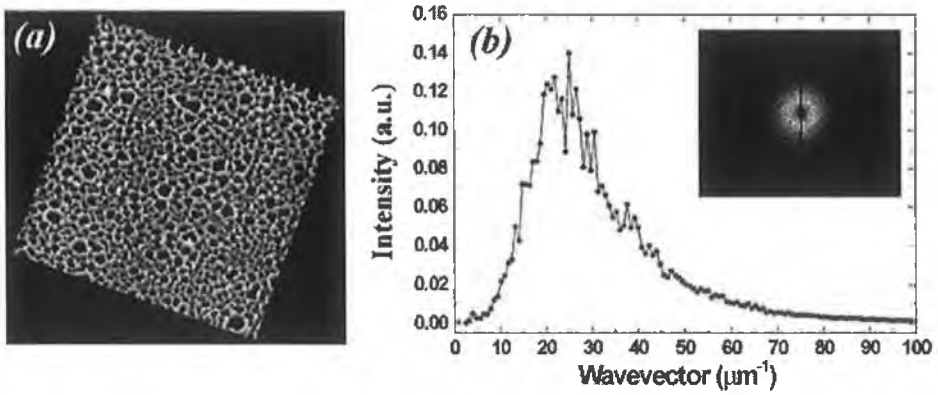

Figure 1. (a) Tapping mode atomic force microscope (AFM) image (8 μm × 8 μm) of a thin stannoxane film spin-cast from toluene onto a native-oxide-terminated Si(111) substrate. The film has a cellular morphology with a mean thickness of ~4 nm. The dewetting holes in the film expose the underlying SiO_2/Si substrate. (b) A radial average of a 2D Fourier transform (FT) of the image shown in (a). The 2D FT is shown in the inset. Note the presence of a peak at a wavevector, q, of ~25 μm^{-1}, suggesting the presence of an intercell correlation length of ~$2\pi/25$ μm (i.e., ~250 nm). Note that the somewhat poor statistics associated with the radially averaged Fourier transforms shown throughout this paper arise from the relatively small scan area (and thus small number of cells) associated with each image.

to establish if the resulting (spin-cast or drop-deposited) thin film is stable, unstable, or metastable and the extent to which it will dewet the underlying substrate/electrode surface.

The issue of wettability is of paramount importance when considering the possibility of hydrogen-bonding-mediated self-assembly of 2D organostannoxane (or other organometallic) overlayers. Hence, the first component of the Results section below details a study of the dewetting of spin-cast organostannoxane thin films on native oxide-terminated silicon substrates. A particular goal of our work was to probe whether organostannoxane thin films on silicon are subject to the spinodal dewetting[13] mechanism that has been shown to drive the break-up of liquid crystal,[14] homopolymer,[15] and, most recently, copolymer[16] films on silicon substrates. As discussed by Brochard-Wyart and Dallinat[13] and Reiter,[17] spinodal dewetting involves the amplification of thin film thickness fluctuations via long range van der Waals forces and leads to the break-up of an adsorbed molecular film. This mode of dewetting is distinctly different from the thermal or heterogeneous nucleation of holes in a metastable film and is analogous to spinodal decomposition in fluid mixtures where the thickness fluctuations correspond to composition fluctuations in the fluid system. A key feature of both spinodal decomposition and spinodal dewetting is the presence of a preferred length scale in the phase separation/film rupture process. (As discussed in section III, however, a spinodal mechanism is not always necessary to account for spatial correlations in the positions of dewetting centers.) The presence of a dominant length scale has considerable implications for controlled self-assembly, and, indeed, spinodal processes have been exploited by a number of groups in the synthesis of a variety of nanoscale patterns in polymer layers.[18] However, to date, there is a paucity of literature on the dewetting of nonpolymeric adsorbed layers on silicon.

The second component of the Results section deals with the solid-state electronic structure of the organostannoxane cluster used in this work as was probed using synchrotron radiation photoemission and resonant photoemission (RESPES). Resonant photoemission, in particular, is a sensitive probe of the density of states associated with the Fe and Sn atoms at the core of the stannoxane and ferrocenyl units.

II. Experimental Section

The organostannoxane cluster used throughout this work was synthesized via the procedure described in ref 7. Briefly, *n*-butylstannonic acid is reacted with ferrocene monocarboxylic acid in benzene to yield the hexaferrocene–stannoxane compound via reaction 1 below:

$$6\mathrm{BuSn(O)OH} + 6\mathrm{FcCOOH} \xrightarrow[80\ ^\circ\mathrm{C}]{\mathrm{C_6H_6}} [\mathrm{[BuSn(O)OC(O)Fc]_6}] + 6\mathrm{H_2O} \quad (1)$$

where, again, "Fc" represents a ferrocenyl moiety. Chandrasekhar et al.[7] point out that not only is reaction 1 important in that it produces a hexaferrocene compound in high yield (as compared to the modest yields of multiferrocene compounds produced via other synthetic routes), but the resulting hexaferrocene–stannoxane cluster is robust and thermally stable up to temperatures of 244 °C.

For both the atomic force microscopy (AFM) and the SR spectroscopy measurements detailed in sections III.A and III.B below, thin films were prepared by spin-coating (at 4 krpm) 15 μL of a 0.25 mM solution of the organostannoxane cluster in toluene onto a 0.7 cm² piece of a native oxide-covered Si(111) sample. For the SR measurements, the silicon samples were simply solvent-rinsed and blow-dried with N_2 before spin-coating. However, for the AFM measurements, where the wetting properties of the molecules were of interest, in addition to solvent-cleaned substrates, we used samples which were subsequently further cleaned with a 1:1 mixture of H_2SO_4:H_2O_2 (30%) for 1 h. These were then thoroughly rinsed with deionized water. This surface treatment strongly improved the reproducibility of the organostannoxane film morphology from sample to sample. Furthermore, dynamic contact angle measurements showed that the wetting properties of the Si substrate were dramatically affected by the H_2SO_4:H_2O_2 treatment. For solvent-rinsed samples, the contact angle was 45° ± 5°, whereas the sulfuric acid–peroxide treatment dramatically reduced the hydrophobicity of the surface so that the contact angle was 5° ± 5°.

(13) Brochart-Wyatt, F.; Dalliant, J. *Can. J. Phys.* **1990**, *68*, 1084.
(14) Herminghaus, S.; Jacobs, K.; Mecke, K.; Bischof, J.; Fery, A.; Ibn-Elhaj, M.; Schlagowski, S. *Science* **1998**, *282*, 916.
(15) Thiele, U.; Velarde, M. G.; Neuffer, K. *Phys. Rev. Lett.* **2001**, *87*, 016104.
(16) Müller-Buschbaum, P.; Wolkenhauer, M.; Wunnicke, O.; Stamm, M.; Cubitt, R.; Petry, W. *Langmuir* **2001**, *17*, 5567.
(17) Reiter, G. *Phys. Rev. Lett.* **1992**, *68*, 75.
(18) Higgins, A. M.; Jones, R. A. L. *Nature* **2000**, *404*, 476.

SR photoemission and RESPES measurements were taken on Beamline 5U1 of the UK Synchrotron Radiation Source (SRS) at Daresbury. The photon energy range of this undulator beamline is 60 eV to 1 keV. Photon energies were calibrated using Ti L_2 X-ray absorption spectra from a TiO_2 thin film (that could be moved into and out of the beam "upstream" from the sample) and Si $L_{2,3}$ edge spectra from the silicon substrate. A VSW HA100 hemispherical electron energy analyzer with single channel detection was used for all photoemission and resonant photoemission (RESPES) measurements. All photoelectron binding energies were calibrated by referencing to the Si 2p photoemission peak (at a binding energy of 99.5 eV) of the native oxide-terminated Si(111) substrate.

III. Results and Discussion

A. Wetting and Dewetting of Organostannoxane Thin Films. Thin adsorbed films play a central role in processes and applications ranging from protective/lubricating coatings to optoelectronic device technology to the functionalization of solid surfaces for biomedical applications. Thin film stability is therefore an issue of far-reaching scientific significance. In terms of the organostannoxane films of interest in this paper, a number of important questions needed to be addressed: (i) Do stannoxane films wet silicon? (ii) What type of film morphology results from spin-coating? (iii) If the films are unstable or metastable, is the dewetting mechanism related to "conventional" nucleation and spreading of holes, or is a spinodal process (giving rise to spatially correlated morphological features) involved? A detailed AFM study (with subsequent quantitative image analysis) of as-prepared and annealed spin-cast organostannoxane thin films has been carried out to address these issues.

Figure 1a is an AFM image of an organostannoxane film spin-cast onto a Si substrate which was simply solvent-cleaned and dried with N_2. Note that even before the sample is annealed, the stannoxane overlayer adopts a cellular morphology. As discussed by a number of authors,[15,17] the cellular network structure arises from the coalescence of the rims of expanding dewetting holes. However, one must distinguish between dewetting processes derived from an intrinsic surface instability (i.e., spinodal dewetting) and heterogeneous or thermal nucleation mechanisms. An important characteristic of spinodal dewetting is that the positions of the dewetting holes should be strongly spatially correlated as a result of the critical wavevector associated with the instability.[13] For a nucleation mechanism, the spatial correlation is absent, and the hole positions should follow a Poisson distribution. (However – and importantly – see the discussion regarding hole coalescence below.)

As a first step in the determination of the degree of interhole correlation, the Fourier transform (FT) of the image may be examined for the presence of a preferred wavevector. As shown in the inset to Figure 1b, a distinct ring is observed in the two-dimensional FT. Similarly, a clear peak appears in the radially averaged transform (Figure 1b). This is already strong evidence for spatial correlations in the hole positions. However, to provide a more quantitative distinction between correlated and uncorrelated dewetting centers, we have adopted a powerful statistical geometry technique based on Minkowski functionals[19] and previously applied by Jacobs et al.[20] to dewetting patterns.

Minkowski functionals are related to important morphological measures. In two dimensions, these are the covered area, boundary length, and Euler characteristic of the pattern of interest.[21] While the covered area and perimeter length are easy-to-visualize geometrical quantities, the third Minkowski measure – the Euler characteristic, χ – is perhaps not encountered so frequently and merits a brief explanation. χ is a key topological measure describing the connectivity of a pattern. In two dimensions – and on a binary image consisting of black and white pixels – the Euler characteristic is the number of separate objects comprising interconnected black pixels minus the number of enclosed white regions.[21]

Using an efficient algorithm based on that put forward by Michielsen and Raedt,[21] we have calculated[22] the behavior of the morphological Minkowski measures for a 2D distribution of points whose coordinates are given by the centers of the cells shown in Figure 1a. Specifically, to determine the degree to which the cell centers in Figure 1a deviate from the Poisson distribution of points expected from a conventional nucleation-driven dewetting scenario, we have adopted the following procedure. To each "germ" (i.e., cell center – see inset to Figure 2a) which has an edge length of 1, we attach a square "grain" of edge length $2r + 1$ (where r is a positive integer whose initial value is 1). Thus, and as described in detail by Michielsen and Raedt,[21] the point pattern arising from the cell centers is transformed into a pattern of square grains. We now systematically vary the grain size r – or, as in Figure 2, the "normalized" quantity $x = \pi/L$, where L is the mean germ separation – and compare the changes in the three Minkowski functionals (see Figure 2) to those expected for a Poisson distribution.

Considering first the x-dependent variation in Minkowski functionals for a Poisson distribution of points (represented by the solid lines in Figure 2a–c), we note that for small x, the grains are isolated. This produces a small covered area, a small boundary length, and a positive Euler characteristic. As the grain size is increased, the degree of overlap rises in a characteristic manner until the entire 2D plane is covered with black pixels producing a "saturated" covered area (Figure 2a). The boundary length curve exhibits a clear peak (Figure 2b) at intermediate values of x, while the Euler characteristic turns negative (Figure 2c). The minimum in the Euler characteristic curve (Figure 2c) arises from the highly interconnected and "void-ridden" structure present at intermediate x values.

The x-dependent behavior of the Minkowski functionals for the distribution of points with coordinates given by the cell centers in Figure 1a is markedly different. In each case – area, perimeter, and Euler characteristic – the curve for the stannoxane film centers (open circles-solid lines in Figure 2a–c) deviates significantly from that for the Poisson distribution. It is particularly interesting to note that the Euler characteristic decreases much more rapidly for a Poisson distribution at low values of x than for the distribution of points derived from the dewetting centers in the stannoxane film. To highlight more clearly the deviations from a Poisson distribution, Figure 2d–f shows graphs of the stannoxane film-related Minkowski functionals minus the corresponding Poisson-derived functional. That the distribution of dewetting centers in the stannoxane film is far removed from that expected for a Poisson distribution of points is clear from these graphs.

(19) Stoyan, D.; Kendall, W. S.; Mecke, J. *Stochastic Geometry and its Applications*; Akademie Verlag: Berlin, 1989.
(20) Jacobs, K.; Herminghaus, S.; Mecke, K. R. *Langmuir* **1998**, *14*, 965.
(21) Michielsen, K.; De Raedt, H. *Comput. Phys. Commun.* **2000**, *132*, 94.
(22) The code to numerically calculate the 2D Minkowski functionals was written in Matlab and is available from C. P. Martin (ppxcpm1@nottingham.ac.uk).

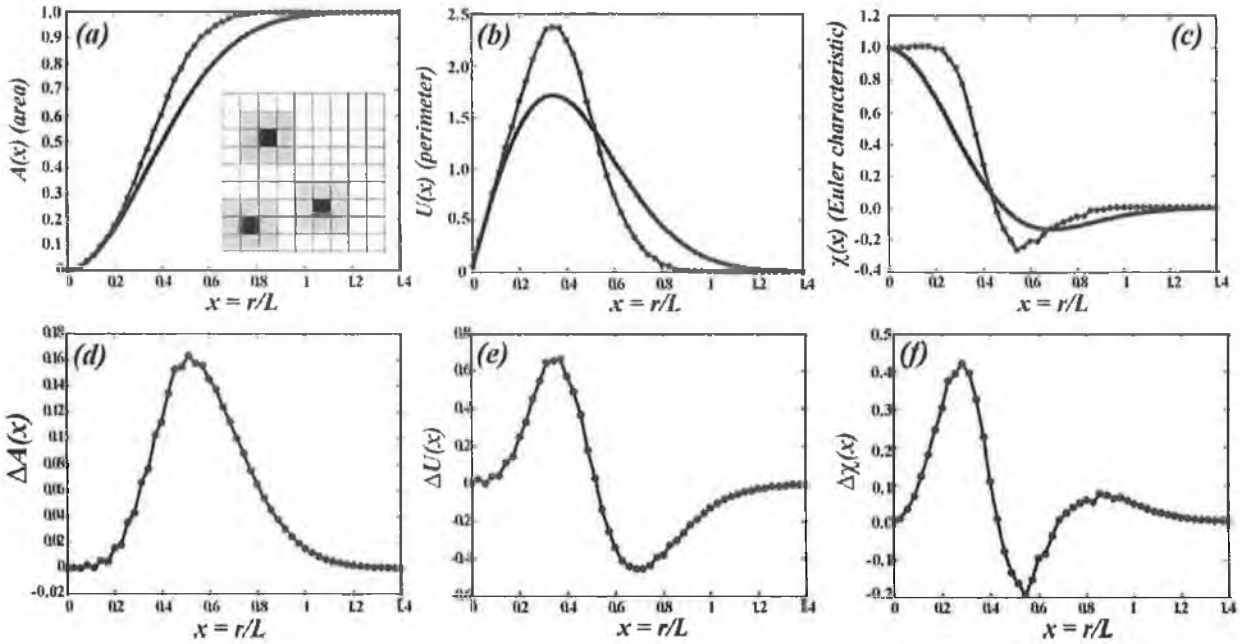

Figure 2. (a–c) Minkowski functionals (covered area, boundary length, and Euler characteristic) for a Poisson distribution of points and a point set based on the coordinates of the dewetting cell centers for the image shown in Figure 1 (solid lines and filled circles/solid lines, respectively). In each case, the functionals are plotted as a function of x, the normalized grain size. The inset to (a) depicts the difference between germs (the black pixels) and grains (grey pixels) centered on the germs. Note the strong deviation of each of the Minkowski functionals for the stannoxane-derived point system from the functionals for a Poisson-distributed set of points. (d–f) Difference between the stannoxane- and Poisson-derived result for each 2D Minkowski functional.

One might now argue that as the spatial distribution of the dewetting centers does not follow a Poisson distribution, there is clear evidence for spinodal dewetting of the organostannoxane film. However, a number of groups[23] have recently pointed out that for the "inverse" problem of droplet (rather than hole) growth on a substrate, deviation from a nonrandom spatial distribution of domains can occur simply by the coalescence of close pairs of droplets. Coalescence "wipes out" the clustering inherent in a Poisson point distribution and introduces a minimum nearest-neighbor distance. This, in turn, produces a spatial correlation length in the droplet – or, in our case, hole – distribution. More detailed morphological comparisons of dewetting center distributions, coupled with simulation studies, are required to address this issue and are underway in our group.

It is important to highlight at this point that the organostannoxane films we have studied have been produced via spin-coating. This is an exceptionally complicated, far-from-equilibrium process that has been considered by Lawerence[24] (among others) to comprise three consecutive phases. Following the initial transient phase where fluid inertia, the Coriolis force, and surface tension are the dominant effects, the second phase of the process involves a balance between viscous and centrifugal forces. In this secondary phase, the dynamics are driven by fluid flow, whereas in the final phase (phase III), the fluid viscosity is so high the evolution of the film is largely driven by solvent evaporation. Unfortunately, our AFM measurements – which provide little or no information on the film growth dynamics – cannot address the question of whether the viscosity of the fluid plays a large role in defining the final film morphology we observe. While one might speculate that the absence of macroscopic spatial uniformity in the organostannoxane films suggests that phase II dynamics are important, we do not observe a "starlike" pattern (previously identified as the signature of hydrodynamic instabilities[25]) at the center of rotation. An optical scattering study may provide some insight into the influence of the spin-coating process on the film morphology.

Having quantitatively ascertained that the morphology of as-cast stannoxane films on native oxide-terminated Si(111) substrates is primarily determined by the presence of a well-defined correlation (but not necessarily spinodal) wavelength, we now consider the dynamics of dewetting. We have carried out a comprehensive series of annealing studies of stannoxane thin films on (both H_2SO_4:H_2O_2-treated and "out of the box" solvent-rinsed) silicon samples to probe whether the evolution of the film morphology is consistent with models of spinodal dewetting. As described below, within the range of annealing times and annealing temperatures used in our study (30 min to 60 h, 75– 125 °C) and for organostannoxane films ranging in thickness from ~4 to 10 nm (on H_2SO_4:H_2O_2-treated silicon), we find no consistent evidence for the evolution of surface wavevector expected from the theory of spinodal dewetting. We also see considerable differences in the annealing-induced morphological evolution for stannoxane films on H_2SO_4:H_2O_2-treated silicon as compared to Si(111) substrates which have simply been solvent-rinsed. We return to this important point below.

Brochard and Dalliant[13] have put forward a variant of Vrij's[26] original capillary wave instability model to treat spinodal dewtting of thin liquid films from solid substrates. Both the Brochard and Dalliant and the Vrij models predict that thickness fluctuations of the film can be approximated by the following expression:

$$z(x,t) = h + \delta h e^{jqx}$$

Here, the fluctuation amplitude, δh, is given by: $\delta h =$

(23) Brinkmann, M. *Phys. Rev. B* **2002**, *66*, 165430. Ruckenstein, E.; Dadyburjor, D. B. *Thin Solid Films* **1978**, *55*, 89.
(24) Lawrence, C. J. *Phys. Fluids* **1988**, *31*, 2786.

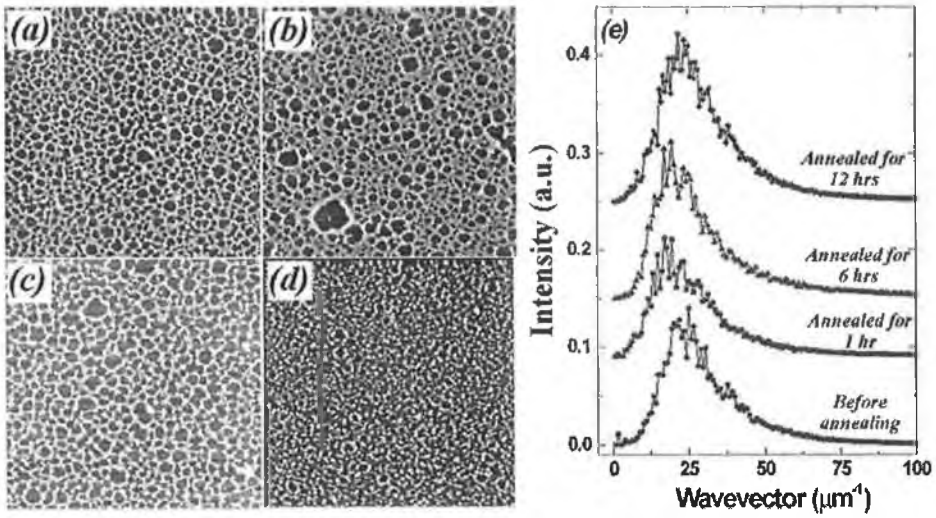

Figure 3. (a–d) 8 μm × 8 μm AFM images for a stannoxane thin film annealed for progressively longer times at a temperature of 75 °C. (a) is a "plan view" representation of the image shown in Figure 1a and illustrates the morphology of the film directly following spin-casting with no annealing. (b–d) are AFM images taken following annealing periods of 1, 6, and 12 h, respectively. It is important to note that, although these images are largely representative of the macroscopic morphology of the film, as described in the text, variations in roughness and peak wavevector were observed at different regions across the film. The progressive break-up of the film (via the Rayleigh instability) into droplets is clear from the images (although following 12 h of annealing, an "imprint" of the original cellular structure remains – cf. Figure 5d). (e) Radially averaged 2D FTs for the images shown in (a–d). From bottom to top: before annealing, following 1 h of annealing, following 6 h of annealing, following 12 h of annealing.

$\delta h_0 e^{t/\tau}$, where τ is the relaxation time (and $1/\tau$ is the growth rate), and δh_0 is the initial fluctuation amplitude. The x coordinate is associated with displacements parallel to the surface, and q denotes the wavevector associated with the wave instability. In this model, thermally driven thickness fluctuations are exponentially amplified if their associated wavevector (q) is less than some critical wavevector, q_C, but are attenuated if $q > q_C$. Importantly, if one now monitors the distribution of wavevectors by, for example, plotting the radially averaged Fourier transform of AFM images of the thin film taken as a function of annealing time, then it is possible to determine a value for q_C by identifying a "crossover" wavevector in the Fourier spectra. Furthermore, the position of the peak in the radially averaged transform shifts to lower wavenumbers as a function of annealing time according to a power law whose exponent yields information on the type of underlying destabilization kinetics. These types of analyses have been successfully adopted by Xie et al.[27] (among others) in the analysis of dewetting of polymer films from silicon substrates.

Figure 3a–d is a series of representative AFM images for a stannoxane film annealed for progressively longer times at a temperature of 75 °C. We have measured the in-plane peak wavevector as a function of annealing time by acquiring similar AFM images at a number of well-separated regions (spaced by millimeters) on the stannoxane film and subsequently calculating the radially averaged Fourier transform. Figure 3e shows the corresponding radially averaged Fourier transforms for Figure 3a–d. As shown in the inset to Figure 4, within the range of annealing times and error limits associated with our study, we do not recover the power-law dependence of wavevector on annealing time which has previously been observed in studies of polymer dewetting from silicon substrates.[16,27] Furthermore, from the Fourier transforms of our AFM data (e.g., Figure 3e), it is extremely problematic to systematically and reproducibly define a crossover wavevector (q_c) above (below) which thickness fluctuations decay (grow) in time. These difficulties in interpreting our experimental data in terms of spinodal dewetting theory arise in part from variations in stannoxane film structure from region to region across the substrate sample. Morphological variations across the film substantially increase the magnitude of the error bars (shown as ±1 standard deviation) on the data points and render detailed comparison with theory difficult.[28] However, it is also important to note that the initial (i.e., preannealed) film is associated with a morphology where the dewetting holes already expose the underlying silicon

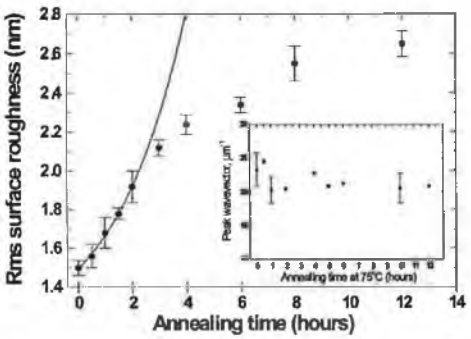

Figure 4. Evolution of surface roughness as a function of annealing time. Error bars represent ±1 standard deviation for a set of 30 measurements taken at various macroscopically separated regions of the film. Although it is possible to fit the early stage annealing data with an exponential function (as expected on the basis of the spinodal dewetting theory), the magnitude of the error bars means that a number of other functional forms can also be used as a fit to the data. Inset: Plot of the peak wavevector as a function of annealing times. Representative error bars for a number of points are shown. Within the error limits, we observe no systematic change of the peak wavevector.

(25) Müller-Buschbaum, P.; Gutmann, J. S.; Wolkenhauer, M.; Kraus, J.; Stamm, M.; Smilgies, D.; Petry, W. *Macromolecules* **2001**, *34*, 1369.
(26) Vrij, A. *Discuss. Faraday Soc.* **1966**, *42*, 23.
(27) Xie, R.; Karim, A.; Douglas, J. F.; Han, C. C.; Weiss, R. A. *Phys. Rev. Lett.* **1998**, *81*, 1251.

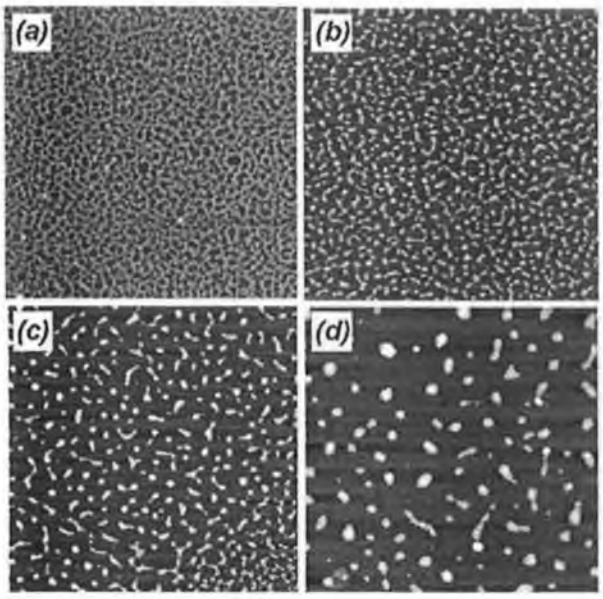

Figure 5. 8 μm × 8 μm AFM images for a stannoxane thin film on a silicon substrate which was simply solvent-rinsed before spin-coating. The evolution of the film as a function of annealing time (again at 75 °C) is markedly different from that observed in Figure 3. (b–d) are images of the film following annealing for 2, 4, and 8 h, respectively. In this case, the film has broken up into well-dispersed droplets following the 8 h of annealing (cf. Figure 3d). Note, however, that the film homogeneity and sample-to-sample reproducibility were substantially poorer for the solvent-rinsed substrates as compared to those substrates which underwent a H_2SO_4:H_2O_2 treatment prior to spin-casting the film.

substrate and the film roughness is rather close to one-half the mean film thickness (2.1 nm). These initial conditions are somewhat different from, for example, previous studies of polymer dewetting from silicon,[27] where the latter criterion was not met until the sample was annealed for some time.

Figure 4 shows the change in surface roughness as a function of annealing time for the stannoxane sample shown in Figures 1 and 3. While it is possible to fit the early stage annealing data (up to ~3 h) with an exponential function – as expected on the basis of spinodal dewetting theory – note again that the error bars are relatively large (and derive once more from morphological variations as a function of lateral position on the sample surface). When coupled with the lack of systematic wavevector variation and the difficulties associated with defining q_c discussed in the previous paragraph, it is clear that, although there is a strong spatial correlation in the positions of the dewetting centers (an important result in itself, given the recent uncertainty regarding spinodal dewetting for adsorbed polymer films on silicon[20]), a quantitative understanding of the dewetting dynamics of the stannoxane film as a function of annealing time is currently lacking.

Further elucidation of the dewetting mechanism will necessitate extremely careful control of substrate heterogeneity and surface chemistry. In particular, substrate surface treatment plays a central role in controlling the dewetting dynamics. Figure 5 shows the evolution of morphology for a film of thickness comparable to that discussed above but spin-cast onto a silicon substrate that was simply solvent treated. It is clear that, although the initial morphology is comparable to that of the H_2SO_4:H_2O_2-treated samples (compare Figure 1a with Figure 5a), the dependence of film morphology on annealing time is dramatically different. In particular, the break-up of the film into droplets via the Rayleigh instability[17,27] occurs on much shorter time scales for the untreated silicon substrate. In addition, sample-to-sample reproducibility and film homogeneity were substantially poorer for the untreated silicon substrates. The stannoxane–substrate interaction potential is clearly particularly sensitive to minor modifications in silicon surface chemistry.

B. Synchrotron Radiation Spectroscopy of Organostannoxane Thin Films. The morphology of the organostannoxane thin film used for the SR-based measurements is shown in the inset to Figure 6. Note that, as for the dewetting studies described in section III.A, the film structure is cellular in nature and thus exposes a substantial amount of the underlying silicon substrate. This, coupled with the presence of adventitious carbon on the silicon substrates and the strong oxygen-derived photoemission signal from the SiO_2 layer make reliable analysis and interpretation of C 1s and O 1s spectra from the organostannoxane film extremely difficult. We have therefore focused on the acquisition of Fe- and Sn-derived core-level photoemission and RESPES spectra (as these signals arise solely from the adsorbed stannoxane clusters).

Valence band spectra ($h\nu = 60$ eV) taken from a silicon sample with and without an adsorbed organostannoxane layer are shown in Figure 6. Although it is clear that the overall shape of the spectrum changes little when the stannoxane overlayer is present (being dominated by the substrate valence band structure), an additional peak at a binding energy of 2 eV is observed. While this peak derives from the highest occupied molecular orbital (HOMO) of the stannoxane cluster, the spectrum shown in Figure 6b yields little information beyond the energetic position of the HOMO below the Fermi level. This is because with conventional photoemission it is extremely difficult – in the absence of a priori knowledge – to identify the electronic character of the peaks in a valence band spectrum. We have, therefore, used RESPES to probe the contribution of Fe and Sn to the frontier orbitals of the adsorbed stannoxane cluster.

RESPES[29] exploits the resonant enhancement of the spectral intensity of valence states associated with a particular chemical element. This occurs when the incoming photon energy is tuned to the absorption threshold of a more strongly bound core-level of that element. In this way, one gains insight into the partial density of states. This process is sketched in Figure 7a. Following threshold excitation of a core-level electron (in this case, from an Fe 2p level) into the unoccupied (Fe 3d-derived) density of states, nonradiant decay of an Fe 3d valence electron to the Fe 2p core-hole is accompanied by the emission of the originally excited core-level electron. Importantly, this process produces a single hole final state that is identical to that associated with direct valence band photoemission (as depicted in Figure 7b). Constructive interference between the two excitation channels leads to resonant enhancement of the spectral intensity of Fe 3d-related features in the valence band. RESPES therefore provides us with an element-specific, localized probe.

(28) The experiment was repeated many times with a number of samples prepared in an identical manner. The morphological variations observed as a function of position on the sample were comparable from sample to sample for H_2SO_4:H_2O_2-treated silicon substrates. Substantially higher levels of film inhomogeneity and sample irreproducibility were observed for substrates that were simply solvent-rinsed.

(29) See, for example: Nilsson, A. *J. Electron Spectrosc. Relat. Phenom.* **2002**, *126*, 3.

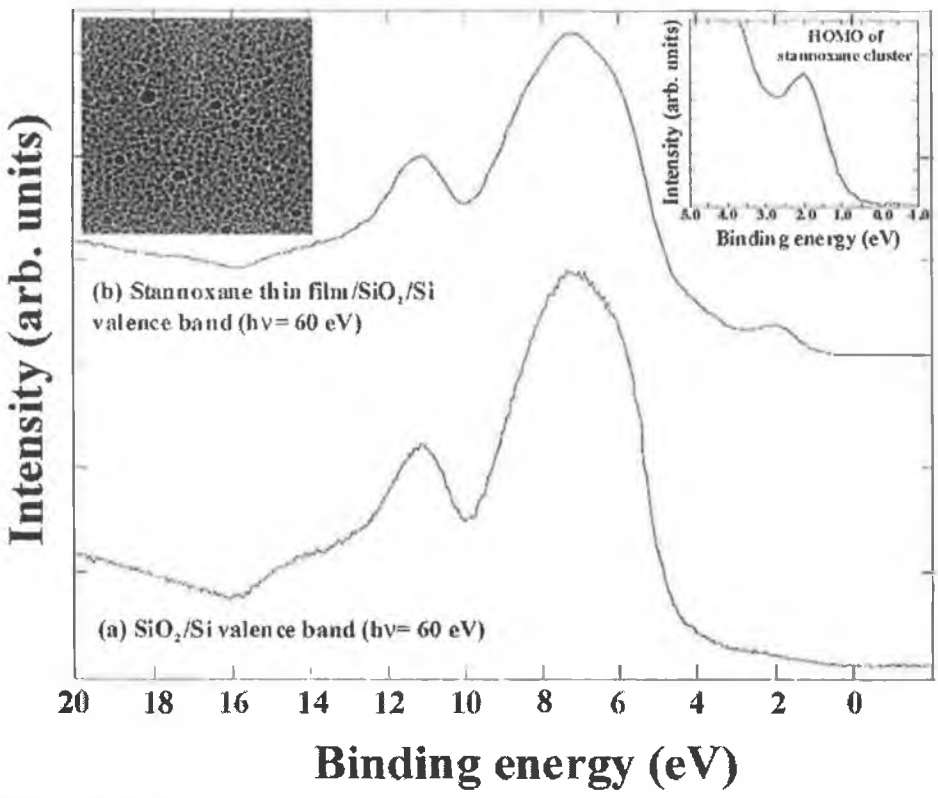

Figure 6. Valence band spectra for (a) native oxide-terminated Si(111) substrate, and (b) a thin organostannoxane film on the SiO_2/Si(111) substrate. Note that, although the substrate valence band structure dominates the spectrum in each case, the highest occupied molecular orbital (HOMO)-derived peak of the stannoxane film is visible in (b). (See also the inset on the right-hand side of the figure). Inset on left: AFM image (8 μm × 8 μm) of stannoxane film used for photoemission measurements.

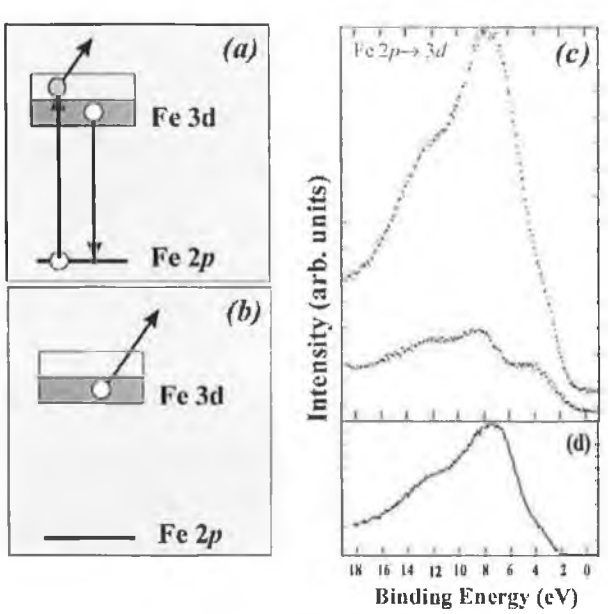

Figure 7. (a,b) Schematic illustrations of the resonant photoemission process for Fe 2p → 3d RESPES (see text for details). (c) On-resonance (upper spectrum) and off-resonance (lower spectrum) valence band spectra taken at photon energies of 711 and 702 eV, respectively. (d) On-resonance−off-resonance difference spectrum.

Valence band spectra from the organostannoxane−SiO_2/Si sample for photon energies of 702 and 711 eV are shown in Figure 7c. Below the Fe 2p threshold ($h\nu$ = 702 eV), the spectra are dominated by photoemission from the SiO_2/Si substrate (compare the off-resonance spectra shown in Figures 7 and 8). As the photon energy is increased toward the Fe 2p threshold, the Fe 3d states are enhanced in the photoemission spectrum. By subtracting the off-resonance spectrum from the on-resonance spectrum, as shown in Figure 7d, the Fe 3d-derived partial density of states may be extracted. Three broad features are identified in the difference spectrum shown in Figure 7d: a shoulder at a binding energy of approximately 4 eV, an intense peak at 7.0 eV, and another shoulder at ~11 eV. (Note that the combined photon and electron energy resolution for the Fe 2p → 3d RESPES measurements shown in Figure 7 was rather poor (>1 eV) due largely to the use of an analyzer pass energy of 90 eV to ensure sufficiently high electron count rates.)

It is now instructive to compare the Fe 2p → 3d RESPES difference spectrum shown in Figure 7c with the calculated and experimentally measured density of states of ferrocene, the "parent" molecule of the ferrocenyl groups at the periphery of the organostannoxane cluster (see Figure 1). A previous photoemission study[30] of adsorbed ferrocene identified a series of peaks at energies of ~2.3, 4.4, 7.9, 12.3, and 17.2 eV with respect to the Fermi level. Through comparison with ground-state theoretical calculations for ferrocene, the various peaks were assigned to their corresponding orbitals. Of particular relevance to the present study, however, Dowben et al.[31] have discussed the enhancement of the ferrocene molecular orbital-

(30) Driscoll, D. C.; Dowben, P. A.; Boag, N. M.; Grade, M.; Barfuss, S. *J. Chem. Phys.* **1986**, *85*, 4802.
(31) Dowben, P. A.; Waldfried, C.; Komesu, T.; Welipitiya, D.; McAvoy, T.; Vescovo, E. *Chem. Phys. Lett.* **1998**, *283*, 44.

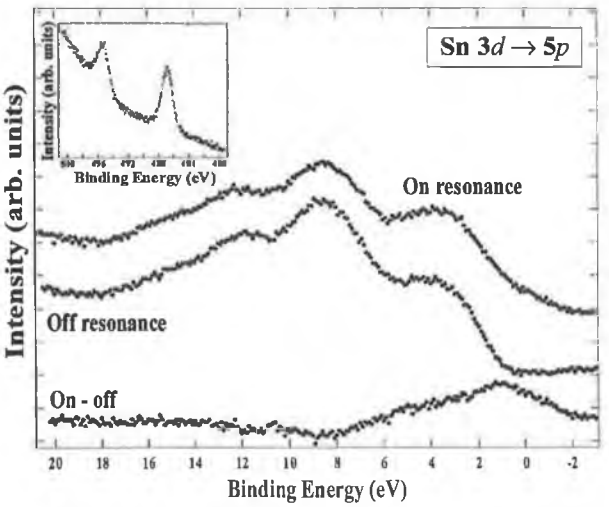

Figure 8. Sn 3d → 5p RESPES spectra. The "on-resonance" and "off-resonance" spectra were taken at photon energies of 488 and 480 eV, respectively. Note that the energy resolution is poor (≫1 eV fwhm), which leads to a substantial overestimate of the density of states at the Fermi level (binding energy = 0 eV). Nevertheless, the data clearly show that there is a substantially stronger contribution of Sn states (as compared to Fe states) to the higher lying occupied molecular orbitals. Inset: Sn 3d core-level photoemission spectrum ($h\nu$ = 550 eV).

derived photoemission features in RESPES. They point out that the $4e_{1g}$, $7a_{1g}$, $6e_{1u}$, and $2e_{1g}$ features (at binding energies of ~7.0, 10.9, and ~13 eV) derive from molecular orbitals which have the highest level of π-Cp ligand orbital hybridization to Fe d states. The $8a_{1g}$ and $4e_{2g}$ molecular orbitals with binding energies of 4−5 eV and ~4 eV, respectively, have strong localized Fe 3d character. Specifically, the $8a_{1g}$ and $4e_{2g}$ features arise from d_{z^2} and d_{xy},$d_{x^2-y^2}$ orbitals, respectively.

In Fe 2p → 3d RESPES, we should expect to observe strong enhancement of the photoemission features which arise from molecular orbitals having a large component of localized Fe 3d character. That intense resonances at ~4 and ~7 eV are observed in the difference spectrum shown in Figure 7c is strongly suggestive that these peaks derive from molecular orbitals with Fe 3d content similar to that of the $8a_{1g}$, $4e_{2g}$, and $4e_{1g}$ orbitals of the "parent" ferrocene molecule. The shoulder observed at an energy of ~11 eV in Figure 6b must also arise from orbitals with a high degree of Fe d character, and a family of orbitals ($3e_{2u}$, $3e_{2g}$, $3e_{1g}$, $5e_{1u}$, and $7a_{1g}$) have previously been identified as contributing to this spectral feature in studies of ferrocene adsorption on Ag(100).[32]

It therefore appears that the ferrocenyl groups at the periphery of the stannoxane cluster retain a high degree of the electronic character of the ferrocene molecule. What is particularly interesting, however, is that with Fe 2p → 3d RESPES we find no evidence for a strong resonant enhancement of the HOMO-derived peak centered at ~2 eV below the Fermi edge (see Figure 6b). This suggests that the highest occupied orbital is associated with very little (localized) Fe 3d character. A RESPES measurement involving photon energies crossing the Sn 3d edge was therefore carried out to probe whether Sn 5p states make a significant contribution to the HOMO of the stannoxane cluster. (The Sn 3d core-level photoemission spectrum is shown as an inset to Figure 8. Note that we expect a less intense resonant enhancement for the Sn 3d → 5p RESPES than for the Fe 3d-related RESPES measurements as the electric dipole transition from a state of orbital angular momentum l to an $l-1$ state is much weaker than $l \rightarrow l+1$.)

It is clear from Figure 8 that there is measurable resonant enhancement of the valence band in the near-Fermi level region when the photon energy is tuned to the Sn 3d threshold ($h\nu$ = 488 eV). The apparent very high density of states at the Fermi level (0 binding energy) is a consequence of the poor energy resolution of the measurement and the associated high degree of broadening of the resonance structure. Notwithstanding the low energy resolution, however, the stronger contribution of the Sn partial density of states to the highest-lying molecular orbitals of the stannoxane complex is readily apparent from Figure 8. (In addition, a strong (and trivial) resonant enhancement of the HOMO feature − and the entire valence band spectrum − was observed for photon energies comparable to that of the C K edge (285 eV).)

IV. Conclusions

We have shown that organostannoxane thin films spin-cast onto native oxide-terminated silicon substrates dewet via a mechanism which leads to the formation of a cellular network having a high degree of spatial correlation in the dewetting centers. While the lack of film stability has important implications for the synthesis of high-quality organostannoxane layers on silicon substrates, the influence of a dewetting process with a well-defined correlation length opens up a number of possibilities related to patterning stannoxane (and other organometallic) thin films at the submicron and nanometer scale levels. In addition, given that a previous application of Minkowski functionals to polymer film stability called into question the presence of spatially correlated dewetting centers,[20] our quantitative analysis represents an important confirmation of morphological deviations from Poisson statistics in a molecular, nonpolymeric thin film. However, although it is tempting to associate the spatial correlations we observe with spinodal dewetting, we stress that early-stage coalescence of Poisson-distributed dewetting holes may also yield a spatial correlation length.[23]

Synchrotron radiation RESPES measurements have shown that the ferrocenyl groups at the periphery of the stannoxane cluster retain a high degree of ferrocene-like electronic character but that there is little Fe 3d contribution to the highest occupied molecular orbital. Instead, Sn 3d → 5p RESPES data highlight the role of Sn-derived states in determining the character of the higher-lying occupied frontier orbitals. Although our RESPES data provide a first insight into the electronic structure of this novel and complex organometallic cluster, a detailed theoretical study (combined with more comprehensive photoemission work) is required to elucidate fully the molecular orbital configuration.

Acknowledgment. This research has been supported by a Marie Curie fellowship (held by F.F.) of the European Community program "Human Potential" under contract number HPMT-CT-2001-00407. In addition, this work was supported by a European Community 5th Framework Research Training and Mobility grant: "Supramolecular Self-Assembly of Interfacial Nanostructures" (HPRN-CT-2002-00185). We also acknowledge the UK Engineering & Physical Sciences Research Council (EPSRC) for funding

(32) Wellpitiya, D.; Dowben, P. A.; Zhang, J.; Pai, W. W.; Wendelken, J. F. *Surf. Sci.* **1996**, *367*, 20.

(under grant GR/01880/01), the Council for the Central Laboratory of the Research Councils (CCLRC) for the provision of beamtime at Daresbury SRS, and Enterprise Ireland for financial support under grant SC/2000/167. The beamtime experiments were facilitated by the expert technical assistance of George Miller, whom we sincerely thank. We also very gratefully acknowledge the assistance, expertise, and advice of V. R. Dhanak at Daresbury Lab.

LA036414Y

Measurement of Lateral Charge Propagation in [Os(bpy)$_2$(PVP)$_n$Cl]Cl Thin Films: A Scanning Electrochemical Microscopy Approach

A. P. O'Mullane, J. V. Macpherson, and P. R. Unwin*

Department of Chemistry, University of Warwick, Coventry CV4 7AL, U.K.

J. Cervera-Montesinos and J. A. Manzanares

Department of Thermodynamics, Faculty of Physics, University of Valencia, E-46100 Burjasot, Spain

F. Frehill and J. G. Vos

School of Chemical Sciences, Dublin City University, Dublin 9, Ireland

Received: February 4, 2004; In Final Form: March 24, 2004

The use of scanning electrochemical microscopy (SECM) to measure charge transport diffusion constants (D_{CT}) in metallopolymers of the type [Os(bpy)$_2$(PVP)$_n$Cl]Cl, bpy = 2,2′-bipyridyl and PVP = poly(4-vinylpyridine), is described. In this approach, a triple potential step technique is employed in which the ultramicroelectrode (UME) tip of the SECM is used to electrogenerate a solution phase oxidant, $Ru(CN)_6^{3-}$, in an initial potential step, via the oxidation of $Ru(CN)_6^{4-}$. This moiety diffuses from the tip to the underlying polymer film where electron transfer occurs, causing the local oxidation of the polymer-bound complex of Os^{II} to Os^{III}. The form of the current−time characteristic in this step provides information on the kinetics of the ET process between the solution species and the polymer-bound moiety, as well as the concentration of redox-active species in the polymer film. This process creates lateral concentration gradients of Os^{II} and Os^{III} along the film. After the first potential step, a waiting period is introduced in which $Ru(CN)_6^{3-}$ is converted back to $Ru(CN)_6^{4-}$ at the UME and Os^{II} can recover in concentration by electron self-exchange between Os^{III} and Os^{II} moieties. After a defined time, the potential of the UME is switched again to cause the generation of the solution-phase oxidant, $Ru(CN)_6^{3-}$. The current−time behavior associated with this step is influenced significantly by the extent of lateral electron hopping in the waiting period. It is shown that SECM is capable of measuring D_{CT} values as low as 10^{-10} cm^2 s^{-1} with good precision. We report experimental measurements on spin-coated films of [Os(bpy)$_2$(PVP)$_n$Cl]Cl, where n = 5 or 10, which indicate that D_{CT} is affected significantly by redox site loading and film structure (as determined by atomic force microscopy).

Introduction

Metallopolymers of the type [M(bpy)$_2$(Pol)$_n$Cl]Cl, where M = Ru or Os, bpy = 2,2′-bipyridyl and Pol = poly(4-vinyl-4-vinylpyridine) (PVP), or poly(*N*-vinylimidazole) (PVI), have received much attention.[1−11] This is due to their potential widespread applications in areas such as sensors, electronic devices, energy storage, and corrosion protection.[10] A possible future application is in the area of molecular electronics where this class of material may act as a linker between metallic nanoparticles, which could be electrochemically switched.

Electron and charge transfer through thin films of metallopolymers on electrode surfaces has been studied extensively.[12−27] It is widely accepted that charge propagation through redox polymers is limited by one of three processes: (i) electron-self-exchange between redox moieties in the film, (ii) the rate of ion diffusion into or out of the film to maintain electroneutrality, and (iii) the degree of polymer chain rearrangement required to juxtapose redox centers. Conventional techniques employed to study charge transport in redox polymers include cyclic voltammetry (CV), potential step chronoamperometry (CA),[3−8] and to a lesser extent, electrochemical impedance spectroscopy (EIS).[28−30] However, there is often a discrepancy in the charge transport coefficients (normally denoted D_{CT}) determined by CV (usually of the order 10^{-10} cm^2 s^{-1}) and CA; the latter measurements often yield D_{CT} values that are an order of magnitude higher than from CV.

It has been suggested that D_{CT} determined by potential step methods is often limited by ion diffusion into the film,[3] whereas for voltammetry the limitation is either polymer chain movement at low redox center loadings/high electrolyte concentration combinations, or ion diffusion at high redox center loadings. Yet, when ion diffusion is regarded as the limiting process, there is still a discrepancy between CV and CA, presumably because the extent of ion movement is distinctively different in these techniques. In CV, over 80% of redox sites in the film are typically oxidized,[3] resulting in widespread ion diffusion within the film and ingress/egress at the film−electrolyte interface. In contrast, the potential step experiments are often made on a shorter time scale, so that ion diffusion within the film is less extensive and probably involves counterions already present in the film. For EIS, the system is perturbed only slightly from the steady state, so that a small fraction of redox states in the film is active during the measurement, most probably charge-compensated by counterions that are already within the film. D_{CT} values on the order of 10^{-8} cm^2 s^{-1} have been reported for [Os(bpy)$_2$(PVP)$_n$Cl]Cl,[29] using this latter technique, which is within the range obtained from steady-state techniques, where ion diffusion and polymer chain movement are no longer

10.1021/jp049500v CCC: $27.50
Published on Web 05/05/2004

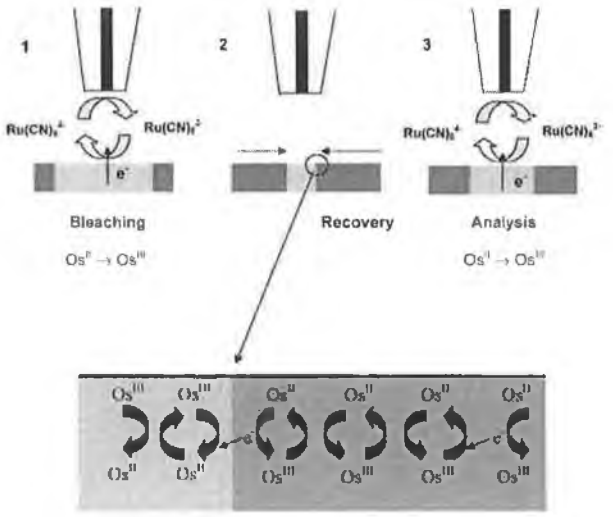

Figure 1. Schematic of the triple step transient technique for measuring lateral charge propagation.

limiting factors.[14,31,32] For (Os II/III) electropolymerized systems, values as high as 10^{-6} cm^2 s^{-1} have been reported for D_{CT}[14] under steady-state conditions.

In this work we investigate the rate of lateral charge propagation in relatively thin films of $[Os(bpy)_2(PVP)_nCl]Cl$ and describe how scanning electrochemical microscopy (SECM) may be used to determine D_{CT}. Several methods have previously been employed to measure lateral charge propagation in thin film and monolayer systems. Majda and co-workers[33,34] have used two-dimensional voltammetric measurements carried out with line microelectrodes to study lateral charge transport in Langmuir monolayers. Murray's group[35,36] used generation-collection measurements at microband electrode arrays to measure lateral charge propagation in polymer films, under both steady-state and time-dependent conditions. Forster and co-workers have used ultramicroelectrodes (UMEs) to measure charge transport dynamics of solid-state osmium bis(bipyridyl)-tetrazine chloride films.[37]

The experimental method employed in this paper utilizes transient SECM measurements. Following initial work on lateral proton transfer in this laboratory,[38−40] SECM has recently been used to study charge injection and lateral propagation in Langmuir−Blodgett films of polyaniline (PANI),[41] the conductivity of PANI monolayers[42] and the lateral (physical) diffusion of *N*-octadecylferrocenecarboxamide ($C_{18}Fc$) in a Langmuir monolayer.[43] Other groups have also recognized the possibility of using SECM to measure lateral charge transport and conductivity in monolayer systems.[44,45]

To study the lateral diffusion of the amphiphile, $C_{18}Fc$, in a mixed Langmuir monolayer, a triple potential step experiment was devised[43] analogous to fluorescence recovery after photobleaching (FRAP), which is widely used to measure lateral diffusion in biomembranes.[46−49] Here, we show how this SECM triple potential step method may be used to measure diffusion constants for charge propagation in a thin film of a redox polymer, illustrated by studies of the $[Os(bpy)_2(PVP)_nCl]Cl$ system. The basic idea is illustrated schematically in Figure 1. An UME is positioned close to the interface between the polymer film and solution and used to electrogenerate a redox species in solution (oxidation of $Ru(CN)_6^{4-}$ to $Ru(CN)_6^{3-}$; step 1). This species diffuses from the UME to the polymer film where electron transfer occurs locally (eq 1).

$$Os^{II}{}_{film} + Ru(CN)_6^{3-}{}_{aq} \leftrightarrows Os^{III}{}_{film} + Ru(CN)_6^{4-}{}_{aq} \quad (1)$$

The kinetics and extent of this process controls the diffusion of the solution product of the reaction, $Ru(CN)_6^{4-}$, back to the UME.

As discussed fully in our previous paper,[43] one can measure the ET kinetics and determine the concentration of redox moieties at the target interface from the current−time response recorded at the UME in this step. For the case of low D_{CT}, the electrode induced process is largely confined to the portion of the film directly under the tip of the UME.[43] Next, there is a waiting period (step 2), in which $Ru(CN)_6^{3-}$ quickly recovers to $Ru(CN)_6^{4-}$ in the gap between the UME and film surface. On a much longer time scale, lateral charge propagation within the polymer film may occur, for example, by electron hopping. For the system here, this process involves electron self-exchange between Os^{II} and Os^{III} moieties that have a lateral gradient in the film, due to the local redox process in step 1. Finally, step 3 is a repeat of step 1, involving oxidant electrogeneration at the tip. The form of the current−time transient for this step may contain information on charge propagation in the film (during the recovery period), depending on the time scale of step 2 relative to D_{CT}. If step 2 is very short (compared to the lateral charge-transfer diffusion time), and the film is extensively oxidized in step 1, the third step shows a current−time response similar to an inert surface. In this case, one can determine the tip−interface separation from the chronoamperometric curve.[43] On the other hand, if the second step is sufficiently long, D_{CT} can be determined from the current−time response in step 3, as there will be a repopulation of Os^{II} moieties, by lateral charge propagation into the zone of the film probed by the UME. This serves to enhance the current response for the third (analysis) step, as it provides reagent in the film for reaction with electrogenerated oxidant.

In earlier work,[43] we studied the physical diffusion of a surfactant with a relatively high lateral diffusion coefficient (ca. 10^{-6} cm^2 s^{-1}). Here, we show that SECM is capable of measuring much lower D_{CT}, as found in redox polymer systems. An advantage of SECM is that the film of interest need not be deposited on an electrode, as charge injection occurs from a solution redox species, which can be tuned to give optimal conditions for the redox reaction. Furthermore, in contrast to conventional time-dependent techniques, the redox reaction and accompanying charge compensation process occur from the same side of the film (starting at the film/electrolyte interface and proceeding across to the underlying inert solid on which the film is deposited). This may be more efficient than CV or CA studies of films on electrodes, where the redox process starts with heterogeneous electron transfer at the electrode/film boundary and charge compensation establishes an ion flux at the film/electrolyte interface, on the opposite side of the film.

Theory

We have treated the triple potential step problem previously, for the case of lateral diffusion in a monolayer.[43] The time scales were relatively short, so that we did not have to be concerned with the spatial domain beyond the thin gap between the tip and interface of interest, allowing us to fix the concentrations at the edge of this zone to the bulk values. In the present study, where much longer time scales are involved, we have avoided setting the conditions in this way. Although there are similarities in the two models, we outline the problem here, as it pertains to the redox polymer system, because this provides a context for results from the model which are reported later.

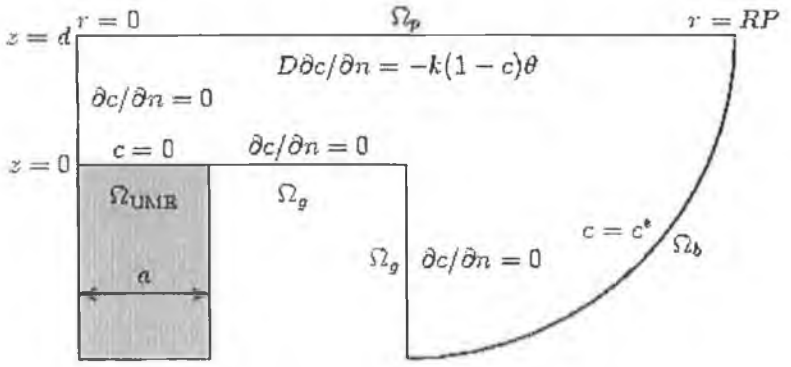

Figure 2. Schematic view (not to scale) of the domain used for the numerical calculations. The boundary conditions imposed to the transport equation of $Ru(CN)_6^{4-}$ are shown. The surface Ω_g is defined as $(z - d)^2 + (r - 10a)^2 = (RP - 10a)^2$, $z \leq d$, $r \geq 10a$.

The coordinate system and principal boundary conditions pertaining to the first potential step in the experiment of interest are depicted in Figure 2.

The presence of an excess supporting electrolyte allows us to describe the transport of $Ru(CN)_6^{4-}$, which is in bulk solution at concentration, c^*, as a diffusional process:

$$\frac{\partial c}{\partial t} = D\left(\frac{\partial^2 c}{\partial r^2} + \frac{1}{r}\frac{\partial c}{\partial r} + \frac{\partial^2 c}{\partial z^2}\right) \tag{2}$$

where c and D are the concentration and diffusion coefficient of $Ru(CN)_6^{4-}$, r and z are the radial and axial coordinates (see Figure 2) and t is time. Initially, the concentration of $Ru(CN)_6^{4-}$ is that of the bulk

$$c(r,z) = c^* \qquad t = 0 \tag{3}$$

In the first step (period $t < \Delta t_1$) we apply a sufficiently driving potential to the UME so that $Ru(CN)_6^{4-}$ is oxidized to $Ru(CN)_6^{3-}$ under diffusion control. The boundary condition at the UME, delimited by surface Ω_{UME}, is then

$$c = 0 \qquad \text{at } \Omega_{UME} \qquad 0 < t < \Delta t_1 \tag{4}$$

The electrogenerated $Ru(CN)_6^{3-}$ ions diffuse away from the UME and reach the polymer film, where they are reduced back to $Ru(CN)_6^{4-}$ by oxidizing the polymer (eq 1). In this process, the polymer acts as a sink for the flux of $Ru(CN)_6^{4-}$. The flux density of $Ru(CN)_6^{3-}$ at the polymer/electrolyte interface Ω_p is controlled by the boundary condition

$$D'\left.\frac{\partial c'}{\partial z}\right|_{z=d} = kc'\theta \tag{5}$$

where D' and c' are the diffusion coefficient and concentration of $Ru(CN)_6^{3-}$, respectively, k is the rate constant for the polymer oxidation, $\theta(r,t)$ is the local fraction of the polymer in the reduced state, and Ω_p is the polymer surface. The time variation of $\theta(r,t)$ depends on the oxidation rate induced by the flux of $Ru(CN)_6^{3-}$ and the recovery process of the polymer. It is described by

$$\frac{\partial \theta}{\partial t} = -\frac{kc'\theta}{\Gamma} + D_{CT}\left(\frac{\partial^2 \theta}{\partial r^2} + \frac{1}{r}\frac{\partial \theta}{\partial r}\right) \tag{6}$$

where Γ (mol cm^{-2}) is the effective surface concentration of osmium redox centers in the thin polymer film. Note that this formulation assumes that there are no diffusional limitations across the thickness of the film (from the electrolyte/film boundary to the underlying film/substrate boundary), only in the radial direction. This is reasonable, in light of the experimental results that follow, compounded by the fact that the film thickness ($l_{film} \sim 100$ nm), is much less than the lateral dimension of the experiment, e.g., electrode radius, $a = 12.5$ μm; overall probe radius of 125 μm. The recovery process is assumed to be described by a diffusion-type equation for the lateral electron transport in the polymer. The initial and boundary conditions for eq 6 are

$$\theta(r) = 1 \qquad t = 0 \tag{7}$$

$$\frac{\partial \theta}{\partial r} = 0 \qquad r = 0 \tag{8}$$

$$\theta = 1 \qquad r = RP \tag{9}$$

Due to the continuity of mass, the flux density of $Ru(CN)_6^{3-}$ that is reduced at the polymer must be equal to the flux density of $Ru(CN)_6^{4-}$ that diffuses normal to the film

$$D\left.\frac{\partial c}{\partial z}\right|_{z=d} = -D'\left.\frac{\partial c'}{\partial z}\right|_{z=d} \tag{10}$$

We assume that the diffusion coefficients of $Ru(CN)_6^{3-}$ and $Ru(CN)_6^{4-}$ are equal, and because the total concentration in the system does not change, the local mass conservation is satisfied

$$c'(r,z) + c(r,z) = c^* \tag{11}$$

This allows c' to be replaced by by $c^* - c$ in eqs 5 and 6, so avoiding the need to solve an equation equivalent to eq 2 for c'. The rest of the boundary conditions of eq 2 are the symmetry condition,

$$\frac{\partial c}{\partial r} = 0 \qquad r = 0 \qquad 0 \leq z \leq d \tag{12}$$

the null flux density at the surface Ω_g of the glass sheath that covers the UME, which is inert to the species in solution,

$$D\frac{\partial c}{\partial z} = 0 \tag{13}$$

where Ω_g is the glass sheath surface, and the assumption that the concentration of $Ru(CN)_6^{4-}$ at the outer boundary of the system delimited by surface Ω_b is the bulk concentration during the whole experiment

$$c = c^* \qquad \text{at } \Omega_b \tag{14}$$

In the waiting period (step 2), the UME is held at a potential to quickly regenerate $Ru(CN)_6^{4-}$ from any $Ru(CN)_6^{3-}$ in its vicinity. Sufficient time elapses for the region of the polymer locally oxidized to recover by lateral electron transfer within the film, which involves the reduction of Os^{III} to Os^{II} in the film region in front of the UME and the oxidation of Os^{II} to Os^{III} in the outer film surface.

$$c = c^* \qquad \text{at } \Omega_{UME} \qquad \Delta t_1 < t < \Delta t_2 \tag{15}$$

The recovery process of the polymer is quite slow, and to have a substantial recovery, Δt_2 is of the order of tens to hundreds of minutes. For this reason the simulation domain was extended significantly with respect to prior studies using the three-step method.[43] The domain must be large enough so that $\theta = 1$ at r = RP and no $Ru(CN)_6^{3-}$ reaches Ω_b. Typically, RP = $40a$, which marked one end of the quarter-circle boundary, Ω_b (Figure 2). The electrode probe had a glass insulator dimension 10 times that of the electrode itself, a.

In step 3, the potential at the UME was applied again to oxidize $Ru(CN)_6^{4-}$ to $Ru(CN)_6^{3-}$. The boundary conditions are those defined for step 1, but the length of step Δt_3 may be different from that of step 1. To proceed to the numerical integration of the differential equations, it is advisable to cast the problem into dimensionless form. We define the variables

$$\tau \equiv tD/a^2 \tag{16}$$

$$R \equiv r/a \tag{17}$$

$$Z \equiv z/a \tag{18}$$

$$C \equiv c/c^* \tag{19}$$

$$K \equiv ka/D \tag{20}$$

$$\gamma \equiv \Gamma/(ac^*) \tag{21}$$

$$D_r \equiv D_{CT}/D \tag{22}$$

The main equations of the problem in normalized form are

$$\frac{\partial C}{\partial \tau} = \frac{\partial^2 C}{\partial R^2} + \frac{1}{R}\frac{\partial C}{\partial R} + \frac{\partial^2 C}{\partial Z^2} \tag{23}$$

$$\frac{\partial \theta}{\partial \tau} = -\frac{K(1-C)\theta}{\gamma} + D_r\left(\frac{\partial^2 \theta}{\partial R^2} + \frac{1}{R}\frac{\partial \theta}{\partial R}\right) \tag{24}$$

$$\frac{\partial C}{\partial Z} = -K(1-C)\theta \qquad \text{at } Z = d/a \tag{25}$$

The problem was solved using the finite element method for the spatial dependency and the finite difference method for the time dependency. It was implemented using the commercial package Femlab. To compare the theoretical simulation with the experimental curves, the current−time response for the first and third steps is calculated from[50,51]

$$\frac{i}{i_\infty} = \frac{\pi}{2}\int_0^1 \left.\frac{\partial C}{\partial Z}\right|_{Z=0} R\, dR \tag{26}$$

where i_∞ is simply the steady-state current at an inlaid disk electrode:[52,53]

$$i_\infty = 4nFDac^* \tag{27}$$

where n is the number of electrons transferred ($n = 1$ in our case) and F is the Faraday constant.

There are four (normalized) parameters that influence the normalized current−time characteristic: d/a, K, γ, and D_r. In the three-step method, the distance is usually obtained by applying relatively long and short time intervals for steps 1 and 2, respectively, so that the redox moieties in the zone of the film probed by the UME essentially react to completion (in step 1) but there is insufficient time for any recovery process in step 2. In step 3, the polymer film then behaves as an inert substrate and the current depends only on d/a (because D is known). By applying the SECM theory in the inert substrate case, the distance between the UME and the polymer can be obtained.[43] However, in the experiments here, we also show that the redox reaction between $Ru(CN)_6^{3-}$ and the Os^{II} moiety in the film is characterized by a high value of K (diffusion-limited) so that initially in step 1, the probe current characteristics display pure positive feedback. This allows d in this interval within step 1 to be obtained. As the polymer is oxidized, its behavior departs from that of a pure conducting substrate, which allows us to fit γ. Finally, the fourth parameter, D_r, is obtained by letting the polymer partially recover in step 2, so that D_r is the only variable needed to fit the transient curve of step 3.

Experimental Section

Materials and Chemicals. $Os(bpy)_2(PVP)_nCl]Cl$ was prepared and characterized as described previously.[54,55] All chemicals were used as received and were $LiClO_4$ (Aldrich), potassium hexacyanoruthenate(II) hydrate (Strem chemicals), methanol (HPLC grade, Fisher chemicals), high purity acetone (Fisher chemicals), and propan-2-ol (HPLC grade, Fisher chemicals). All aqueous solutions were prepared from Milli-Q reagent water (Millipore Corp.).

Procedures. Glass and ITO substrates were cleaned by sonicating for 10 min in acetone and then in propan-2-ol and finally blown dry with nitrogen. Thin films of $[Os(bpy)_2(PVP)_nCl]Cl$ were spin coated (2500 rpm for 60 s) onto substrates by using a 1 wt % solution of the polymer in methanol. The thickness and topography of films were determined using both contact mode AFM (Digital Instruments, Nanoscope E) and tapping mode AFM (Digital Instruments, Multimode). Mean values of 90 ± 10 nm for $[Os(bpy)_2(PVP)_5Cl]Cl$ films and 100 ± 25 nm for $[Os(bpy)_2(PVP)_{10}Cl]Cl$ films were obtained.

CV measurements were made using a three-electrode arrangement. An ITO covered substrate, with a surface area of 0.35 cm^2, was used as the working electrode, a platinum gauze served as the counter electrode and a saturated calomel electrode (SCE) was used as the reference electrode. The SECM was a simple home-built instrument comprising a manual x, y, z stage (M-431, Newport Corp., CA) and a z-axis piezoelectric positioner and controller (models P-843.30 and E-501.00, Physik Instrumente, Waldbronn, Germany) to give fine control of the Pt UME working electrode in the direction normal to the sample. Transient SECM measurements of films on glass were carried out using a two electrode arrangement,[43] with a Pt UME as the working electrode and a silver wire as a quasi-reference electrode (AgQRE). Transients were recorded with the probe UME positioned at fresh spots on the sample, with a separation of at least 200 μm from the regions of any previous measurements. The Pt UME used was a 25 μm diameter disk electrode with a glass insulating sheath, characterized by an RG value of 10 (RG = r_{glass}/a; where r_{glass} is the radius of the sheath around the probe). Cyclic voltammetry and current−time transients were recorded using an electrochemical analyzer (CH Instruments,

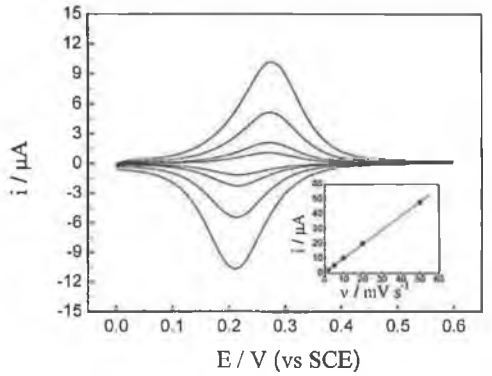

Figure 3. Cyclic voltammograms for an ITO electrode covered with $[Os(bpy)_2(PVP)_5Cl]Cl$ in 0.1 M $LiClO_4$ at 1, 2, 5, and 10 mV s^{-1}. The inset shows the linear relationship between anodic peak current and sweep rate.

model CHI730A). The diffusion coefficient of $Ru(CN)_6^{4-}$ was deduced by steady-state microdisk measurements in a bulk solution of 0.1 M $LiClO_4$ and 0.2 mM $Ru(CN)_6^{4-}$ yielding a value of $(7.46 \pm 0.03) \times 10^{-6}$ cm^2 s^{-1}. This solution was used for all SECM measurements reported.

Results and Discussion

Voltammetry of Spin Cast Films. Although there are several reports on the electrochemistry of film electrodes of the type of interest here,[3,4,7,9,10,54] these previous studies are generally for much thicker drop cast films where values obtained for D_{CT} for $[Os(bpy)_2(PVP)_5Cl]Cl$ are of the order of[3] 1.3×10^{-11} cm^2 s^{-1}. In this work, we use much thinner spin cast films. Typical slow sweep cyclic voltammograms for an $[Os(bpy)_2(PVP)_5Cl]Cl$ spin cast film in 0.1 M $LiClO_4$ electrolyte are shown in Figure 3. There is a linear relationship between the peak current and sweep rate, when the latter is less than 100 mV s^{-1}, as illustrated by the inset of Figure 3. The peak to peak separation (ΔE_p) is 60 mV, and the full width at half-maximum current (fwhm) is 120 mV. This latter value is broader than expected for an ideal single electron process (90.6 mV) and may be due to repulsive interactions between redox centers[5] or heterogeneity in the film. The surface coverage of osmium redox centers in the films was determined from slow sweep cyclic voltammetry (1 mV s^{-1}) in 0.1 M $LiClO_4$, by integrating the charge under the oxidation and reduction peaks [$(4.6 \pm 0.6) \times 10^{-9}$ mol cm^{-2}].

SECM Measurements. To measure the electron-transfer kinetics between the Os^{II} redox centers in a $[Os(bpy)_2(PVP)_5Cl]Cl$ film and the solution mediator, SECM CA experiments were undertaken with the tip in close proximity to the film, deposited on an inert glass substrate. These measurements involved stepping the tip potential from 0 V (vs SCE) where no faradaic process occurred to 1.0 V, where the oxidation of $Ru(CN)_6^{4-}$ occurred at a diffusion-controlled rate. Figure 4 illustrates the current–time responses recorded at several different distances varying from 1.7 to 11 μm above the $[Os(bpy)_2(PVP)_5Cl]Cl$ film. The tip currents, i, have been normalized by the steady-state diffusion-limited current, i_∞, recorded in bulk solution. Values for each of the distances were obtained from the long time current response, when Os^{II} is effectively depleted at the portion of the film under the electrode.

The form of the current transient responses is as follows: after an initial charging current the faradaic current quickly decays to a quasi steady-state value, due to the feedback process illustrated in Figure 1, which subsequently falls to a hindered

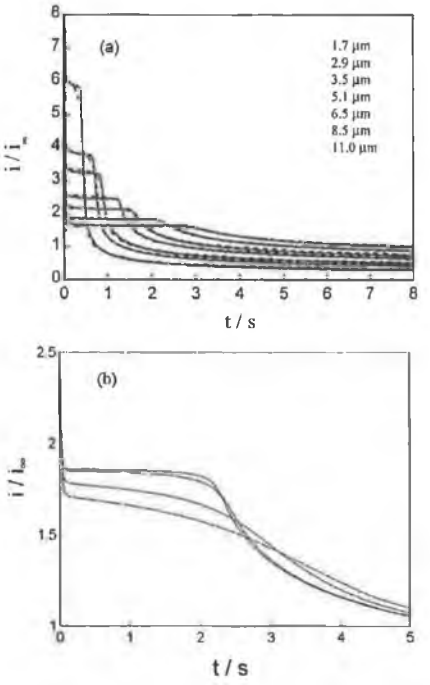

Figure 4. (a) Current–time responses of a Pt UME held at different distances, from 1.7 (top curve) to 11 μm (bottom curve) above a $[Os(bpy)_2(PVP)_5Cl]Cl$ spin cast film. The UME potential was stepped from 0 to 1.0 V (vs SCE) in a 0.2 mM $Ru(CN)_6^{4-}$ and 0.1 M $LiClO_4$ solution to generate $Ru(CN)_6^{3-}$ at a diffusion-limited rate. The thick lines are the experimental results and the dashed lines are the modeled results (see text). (b) Simulated results, showing the effect of k on the current–time response recorded for step 1. Values of k (bottom to top) = 0.05, 0.1, 0.5, and 1 cm s^{-1}, $d = 8.5$ μm, $D_{CT} = 0$, and $\Gamma = 3.5 \times 10^{-9}$ mol cm^{-2} were employed.

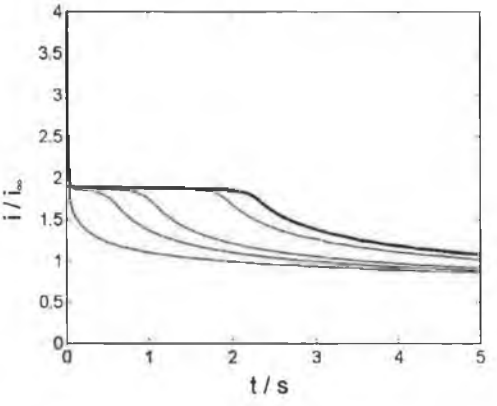

Figure 5. Simulated results showing the effect of D_{CT} on the current–time response for step 3 with the periods for step 1 (5 s) and 2 (waiting time of 30 min) kept constant. D_{CT} was varied as follows: 7.5×10^{-11} (fine curve on left), 3.8×10^{-10}, 7.5×10^{-10}, and 3.8×10^{-9} (fine curve on right) cm^2 s^{-1}. The thick line (on the right) is the transient for step 1. The following parameters were used: $d = 8.5$ μm, $D_{CT} = 0$, $\Gamma = 3.5 \times 10^{-9}$ mol cm^{-2}, $k = 1$ cm s^{-1}.

diffusion-limited value. The SECM current response also shows a strong distance effect; the closer the tip/surface distance, the larger is the initial feedback response and the earlier the subsequent fall in current. This can be explained as follows: $Ru(CN)_6^{3-}$ generated at the UME diffuses and reacts with the Os^{II} centers within the film until the whole area of the film opposite the electrode is oxidized. On the time scale of this

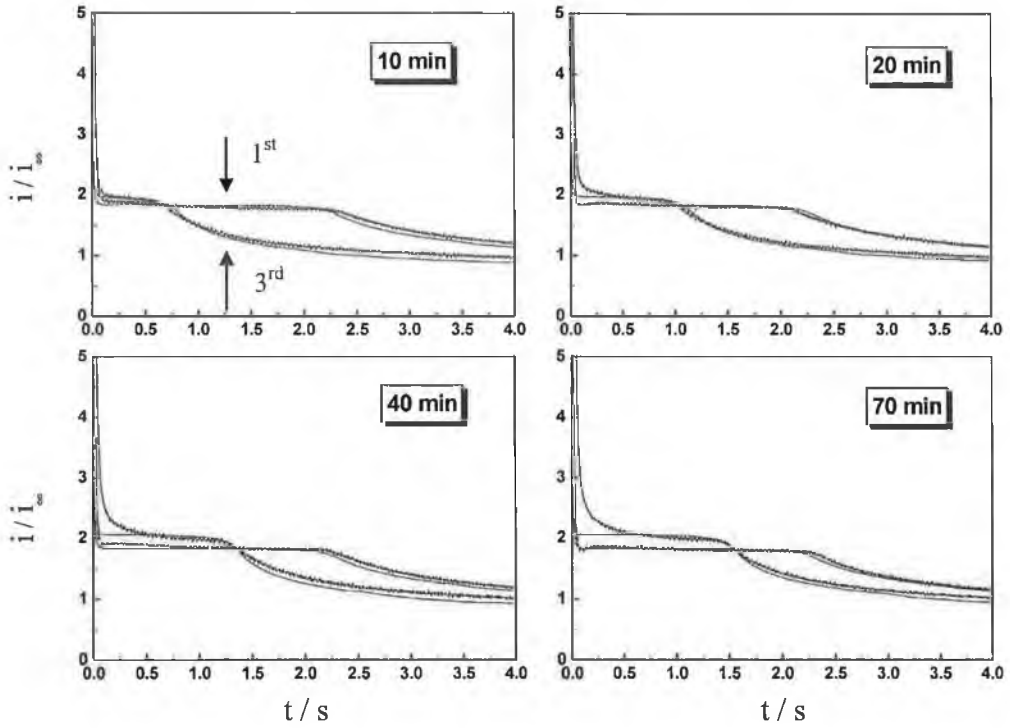

Figure 6. Current–time transients (for the first and third steps) to show the effect of waiting time (see box in each plot) on the recovery of charge carriers in a $[Os(bpy)_2(PVP)_5Cl]Cl$ film. The thick lines are the experimental results, and the thin lines are the modeled results using a value of 1.9 $\times$ 10^{-9} cm^2 s^{-1} for D_{CT}. For step 1: $d = 8.5$ μm, $D_{CT} = 0$, $\Gamma = 3.5 \times 10^{-9}$ mol cm^{-2}, $k = 1$ cm s^{-1}. For step 3 the same parameters were used, except $d = 7.5$ μm (10 and 20 min waiting time) and $d = 7$ μm (40 and 70 min waiting time).

first step there is effectively no lateral charge propagation within the film to regenerate the Os^{II} centers (because D_{CT} is comparatively small) and so the current falls. With an increase in the flux of $Ru(CN)_6^{4-}$ from the tip, due to feedback, as the distance between the tip and the surface decreases, this electrochemical "bleaching" process occurs faster and so results in an earlier fall in the probe current.

Figure 4 also shows the simulated current–time transients, which are seen to match extremely well with experiment. As discussed in the Theory, the parameters involved in this step are the concentration of redox centers in the film, the concentration and diffusion coefficient of the solution mediator, $Ru(CN)_6^{4-}$, the tip–sample distance, electron-transfer kinetics between the solution mediator and the polymer redox centers, and D_{CT}, which is taken as zero on this time scale. Having obtained d as described above, k was deduced from the initial plateau current of each transient. The best fit was obtained for diffusion-limited electron transfer between $Ru(CN)_6^{3-}$ and the Os^{II} redox centers ($k \geq 1$ cm s^{-1}). A rapid reaction is not unexpected for this outer sphere electron-transfer process for which the driving force is large, as judged by the fact that the oxidation wave observed in Figure 3 occurs at ca. 0.27 V (SCE) compared to the formal potential of the $Ru(CN)_6^{4-/3-}$ couple of 0.68 V (vs SCE).

The influence of k on the response for this first step is illustrated in Figure 4b, through simulations for a typical case of a tip–substrate distance of 8.5 μm, $D_{CT} = 0$, and $\Gamma = 3.5 \times 10^{-9}$ mol cm^{-2} and by using a redox mediator concentration ($Ru(CN)_6^{4-}$) of 0.2 mM that has a diffusion coefficient of 7.46 $\times$ 10^{-6} cm^2 s^{-1}. It can clearly be seen that the initial response converges to a limit at $k = 1$ cm s^{-1}, where the reaction is effectively controlled by feedback diffusion between the tip and the surface. Once k was known, the charge carrier concentration could be determined by varying this parameter to obtain the

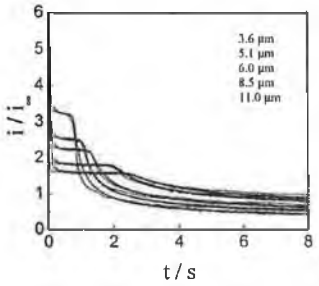

Figure 7. Current–time response (first potential step) of a Pt UME held at different distances, from 3.6 (top curve) to 11 (bottom curve) μm above a $[Os(bpy)_2(PVP)_{10}Cl]Cl$ spin cast film. The UME potential was stepped from 0 to 1.0 V (SCE) in a 0.2 mM $Ru(CN)_6^{4-}$ and 0.1 M $LiClO_4$ solution. The thick lines are the experimental results and the thinner lines are the modeled results using $D_{CT} = 0$, $\Gamma = 2.8 \times 10^{-9}$ mol cm^{-2}, $k = 1$ cm s^{-1}.

best fit to the decay of the transient between the positive feedback and hindered diffusion regimes. $\Gamma = (3.5 \pm 0.2) \times 10^{-9}$ mol cm^{-2} gave the best fit to the transients at all tip-interface distances. This corresponds reasonably well with the coverage of $(4.6 \pm 0.6) \times 10^{-9}$ mol cm^{-2} obtained from the CV measurements.

To determine D_{CT} for lateral charge propagation, the full triple potential step method was employed. Figure 5 shows simulated results for the effect of D_{CT} on the transient for step 3, compared to the characteristics for step 1, with a waiting time of 30 min (for step 2) between the two steps. The results are shown for real parameter values, comparable to those encountered for this system: $k = 1$ cm s^{-1}, $d = 8.5$ μm ($a = 12.5$ μm), $\Gamma = 3.5 \times 10^{-9}$ mol cm^{-2}, $c^* = 0.2$ mM, $D = (7.46 \pm 0.03) \times 10^{-6}$ cm^2 s^{-1}; D_{CT} was varied over 2 orders of magnitude from 10^{-11} to

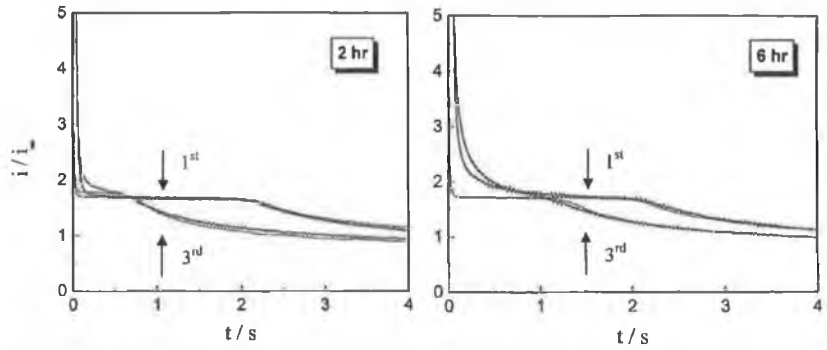

Figure 8. Current–time transients (for the first and third steps) to show the effect of waiting time (see box in each plot) on the recovery of charge carriers in a $[Os(bpy)_2(PVP)_{10}Cl]Cl$ film. The thick lines are the experimental results, and the thin lines are the results of simulations using a value of $D_{CT} = 1.3 \times 10^{-10}$ cm^2 s^{-1}. For the waiting period of 2 h, $d = 8.8$ μm and for the waiting period of 6 h, $d = 9.7$ μm. For both cases, $\Gamma = 2.8 \times 10^{-9}$ mol cm^{-2} and $k = 1$ cm s^{-1} were used for the simulations.

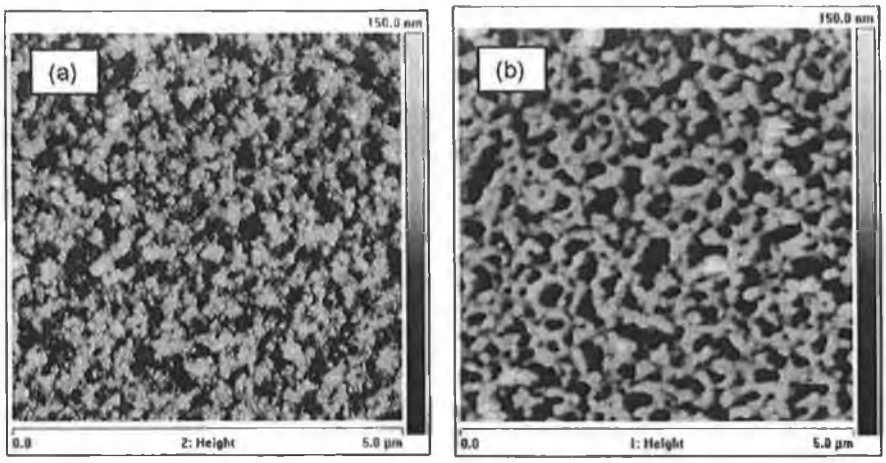

Figure 9. Tapping mode AFM topography images (5 μm × 5 μm) for (a) $[Os(bpy)_2(PVP)_5Cl]Cl$ and (b) $[Os(bpy)_2(PVP)_{10}Cl]Cl$ spin cast films.

10^{-9} cm^2 s^{-1}. It can be seen quite clearly that the recovery is highly dependent on D_{CT}: the larger the D_{CT} value, the greater the recovery of Os^{II} centers in step 2 and the greater tendency of the transient for step 3 toward that obtained in step 1. This figure also shows that the time at which the current decays between the positive feedback value and the hindered diffusion value is highly diagnostic of D_{CT}.

To determine D_{CT} experimentally, the optimum approach is to measure current–time transients for steps 1 and 3, while varying the length of the recovery period. Figure 6 shows typical experimental results for steps 1 and 3, for recovery times of 10, 20, 40, and 70 min. In these measurements, the length of the step 1 transient was shortened to 4 s (compared to the data in Figure 4a) to ensure recovery of the film on a reasonable time scale. The initial tip–sample distance was kept constant for each experiment at 8.5 μm, confirmed by simulating the tip current response with the parameters defined above. It can be seen quite clearly that the extent to which the feedback current flows in step 3 depends on the waiting period: the larger the waiting period, the greater the recovery toward the transient recorded in step 1. The data in Figure 6 were modeled for steps 1 and 3, using the parameters defined, yielding a value of (1.9 ± 0.2) × 10^{-9} cm^2 s^{-1} for D_{CT}. It can be seen in Figure 6 that the transients recorded for step 3 give a feedback current that increases slightly, with waiting time, compared to step 1. The origin of this effect is most likely slight piezo drift in the direction normal to the interface over these long waiting times. For the 10 and 20 min waiting times, the tip–sample distance was 7.5 μm, whereas for the 40 and 70 min waiting times a tip–sample distance of 7 μm was most appropriate when modeling these transients.

Under conditions where there is no physical diffusion of redox centers within the film and charge transport is due entirely to electron hopping, D_{CT} can be related to the electron self-exchange rate constant k_{ex} in the metallopolymer by the following[27]

$$D_{CT} = \lambda k_{ex} \delta^2 c_{film} \quad (28)$$

where c_{film} is the concentration of charge carriers (surface coverage is taken as 3.5 × 10^{-9} mol cm^{-2} and the thickness as 90 nm), δ is the intersite separation between redox centers (1.25 nm as measured by Vos[4]), and λ depends on the dimensionality of the system. Although charge transport is lateral, the thickness of the film dictates that charge propagation is three-dimensional, for which $\lambda = 1/6$. For $D_{CT} = 1.9 \times 10^{-9}$ cm^2 s^{-1}, a value $k_{ex} = 1.9 \times 10^9$ mol^{-1} cm^3 s^{-1} results, which is in close agreement with the value obtained by Murray and co-workers[56] for a similar type of osmium metallopolymer.

Experiments using the same protocol were also carried out on $[Os(bpy)_2(PVP)_{10}Cl]Cl$ films, in which the redox center concentration was lower than for the case discussed above. For this material, diffusion-controlled electron-transfer kinetics between the solution mediator and the redox centers was also observed ($k \gtrsim 1$ cm s^{-1}) with again a strong distance effect for step 1, as illustrated in Figure 7. To model step 1 in this case,

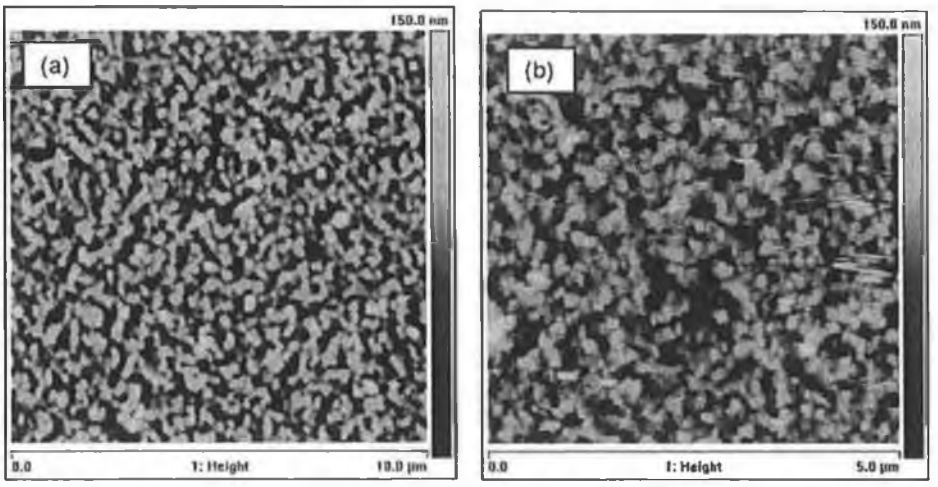

Figure 10. Contact mode AFM topography images of $[Os(bpy)_2(PVP)_5Cl]Cl$ in 0.1 M $LiClO_4$ solution at scan sizes of (a) (10 μm × 10 μm) and (b) (5 μm × 5 μm).

an Os redox center concentration of 2.8×10^{-9} mol cm^{-2} gave the best fit, which was again close to the value deduced from CV measurements (not shown). This value for the effective surface coverage of Os^{II} moieties is only slightly less than measured for $Os(bpy)_2(PVP)_5Cl]Cl$ because, as discussed below, there is a difference in the quality of the two films, with the $[Os(bpy)_2(PVP)_{10}Cl]Cl$ film showing a rougher surface and greater thickness of 100 ± 25 nm.

Figure 8 illustrates the response recorded for step 3 after waiting times of 2 and 6 h. The tip−sample distance for step 1 was 8.8 μm for the 2 h experiment and 9.7 μm for the 6 h experiment. To detect any recovery in the film, waiting times employed for step 2 were of the order of hours as compared to tens of minutes for the polymer of higher loading. Comparing the data in Figure 8 with that Figure 6, it can be seen that even after 6 h, recovery has occurred to a lesser extent than for the $[Os(bpy)_2(PVP)_5Cl]Cl$ film after 70 min. By fitting the transients in Figure 8 to the model outlined earlier, a value of $(1.3 \pm 0.5) \times 10^{-10}$ cm^2 s^{-1} for D_{CT} gave the best fit. This is an order of magnitude lower than that obtained for the $[Os(bpy)_2(PVP)_5Cl]$-Cl film. The lower value of D_{CT} for $[Os(bpy)_2(PVP)_{10}Cl]Cl$ is expected, given the greater intersite separation between redox centers, which was calculated to be 2.5 nm by Vos.[4] We have not estimated k_{ex} from eq 28 for this case because of heterogeneities in film structure highlighted below. However, the trend seen is clearly consistent with electron hopping as the limiting process in these measurements in contrast to earlier CV measurements where such effects were not apparent due to limiting ion transfer at the film/electrolyte interface.[4]

AFM Measurements. Tapping mode AFM images in air (Figure 9) indicate that these films have a fairly open, porous structure, although the $[Os(bpy)_2(PVP)_5Cl]Cl$ films appear to be more compact and homogeneous than the $[Os(bpy)_2$-$(PVP)_{10}Cl]Cl$ films. This may also be a significant factor in the larger values obtained for D_{CT} for $[Os(bpy)_2(PVP)_5Cl]Cl$ compared to $[Os(bpy)_2(PVP)_{10}Cl]Cl$. Contact mode AFM studies of $[Os(bpy)_2(PVP)_5Cl]Cl$ films under 0.1 M aqueous $LiClO_4$ solution show that the structure is maintained, as illustrated by the images in Figure 10.

Conclusions

We have shown that the SECM triple potential step technique is a viable approach for measuring the coefficient for lateral electron hopping (D_{CT}) in thin redox polymer films, and is capable of measuring values as low as 10^{-10} cm^2 s^{-1}. An advantage of the SECM approach is that it is entirely homogeneous and there are no complications from heterogeneous charge transfer from a metal electrode to the metallopolymer film, as required for conventional electrochemical techniques. Moreover, in the SECM technique, electron transfer and ion transfer occur at the same side of the film, and the perturbation in the redox state of the film occurs on relatively small length scales. This means that electron hopping is likely to be the limiting process measured.

For $[Os(bpy)_2(PVP)_5Cl]Cl$, D_{CT} was higher by an order of magnitude than for $[Os(bpy)_2(PVP)_{10}Cl]Cl$. Undoubtedly, the greater separation between redox sites in $[Os(bpy)_2(PVP)_{10}Cl]$-Cl was likely to be an important factor in the smaller value of D_{CT}, but a clear difference in film structure was also expected to have a contributory effect, with the more compact nature of the $[Os(bpy)_2(PVP)_5Cl]Cl$ films leading to a higher D_{CT} value.

Acknowledgment. We thank the EU Human Potential Program SUSANA (Supramolecular Self-Assembly of Interfacial Nanostructures), contract HPRN-CT-2002-00185, for funding. J.C. also thanks the financial support from CICYT (Ministry of Science and Technology of Spain) and FEDER (European Funds for Regional Development) under project No. MAT2002-00646.

References and Notes

(1) Anson, F. C.; Savéant, J.-M.; Shigehara, K. *J. Electroanal. Chem.* **1988**, *145*, 423.
(2) Feldman, B. J.; Ewing, A.; Murray, R. W. *J. Electroanal. Chem.* **1985**, *194*, 63.
(3) Forster, R. J.; Vos, J. G. *Electrochim. Acta* **1992**, *37*, 159.
(4) Forster, R. J.; Vos, J. G. *Langmuir* **1994**, *10*, 4330.
(5) Xie, Y.; Anson, F. C. *J. Electroanal. Chem.* **1995**, *384*, 145.
(6) Doherty, A. P.; Vos, J. G. *Anal. Chim. Acta* **1997**, *344*, 159.
(7) Pickup, P. G.; Kuo, K. N.; Murray, R. W. *J. Electrochem. Soc.* **1983**, *130*, 2205.
(8) Wilson, R. W.; Cubitt, R.; Glidle, A.; Hillman, A. R.; Saville, P. M.; Vos, J. G. *Electrochim. Acta* **1999**, *44*, 3533.
(9) Hogan, C. F.; Forster, R. J. *Anal. Chim. Acta* **1999**, *396*, 13.
(10) Ju, H.; Gong, Y.; Zhu, H. *Anal. Sci.* **2001**, *17*, 59.
(11) Forster, R. J.; Figgemeir, E.; Lees, A. C.; Hjelm, J.; Vos, J. G. *Langmuir* **2000**, *16*, 7867.
(12) Murray, R. W. *Molecular Design of Electrode Surfaces, Techniques of Chemistry*; Wiley-Interscience: Toronto, 1992; Vol. XXII.

(13) Schmel, R. H.; Murray, R. W. *J. Electroanal. Chem.* **1983**, *152*, 97.
(14) Jernigan, J. C.; Murray, R. W. *J. Am. Chem. Soc.* **1987**, *109*, 1738.
(15) Sosnoff, C. S.; Sullivan, M.; Murray, R. W. *J. Phys. Chem.* **1994**, *98*, 13643.
(16) Buttry, D. A.; Anson, F. C. *J. Electroanal. Chem.* **1981**, *130*, 333.
(17) Buttry, D. A.; Anson, F. C. *J. Am. Chem. Soc.* **1983**, *105*, 685.
(18) Anson, F. C.; Blauch, D. N.; Savéant, J.-M.; Shu, C.-F. *J. Am. Chem. Soc.* **1991**, *113*, 1922.
(19) Sabatani, R.; Anson, F. C. *J. Phys. Chem.* **1993**, *97*, 10158.
(20) Andrieux, C. P.; Dumas-Bouchiat, J. M.; Savéant, J. M. *J. Electroanal. Chem.* **1980**, *114*, 159.
(21) Andrieux, C. P.; Savéant, J. M. *J. Electroanal. Chem.* **1980**, *111*, 377.
(22) Savéant, J. M. *J. Electroanal. Chem.* **1987**, *238*, 1.
(23) Buck, R. P. *J. Electroanal. Chem.* **1988**, *243*, 279.
(24) Buck, R. P. *J. Phys. Chem.* **1988**, *92*, 4196.
(25) Buck, R. P.; Mădăraş, M. B. *J. Electroanal. Chem.* **1993**, *362*, 33.
(26) Kaneko, M. *Prog. Polm. Sci.* **2001**, *26*, 1101.
(27) Lyons, M. E G. In *Fundamentals*; Electroactive Polymer Chemistry, Part 1; Lyons, M. E. G., Ed.; Plenum Press: New York, 1994; Chapter 1, pp 1−226.
(28) Musiani, M. *Electrochim. Acta* **1990**, *35*, 1665.
(29) Larsson, H.; Sharp, M. *J. Electroanal. Chem.* **1995**, *381*, 133.
(30) Aoki, A.; Miyashita, T. *Colloids Surf. A: Physiochem. Eng. Aspects* **2002**, *198−200*, 671.
(31) Chidsey, C. E. D. *Science* **1986**, *231*, 25.
(32) Dalton, E. F.; Surridge, N. A.; Jernigan, J. C.; Wilbourn, K. O.; Facci, J. S.; Murray, R. W. *Chem. Phys.* **1990**, *141*, 143.
(33) Forster, R. J.; Keyes, T. E.; Majda, M. *J. Phys. Chem. B* **2000**, *104*, 4425.
(34) Wittek, M.; Moller, G.; Johnson, M. J.; Majda, M. *Anal. Chem.* **2001**, *73*, 870.
(35) Feldman, B. J.; Murray, R. W. *Anal. Chem.* **1986**, *58*, 2844.
(36) Feldman, B. J.; Feldberg, S. W.; Murray, R. W. *J. Phys. Chem.* **1987**, *91*, 6558.
(37) Forster, R. J.; Keyes, T. E.; Bond, A. M. *J. Phys. Chem. B* **2000**, *104*, 6389.
(38) Slevin, C. J.; Unwin, P. R. *J. Am. Chem. Soc.* **2000**, *122*, 2597.
(39) Zhang, J.; Unwin, P. R. *J. Am. Chem. Soc.* **2002**, *124*, 2379.
(40) Zhang, J.; Unwin, P. R. *Phys. Chem. Chem. Phys.* **2002**, *4*, 3814.
(41) Mandler, D.; Unwin, P. R. *J. Phys. Chem. B* **2003**, *107*, 407.
(42) Zhang, J.; Barker, A. L.; Mandler, D.; Unwin, P. R. *J. Am. Chem. Soc.* **2003**, *125*, 9312.
(43) Zhang, J.; Slevin, C. J.; Morton, C.; Scott, P.; Walton, D. J.; Unwin, P. R. *J. Phys. Chem. B* **2001**, *105*, 11120.
(44) Quinn, B. M.; Prieto, I.; Haram, S. K.; Bard, A. J. *J. Phys. Chem. B* **2001**, *105*, 7474.
(45) Liljeroth, L.; Quinn, B. M.; Ruiz, V.; Konturri, K. *Chem. Commun.* **2003**, 1570.
(46) (a) Wolf, D. E. In *Fluorescence Microscopy of Living Cells in Culture*; Taylor, D. L., Wang, Y. L., Eds.; Academic Press: San Diego, 1989; Part B, Chapter 10, p 271. (b) Elson, E. L.; Qian, H. In *Fluorescence Microscopy of Living Cells in Culture*; Taylor, D. L., Wang, Y. L., Eds.; Academic Press: San Diego, 1989; Part B, Chapter 11, p 307.
(47) Auch, M.; Ficher, B.; Möhwald, H. *Colloid Surf. A* **2000**, *164*, 39.
(48) Mullineaux, C. W.; Tobin, M. J.; Jones, G. R. *Nature* **1997**, *390*, 421.
(49) Axelrod, D.; Koppel, D. E.; Schlessinger, J.; Elson, E.; Webb, W. W. *Biophys. J.* **1976**, *16*, 1055.
(50) Unwin, P. R.; Bard, A. J. *J. Phys. Chem.* **1991**, *95*, 7814.
(51) Unwin, P. R.; Bard, A. J. *J. Phys. Chem.* **1992**, *96*, 5035.
(52) Newman, J. *J. Electrochem. Soc.* **1966**, *113*, 501.
(53) Saito, Y. *Rev. Polarogr. Jpn.* **1968**, *15*, 177−187.
(54) Forster, R. J.; Vos, J. G. *Macromolecules* **1990**, *23*, 4372.
(55) Kelly, D. M.; Vos, J. G. *J. Electroanal. Chem.* **1996**, *41*, 1825.
(56) Dalton, E. F.; Surridge, N. A.; Jernigan, J. C.; Wilbourn, K. O.; Facci, J. S.; Murray, R. W. *Chem. Phys.* **1990**, *141*, 143.

Appendix G

Molecular Orbital Energy Level Diagram

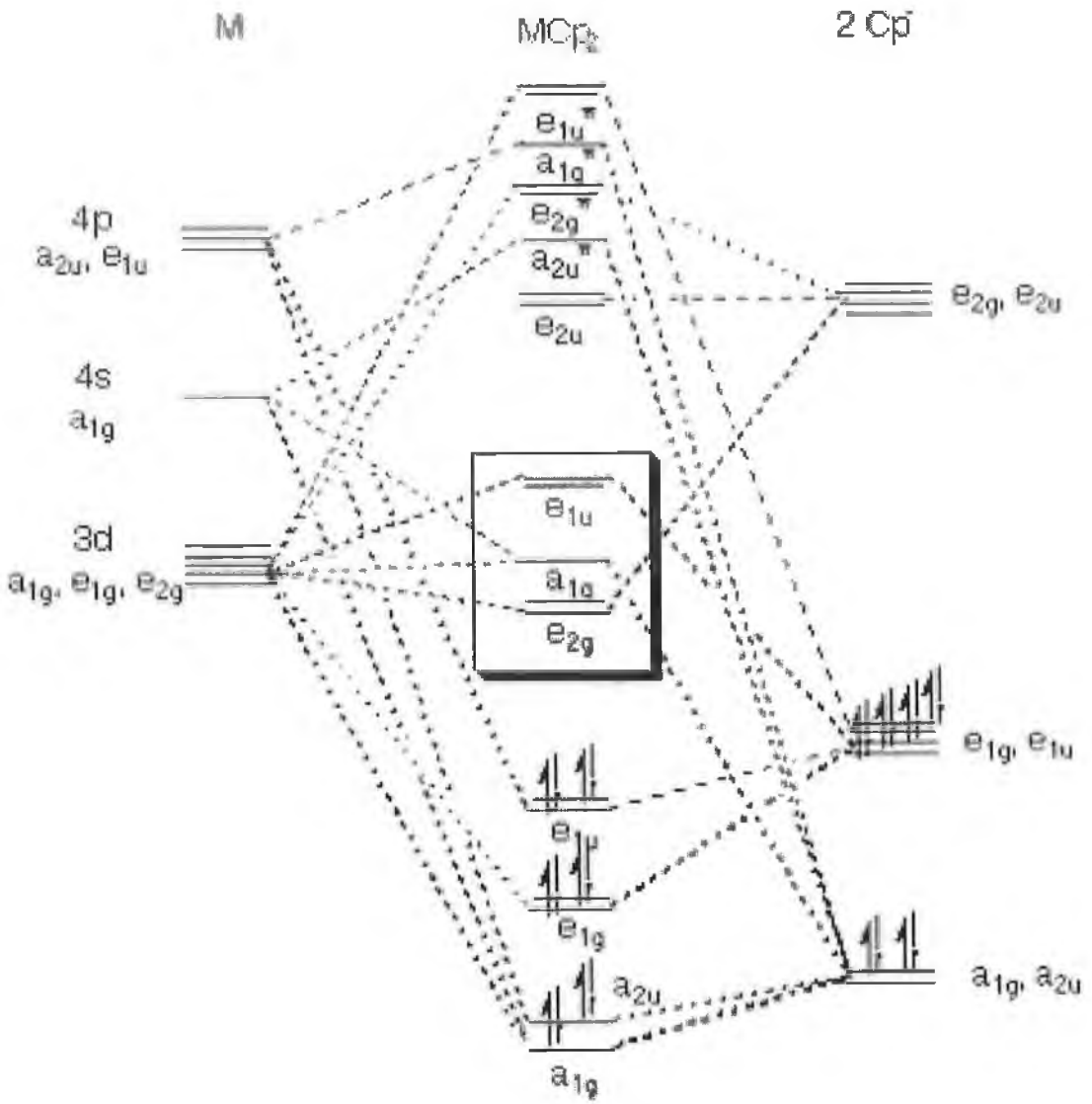

The MO diagram for generic metallocenes, Cp_2M is shown above.